

1 LEVERAGING MULTI-MESSENGER ASTROPHYSICS FOR DARK MATTER SEARCHES

By

Daniel Nicholas Salazar-Gallegos

A DISSERTATION

Submitted to
Michigan State University
in partial fulfillment of the requirements
for the degree of

Physics—Doctor of Philosophy
Computational Mathematics in Science and Engineering—Dual Major

Today

ABSTRACT

3 I did Dark Matter with HAWC and IceCube. I also used Graph Neural Networks

⁴ Copyright by

⁵ DANIEL NICHOLAS SALAZAR-GALLEGOS

⁶ Today

ACKNOWLEDGMENTS

8 I love my friends. Thanks to everyone that helped me figure this out. Amazing thanks to the people
9 at LANL who supported me. Eames, etc Dinner Parties Jenny and her child Kaydince Kirsten, Pat,
10 Andrea Family. You're so far but so critical to my formation. Unconditional love. Roommate

TABLE OF CONTENTS

12	LIST OF TABLES	vii
13	LIST OF FIGURES	ix
14	LIST OF ABBREVIATIONS	xx
15	CHAPTER 1 INTRODUCTION	1
16	CHAPTER 2 DARK MATTER IN THE COSMOS	2
17	2.1 Introduction	2
18	2.2 Dark Matter Basics	3
19	2.3 Evidence for Dark Matter	4
20	2.4 Searching for Dark Matter: Particle DM	11
21	2.5 Sources for Indirect Dark Matter Searches	16
22	2.6 Multi-Messenger Dark Matter	18
23	CHAPTER 3 HIGH ALTITUDE WATER CHERENKOV (HAWC) OBSERVATORY	21
24	3.1 The Detector	21
25	3.2 Event Reconstruction	26
26	3.3 Background Estimation: Direct Integration	34
27	CHAPTER 4 GLORY DUCK: MULTI-WAVELENGTH SEARCH FOR DARK MATTER ANNIHILATION TOWARDS DWARF SPHEROIDAL GALAXIES	36
28	4.1 Introduction	36
29	4.2 Dataset and Background	38
30	4.3 Analysis	40
31	4.4 Likelihood Methods	44
32	4.5 HAWC Results	51
33	4.6 Glory Duck Combined Results	53
34	4.7 HAWC Systematics	58
35	4.8 <i>J</i> -factor distributions	60
36	4.9 Discussion and Conclusions	66
39	CHAPTER 5 MULTITHREADING HAWC ANALYSES FOR DARK MATTER SEARCHES	70
40	5.1 Introduction	70
41	5.2 Dataset and Background	70
42	5.3 Analysis	72
43	5.4 Likelihood Methods	76
44	5.5 Computational Methods: Multithreading	76
45	5.6 Analysis Results	82
46	5.7 Systematics	87
47	5.8 Conclusion and Discussion	87

49	CHAPTER 6	ICECUBE NEUTRINO OBSERVATORY	89
50	6.1	The Detector	90
51	6.2	Track Event Reconstruction	92
52	6.3	Background	92
53	6.4	North Sky Tracks	92
54	CHAPTER 7	HEAVY DARK MATTER ANNIHILATION SEARCH WITH ICE-CUBE'S NORTH SKY TRACK DATA	93
56	7.1	Introduction	93
57	7.2	Dataset and Background	93
58	7.3	Analysis	95
59	7.4	Likelihood Methods	104
60	7.5	Background Simulation	104
61	7.6	Signal Recovery	122
62	7.7	Systematics	125
63	7.8	Conclusions	128
64	CHAPTER 8	NU DUCK: CONCLUSIONS AND FUTURE DIRECTIONS	130
65	8.1	Conclusions	130
66	8.2	Future Directions: Multi-Messenger Dark Matter Search	131
67	APPENDIX A	MULTI-EXPERIMENT SUPPLEMENTARY FIGURES	133
68	APPENDIX B	MULTITHREADING DARK MATTER ANALYSES SUPPLEMENTARY MATERIAL	134
70	B.1	Remaining Spectral Models	134
71	B.2	<code>mpu_analysis.py</code>	135
72	B.3	Comparison with Glory Duck	144
73	APPENDIX C	ICECUBE HEAVY DARK MATTER ANALYSIS SUPPLEMENTARY MATERIAL	147
75	C.1	Docker Image for Oscillating Neutrino Spectra	147
76	C.2	Spline Fitting Statuses	150
77	C.3	Neutrino Composite Spectra	151
78	C.4	Segue 1 And Ursa Major II Signal Recovery	152
79	C.5	n_s Sensitivities	158
80	BIBLIOGRAPHY		160

LIST OF TABLES

82	Table 3.1	Definitions of f_{hit} energy estimator bins. Bins are defined by the fraction of available PMTs that are triggered during an air shower event. The angular resolution, Θ_{68} , is the bin containing 68% of events [34].	30
85	Table 4.1	Summary of the relevant properties of the dSphs used in the present work. Column 1 lists the dSphs. Columns 2 and 3 present their heliocentric distance and galactic coordinates, respectively. Columns 4 and 5 report the J -factors of each source given from the \mathcal{GS} and \mathcal{B} independent studies and their estimated $\pm 1\sigma$ uncertainties. The values $\log_{10} J$ (\mathcal{GS} set) [59] correspond to the mean J -factor values for a source extension truncated at the outermost observed star. The values $\log_{10} J$ (\mathcal{B} set) [63] are provided for a source extension at the tidal radius of each dSph. Bolded sources are within HAWC's field of view and provided to the Glory Duck analysis.	45
94	Table 4.2	Summary of dSph observations by each experiment used in this work. A '-' indicates the experiment did not observe the dSph for this study. For Fermi-LAT, the exposure at 1 GeV is given. For HAWC, $ \Delta\theta $ is the absolute difference between the source declination and HAWC latitude. HAWC is more sensitive to sources with smaller $ \Delta\theta $. For IACTs, we show the zenith angle range, the total exposure, the energy range, the angular radius θ of the signal or ON region, the ratio of exposures between the background-control (OFF) and signal (ON) regions (τ), and the significance of gamma-ray excess in standard deviations, σ	46
103	Table 5.1	Summary of the relevant properties of the dSphs used in the present work. Column 1 lists the dSphs. Columns 2 and 3 present their heliocentric distance and galactic coordinates, respectively. Column 4 reports the J -factors of each source given from the \mathcal{LS} studies and estimated $\pm 1\sigma$ uncertainties. The values $\log_{10} J$ (\mathcal{LS} set) [80] correspond to the mean J -factor values for a source extension truncated at 0.5°	76
109	Table 5.2	Timing summaries for analyses for serial and multithreaded processes. M tasks is the number of functional-parallel tasks ran for the computation. $T_{p,c}$ is a single run time in hours:minutes:seconds for runs utilizing p nodes and c threads. Runs are run interactively on the same computer to maximize consistency. Empty entries are indicated with '-'. (\cdot) entries are estimated entries extrapolated from data earlier in the column.	80
115	Table 5.3	Speed up summaries for analyses for serial and multithreaded processes. M tasks is the number of functional-parallel tasks ran for the computation. $S_{p,c}$ is a single speedup comparison for runs utilizing p nodes and c threads. $[\cdot]$ are the estimated speedups calculated from Tab. 5.2, Eq. (5.7), and Eq. (5.4). Empty entries are indicated with '-'.	82

120	Table 7.1 Spline err tolerances used for input in particle physics component to Eq. (4.1).	
121	Column 1 is the DM annihilation channel being fit. Columns 2, 3, and 4	
122	are the tolerances for "GOOD" (pass), "OK" requires inspection, and "FAIL"	
123	(tune and refit) respectively. Column 5 has the X ranges over which the error	
124	is evaluated. MAX/MIN [.,.] takes the maximum or minimum of the two	
125	enclosed values.	101
126	Proof I know how to include	

LIST OF FIGURES

128	Figure 2.1	Rotation curve fit to NGC 6503 from [7]. Dashed line is the contribution 129 from visible matter. Dotted curves are from gas. Dash-dot curves are from 130 dark matter (DM). Solid line is the composite contribution from all matter 131 and DM sources. Data are indicated with bold dots with error bars. Data 132 agree strongly with a matter + DM composite prediction.	5
133	Figure 2.2	Light from distant galaxy is bent in unique ways depending on the distribution 134 of mass between the galaxy and Earth. Yellow dashed lines indicate where 135 the light would have gone if the matter were not present [8].	7
136	Figure 2.3	(left) Optical image of galactic cluster 1E0657-558. (right) X-ray image of the 137 cluster with redder meaning hotter and higher baryon density. (both) Green 138 contours are reconstruction of gravity contours from weak lensing. White 139 rings are the best fit mass maxima at 68.3%, 95.5%, and 99.7% confidence. 140 The matter maxima of the clusters are clearly separated from x-ray maxima. [9]	8
141	Figure 2.4	Plank CMB sky. Sky map features small variations in temperature in primor- 142 dial light. These anisotropies are used to make inferences about the universe's 143 energy budget and developmental history. [10]	9
144	Figure 2.5	Observed Cosmic Microwave Background power spectrum as a function of 145 multipole moment from Plank [10]. Blue line is best fit model from Λ CDM. 146 Red points and lines are data and error, respectively.	10
147	Figure 2.6	Predicted power spectra of CMB for different $\Omega_m h^2$ values for fixed baryon 148 density from [11]. (left) Low $\Omega_m h^2$ increases the prominence of first and 149 second peaks. (middle) $\Omega_m h^2$ is most similar to the observed power spectrum. 150 The second and third peaks are similar in height. (right) $\Omega_m h^2$ is large which 151 suppresses the first peak and raises the prominence of the third peak.	10
152	Figure 2.7	The Standard Model (SM) of particle physics. Figure taken from http://www.quantumdiaries.org/2014/03/14/the-standard-model-a-beautiful-but-flawed-theory/	12
155	Figure 2.8	Simplified Feynman diagram demonstrating with different ways DM can 156 interact with SM particles. The 'X's refer to the DM particles whereas the 157 SM refer to fundamental particles in the SM. The large circle in the center 158 indicates the vertex of interaction and is purposely left vague. The colored 159 arrows refer to different directions of time as well as their respective labels. 160 The arrows indicate the initial and final state of the DM -SM interaction in time.	13

161	Figure 2.9 A single jet event in ATLAS detector from 2017 [16]. Jet momentum was 162 observed to be 1.9 TeV. Missing transverse momentum was observed to be 163 1.9 TeV compared to the initial transverse momentum of the event was 0. 164 Implied MET is traced by a red dashed line in event display.	14
165	Figure 2.10 More detailed pseudo-Feynman diagram of particle cascade from dark matter 166 annihilation into 2 quarks. The quarks hadronize and down to stable particles 167 like γ or the anti-proton (p^-). Diagram pulled from ICRC 2021 presentation 168 on DM annihilation search [17].	15
169	Figure 2.11 Dark Matter (DM) decay spectrum for $b\bar{b}$ initial state and γ final state. Redder 170 spectra are for larger DM masses. Bluer spectra are light DM masses. x is a 171 unitless factor defined as the ratio of the mass of DM, m_χ , and the final state 172 particle energy E_γ . Figure from [19].	17
173	Figure 2.12 Different dark matter density profiles compared. Some models produce ex- 174 ceptionally large densities at small r [20].	18
175	Figure 2.13 The Milky Way Galaxy in photons (γ) and neutrinos (ν) [22]. The Galactic 176 center is at $l=0^\circ$ and is the brightest region in all panels. (top) An Optical 177 color image of the Milky Way galaxy seen from Earth. Clouds of gas and dust 178 obscure some light from stars. (2nd down) Integrated flux of γ -rays observed 179 by the Fermi-LAT telescope [23]. (middle) Expected neutrino emission 180 that corresponds with Fermi-LAT observations. (2nd up) Expected neutrino 181 emission profile after considering detector systematics of IceCube. (bottom) 182 Observed neutrino emission from region of the galactic plane. Substantial 183 neutrino emission was detected.	19
184	Figure 2.14 Dark Matter annihilation spectra for different final state particle and standard 185 model annihilation channels [24]. Photons (red), e^\pm (green), \bar{p} (blue), ν (black).	20
186	Figure 3.1 Photo of the HAWC detector that I took on May 17, 2023. Main array is 187 centered in the photo and comprised of the larger tanks. Outriggers are the 188 smaller tanks around the main array.	21
189	Figure 3.2 A particle physics illustration of high energy particle showers. Left shower is 190 an electromagnetic shower from a high energy gamma-ray. Most particles in 191 the shower will be a combination of photons and charged leptons, in this case 192 electrons (e). Right figure shows a cosmic ray particle shower. The cosmic 193 ray will produce many more types of particles including pions (π), neutrinos, 194 and charged leptons. Figure pulled from [26].	22
195	Figure 3.3 The WCDs. Left image features several WCDs looking from within the main 196 array of HAWC. Right image shows a schematic of a WCD pulled from [25].	23

197	Figure 3.4	Overview of HAWC control and data electronics. The LoToT and HiToT threshold signals are discussed in Section 3.1.2. Figure from [27]	24
199	Figure 3.5	Schematic of data flow in HAWC data acquisition and online processing system. Pulled from [29].	25
201	Figure 3.6	How HAWC FEB intially processes analog PMT signals. Signals are split through an amplifier and discriminator circuit. Each path is designated for ei- ther the HIGH or LOW threshold for the signal. The 2-edge event corresponds to LOW, while the 4 edge corresponds to HIGH.	25
205	Figure 3.7	An particle shower incident on WCDs. Secondary particles of an air shower travel in a cone centered on primary incident particle. Reconstruction of the initial angle is possible with arrival time of hits in PMTs inside WCDs. Figure from [33].	27
209	Figure 3.8	Charge deposition in each PMT for a reconstructed gamma-ray event. WCDs are outlined in black surrounding the 4 smaller circles that represent PMTs. The color scale indicates the charge deposition in each PMT. The best shower core fit from SFCF is noted with a red star in the center of the dashed circle [34].	28
213	Figure 3.9	Simulated normalized energy distribution of each f_{hit} bin defined in Tab. 3.1. Monte Carlo simulation of gamma-rays with $E^{-2.63}$ spectral shape and sim- ulated source at 20° declination. Figure from [34].	30
216	Figure 3.10	Neural Network energy estimator performance compared to true energy. The dotted line is the identity line where the estimator and injection agree. Gam- ma/hadron separation cuts were applied with the energy estimation. Figure pulled from [37]	32
220	Figure 3.11	Lateral distribution functions (LDFs) for cosmic ray (left) and a photon can- didate from the Crab Nebula (right). Cosmic ray LDF has clearly isolated hits far from the reconstructed shower core. Gamma-ray shower shows a more cuspy event [34].	33

224	Figure 4.1 Sensitivities of five gamma-ray experiments compared to percentages of the 225 Crab nebula's emission and dark matter annihilation. Solid lines present 226 estimated sensitivities to power law spectra [FACT CHECK THIS]for each 227 experiment. Green lines are Fermi-LAT sensitivities where lighter green is 228 the sensitivity to the galactic center and dark green is its sensitivity to higher 229 declinations. Orange, red, and purple solid lines represent the MAGIC, HESS, 230 and VERITAS 50 hour sensitivities respectively. The maroon and brown lines 231 are the HAWC 1 year and 5 year sensitivities. Across four decades of gamma- 232 ray energy, these experiments have similar sensitivities on the order 10^{-12} 233 erg cm $^{-2}$ s $^{-1}$. The dotted lines are estimated dark matter fluxes assuming 234 $m_\chi = 5$ TeV DM annihilating to bottom quarks (red), tau leptons (blue), 235 and W bosons (green). Faded gray lines outline percentage flux of the Crab 236 nebula. Figure is an augmented version of [40]	37
237	Figure 4.2 Effect of Electroweak (EW) corrections on expected DM annihilation spec- 238 trum for $\chi\chi \rightarrow W^-W^+$. Solid lines are spectral models that consider EW 239 corrections. Dash-dot lines are spectral models without EW corrections. Red 240 lines are models for $M_\chi = 1$ TeV. Blue lines represent models for $M_\chi = 100$ 241 TeV. All models are sourced from the PPPC4DMID [58].	41
242	Figure 4.3 $\frac{dJ}{d\Omega}$ maps for Segue1 (top) and Coma Berenices (bottom). Origin is centered 243 on the specific dwarf spheroidal galaxies (dSph). X and Y axes are the angular 244 separation from the center of the dwarf. Profile is truncated at the scale radius. 245 Plots of the remaining 11 dSph HAWC studied are linked in Fig. A.1.	43
246	Figure 4.4 Illustration of the combination technique showing a comparison between 247 $-2 \ln \lambda$ provided by four instruments (colored lines) from the observation 248 of the same dSph without any J nuisance and their sum, <i>i.e.</i> the resulting 249 combined likelihood (thin black line). According to the test statistics of 250 Equation (4.7), the intersection of the likelihood profiles with the line $-2 \ln \lambda$ 251 = 2.71 indicates the 95% C.L. upper limit on $\langle \sigma v \rangle$. The combined likelihood 252 (thin black line) shows a smaller value of upper limit on $\langle \sigma v \rangle$ than those 253 derived by individual instruments. We also show how the uncertainties on 254 the J factor effects the combined likelihood and degrade the upper limit on 255 $\langle \sigma v \rangle$ (thick black line). All likelihood profiles are normalized so that the global 256 minimum $\widehat{\langle \sigma v \rangle}$ is 0. We note that each profile depends on the observational 257 conditions in which a target object was observed. The sensitivity of a given 258 instrument can be degraded and the upper limits less constraining if the 259 observations are performed in non-optimal conditions such as a high zenith 260 angle or a short exposure time.	49
261	Figure 4.5	52

262	Figure 4.6 HAWC TS values for best fit $\langle\sigma v\rangle$ versus m_χ for seven SM annihilation channels with J factors from \mathcal{GS} . The solid black line shows the combined best fit TS values. The colored, dashed lines are the TS values for each of the 13 sources HAWC studied.	53
266	Figure 4.7 HAWC Brazil bands at 95% confidence level on $\langle\sigma v\rangle$ versus DM mass for seven annihilation channels with J -factors from \mathcal{GS} [69]. The solid line represents the combined limit from 13 dSphs. The dashed line is the expected limit. The green band is the 68% containment. The yellow band is the 95% containment.	54
271	Figure 4.8 Upper limits at 95% confidence level on $\langle\sigma v\rangle$ in function of the DM mass for eight annihilation channels, using the set of J factors from Ref. [69] (\mathcal{GS} set in Table 4.1). The black solid line represents the observed combined limit, the black dashed line is the median of the null hypothesis corresponding to the expected limit, while the green and yellow bands show the 68% and 95% containment bands. Combined upper limits for each individual detector are also indicated as solid, colored lines. The value of the thermal relic cross-section in function of the DM mass is given as the red dotted-dashed line [70].	55
280	Figure 4.9 Same as Fig. 4.8, using the set of J factors from Ref. [63, 71] (\mathcal{B} set in Table 4.1).	56
281	Figure 4.10 Comparisons of the combined limits at 95% confidence level for each of the eight annihilation channels when using the J factors from Ref. [69] (\mathcal{GS} set in Table 4.1), plain lines, and the J factor from Ref. [63, 71] (\mathcal{B} set in Table 4.1), dashed lines. The cross-section given by the thermal relic is also indicated [70].	58
285	Figure 4.11 Comparisons of the combined limits at 95% confidence level for a point source analysis and extended source using [69] \mathcal{GS} J-factor distributions and PPPC [58] annihilation spectra. Shown are the limits for Segue1 which will have the most significant impact on the combined limit. 6 of the 7 DM annihilation channels are shown. Solid lines are extended source studies. Dashed lines are point source studies. Overall, the extended source analysis improves the limit by a factor of 2.	60
292	Figure 4.12 Same as Fig. 4.11 on Coma Berenices. This dSph also contributes significantly to the limit. The limits are identical in this case.	61
294	Figure 4.13 Comparison of combined limits when correcting for HAWC's pointing systematic. All DM annihilation channels are shown. The solid black line is the ratio between published limit to the declination corrected limit. The blue solid line or "Combined_og" represented the limits computed for Glory Duck. The solid orange line or "Combined_ad" represented the limits computed after correcting for the pointing systematic.	62

300	Figure 4.14 Differential map of dJ/Ω from model built in Section 4.8.1 and profiles provided directly from authors. (Top) Differential from Segue1. (bottom) Differential from Coma Berenices. Note that their scales are not the same. Segue1 shows the deepest discrepancies which is congruent with its large uncertainties. Both models show anuli where unique models become apparent.	63
305	Figure 4.15 HAWC limits for Coma Berenices (top) and Segue1 (bottom) for two different map sets. Blue lines are limits calculated on maps with poor model representation. Orange lines are limits calculated on spatial profiles provided by the authors of [59]. Black line is the ratio of the poor spatial model limits to the corrected spatial models. The left y-axis measures $\langle\sigma v\rangle$ for the blue and orange lines. The right y-axis measures the ratio and is unitless.	64
311	Figure 4.16 Comparisons between the J -factors versus the angular radius for the computation of J factors from Ref. [69] (\mathcal{GS} set in Table 4.1) in blue and for the computation from Ref. [63, 71] (\mathcal{B} set in Tab. 4.1) in orange. The solid lines represent the central value of the J -factors while the shaded regions correspond to the 1σ standard deviation.	66
316	Figure 4.17 Comparisons between the J -factors versus the angular radius for the computation of J factors from Ref. [69] (\mathcal{GS} set in Tab. 4.1) in blue and for the computation from Ref. [63, 71] (\mathcal{B} set in Tab. 4.1) in orange. The solid lines represent the central value of the J -factors while the shaded regions correspond to the 1σ standard deviation.	67
321	Figure 5.1 Spectral hypotheses from PPPC [58] and HDM [79] for DM annihilation: $\chi\chi \rightarrow W^-W^+$. Solid lines are spectral models with EW corrections from the PPPC. Dash-dot lines are spectral models from HDM. Red lines are models for $M_\chi = 1$ TeV. Blue lines represent models for $M_\chi = 100$ TeV.	72
325	Figure 5.2 Photon spectra for $\chi\chi \rightarrow \gamma\gamma$ (left) and $\chi\chi \rightarrow ZZ$ (right) after Gaussian convolution of line features. Both spectra have δ -features at photon energies equal to the DM mass. Bluer lines are annihilation spectra with lower DM mass. Redder lines are spectra from larger DM mass. All spectral models are sourced from the Heavy Dark Matter models [79]. Axes are drawn roughly according to the energy sensitivity of HAWC.	73
331	Figure 5.3 $\frac{dJ}{d\Omega}$ maps for Coma Berenices, Draco, Segue1, and Sextans. Columns are divided for the $\pm 1\sigma$ uncertainties in $dJ/d\Omega$ around the mean value from \mathcal{LS} [80]. Origin is centered on the specific dwarf spheroidal galaxies (dSph). θ and ϕ axes are the angular separation from the center of the dwarf. Profiles are truncated at 1° and flattened beyond.	75

336	Figure 5.4	Infographic on how jobs and DM computation was organized in Section 4.3. Jobs were built for each permutation of CHANS and SOURCES shown by the left block in the figure. Each job, which took on the order 2 hrs to compute, had the following work flow: 1. Import HAWC analysis software, 2 min to run. 2. Load HAWC count maps, 5 min to run. 3. Load HAWC energy and spatial resolutions, 4 min. 5. Load DM spatial source templates and spectral models, less than 1 s. 6. Perform likelihood fit on data and model, about 8 min per DM mass. 7. Write results to file, less than 1s.	77
344	Figure 5.5	Graphic of Gustafson parallel coding pattern. f_s is the fraction of a program, in time, spent on serial computation. f_p is the fraction of computing time that is parallelizable. T_p is the total time for a parallel program to run. T_1 is the total time for a parallel program to run if only 1 processor is allocated. P_N is the N -th processor where it's row is the computation the processor performs. The Gustafson pattern is most similar to what is implemented for this analysis. Figure is pulled from [82].	78
351	Figure 5.6	Task chart for one multithreaded job developed for this project. Green blocks indicate a shared resource across the threads AND computation performed serially. Red blocks indicate functional parallel processing within each thread. 3 threads are represented here, yet many more can be employed during the full analysis. Jobs are defined by the SOURCE as these require unique maps to be loaded into the likelihood estimator. The m_χ , CHAN, and $\langle\sigma v\rangle$ variables are entered into the thread pool and allocated as evenly as possible across the threads.	80
359	Figure 5.7	HAWC upper limits at 95% confidence level on $\langle\sigma v\rangle$ versus m_χ for $\chi\chi \rightarrow b\bar{b}$, $t\bar{t}$, $u\bar{u}$, $d\bar{d}$, $s\bar{s}$, $c\bar{c}$, gg , W^+W^- , and hh . Limits are with \mathcal{LS} J -factors [80]. The solid line represents the observed combined limit. Dashed lines represent limits from individual dSphs.	83
363	Figure 5.8	HAWC upper limits at 95% confidence level on $\langle\sigma v\rangle$ versus m_χ for $\chi\chi \rightarrow \nu_e \overline{\nu}_e$, $\nu_\mu \overline{\nu}_\mu$, $\nu_\tau \overline{\nu}_\tau$, $e\bar{e}$, $\mu\bar{\mu}$, $\tau\bar{\tau}$, $\gamma\gamma$ and ZZ . Limits use \mathcal{LS} J -factors [80]. The solid line represents the observed combined limit. Dashed lines represent limits from individual dSphs.	84
367	Figure 5.9	HAWC TS values for best fit $\langle\sigma v\rangle$ versus m_χ for SM annihilation channels: $\chi\chi \rightarrow b\bar{b}$, $t\bar{t}$, $u\bar{u}$, $d\bar{d}$, $s\bar{s}$, $c\bar{c}$, gg , W^+W^- , and hh . Limits use \mathcal{LS} J -factors. The solid black line shows the combined best fit TS values. The colored, dashed lines are the TS values from each dSph.	85
371	Figure 5.10	HAWC TS values for best fit $\langle\sigma v\rangle$ versus m_χ for SM annihilation channels: $\chi\chi \rightarrow \nu_e \overline{\nu}_e$, $\nu_\mu \overline{\nu}_\mu$, $\nu_\tau \overline{\nu}_\tau$, $e\bar{e}$, $\mu\bar{\mu}$, $\tau\bar{\tau}$, $\gamma\gamma$ and ZZ . Limits use \mathcal{LS} J -factors. The solid black line shows the combined best fit TS values. The colored, dashed lines are the TS values from each dSph.	86

375	Figure 5.11 Comparison of HAWC limits from this analysis to Glory Duck (Fig. 4.5) for 3 dSphs and 3 DM annihilation channels: $b\bar{b}$, $\tau\bar{\tau}$, and $e\bar{e}$. Each sector shows the 95% confidence limit from Glory Duck (blue line) and this analysis (orange line) in the top plot. The lower plot features the ratio in log scale of Glory Duck to this analysis in a red solid line. Horizontal dashed lines are for ratios of 1.0 (black) and $\sqrt{2}$ (blue). Ratios larger than 1.0 are for limits smaller, or stricter, than Glory Duck. Ratios larger than $\sqrt{2}$ indicates limits are stricter than a simple doubling of the Glory Duck data.	88
383	Figure 6.1 TODO: IceCube[NEEDS A SOURCE][FACT CHECK THIS]	89
384	Figure 6.2 TODO: DOM photo[NEEDS A SOURCE][FACT CHECK THIS]	90
385	Figure 6.3 TODO: ICL[NEEDS A SOURCE][FACT CHECK THIS]	91
386	Figure 7.1 Neutrino spectra at production (left panels) and after oscillation at Earth (right panels). Blue, orange, and green lines are the ν_e , ν_μ , and ν_τ spectra respectively. Top panels show the spectra in $\frac{dN}{dE}$. Lower panels plot the flavor ratio to $\nu_e + \nu_\mu + \nu_\tau$. SM annihilation channels $b\bar{b}$, $\tau\bar{\tau}$, and $\nu_\mu\bar{\nu}_\mu$ are shown for $M_\chi = 1$ Pev, TeV, and EeV.	97
391	Figure 7.2 Signal recovery for 100 TeV DM annihilation into $\nu_\mu\bar{\nu}_\mu$ for a source at Dec = 16.06° . n_{inj} is the number of injected signal events in simulation. n_s is the number of reconstructed signal events from the simulation data. Although the uncertainties are small and tight, the reconstructed n_s are systematically underestimated.	98
396	Figure 7.3 Left panel shows the two kernels overlaying the original spectrum from χ aronv after propagation to Earth [86]. The vertical red line indicates where the original neutrino line is maximized. Blue line is the output from χ arov. Green line is the spectrum after convolution with a flat kernel. Orange line is the spectrum after Gaussian convolution. Right panel shows the signal recovery of the spectral model using the Gaussian kernel with parameters enumerated above.	99
403	Figure 7.4 Example spline that failed the fit. Failed splined are corrected on a case by case basis unless the SM channel has a systematic problem fitting the splines. In this case, I made a bookkeeping error and loaded the incorrect spectral model	101
406	Figure 7.5 Summary of input spectral models that were smoothed with Gaussian kernels. Spectral models are for $\chi\chi \rightarrow e\bar{e}, \mu\bar{\mu}, \tau\bar{\tau}, \nu_e\bar{\nu}_e, \nu_\mu\bar{\nu}_\mu$, and $\nu_\tau\bar{\nu}_\tau$. These spectra are the composite ($\nu_\mu + \nu_\tau$) of neutrino flavors. Every spectral model used for this analysis is featured as a colored solid line. Bluer lines are for low m_χ models. m_χ ranges from 681 GeV to 100 PeV. HDM [79], χ arov [86], and Photospline [90] are used to generate these spectra. Energy (x-axis) was chosen to roughly represent the energy sensitivity of NST.	102

413	Figure 7.6 Test statistic (TS) distributions for Segue 1 and $\chi\chi \rightarrow b\bar{b}$. Each subplot, 414 except the final, is the TS distribution for a specific DM mass listed in the 415 subplot. Orange dashed lines are the traces for a χ^2 distribution with 1 degree 416 of freedom. $\epsilon[\cdot]$ is the fraction of trials smaller than the bracketed value. The 417 final subplot features the all DM spectral models, similar to Fig. 7.5, used as 418 input for the TS distributions.	105
419	Figure 7.7 Same as Fig. 7.6 for Segue 1 $\chi\chi \rightarrow \tau\bar{\tau}$	106
420	Figure 7.8 Same as Fig. 7.6 for Segue 1 $\chi\chi \rightarrow \nu_\mu\bar{\nu}_\mu$	107
421	Figure 7.9 Same as Fig. 7.6 for Ursa Major II 1 $\chi\chi \rightarrow b\bar{b}$	108
422	Figure 7.10 Same as Fig. 7.6 for Ursa Major II 1 $\chi\chi \rightarrow \tau\bar{\tau}$	109
423	Figure 7.11 Same as Fig. 7.6 for Ursa Major II 1 $\chi\chi \rightarrow \nu_\mu\bar{\nu}_\mu$	110
424	Figure 7.12 Same as Fig. 7.6 for 15, GS J -factor, stacked sources and $\chi\chi \rightarrow b\bar{b}$	111
425	Figure 7.13 Same as Fig. 7.6 for 15, GS J -factor, stacked sources and $\chi\chi \rightarrow t\bar{t}$	112
426	Figure 7.14 Same as Fig. 7.6 for 15, GS J -factor, stacked sources and $\chi\chi \rightarrow u\bar{u}$	113
427	Figure 7.15 Same as Fig. 7.6 for 15, GS J -factor, stacked sources and $\chi\chi \rightarrow d\bar{d}$	114
428	Figure 7.16 Same as Fig. 7.6 for 15, GS J -factor, stacked sources and $\chi\chi \rightarrow e\bar{e}$	115
429	Figure 7.17 Same as Fig. 7.6 for 15, GS J -factor, stacked sources and $\chi\chi \rightarrow \mu\bar{\mu}$	116
430	Figure 7.18 Same as Fig. 7.6 for 15, GS J -factor, stacked sources and $\chi\chi \rightarrow \tau\bar{\tau}$	117
431	Figure 7.19 Same as Fig. 7.6 for 15, GS J -factor, stacked sources and $\chi\chi \rightarrow W^+W^-$	118
432	Figure 7.20 Same as Fig. 7.6 for 15, GS J -factor, stacked sources and $\chi\chi \rightarrow ZZ$	119
433	Figure 7.21 Same as Fig. 7.6 for 15, GS J -factor, stacked sources and $\chi\chi \rightarrow \nu_e\bar{\nu}_e$	120
434	Figure 7.22 Same as Fig. 7.6 for 15, GS J -factor, stacked sources and $\chi\chi \rightarrow \nu_\mu\bar{\nu}_\mu$	121

435	Figure 7.23 Signal Recovery study for an analysis with 15 stacked sources using the \mathcal{GS}	123
436	J -factors [59]. Above shows 14 studies for DM mass ranging between 1	
437	TeV and 20 PeV for $\chi\chi \rightarrow \mu_\mu\overline{\mu_\mu}$. The bottom right subplot features every	
438	spectral model used as input for the remaining subplots. The remaining	
439	subplots show n_{inj} as the number of signal events injected into background	
440	simulation. Whereas, n_s is the number of signal events recovered from	
441	analyzing the injected simulation. Blue line represents the median values of	
442	100 simulations. Light blue bands show the 1σ statistical uncertainty around	
443	the median.	
444	Figure 7.24 Same as Fig. 7.23 but for $\chi\chi \rightarrow t\bar{t}$ (top) and $b\bar{b}$ (bottom).	124
445	Figure 7.25 IceCube North Sky Track Sensitivities. Each panel shows sensitivity curves	126
446	for various DM annihilation channels. Sensitivities are for the velocity-	
447	weighted cross-section $\langle\sigma v\rangle$ versus m_χ . Dotted, colored lines are sensitivities	
448	for individual sources. Solid white lines are for the combined sensitivity of	
449	all 15 \mathcal{GS} sources used in this study.	
450	Figure 7.26 Same as Fig. 7.25 for three additional DM annihilation channels.	127
451	Figure 7.27 Panel A: Neutrino's from the Northern sky and incident on the IceCube	128
452	detector will travel through the Earth. How much of the Earth these neutrinos	
453	travels is a function of zenith from the vertical axis. Panel B: SM prediction of	
454	neutrino transmission probabilities for neutrinos arriving at $90^\circ - 180^\circ$ zenith	
455	and with 100 GeV to 100 PeV energies. High-energy neutrinos traversing	
456	the whole Earth are completely absorbed, whereas low-energy neutrinos pass	
457	through unimpeded. Neutrinos coming from above the horizon will arrive	
458	unimpeded for all neutrino energies. Figure pulled from [93].	
459	Figure 7.28 $\langle\sigma v\rangle$ sensitivities for 5 imaginary sources with $\log_{10} J = 19.42 \log_{10}(\text{GeV}^2\text{cm}^{-5})$.	129
460	Each imaginary source shares a declination with a source in Tab. 4.1	
461	Figure 8.1 The prompt electron neutrino and photon spectrum resulting from the decay	131
462	of a 2EeV DM particle to $\nu_e\overline{\nu}_e$, as currently being searched for at IceCube	
463	[5]. Solid curves represent the results of this work, and predict orders of	
464	magnitude more flux at certain energies than the dashed results of Pythia 8.2,	
465	one of the only existing methods to generate spectra at these masses. In both	
466	cases energy conservation is satisfied: there is a considerable contribution to	
467	a δ -function at $x = 1$, associated with events where an initial W or Z was never	
468	emitted and thus no subsequent shower developed. Large disagreements are	
469	generically observed at these masses for electroweak dominated channels,	
470	while the agreement is better for colored initial SM states.	
471	Figure 8.2 TODO: neutrino and bb plot with nu Sensitivities[NEEDS A SOURCE][FACT	132
472	CHECK THIS]	

473	Figure A.1	Sister figure to Figure 4.3. Sources in the first row from left to right: Bootes I, Canes Venatici I, II. In second row: Draco, Hercules, Leo I. In the first row: Leo II, Leo IV, Sextans. In the final row: Ursa Major I, Ursa Major II.	133
476	Figure B.1	Sister figure to Figure 5.2 for remaining SM primary annihilation channels studied for this thesis. These did not require any post generation smoothing and so are directly pulled from [79] with a binning scheme most helpful for a HAWC analysis.	134
480	Figure B.2	Comparison of HAWC limits from this analysis to Glory Duck (Fig. 4.5) for Coma Berenices and 7 DM annihilation channels.	144
482	Figure B.3	Same as Fig. B.2 but for Segue 1.	145
483	Figure B.4	Same as Fig. B.2 but for Sextans.	146
484	Figure C.1	Current status of spline tables according to constraints defined by Tab. 7.1. Green splines are splines that passed under the GOOD tolerance. Yellow are splines that are OK. Red are splines that FAIL. All yellow splines were inspected individually before running the analysis. Splines were made for the μ (PID 14; top panel) flavor and τ (PID 16; bottom panel) neutrino flavors.	150
489	Figure C.2	Sister figure to Fig. 7.5 for annihilation channels that did not require kernel smoothing. These spectra are the composite ($\nu_\mu + \nu_\tau$) of neutrino flavors. Every spectral model used for this analysis is featured as a colored solid line. Bluer lines are for lower DM mass spectral models. DM masses range from 681 GeV to 100 PeV.	151
494	Figure C.3	Same as Fig. 7.23 but for Segue 1 and $\chi\chi \rightarrow b\bar{b}$	152
495	Figure C.4	Same as Fig. 7.23 but for Segue 1 and $\chi\chi \rightarrow t\bar{t}$	153
496	Figure C.5	Same as Fig. 7.23 but for Segue 1 and $\chi\chi \rightarrow \nu_\mu\bar{\nu}_\mu$	154
497	Figure C.6	Same as Fig. 7.23 but for Ursa Major II and $\chi\chi \rightarrow b\bar{b}$	155
498	Figure C.7	Same as Fig. 7.23 but for Ursa Major II and $\chi\chi \rightarrow t\bar{t}$	156
499	Figure C.8	Same as Fig. 7.23 but for Ursa Major II and $\chi\chi \rightarrow \nu_\mu\bar{\nu}_\mu$	157
500	Figure C.9	IceCube North Sky Track Sensitivities for $n_s/\langle N \rangle$. n_s values are the counts fed into Eq. (7.8) to produce Fig. 7.26 and Fig. 7.25.	158
502	Figure C.10	Same as Fig. C.9 for three additional DM annihilation channels.	159

LIST OF ABBREVIATIONS

- 504 **MSU** Michigan State University
505 **LANL** Los Alamos National Laboratory
506 **DM** Dark Matter
507 **SM** Standard Model
508 **HAWC** High Altitude Water Cherenkov Observatory
509 **dSph** Dwarf Spheroidal Galaxy

CHAPTER 1

INTRODUCTION

511 Is the text not rendering right? Ah ok it knows im basically drafting the doc still

CHAPTER 2

512

DARK MATTER IN THE COSMOS

513 2.1 Introduction

514 The dark matter problem can be summarized in part by the following thought experiment.

515 Let us say you are the teacher for an elementary school classroom. You take them on a field
516 trip to your local science museum and among the exhibits is one for mass and weight. The exhibit
517 has a gigantic scale, and you come up with a fun problem for your class.

518 You ask your class, "What is the total weight of the classroom? Give your best estimation to
519 me in 30 minutes, and then we'll check your guess on the scale. If your guess is within 10% of the
520 right answer, we will stop for ice cream on the way back."

521 The students are ecstatic to hear this, and they get to work. The solution is some variation of
522 the following strategy. The students should give each other their weight or best guess if they do
523 not know. Then, all they must do is add each student's weight and get a grand total for the class.

524 The measurement on the giant scale should show the true weight of the class. When comparing
525 the measured weight to your estimation, multiply the measurement by 1.0 ± 0.1 to get the $\pm 10\%$
526 tolerances for your estimation.

527 Two of your students, Sandra and Mario, return to you with a solution.

528 They say, "We weren't sure of everyone's weight. We used 65 lbs. for the people we didn't
529 know and added everyone who does know. There are 30 of us, and we got 2,000 lbs.! That's a ton!"

530 You estimated 1,900 lbs. assuming the average weight of a student in your class was 60 lbs.
531 So, you are pleased with Sandra's and Mario's answer. You instruct your students to all gather on
532 the giant scale and read off the weight together. To all your surprise, the scale reads *10,000 lbs.*!
533 10,000 is significantly more than a 10% error from 2,000. In fact, it is approximately 5 times more
534 massive than either your or your students' estimates. You think to yourself and conclude there
535 must be something wrong with the scale. You ask an employee to check the scale and verify it is
536 well calibrated. They confirm that the scale is in working order. You weigh a couple of students
537 individually to assess that the scale is well calibrated. Sandra weighs 59 lbs., and Mario weighs

538 62 lbs., typical weights for their age. You then weigh each student individually and see that their
539 weights individually do not deviate greatly from 60 lbs. So, where does all the extra weight come
540 from?

541 This thought experiment serves as an analogy to the Dark Matter problem. The important
542 substitution to make however is to replace the students with stars and the classroom with a galaxy,
543 say the Milky Way. Individually the mass of stars is well measured and defined with the Sun as our
544 nearest test case. However, when we set out to measure the mass of a collection of stars as large as
545 galaxies, our well-motivated estimation is wildly incorrect. There simply is no way to account for
546 this discrepancy except without some unseen, or dark, contribution to mass and matter in galaxies.
547 I set out in my thesis to narrow the possibilities of what this Dark Matter could be.

548 This chapter is organized like the following... **TODO: Text should look like ... Chapter x has**
549 **blah blah blah.**

550 2.2 Dark Matter Basics

551 Presently, a more compelling theory of cosmology that includes Dark Matter (DM) in order
552 to explain a variety of observations is Λ Cold Dark Matter, or Λ CDM. I present the evidence
553 supporting Λ CDM in Section 2.3 yet discuss the conclusions of the Λ CDM model here. According
554 to Λ CDM fit to observations on the Cosmic Microwave Background (CMB), DM is 26.8% of the
555 universe's current energy budget. Baryonic matter, stuff like atoms, gas, and stars, contributes to
556 4.9% of the universe's current energy budget [1, 2, 3].

557 DM is dark; it does not interact readily with light at any wavelength. DM also does not interact
558 noticeably with the other standard model forces (Strong and Weak) at a rate that is readily observed
559 [3]. DM is cold, which is to say that the average velocity of DM is below relativistic speeds [1].
560 'Hot' DM would not likely manifest the dense structures we observe like galaxies, and instead
561 would produce much more diffuse galaxies than what is observed [3, 1]. DM is old; it played a
562 critical role in the formation of the universe and the structures within it [1, 2].

563 Observations of DM have so far been only gravitational. The parameter space available to what
564 DM could be therefore is extremely broad. The broad DM parameter space is iteratively tested in

565 DM searches by supposing a hypothesis that has not yet been ruled out and performing observations
566 to test them. When the observations yield a null result, the parameter space is constrained further.
567 I present some approaches for DM searches in Section 2.4.

568 **2.3 Evidence for Dark Matter**

569 Dark Matter (DM) has been a looming problem in physics for almost 100 years. Anomalies
570 have been observed by astrophysicists in galactic dynamics as early as 1933 when Fritz Zwicky
571 noticed unusually large velocity dispersion in the Coma cluster. Zwicky's measurement was the
572 first recorded to use the Virial theorem to measure the mass fraction of visible and invisible matter
573 in celestial bodies [4]. From Zwicky in [5], "*If this would be confirmed, we would get the surprising*
574 *result that dark matter is present in much greater amount than luminous matter.*" Zwicky's and
575 others' observation did not instigate a crisis in astrophysics because the measurements did not
576 entirely conflict with their understanding of galaxies [4]. In 1978, Rubin, Ford, and Norbert
577 measured rotation curves for ten spiral galaxies [6]. Rubin et al.'s 1978 publication presented a
578 major challenge to the conventional understanding of galaxies that could no longer be dismissed by
579 measurement uncertainties. Evidence has been mounting ever since for this exotic form of matter.
580 The following subsections provide three compelling pieces of evidence in support of the existence
581 of DM.

582 **2.3.1 First Clues: Stellar Velocities**

583 Zwicky, and later Rubin, measured the stellar velocities of various galaxies to estimate their
584 virial mass. The Virial Theorem upon which these observations are interpreted is written as

$$2T + V = 0. \quad (2.1)$$

585 Where T is the kinetic energy and V is the potential energy in a self-gravitating system. The
586 classical Newton's law of gravity from stars and gas was used for gravitational potential modeled in
587 the observed galaxies:

$$V = -\frac{1}{2} \sum_i \sum_{j \neq i} \frac{m_i m_j}{r_{ij}}. \quad (2.2)$$

588 Zwicky et al. measured just the velocities of stars apparent in optical wavelengths [5]. Rubin et al.
 589 added by measuring the velocity of the hydrogen gas via the 21 cm emission line of Hydrogen [6].
 590 The velocities of the stars and gas are used to infer the total mass of galaxies and galaxy clusters
 591 via Equation (2.1). An inferred mass is obtained from the luminosity of the selected sources. The
 592 two inferences are compared to each other as a luminosity to mass ratio which typically yielded [1]

$$\frac{M}{L} \sim 400 \frac{M_{\odot}}{L_{\odot}} \quad (2.3)$$

593 M_{\odot} and L_{\odot} referring to stellar mass and stellar luminosity, respectively. These ratios clearly indicate
 594 a discrepancy in apparent light and mass from stars and gas and their velocities.

595 Rubin et al. [6] demonstrated that the discrepancy was unlikely to be an underestimation of
 596 the mass of the stars and gas. The inferred "dark" mass was up to 5 times more than the luminous
 597 mass. This dark mass also needed to extend well beyond the extent of the luminous matter.

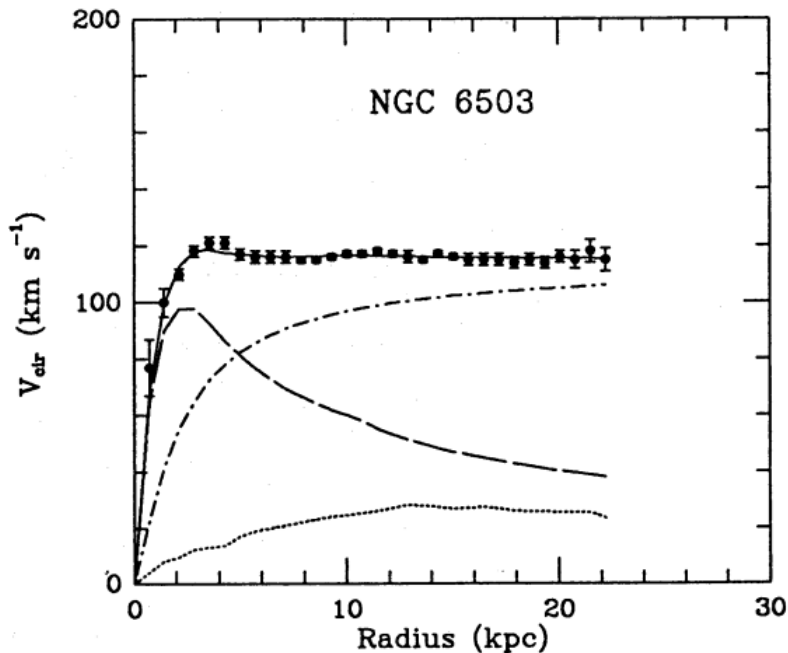


Figure 2.1 Rotation curve fit to NGC 6503 from [7]. Dashed line is the contribution from visible matter. Dotted curves are from gas. Dash-dot curves are from dark matter (DM). Solid line is the composite contribution from all matter and DM sources. Data are indicated with bold dots with error bars. Data agree strongly with a matter + DM composite prediction.

598 Figure 2.1 features one of many rotation curves plotted from the stellar velocities within galaxies.

599 The measured rotation curves mostly feature a flattening of velocities at higher radius which is not
600 expected if the gravity was only coming from gas and luminous matter. The extension of the
601 flat velocity region also indicates that the DM is distributed far from the center of the galaxy.
602 Modern velocity measurements include significantly larger objects, galactic clusters, and smaller
603 objects, dwarf galaxies. Yet, measurements along this regime are leveraging the Virial theorem
604 with Newtonian potential energies. We know Newtonian gravity is not a comprehensive description
605 of gravity. New observational techniques have been developed since 1978, and those are discussed
606 in the following sections.

607 **2.3.2 Evidence for Dark Matter: Gravitational Lensing**

608 Modern evidence for dark matter comes from new avenues beyond stellar velocities. Grav-
609 itational lensing from DM is a new channel from general relativity. General relativity predicts
610 aberrations in light caused by massive objects. In recent decades we have been able to measure the
611 lensing effects from compact objects and DM halos. Figure 2.2 shows how different massive ob-
612 jects change the final image of a faraway galaxy resulting from gravitational lensing. Gravitational
613 lensing developed our understanding of dark matter in two important ways.

614 Gravitational lensing provides additional compelling evidence for DM. The observation of two
615 merging galactic clusters in 2006, shown in Figure 2.3, provided a compelling argument for DM
616 outside the Standard Model. These clusters merged recently in astrophysical time scales. Galaxies
617 and star cluster have mostly passed by each other as the likelihood of their collision is low. Therefore,
618 these massive objects will mostly track the highest mass, dark and/or baryonic, density. Yet, the
619 intergalactic gas is responsible for the majority of the baryonic mass in the systems [4]. These gas
620 bodies will not phase through and will heat up as they collide together. The hot gas is located via
621 x-ray emission from the cluster. Two observations of the clusters were performed independently of
622 each other.

623 The first was the lensing of light around the galaxies due to their gravitational influences.
624 When celestial bodies are large enough, the gravity they exert bends space and time itself. The
625 warped space-time lenses light and will deflect in an analogous way to how glass lenses will bend

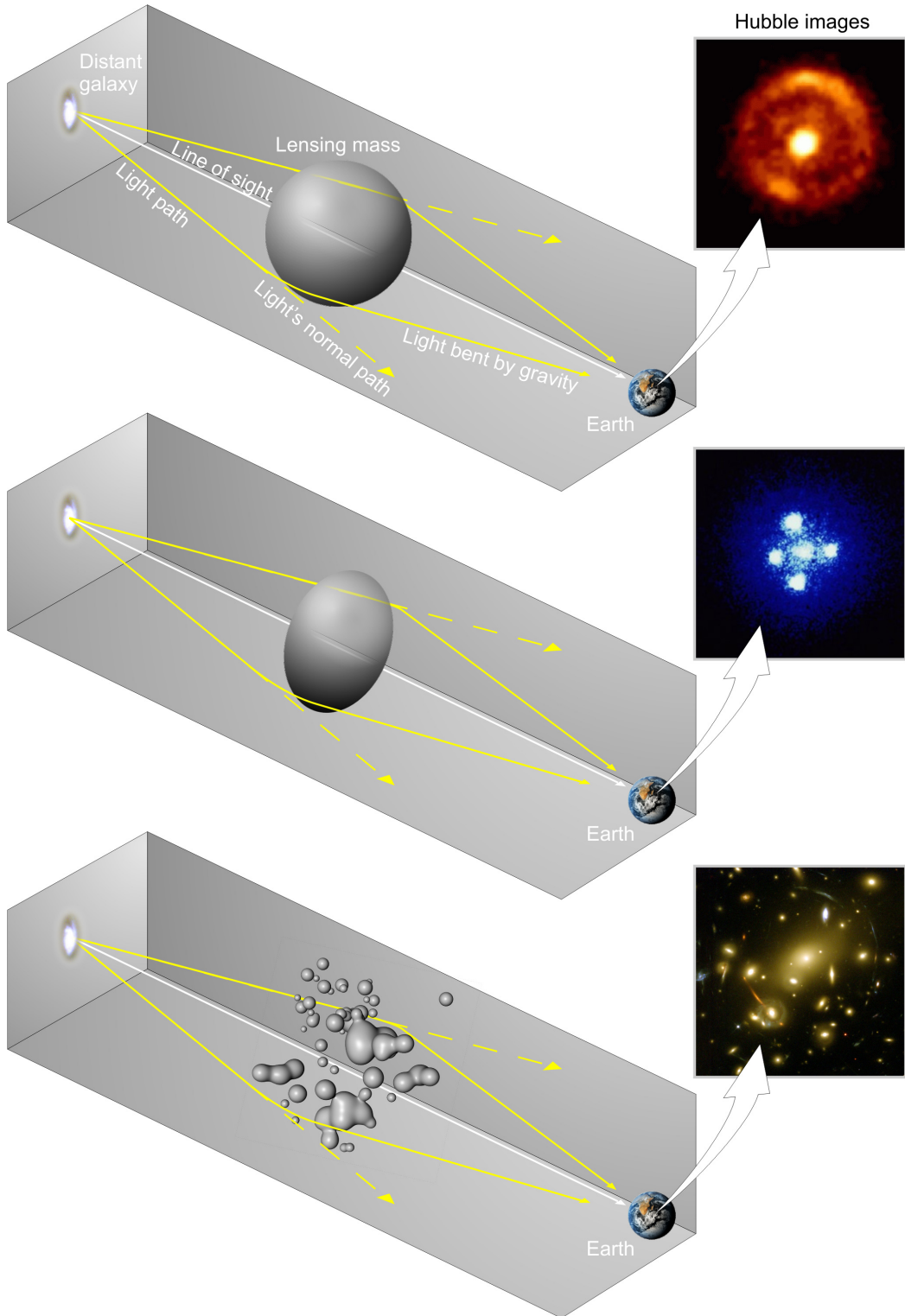


Figure 2.2 Light from distant galaxy is bent in unique ways depending on the distribution of mass between the galaxy and Earth. Yellow dashed lines indicate where the light would have gone if the matter were not present [8].

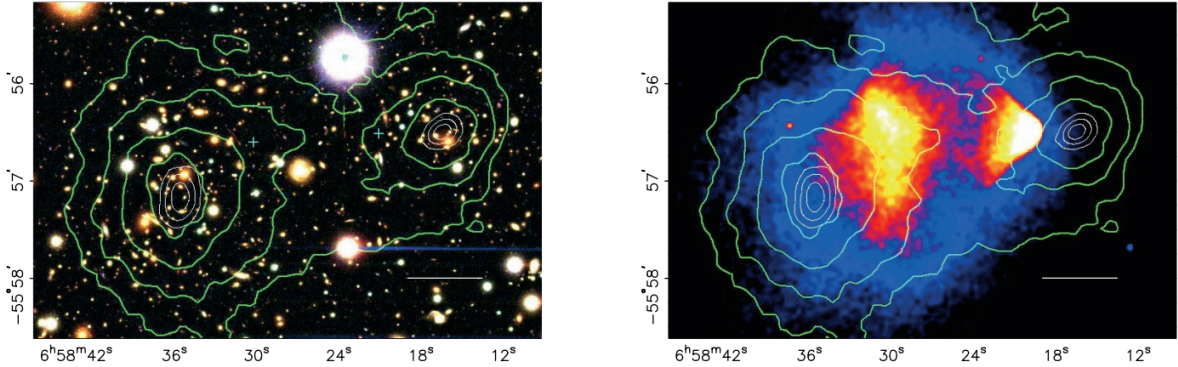


Figure 2.3 (left) Optical image of galactic cluster 1E0657-558. (right) X-ray image of the cluster with redder meaning hotter and higher baryon density. (both) Green contours are reconstruction of gravity contours from weak lensing. White rings are the best fit mass maxima at 68.3%, 95.5%, and 99.7% confidence. The matter maxima of the clusters are clearly separated from x-ray maxima. [9]

626 light, see Figure 2.2. With a sufficient understanding of light sources behind a massive object, we
 627 can reconstruct the contours of the gravitational lenses. The gradient of the contours shown in
 628 Figure 2.3 then indicates how dense the matter is and where it is.

629 The x-ray emission can then be observed from the clusters. Since these galaxies are mostly gas
 630 and are merging, then the gas should be getting hotter. If they are merging, the x-ray emissions
 631 should be the strongest where the gas is mostly moving through each other. Hence, X-ray emission
 632 maps out where the gas is in the merging galaxy cluster.

633 The lensing and x-ray observations were done on the Bullet cluster featured on Figure 2.3.
 634 The x-ray emissions do not align with the gravitational contours from lensing. The incongruence
 635 in mass density and baryon density suggests that there is a lot of matter somewhere that does
 636 not interact with light. Moreover, this dark matter cannot be baryonic [9]. The Bullet Cluster
 637 measurement did not really tell us what DM is exactly, but it did give the clue that DM also does
 638 not interact with itself very strongly. If DM did interact strongly with itself, then it would have been
 639 more aligned with the x-ray emission [9]. There have been follow-up studies of galaxy clusters with
 640 similar results. The Bullet Cluster and others like it provide a persuasive case against something
 641 possibly amiss in our gravitational theories.

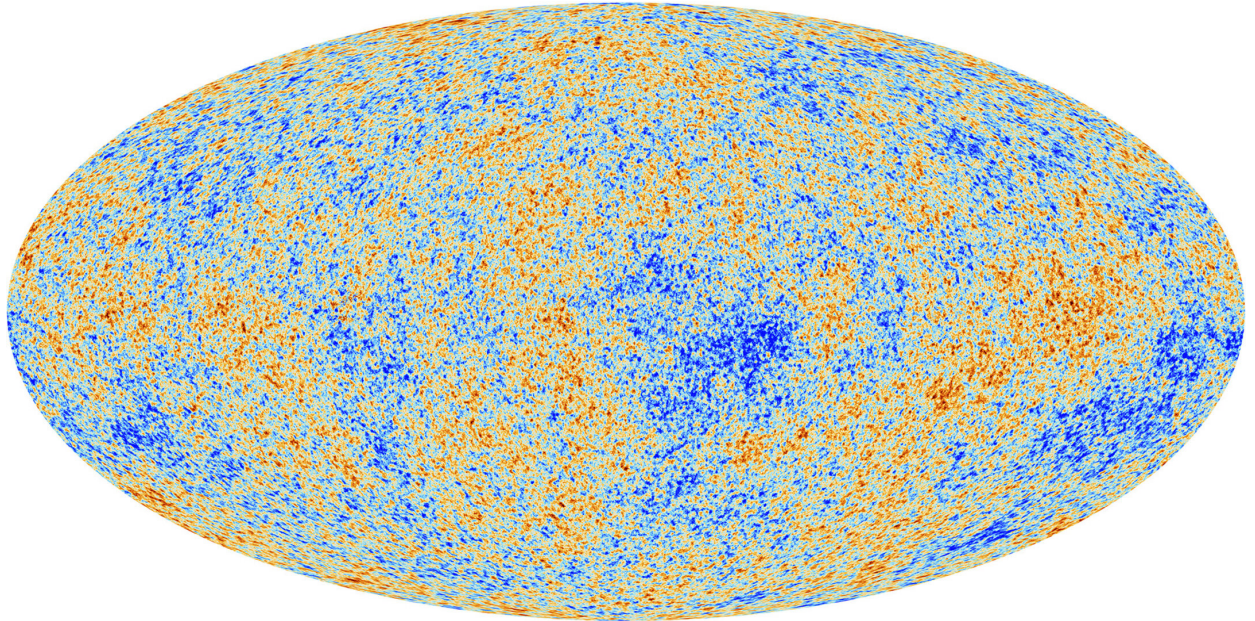


Figure 2.4 Plank CMB sky. Sky map features small variations in temperature in primordial light. These anisotropies are used to make inferences about the universe’s energy budget and developmental history. [10]

642 2.3.3 Evidence for Dark Matter: Cosmic Microwave Background

643 The Cosmic Microwave Background (CMB) is the primordial light from the early universe
644 when Hydrogen atoms formed from the free electron and proton soup in the early universe. The
645 CMB is the earliest light we can observe; released when the universe was about 380,000 years old.
646 Then we look at how the simulated universes look like compared to what we see. Figure 2.4 is the
647 most recent CMB image from the Plank satellite after subtracting the average value and masking the
648 galactic plane [10]. Redder regions indicate a slightly hotter region in the CMB, and blue indicates
649 colder. The intensity variations are on the order of 1 in 1000 with respect to the average value.

650 The Cosmic Microwave Background shows that the universe had DM in it from an incredibly
651 early stage. To measure the DM, Dark Energy, and matter fractions of the universe from the CMB,
652 the image is analyzed into a power spectrum, which shows the amplitude of the fluctuations as
653 a function of spherical multipole moments. Λ CDM provides the best fit to the power spectra of
654 the CMB as shown in Figure 2.5. The CMB power spectrum is quite sensitive to the fraction
655 of each energy contribution in the early universe. Low l modes are dominated by variations
656 in gravitational potential. Intermediate l emerge from oscillations in photon-baryon fluid from

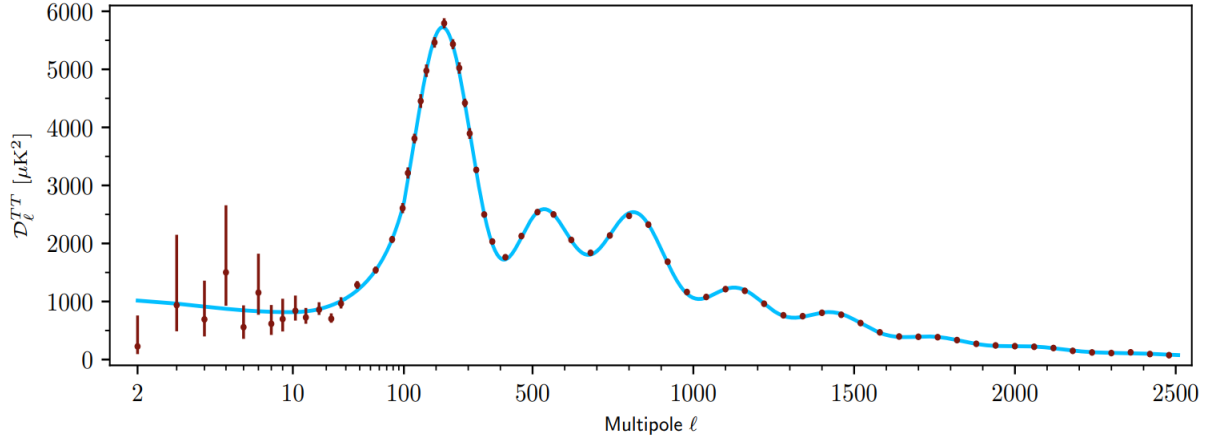


Figure 2.5 Observed Cosmic Microwave Background power spectrum as a function of multipole moment from Plank [10]. Blue line is best fit model from Λ CDM. Red points and lines are data and error, respectively.

657 competing baryon pressures and gravity. High l is a damped region from the diffusion of photons
 658 during electron-proton recombination. [1]

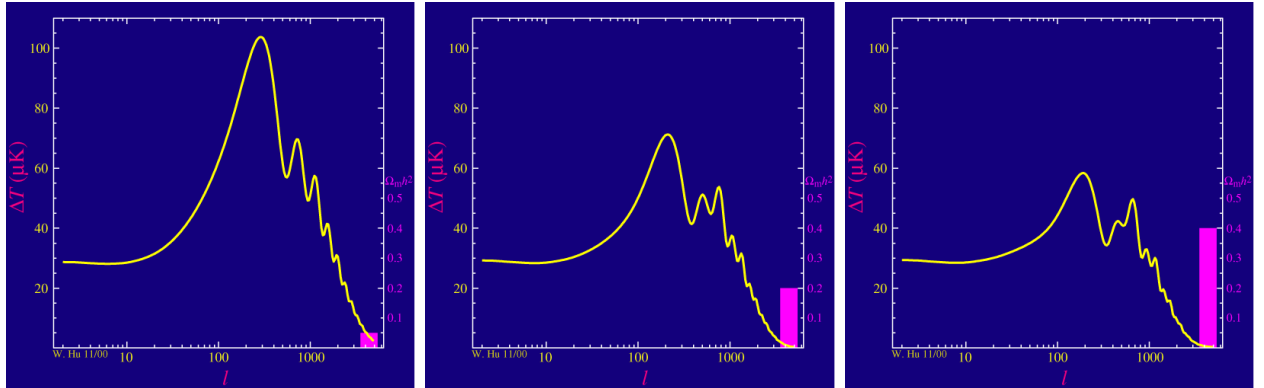


Figure 2.6 Predicted power spectra of CMB for different $\Omega_m h^2$ values for fixed baryon density from [11]. (left) Low $\Omega_m h^2$ increases the prominence of first and second peaks. (middle) $\Omega_m h^2$ is most similar to the observed power spectrum. The second and third peaks are similar in height. (right) $\Omega_m h^2$ is large which suppresses the first peak and raises the prominence of the third peak.

659 The harmonics would look quite different for a universe with less DM. Figure 2.6 demonstrates
 660 the effect $\Omega_m h^2$ has on the expected power spectrum for fixed baryon matter density. [11] Sweeping
 661 $\Omega_m h^2$ in this way clearly shows the effect dark matter has on the CMB power spectrum. The
 662 observations fit well with the Λ CDM model, and the derived fractions are as follows. The matter
 663 fraction: $\Omega_m = 0.3153$; and the baryon fraction: $\Omega_b = 0.04936$ [10]. Plank's observations also
 664 provide a measure of the Hubble constant, H_0 . H_0 especially has seen a growing tension in the

665 past decade that continues to deepened with observations from instruments like the James Webb
666 Telescope [12, 13]. As Hubble tensions deepen, we may find that perhaps Λ **CDM**, despite its
667 successes, is missing some critical physics.

668 Overall, the Newtonian motion of stars in galaxies, weak lensing from galactic clusters, and
669 power spectra from primordial light form a compelling body of research in favor of dark matter.
670 It takes another leap of theory and experimentation to make observations of DM that are non-
671 gravitational in nature. In Section 2.3, the evidence for DM implies strongly that the DM is matter
672 and not a lost parameter in the gravitational fields between massive objects. Finally, if we take one
673 axiom: that this matter has quantum behavior, such as being described by some Bohr wavelength
674 and abiding by some fermion or boson statistics; then we arrive at particle dark matter. One particle
675 DM hypothesis is the Weakly Interacting Massive Particle (WIMP). This DM candidate theory is
676 discussed further in the next section and is the focus of this thesis.

677 **2.4 Searching for Dark Matter: Particle DM**

678 Section 2.4 shows the Standard Model of particle physics and is currently the most accurate
679 model for the dynamics of fundamental particles like electrons and photons. The current status
680 of the SM does not have a viable DM candidate. When looking at the standard model, we can
681 immediately exclude any charged particle because charged particles interact strongly with light.
682 Specifically, this will rule out the following charged, fundamental particles: $e, \mu, \tau, W, u, d, s, c, t, b$
683 and their corresponding antiparticles. Recalling from Section 2.2 that DM must be long-lived and
684 stable over the age of the universe which excludes all SM particles with decay half-lives at or shorter
685 than the age of the universe. The lifetime constraint additionally eliminates the Z and H bosons.
686 Finally, the candidate DM needs to be somewhat massive. Recall from Section 2.2 that DM is cold
687 or not relativistic through the universe. This eliminates the remaining SM particles: $\nu_{e,\mu,\tau}, g, \gamma$ as
688 DM candidates. Because there are no DM candidates within the SM, the DM problem strongly
689 hints to physics beyond the SM (BSM).

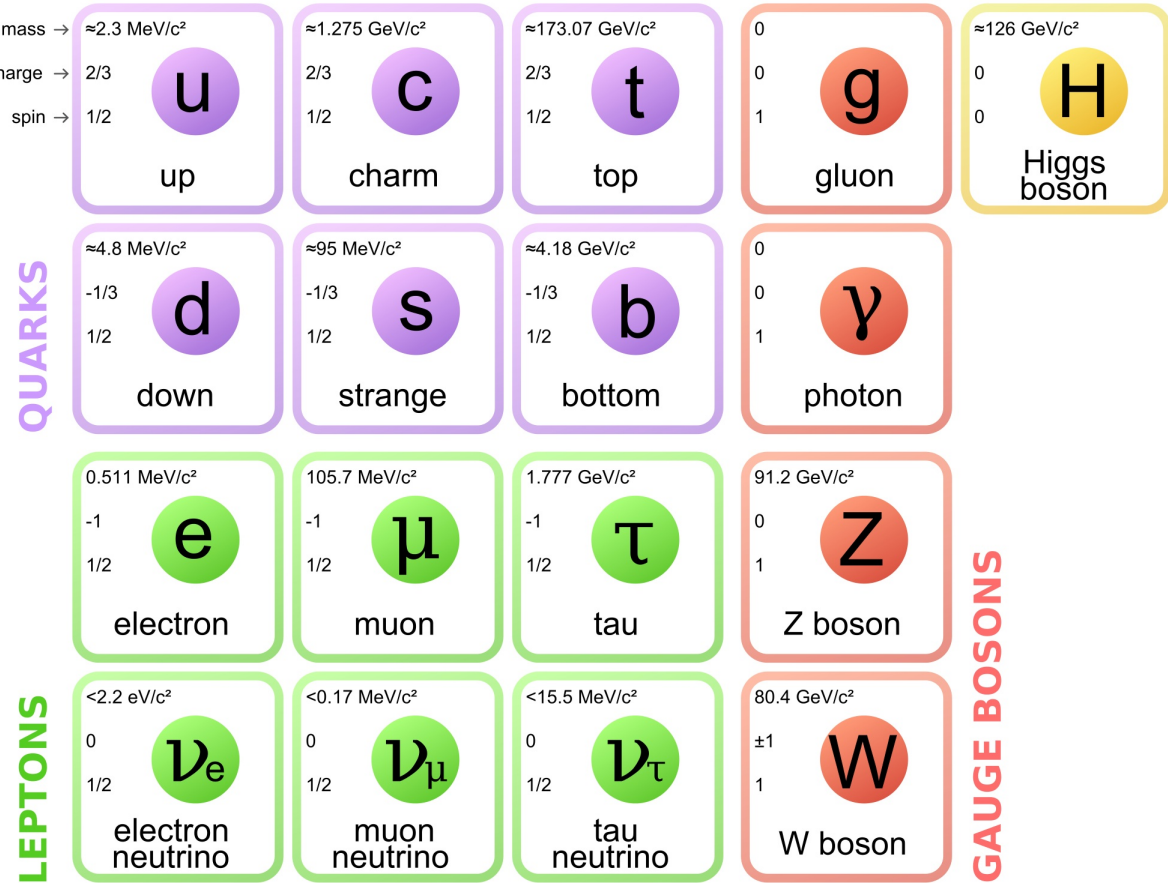


Figure 2.7 The Standard Model (SM) of particle physics. Figure taken from <http://www.quantumdiaries.org/2014/03/14/the-standard-model-a-beautiful-but-flawed-theory/>

690 2.4.1 Shake it, Break it, Make it

When considering DM that couples in some way with the SM, the interactions are roughly demonstrated by interaction demonstrated in Figure 2.8. The figure is a simplified Feynman diagram where the arrow of time represents the interaction modes of: **Shake it, Break it, Make it.**

Shake it refers to the direct detection of dark matter. Direct detection interactions start with a free DM particle and an SM particle. The DM and SM interact via elastic or inelastic collision and recoil away from each other. The DM remains in the dark sector and imparts some momentum onto the SM particle. The hope is that the momentum imparted onto the SM particle is sufficiently high enough to pick up with extremely sensitive instruments. Because we cannot create the DM in the lab, a direct detection experiment must wait until DM is incident on the detector. Most direct detection experiments are therefore placed in low-background environments with inert detection

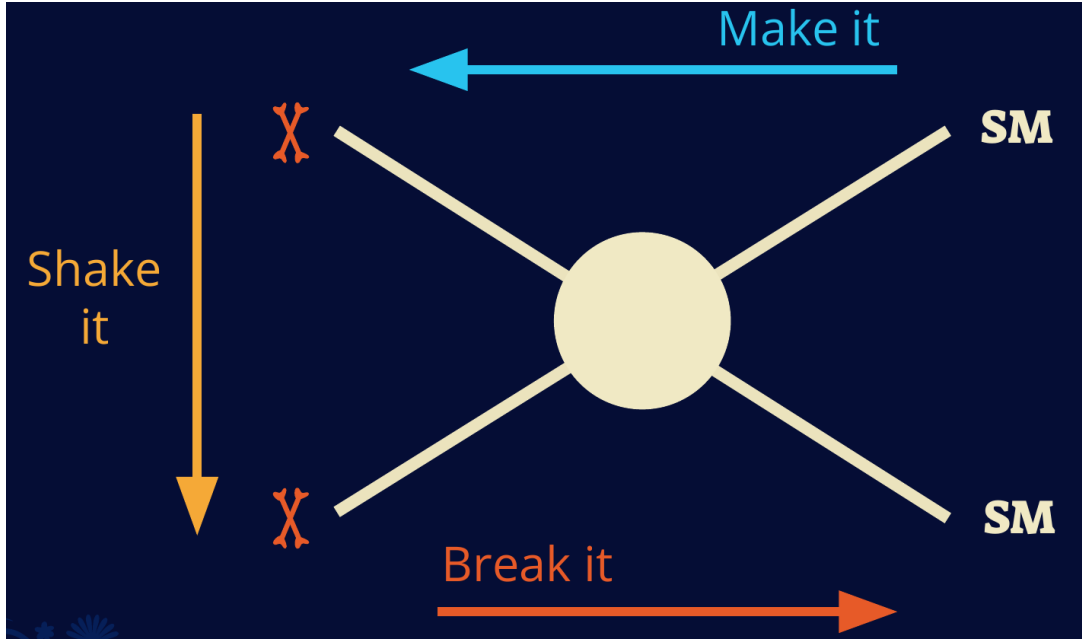


Figure 2.8 Simplified Feynman diagram demonstrating different ways DM can interact with SM particles. The 'X's refer to the DM particles whereas the SM refer to fundamental particles in the SM. The large circle in the center indicates the vertex of interaction and is purposely left vague. The colored arrows refer to different directions of time as well as their respective labels. The arrows indicate the initial and final state of the DM -SM interaction in time.

⁷⁰¹ media like the noble gas Xenon. [14]

⁷⁰² **Make it** refers to the production of DM from SM initial states. The experiment starts with
⁷⁰³ particles in the SM. These SM particles are accelerated to incredibly high energies and then collide
⁷⁰⁴ with each other. In the confluence of energy, DM hopefully emerges as a byproduct of the SM
⁷⁰⁵ annihilation. Often it is the collider experiments that are energetic enough to hypothetically produce
⁷⁰⁶ DM. These experiments include the world-wide collaborations ATLAS and CMS at CERN where
⁷⁰⁷ proton collide together at extreme energies. The DM searches, however, are complex. DM likely
⁷⁰⁸ does not interact with the detectors and lives long enough to escape the detection apparatus of
⁷⁰⁹ CERN's colliders. This means any DM production experiment searches for an excess of events
⁷¹⁰ with missing momentum or energy in the events. An example event with missing transverse
⁷¹¹ momentum is shown in Figure 2.9. The missing momentum with no particle tracks implies a
⁷¹² neutral particle carried the energy out of the detector. However, there are other neutral particles
⁷¹³ in the SM, like neutrons or neutrinos, so any analysis has to account for SM signatures of missing

714 momentum. [15]

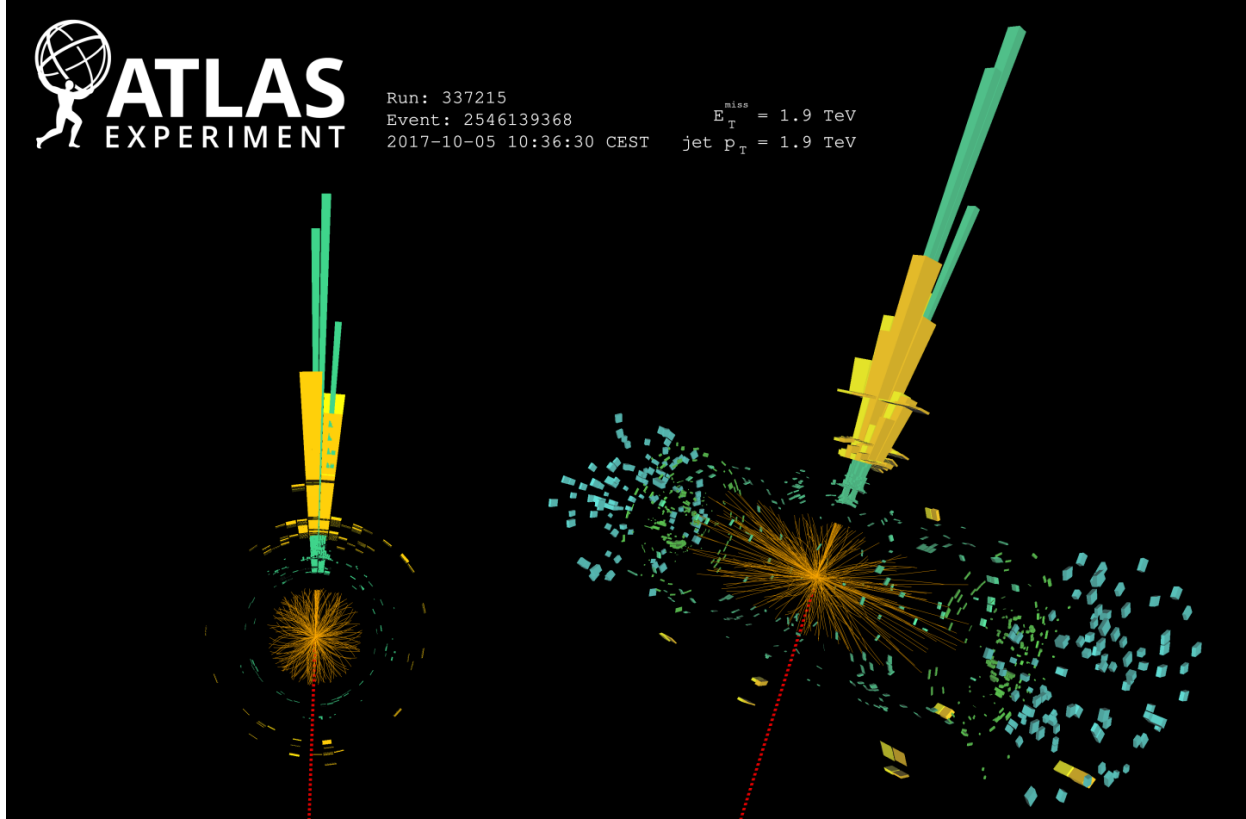


Figure 2.9 A single jet event in ATLAS detector from 2017 [16]. Jet momentum was observed to be 1.9 TeV. Missing transverse momentum was observed to be 1.9 TeV compared to the initial transverse momentum of the event was 0. Implied MET is traced by a red dashed line in event display.

715 **2.4.2 Break it: Standard Model Signatures of Dark Matter through Indirect Searches**

716 **Break it** refers to the creation of SM particles from the dark sector, and it is the primary focus
717 of this thesis. The interaction begins with DM or in the dark sector. The hypothesis is that this
718 DM will either annihilate with itself or decay and produce an SM byproduct. This method is
719 often referred to as the Indirect Detection of DM because we have no lab to directly control or
720 manipulate the DM. Therefore, most indirect DM searches are performed using observations of
721 known DM densities among the astrophysical sources. The strength is that we have the whole of the
722 universe and its 13.6-billion-year lifespan to use as a detector and particle accelerator. Additionally,
723 locations of dark matter are well cataloged since it was astrophysical observations that presented

724 the problem of DM in the first place.

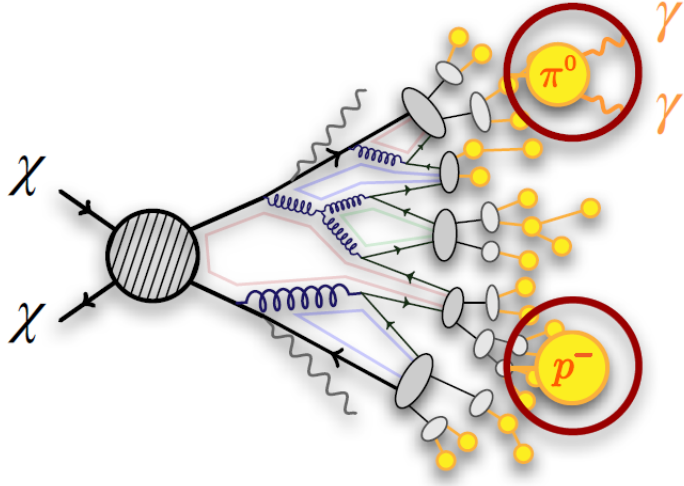


Figure 2.10 More detailed pseudo-Feynman diagram of particle cascade from dark matter annihilation into 2 quarks. The quarks hadronize and down to stable particles like γ or the anti-proton (p^-). Diagram pulled from ICRC 2021 presentation on DM annihilation search [17].

725 However, anything can happen in the universe. There are many difficult to deconvolve back-
726 grounds when searching for DM. One prominent example is the galactic center. We know the
727 galactic center has a large DM content because of stellar kinematics in our Milky Way and DM halo
728 simulations. Yet, any signal from the galactic center is challenging to parse apart from the extreme
729 environment of our supermassive black hole, unresolved sources, and diffuse emission from the
730 interstellar medium [18]. Despite the challenges, any DM model that yields evidence in the other
731 two observation methods, **Shake it or Make it** must be corroborated with indirect observations of
732 the known DM sources. Without corroborating evidence, DM observation in the lab is hard-pressed
733 to demonstrate that it is the model contributing to the DM seen at the universal scale.

734 In the case of WIMP DM, signals are described in terms of primary SM particles produced
735 from DM decay or annihilation. The SM initial state particles are then simulated down to stable
736 final states such as the γ , ν , p , or e which can traverse galactic lengths to reach Earth.

737 Figure 2.10 shows the quagmire of SM particles that emerges from SM initial states that are not
738 stable [17]. There are many SM particles with varying energies that can be produced in such an

739 interaction. For any arbitrary DM source and stable SM particle, the SM flux from DM annihilating
 740 to a neutral particle in the SM, ϕ , from a region in the sky is described by the following.

$$\frac{d\Phi_\gamma}{dE_\gamma} = \frac{\langle\sigma v\rangle}{8\pi m_\chi^2} \frac{dN_\gamma}{dE_\gamma} \times \int_{\text{source}} d\Omega \int_{l.o.s} \rho_\chi^2 dl(r, \theta') \quad (2.4)$$

741 In Equation (4.1), $\langle\sigma v\rangle$ is the velocity-weighted annihilation cross-section of DM to the SM. m_χ
 742 refers to the mass of DM, noted with Greek letter χ . $\frac{dN_\phi}{dE_\phi}$ is the N particle flux weighted by the
 743 particle energy. An example is provided in Figure 2.11 for the γ final state. The integrated terms
 744 are performed over the solid angle, $d\Omega$, and line of sight, l.o.s. ρ is the density of DM for a
 745 location (r, θ') in the sky. The terms left of the '×' are often referred to as the particle physics
 746 component. The terms on the right are referred to as the astrophysical component. For decaying
 747 DM, the equation changes to...

$$\frac{d\Phi_\phi}{dE_\phi} = \frac{1}{4\pi\tau m_\chi} \frac{dN_\phi}{dE_\phi} \times \int_{\text{source}} d\Omega \int_{l.o.s} \rho_\chi dl(r, \theta') \quad (2.5)$$

748 In Equation (2.5), τ is the decay lifetime of the DM. Just as in Equation (4.1), the left and right
 749 terms are the particle physics and the astrophysical components respectively. The integrated
 750 astrophysical component of Equation (4.1) is often called the J-Factor. Whereas the integrated
 751 astrophysical component of Equation (2.5) is often called the D-Factor.

752 Exact DM $\text{DM} \rightarrow \text{SM SM}$ branching ratios are not known, so it is usually assumed to go 100%
 753 into an SM particle/anti-particle. Additionally, when a DM annihilation or decay produces one of
 754 the neutral, long-lived SM particles (ν or γ), the particle is traced back to a DM source. For DM
 755 above GeV energies, there are very few SM processes that can produce particles with such a high
 756 energy. Seeing such a signal would almost certainly be an indication of the presence of dark matter.
 757 Fortunately, the universe provides us with the largest volume and lifetime ever for a particle physics
 758 experiment.

759 2.5 Sources for Indirect Dark Matter Searches

760 The first detection of DM relied on optical observations. Since then, we have developed new
 761 techniques to find DM dense regions. As described in Section 2.3.1, many DM dense regions were
 762 through observing galactic rotation curves. Our Milky Way galaxy is among DM dense regions

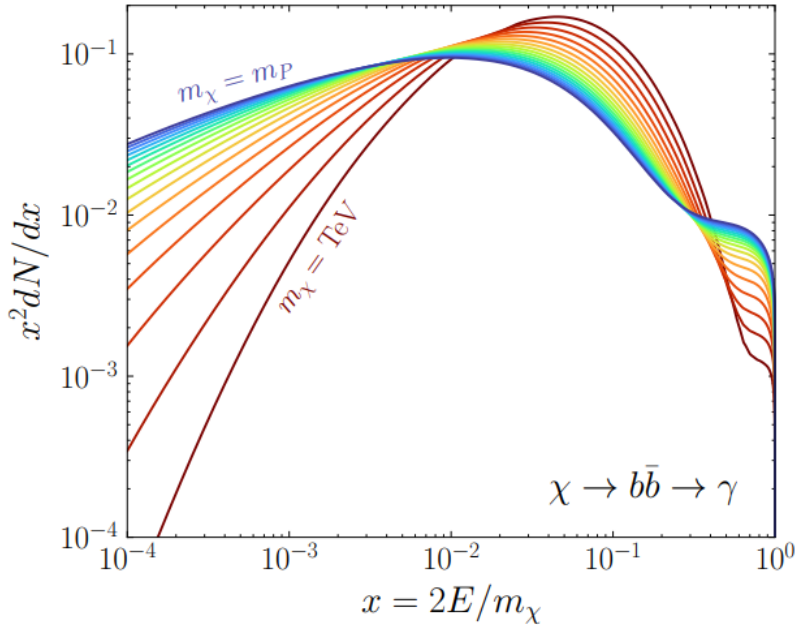


Figure 2.11 Dark Matter (DM) decay spectrum for $b\bar{b}$ initial state and γ final state. Redder spectra are for larger DM masses. Bluer spectra are light DM masses. x is a unitless factor defined as the ratio of the mass of DM, m_χ , and the final state particle energy E_γ . Figure from [19].

discovered, and it is the largest nearby DM dense region to look at. Additionally, the DM halo surrounding the Milky Way is clumpy [18]. There are regions in the DM halo of the Milky Way that have more DM than others that have captured gas over time. These sub-halos were dense enough to collapse gas and form stars. These apparent sub galaxies are known as dwarf spheroidal galaxies and are the main sources studied in this thesis. Each source type comes with different trade-offs. Galactic Center studies will be very sensitive to the assumed distribution of DM. The central DM density can vary substantially as demonstrated in Figure 2.12. At distances close to the center of the galaxy, or small r , the differences in DM densities can be 3-4 orders of magnitude. Searches toward the galactic center will therefore be quite sensitive to the assumed DM distribution.

Searches toward Dwarf Spheroidal Galaxies (dSph's) suffer from uncertainties in the DM density less than the galactic center studies. This is mostly from their diminutive size being smaller than the angular resolution of most γ -ray observatories [18]. The DM content dSph's are typically determined with the Virial theorem, Equation (2.1), and are usually majority DM [18] in mass. DSph's tend to be ideal sources to look at for DM searches. Their environments are quiet with little

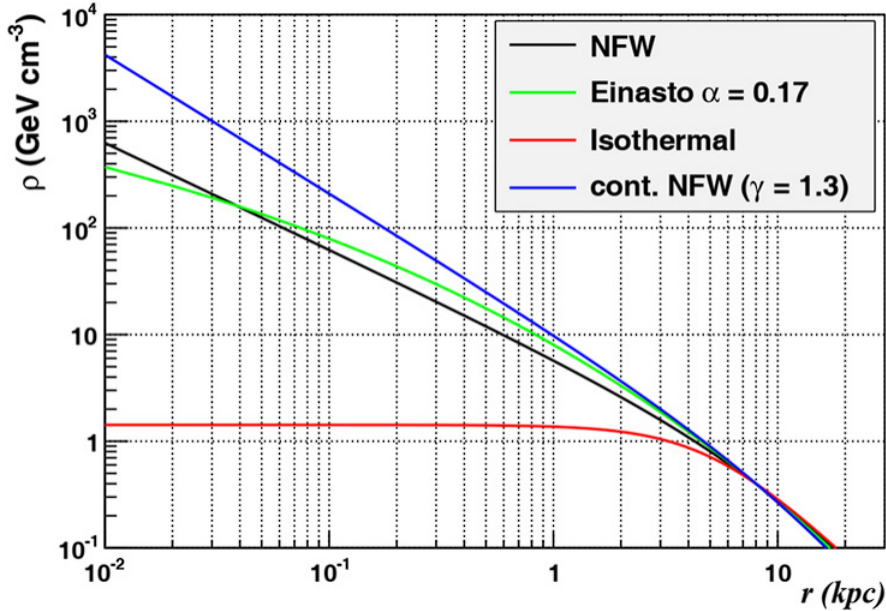


Figure 2.12 Different dark matter density profiles compared. Some models produce exceptionally large densities at small r [20].

777 astrophysical background. Unlike the galactic center, the most active components of dSph's are the
 778 stars within them versus a violent accretion disc around a black hole. All this together means that
 779 dSph's are among the best sources to look at for indirect DM searches. dSph's are the targets of
 780 focus for this thesis.

781 2.6 Multi-Messenger Dark Matter

782 Astrophysics entered a new phase in the past few decades that leverages our increasing sensitivity
 783 to SM channels and general relativity (GR). Up until the 21st century, astrophysical observations
 784 were performed with photons (γ) only. Astrophysics with this 'messenger' is fairly mature now.
 785 Novel observations of the universe have since only adjusted the sensitivity of the wavelength of
 786 light that is observed except at MeV energies. Gems like the CMB [10], and more have ultimately
 787 been observations of different wavelengths of light. Multi-messenger astrophysics proposes using
 788 other SM particles such the p^{+-} , or ν or gravitation waves predicted by general relativity.

789 The experiment LIGO had a revolutionary discovery in 2016 with the first detection of a binary
 790 black hole merger [21]. This opened the collective imagination to observing the universe through
 791 gravitational waves. There has also been a surge of interest in the neutrino (ν) sector. IceCube

792 demonstrated that we are sensitive to neutrinos in regions that correlate with significant photon
 793 emission like the galactic plane [22]. Neutrinos, like gravitational waves and light, travel mostly
 794 unimpeded from their source to our observatories. This makes pointing to the originating source
 795 of these messengers much easier than it is for cosmic rays which are deflected from their source by
 796 magnetic fields.

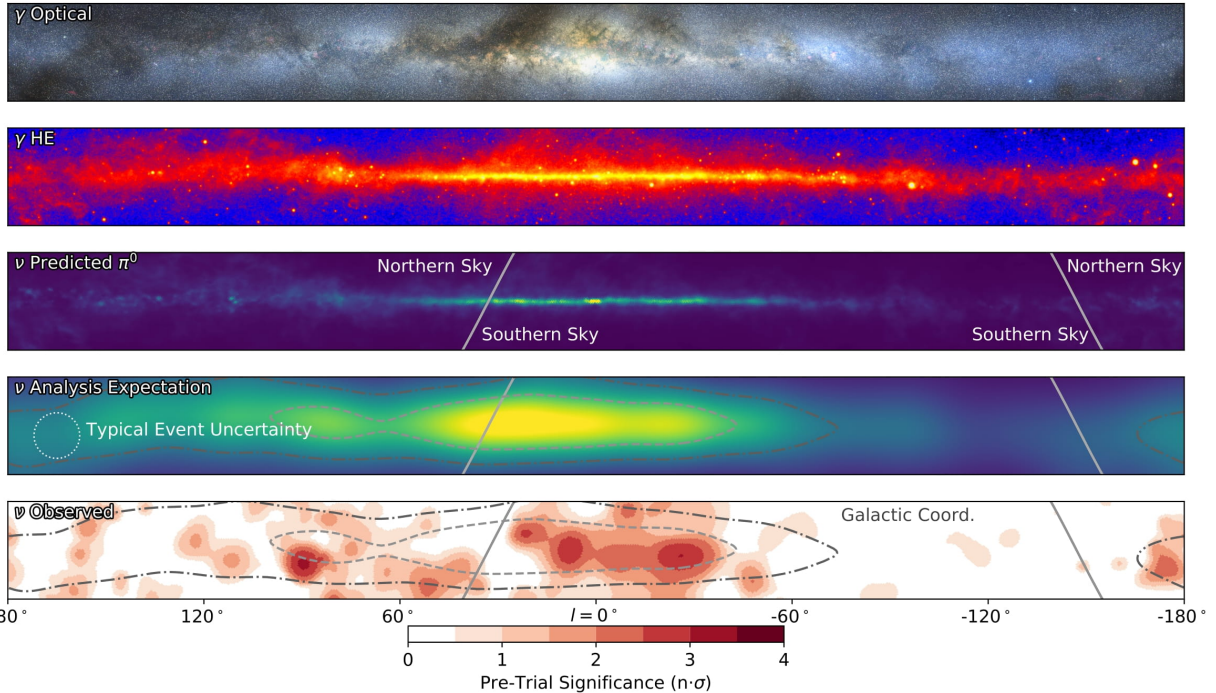


Figure 2.13 The Milky Way Galaxy in photons (γ) and neutrinos (ν) [22]. The Galactic center is at $l=0^\circ$ and is the brightest region in all panels. (top) An Optical color image of the Milky Way galaxy seen from Earth. Clouds of gas and dust obscure some light from stars. (2nd down) Integrated flux of γ -rays observed by the Fermi-LAT telescope [23]. (middle) Expected neutrino emission that corresponds with Fermi-LAT observations. (2nd up) Expected neutrino emission profile after considering detector systematics of IceCube. (bottom) Observed neutrino emission from region of the galactic plane. Substantial neutrino emission was detected.

797 The IceCube collaboration recently published a groundbreaking result of the Milky Way in
 798 neutrinos. The recent result from IceCube, shown in Figure 2.13, proves that we can make
 799 observations under different messenger regimes. The top two panels show the appearance of the
 800 galactic plane to different wavelengths of light. Some sources are more apparent in some panels,
 801 while others are not. This new channel is powerful because neutrinos are readily able to penetrate
 802 through gas and dust in the Milky Way. This new image also refines our understanding of how high

803 energy particles are produced. For example, the fit to IceCube data prefers neutrino production
 804 from the decay of π^0 [22].

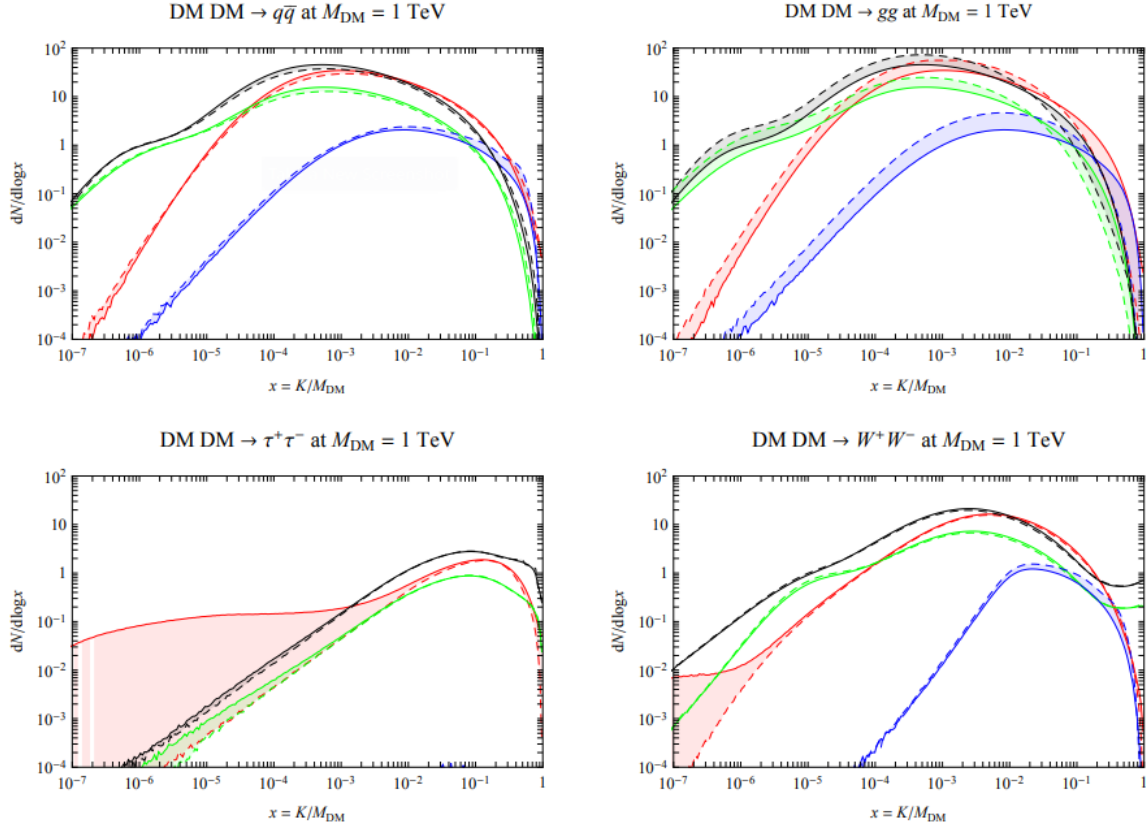


Figure 2.14 Dark Matter annihilation spectra for different final state particle and standard model annihilation channels [24]. Photons (red), e^\pm (green), \bar{p} (blue), ν (black).

805 Exposing our observations to more cosmic messengers greatly increases our sensitivity to
 806 rare processes. In the case of DM, Figure 2.14, there are many SM particles produced in DM
 807 annihilation. Among the final state fluxes are gammas and neutrinos. Charged particles are also
 808 produced however they would not likely make it to Earth since they will be deflected by magnetic
 809 fields between the source and Earth. This means observatories that can see the neutral messengers
 810 are especially good for DM searches and for combining data for a multi-messenger DM search.

CHAPTER 3

811 HIGH ALTITUDE WATER CHERENKOV (HAWC) OBSERVATORY

812 3.1 The Detector



Figure 3.1 Photo of the HAWC detector that I took on May 17, 2023. Main array is centered in the photo and comprised of the larger tanks. Outriggers are the smaller tanks around the main array.

813 The High Altitude Water Cherenkov (HAWC) Observatory is a specialized instrument designed
814 for the observation of high energy gamma-rays and cosmic rays [25]. Located on the Sierra
815 Negra volcano in Mexico, HAWC observes gamma rays and cosmic rays in the energy range of
816 approximately 100 GeV to 100's of TeV. HAWC is strategically situated to maximize observational
817 efficiency due to its high altitude. At an elevation of 4,100 meters, it monitors about two-thirds of
818 the sky every day with an uptime above 90%. This capability is essential for studying high-energy
819 astrophysical phenomena.

820 HAWC consists of 300 water Cherenkov detectors (WCDs) spread over $22,000 \text{ m}^2$. Each main
821 array detector is filled with purified water and equipped with four, upward-facing photomultiplier
822 tubes (PMTs). See Fig. 3.3 for schematic of WCDs. These PMTs detect Cherenkov radiation from
823 charged particles passing through the tanks. These charged particles are generated when a high

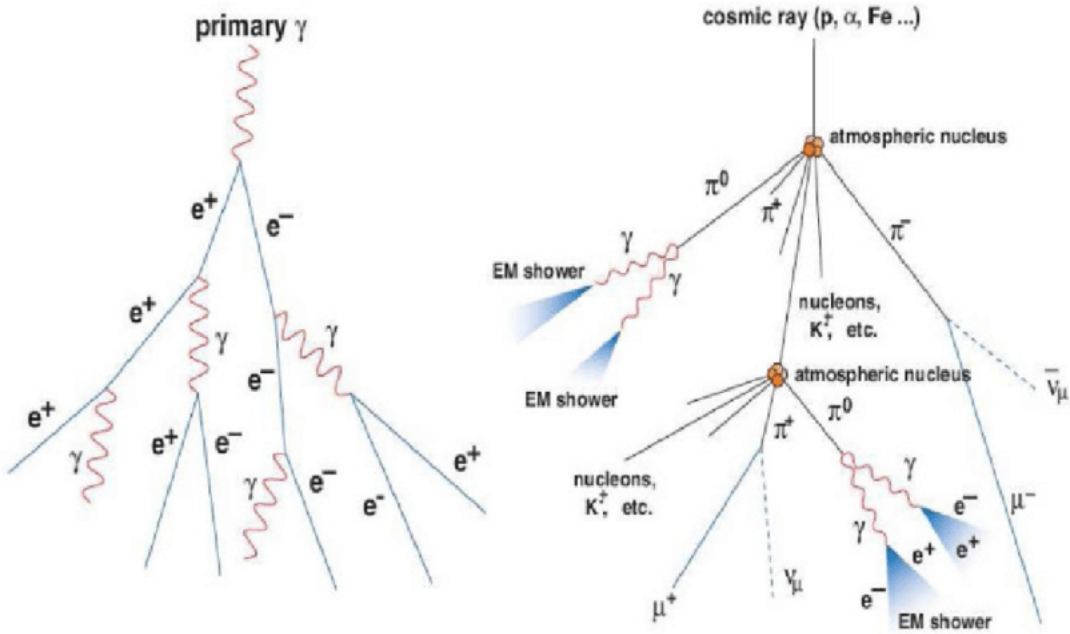


Figure 3.2 A particle physics illustration of high energy particle showers. Left shower is an electromagnetic shower from a high energy gamma-ray. Most particles in the shower will be a combination of photons and charged leptons, in this case electrons (e). Right figure shows a cosmic ray particle shower. The cosmic ray will produce many more types of particles including pions (π), neutrinos, and charged leptons. Figured pulled from [26].

824 energy gamma or cosmic ray collides with gas in the atmosphere to create a charged particle shower,
 825 see Fig. 3.2. The observatory includes a separate tank configuration which are referred to as the
 826 outriggers. They are a secondary array of 345 smaller WCD's. Surrounding the main array, each
 827 outrigger tank measures 1.55 meters in diameter and height and contain a single upward-facing
 828 eight-inch PMT. This add-on increases the instrumented footprint fourfold. The outriggers are
 829 meant to improve the reconstruction of showers extending beyond the main array, especially for
 830 events above 10 TeV. However, at the time of writing this thesis, the outriggers have not been fully
 831 integrated into HAWC's reconstruction software.

832 3.1.1 Construction and Hardware

833 Each main array WCD, see Fig. 3.3, is a cylindrical tank with dimensions of 7.3 m in diameter
 834 and 5.4 m in height and filled with 180,000 L of water [25]. The metal shell of these tanks is made
 835 from bolted together, corrugated, galvanized steel panels. The tanks are placed into 0.6 m deep

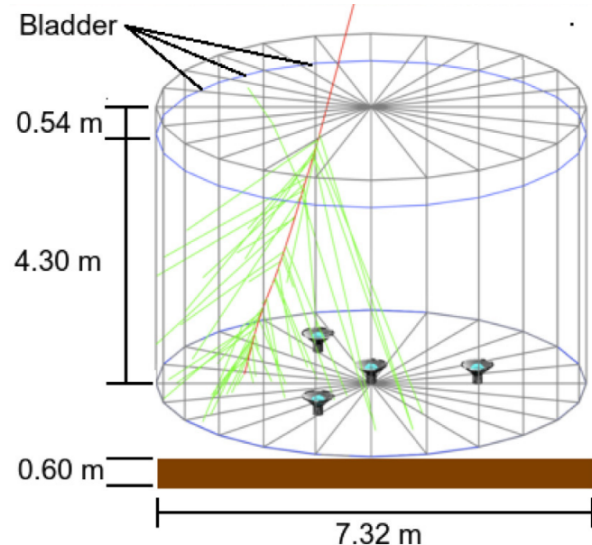


Figure 3.3 The WCDs. Left image features several WCDs looking from within the main array of HAWC. Right image shows a schematic of a WCD pulled from [25].

836 trenches filled with rammed earth to secure it against seismic activity [27]. The interior of each
 837 tank is lined with a black, low-density polyethylene bladder, designed to be impermeable to external
 838 light and to prevent reflection of Cherenkov light within the tank. This bladder is approximately 0.4
 839 mm thick and composed of two layers of three-substrate film. To further minimize light penetration,
 840 a black agricultural foil covers the bladder. The ground and walls inside the tank are protected
 841 with felt and sand to safeguard against punctures. The tanks are filled 4.5 m deep of purified water,
 842 achieving a photon attenuation length for Cherenkov photons that exceeds the tank's dimensions
 843 [27]. This purification level ensures the optimal detection environment for the photons generated
 844 by traversing charged particles.

845 At the base of each tank, four photomultiplier tubes (PMTs) are installed to detect the Cherenkov
 846 radiation emitted by charged particles in water. Three 8-inch diameter PMTs surround a larger
 847 10 inch PMT from Hamamatsu [28]. The variation in PMT response is carefully accounted for
 848 in event reconstruction algorithms. Signals from the PMTs traverse 610 ft cables to the counting
 849 house, where they are processed by Front-End Boards (FEBs), see Figs. 3.4 and 3.5. These FEBs,
 850 along with Time to Digital Converters (TDCs), digitize the signals and manage the high voltage
 851 supply to the PMTs.

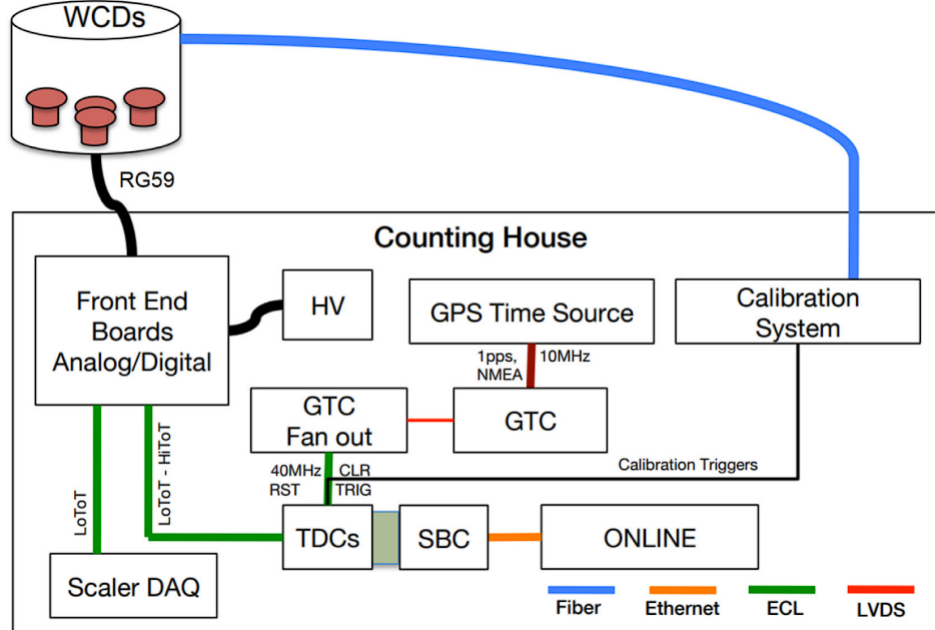


Figure 3.4 Overview of HAWC control and data electronics. The LoToT and HiToT threshold signals are discussed in Section 3.1.2. Figure from [27]

852 3.1.2 Data Acquisition and Signal Processing

853 The HAWC data acquisition (DAQ) and signal processing systems convert the physical detection
 854 of particles into analyzable data. This process involves a series of steps from initial signal detection
 855 by PMTs to digital conversion and preliminary analysis, see Figs. 3.5 and 3.6.

856 Once the signal from the PMTs arrive at the counting house, they enter the Front-End Boards
 857 (FEBs). The FEBs are responsible for the initial processing of these signals, which includes
 858 amplification and integration [30]. Each PMT signal is compared against preset LOW/HIGH
 859 voltage thresholds in the FEBs, see Fig. 3.6, identifying signals that correspond to about 1/4 and
 860 4 photoelectrons, respectively. This differentiation allows the system to gauge the strength of
 861 the detected Cherenkov radiation. The processed signals are then digitized by Time to Digital
 862 Converters (TDCs). These converters measure the time over threshold (ToT) for each signal, a
 863 parameter that reflects both the duration and amplitude of the signal. This digitization facilitates
 864 reconstruction of the original event for translating the physical interactions within the detectors into
 865 data [27, 29, 30].

866 Synchronization across the HAWC observatory is maintained by a central GPS Timing and

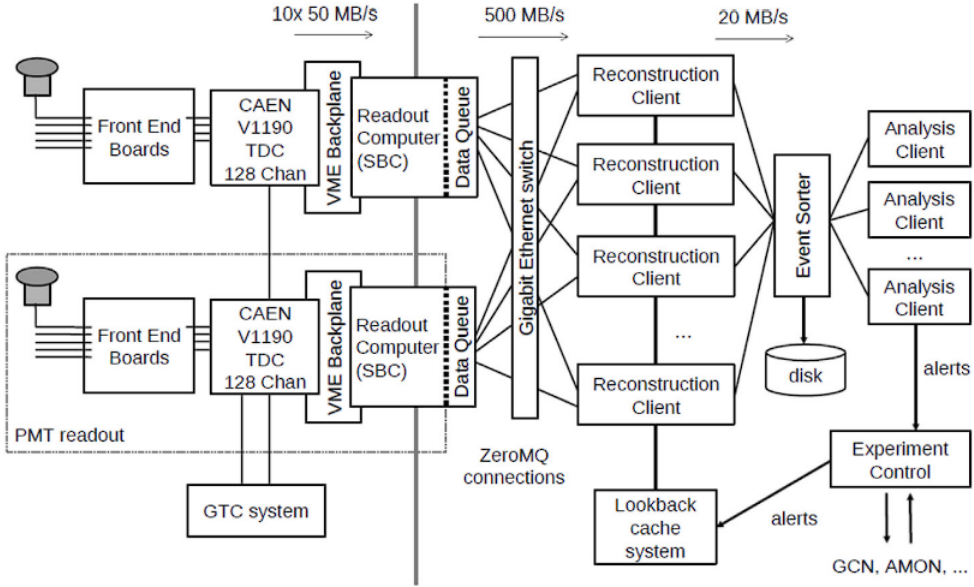


Figure 3.5 Schematic of data flow in HAWC data acquisition and online processing system. Pulled from [29].

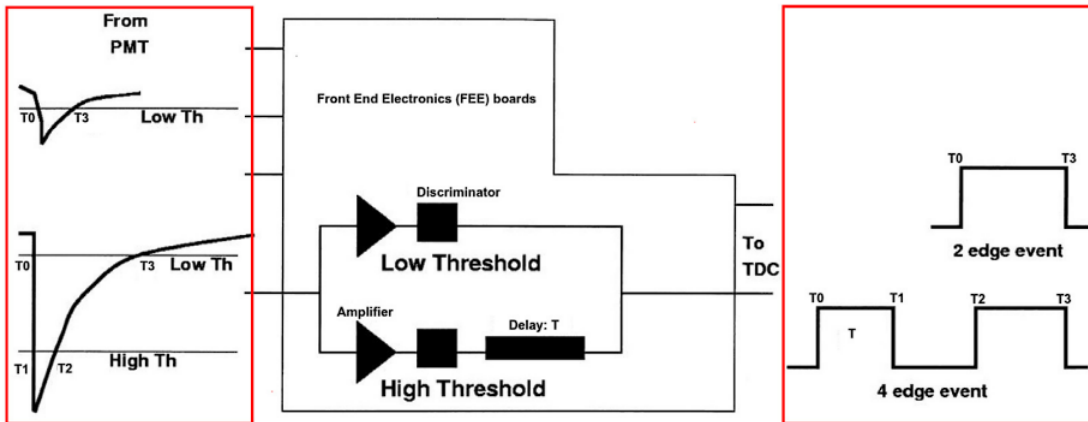


Figure 3.6 How HAWC FEB intially processes analog PMT signals. Signals are split through an amplifier and discriminator circuit. Each path is designated for either the HIGH or LOW threshold for the signal. The 2-edge event corresponds to LOW, while the 4 edge corresponds to HIGH.

867 Control (GTC) system, which achieves a timing resolution of 98 ps. This high-resolution timing
868 is vital for accurately reconstructing the timing and location of air showers initiated by cosmic
869 and gamma rays. The GTC system ensures that all components of the DAQ operate in unison to
870 preserve the temporal integrity of the detected events [27, 31].

871 Once digitized, the data are transferred to an online event reconstruction system. This system
872 runs the Reconstruction Client, which utilizes the raw PMT data to reconstruct the characteristics
873 of the air showers, such as their direction and energy [29]. The capacity for real-time analysis
874 allows HAWC to promptly respond to astrophysical phenomena like Gamma Ray Bursts (GRBs)
875 and to participate in multi-messenger astronomy by following up on alerts from other observatories.
876 This real-time processing system is designed to handle high data throughput, using ZeroMQ [32]
877 for efficient data transfer between software components. Analysis Clients perform specific online
878 analyses that require immediate data, including monitoring for GRBs, solar flare activity, and
879 participation in global efforts to track gravitational waves and neutrinos [27].

880 The DAQ system is overseen by an Experiment Control system and crew that manage the
881 operational aspects of data collection. This includes initiating and terminating data collection
882 runs and monitoring the experiment for errors. In the event of a system crash, often caused by
883 environmental factors such as lightning, the Experiment Control system is designed to automatically
884 restart the experiment and minimize downtime [27, 29].

885 3.2 Event Reconstruction

886 Event reconstruction at the HAWC Observatory is a critical procedure that converts the raw data
887 from the observatory’s WCDs into a coherent framework for understanding cosmic and gamma-
888 ray events. This process includes several distinct steps. Core Fitting determines the geometric
889 center of the air shower on the detector plane. Angle Reconstruction assesses the trajectory of the
890 incoming particle, revealing its origin in the sky. Energy Estimation is performed using both f -hit
891 and Neural Network (NN) methods to quantify the energy of the detected events. Gamma/Hadron
892 discrimination differentiates between gamma-ray and hadronic cosmic ray initiated showers, a vital
893 step for astrophysical interpretations. Each of these steps is integral to the observatory’s objective

894 of investigating the high-energy universe and enable the transformation of signals into detailed
 895 insights about high energy cosmic phenomena.

896 **3.2.1 Core Fitting**

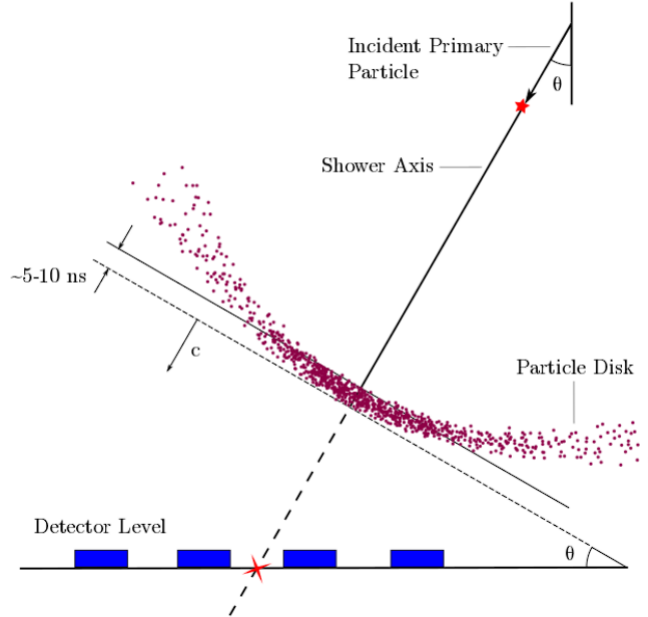


Figure 3.7 An air shower incident on WCDs. Secondary particles of an air shower travel in a cone centered on primary incident particle. Reconstruction of the initial angle is possible with arrival time of hits in PMTs inside WCDs. Figure from [33].

897 In the study of air showers, accurately determining the location of the air shower core on the
 898 ground is crucial for reconstructing the direction of the originating primary particle. An illustration
 899 of this can be seen in a HAWC event plot, Figs. 3.2 and 3.11, where the lateral charge distribution
 900 across the array is displayed. The core is identified and marked with a red star, reconstructed using
 901 a predetermined functional form, Eq. (3.1).

902 We model signal S_i from the i th PMT is given by the following equation:

$$S_i = S(A, \tilde{x}, \tilde{x}_i) = A \left(\frac{1}{2\pi\sigma^2} e^{-\frac{|\vec{x}_i - \vec{x}|^2}{2\sigma^2}} + \frac{N}{(0.5 + |\vec{x}_i - \vec{x}|/R_m)^3} \right) \quad (3.1)$$

903 In this model, \tilde{x} represents the core location and \tilde{x}_i is the position of the i th PMT. R_m stands for
 904 the Molière radius, which is approximately 120 meters at the altitude of HAWC. σ is the standard
 905 deviation of the Gaussian distribution. N is the normalization factor for the tail of the distribution.

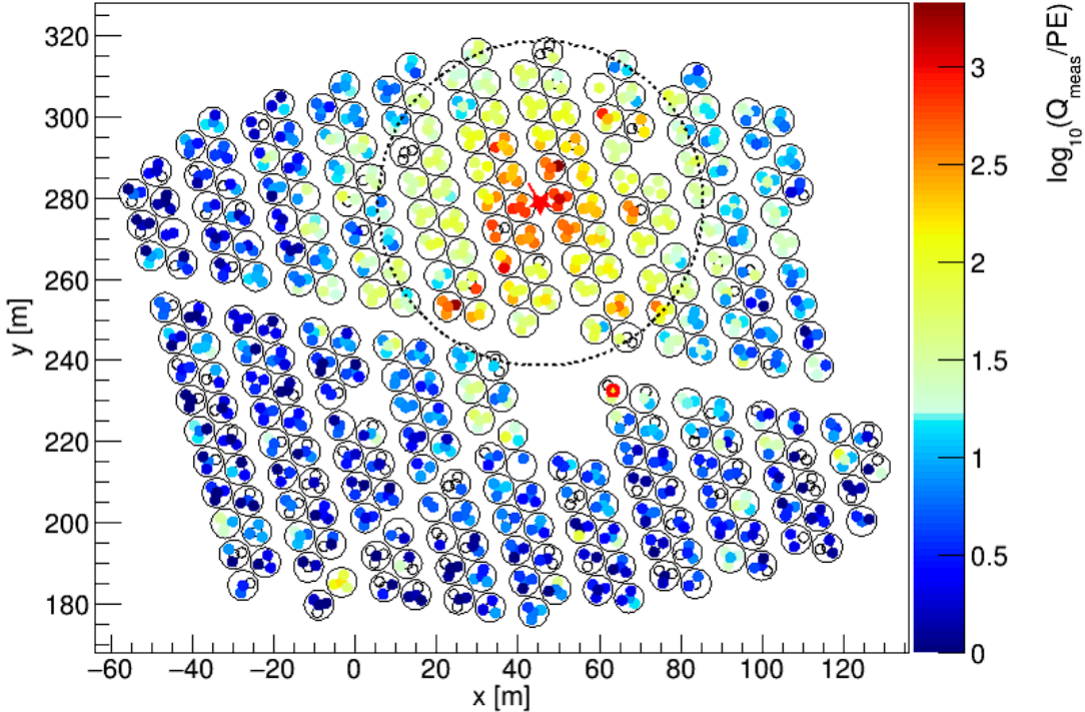


Figure 3.8 Charge deposition in each PMT for a reconstructed gamma-ray event. WCDs are outlined in black surrounding the 4 smaller circles that represent PMTs. The color scale indicates the charge deposition in each PMT. The best shower core fit from SFCF is noted with a red star in the center of the dashed circle [34].

906 The equation incorporates fixed values of $\sigma = 10$ m and $N = 5 \cdot 10^{-5}$. This leaves the core location
 907 and overall amplitude A as the free parameters to be determined during fitting.

908 The chosen functional form for the Super Fast Core Fit (SFCF) algorithm is a simplified version
 909 of a modified Nishimura-Kamata-Greisen (NKG) function [35], selected for its computational
 910 efficiency which is essential for rapid fitting of air shower cores. The SFCF form allows numerical
 911 minimization to converge more quickly due to the function's simplicity, the analytical computation
 912 of its derivatives, and the absence of a pole at the core location [34]. Figure 3.8 provides a
 913 visualization of a recorded event, with the plot depicting the charge recorded by each PMT as a
 914 function of the distance to the reconstructed shower core. Through the application of the SFCF,
 915 core locations can be identified with a median error of approximately 2 m for large events and about
 916 4 m for smaller ones, assuming the gamma-ray event core impacts directly upon the HAWC detector
 917 array [34]. It is noted that as the core's distance from the main array increases, the precision in

918 locating the core diminishes [34], highlighting the importance of proximity in the accuracy of core
919 reconstruction.

920 **3.2.2 Angle Reconstruction**

921 After establishing the core position, the next step is angle reconstruction. This process deter-
922 mines the primary particle's trajectory. The angle of arrival is indicative of the originating gamma
923 ray's direction. It correlates to the cosmic source of the gamma-ray. We deduce this angle using
924 the timing of PMT hits [34].

925 The air shower's front is conically shaped, not flat. This shape arises from the travel patterns
926 of secondary particles. An event example is illustrated in Fig. 3.7. Far from the core, secondary
927 particles undergo multiple scattering. They also travel longer distances [36]. Particle sampling
928 decreases with distance from the core. This decrease results in measurable delays in arrival times
929 [36, 34]. Simulations provide a corrective measure for these effects. The correction is a function of
930 shower parameters [34]. It adjusts both curvature and sampling. The distance from the shower core
931 and the charge recorded by PMTs are crucial to this correction. A function based on simulation
932 and Crab Nebula observations is used for this purpose [34]. This curvature correction allows us to
933 fit the particle front as a plane wave.

934 Corrections lead to the χ^2 minimization step. This technique fits a plane to the timing data of
935 the PMTs. It then calculates the shower's angle of arrival. The zenith and azimuth angles are the
936 results of this fit [36]. The local angles are converted to celestial coordinates. These coordinates
937 allow correlation with gamma-ray sources. Right ascension (RA) and declination (Dec) are used
938 for this purpose. RA is akin to longitude, and Dec to latitude.

939 The reconstructed angle's resolution ranges from 0.1° to 1° . This range depends on the incoming
940 particle's energy and zenith angle [36]. The analysis uses a curvature/sampling correction. This
941 correction applies a quadratic function based on distance from the core [34]. The adjustment
942 improves angular resolution. However, discrepancies between simulation and observation persist.
943 These discrepancies introduce systematic errors into HAWC analyses [34].

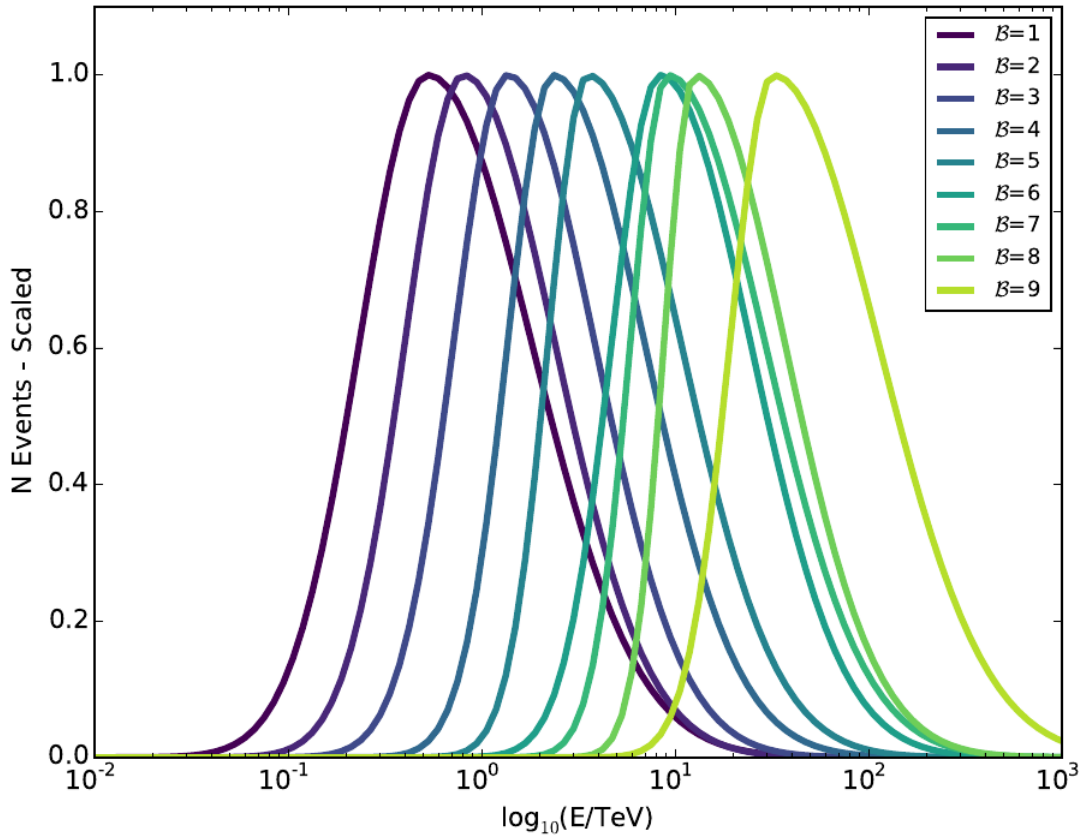


Figure 3.9 Simulated normalized energy distribution of each f_{hit} bin defined in Tab. 3.1. Monte Carlo simulation of gamma-rays with $E^{-2.63}$ spectral shape and simulated source at 20° declination. Figure from [34].

Bin	Lower Edge %	Upper Edge %	Θ_{68} ($^\circ$)
1	6.7	10.5	1.05
2	10.5	16.2	0.69
3	16.2	24.7	0.50
4	24.7	35.6	0.39
5	35.6	48.5	0.30
6	48.5	61.8	0.28
7	61.8	74.0	0.22
8	74.0	84.0	0.20
9	84.0	100	0.17

Table 3.1 Definitions of f_{hit} energy estimator bins. Bins are defined by the fraction of available PMTs that are triggered during an air shower event. The angular resolution, Θ_{68} , is the bin containing 68% of events [34].

944 **3.2.3 f_{hit} Energy Estimation**

945 The HAWC Observatory quantifies the primary particle energy of air showers using a metric
946 known as f_{hit} . This ratio compares the count of PMTs involved in the event reconstruction to the
947 total number of functional PMTs at the time [34]. The main array consists of about 1200 PMTs,
948 but the count may vary due to maintenance or other operational factors.

949 Events are stratified into several f_{hit} bins. Each bin corresponds to a specific range of angular
950 resolutions, enabling a structured approach to event analysis based on the extent of the shower
951 footprint, see Tab. 3.1. The f_{hit} metric, while effective, has several limitations. It is dependent on
952 the zenith angle and the spectral characteristics presumed for the observed source. The variable
953 also reaches a saturation point around 10 TeV, after which the detector's ability to discriminate
954 between higher energy levels diminishes [34]. Furthermore, the energy distribution for each f_{hit}
955 bin is notably broad, see Fig. 3.9. In response to these limitations, HAWC has developed more
956 intricate algorithms for energy estimation. These algorithms incorporate the zenith angle and
957 the distribution of charge around the shower core for a more accurate assessment of the primary
958 particle's energy, particularly at energies surpassing 10 TeV [36].

959 The relationship between f_{hit} and primary energy is complex. Atmospheric attenuation can
960 cause high-energy showers to present a smaller footprint, misrepresenting their energy in the f_{hit}
961 metric. This effect is captured in simulations that chart the actual energy distribution across f_{hit}
962 categories [36]. Such distributions vary with the declination of the source and the theoretical
963 energy spectrum used in the model.

964 **3.2.4 Neural Network Energy Estimation**

965 The energy estimation for photon events at the HAWC Observatory is refined through an
966 artificial neural network (NN) algorithm. This method, based on the Toolkit for Multivariate
967 Analysis NN, adopts a multilayer-perceptron model with logistic activation functions across its
968 layers. The structure includes two hidden layers, the first with 15 nodes and the second with 14,
969 designed to process input variables through a neural network optimized to estimate primary particle
970 energies [38].

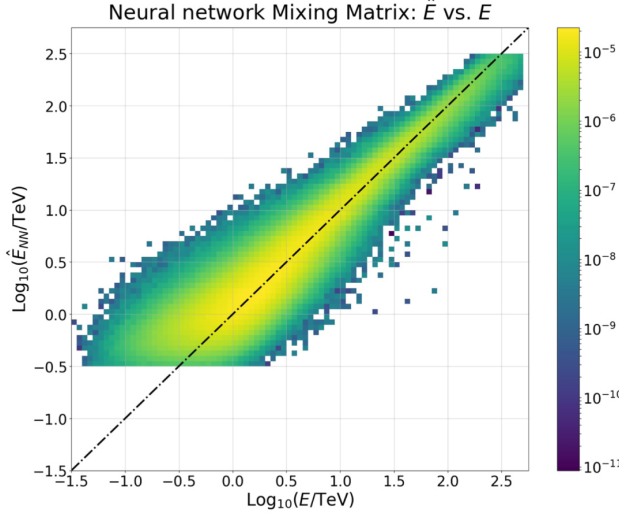


Figure 3.10 Neural Network energy estimator performance compared to true energy. The dotted line is the identity line where the estimator and injection agree. Gamma/hadron separation cuts were applied with the energy estimation. Figure pulled from [37]

971 The NN is trained to minimize a specific error function that measures discrepancies between the
 972 NN's energy predictions and the actual energies from Monte Carlo simulations. This minimization
 973 targets an error function that incorporates the relative importance of each event, weighting more
 974 the importance to mimic an E^{-2} power law spectrum. This approach helps achieve a uniform
 975 error rate across energies ranging from 1 to 100 TeV. The optimization process leverages the
 976 Broyden-Fletcher-Goldfarb-Shanno algorithm that calibrates the NN's 479 weights [37].

977 The spectral analysis employs a binned likelihood method, using a forward-folding technique
 978 to accommodate the energy estimate's bias and resolution [37]. This establishes a 2D binning
 979 scheme that categorizes events by both their f_{hit} value and estimated energy. The decision to use
 980 this scheme over a simple energy-based binning lies in the correlation between gamma/hadron
 981 separation parameters and the angular resolution with both the size and energy of the event. The
 982 spectrum of interest is partitioned into nine f_{hit} bins, each further divided into 12 energy bins,
 983 spanning from 0.316 TeV to 316 TeV, encompassing a total of 108 bins [37]. However, not all
 984 bins contribute to the final estimate. Bins with low event populations or insufficient Monte Carlo
 985 simulation are excluded. This approach focuses on the central 99% of events by estimated energy
 986 within each f_{hit} bin, effectively removing outliers [37].

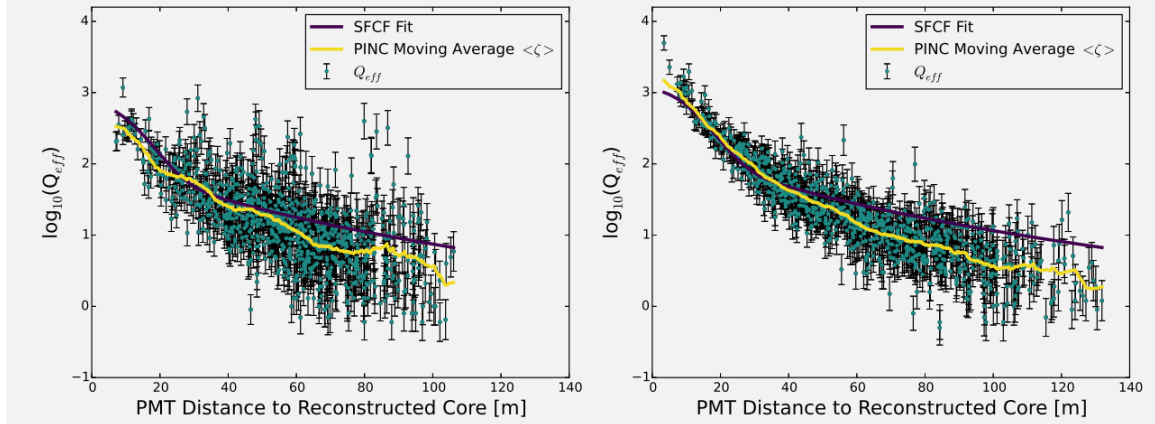


Figure 3.11 Lateral distribution functions (LDFs) for cosmic ray (left) and a photon candidate from the Crab Nebula (right). Cosmic ray LDF has clearly isolated hits far from the reconstructed shower core. Gamma-ray shower shows a more cuspy event [34].

987 Input variables for the NN are selected to capture key characteristics of the air shower: energy
 988 deposition, containment, and atmospheric attenuation. The algorithm calculates energy deposition
 989 using the fraction of PMTs and tanks activated, alongside the logarithm of the normalization from
 990 the lateral distribution fit. Containment is inferred from the distance between the shower core and
 991 the array's center, while atmospheric attenuation is evaluated using the reconstructed zenith angle
 992 and a detailed analysis of the shower's lateral charge distribution [38, 37].

993 This refined NN energy estimation methodology is an integral component of HAWC's toolkit,
 994 enabling precise analysis of high-energy gamma-ray events. It represents a significant advancement
 995 in the field by more accurately mapping observed shower characteristics to primary particle energies.

996 3.2.5 G/H Discrimination

997 At the HAWC Observatory, distinguishing between air showers initiated by gamma rays and
 998 those by hadronic cosmic rays is fundamental for astrophysical data purity. The separation process
 999 leverages differences in shower characteristics: electromagnetic showers from gamma rays typically
 1000 display fewer muons and a smoother lateral distribution, whereas hadronic showers are more chaotic
 1001 due to the abundance of muons and hadronic sub-showers.

1002 Two primary parameters facilitate the identification of cosmic-ray events [34]:

1003 Compactness (C): This parameter evaluates the charge captured by PMTs, particularly focusing
 1004 on the PMT with the highest effective charge beyond a 40-meter radius from the shower core.

1005 Compactness is inversely proportional to this effective charge, as higher charges at extended
1006 distances from the core are indicative of hadronic showers. It is mathematically expressed as:

$$C = \frac{N_{\text{hit}}}{CxPE_{40}} \quad (3.2)$$

1007 where N_{hit} is the number of PMTs hit and $CxPE_{40}$ is the effective charge measured outside a 40 m
1008 radius from the shower cores [34].

1009 PINCness (P): PINCness quantifies the "clumpiness" of a shower using the charges recorded
1010 by PMTs and is short for Parameter for Identifying Nuclear Cosmic Rays. It is computed from the
1011 logarithm of the effective charge, $Q_{\text{eff},i}$, of each PMT hit, i , compared to an expected average for
1012 that annular region. A higher PINCness suggests a less smooth distribution, typical of hadronic
1013 showers. The formula is:

$$P = \frac{1}{N} \sum_{i=0}^N \frac{(\zeta_i - \langle \zeta \rangle)^2}{\sigma_{\zeta_i}^2} \quad (3.3)$$

1014 where $\zeta_i = \log_{10}(Q_{\text{eff},i})$. The average, $\langle \zeta \rangle$ is the average over an annular region surrounding the
1015 shower core. The errors, σ_{ζ_i} , are computed and allocated from gamma-ray candidates close to the
1016 Crab.

1017 These parameters are tested and modeled in simulations and with observational data near the
1018 Crab Nebula. Figure 3.11 illustrating the lateral distributions for representative cosmic-ray and
1019 photon candidate showers, as well as the distribution of these discrimination parameters, affirm
1020 their efficacy [34].

1021 The discrimination technique has remained consistent, but cut values have been reoptimized
1022 for the 2D bins based on f_{hit} and NN estimated energy. This refinement enhances the selection
1023 of high-energy events. Each bin ensures at least 50% efficiency for gamma-ray detection, with
1024 efficiencies extending up to nearly 100% in certain bins [34, 37].

1025 3.3 Background Estimation: Direct Integration

1026 The ratio of cosmic rays to gamma rays can be as high as 10,000 to 1, depending on the energy.
1027 At HAWC, we confront a significant challenge even after gamma/hadron cuts: our gamma-ray data
1028 is still inundated with cosmic-ray events. To tackle this, we rely on the direct integration method

1029 developed by Milagro [39]. This method capitalizes on the cosmic rays' isotropic nature resulting
1030 from their deflection by interstellar magnetic fields.

1031 The direct integration method estimates background events by integrating over a stable two-
1032 hour period of detector operation. The expected number of background events at a particular sky
1033 coordinate (ϕ, θ) is determined by integrating the normalized detector's efficiency with the all-sky
1034 event rate:

$$N_{\text{exp}}(\phi, \theta) = \int \int E(\text{ha}, \theta) \cdot R(t) dt \quad (3.4)$$

1035 Here, $E(\text{ha}, \theta)$, represents the detector's efficiency, which varies with local coordinates (hour angle
1036 and declination). $R(t)$ is the event rate as a function of time [39].

1037 Our background estimation is expected to falter in high-energy ranges where cosmic-ray events
1038 are less frequent due to enhanced gamma/hadron discrimination. Sparsity in our background and
1039 data also arise at the limits of HAWC's sensitivity and during short-term analyses of transient events.
1040 HAWC addresses these issues by using a pixel size of 0.5° in our direct integration to maintain
1041 robustness in our estimation [34, 36]. In constructing the background model, it's crucial to exclude
1042 areas of the sky with known gamma-ray sources. Regions containing the Crab Nebula, Mrk 421,
1043 Mrk 501, and the Galactic Plane are masked to prevent their significant gamma-ray signals from
1044 biasing our background estimate [34].

CHAPTER 4

1045 **GLORY DUCK: MULTI-WAVELENGTH SEARCH FOR DARK MATTTER** 1046 **ANNIHILATION TOWARDS DWARF SPHEROIDAL GALAXIES**

1047 **4.1 Introduction**

1048 The field of astrophysics now has several instruments and observatories sensitive to high energy
1049 gamma-rays. The energy sensitivity for the modern gamma-ray program spans many orders of
1050 magnitude. Figure 4.1 demonstrates these comparable sensitivities across energies for the five
1051 experiments: Fermi-LAT, HAWC, HESS, MAGIC, and VERITAS.

1052 Each of the five experiments featured in Figure 4.1 have independently searched for DM
1053 annihilation from dwarf spheroidal galaxies (dSph) and set limits on annihilation cross-section of
1054 WIMPs. Intriguingly, there are regions of substantial overlap in their energy sensitivities. This
1055 clearly motivates an analysis that combines data from these five. Each experiment has unique
1056 gamma-ray detection methods and their weaknesses and strengths can be leveraged with each other.
1057 The HAWC gamma-ray observatory is extensively introduced in chapter 3, so it is not introduced
1058 here. A brief description of the remaining experiments are in the following paragraphs.

1059 The Large Area Telescope (LAT) is a pair conversion telescope mounted on the NASA Fermi
1060 satellite in orbit \sim 550 km above the Earth [41]. LAT's field of view covers about 20% of the
1061 whole sky, and it sweeps the whole sky approximately every 3 hours. LAT's gamma-ray energy
1062 sensitivity ranges from 20 MeV up to 1 TeV. Previous DM searches towards dSphs using Fermi-LAT
1063 are published in [42] and [43].

1064 The High Energy Spectroscopic System (HESS), Major Atmospheric Gamma Imaging
1065 Cherenkov (MAGIC), and Very Energetic Radiation Imaging Telescope Array System (VERI-
1066 TAS) are arrays of Imaging Atmospheric Cherenkov Telescopes (IACT). These telescopes observe
1067 the Cherenkov light emitted from gamma-ray showers in the Earth's atmosphere. The field of
1068 view for these telescopes is no larger than 5° with energy sensitivities ranging from 30 GeV up
1069 to 100 TeV [44, 45, 46]. IACTs are able to make precise observations in selected regions of the
1070 sky, however can only be operated in ideal dark conditions. HESS's observations of the dwarves

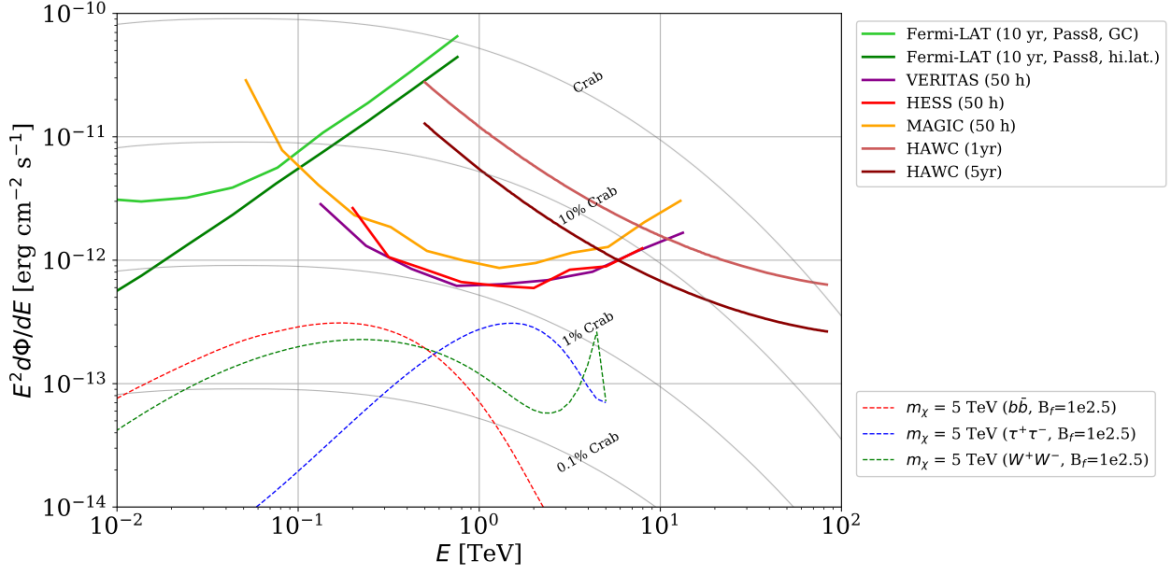


Figure 4.1 Sensitivities of five gamma-ray experiments compared to percentages of the Crab nebula's emission and dark matter annihilation. Solid lines present estimated sensitivities to power law spectra [FACT CHECK THIS] for each experiment. Green lines are Fermi-LAT sensitivities where lighter green is the sensitivity to the galactic center and dark green is its sensitivity to higher declinations. Orange, red, and purple solid lines represent the MAGIC, HESS, and VERITAS 50 hour sensitivities respectively. The maroon and brown lines are the HAWC 1 year and 5 year sensitivities. Across four decades of gamma-ray energy, these experiments have similar sensitivities on the order 10^{-12} erg $\text{cm}^{-2}\text{s}^{-1}$. The dotted lines are estimated dark matter fluxes assuming $m_\chi = 5$ TeV DM annihilating to bottom quarks (red), tau leptons (blue), and W bosons (green). Faded gray lines outline percentage flux of the Crab nebula. Figure is an augmented version of [40]

1071 Sculptor and Carina were between January 2008 and December 2009. HESS's observations of
 1072 Coma Berenices were taken from 2010 to 2013, and Fornax was observed in 2010 [47, 48, 49].
 1073 MAGIC provided deep observations of Segue1 between 2011 and 2013 [50]. MAGIC also provides
 1074 data for three additional dwarves: Coma Berenices, Draco, and Ursa Major II where observations
 1075 were made in: January - June 2019 [51], March - September 2018 [51], and 2014 - 2016 [52]
 1076 respectively. VERITAS provided data for Boötes I, Draco, Segue 1, and Ursa Minor from 2009 to
 1077 2016 [53].

1078 This chapter presents the Glory Duck analysis, the name given for the search for dark matter
 1079 annihilation from dSph by combining data from the five gamma-ray observatories: Fermi-LAT,
 1080 HAWC, HESS, MAGIC, and VERITAS. Specifically, the methods in analysis and modeling are
 1081 presented for the HAWC gamma-ray observatory. This work will be published in the Journal of

1082 Cosmology and Astroparticle Physics and presented at the International Cosmic Ray Conference
1083 in 2019, 2021, and 2023 [54, 55, 56] and others.

1084 **4.2 Dataset and Background**

1085 This section enumerates the data analysis and background estimation methods used for HAWC's
1086 study of dSphs. Section 4.2.1 and Section 4.2.2 are most useful for fellow HAWC collaborators
1087 looking to replicate the Glory Duck analysis.

1088 **4.2.1 Itemized HAWC files**

1089 These files are only available withing HAWC's internal documentation and collaborators. They
1090 are not meant for public access, and are presented here so that HAWC collaborators can reproduce
1091 results accurately.

- 1092 • Detector Response: `response_aerie_svn_27754_systematics_best_mc_test_noBr`
1093 `oadpulse\10pctlogchargesmearing_0.63qe_25kHzNoise_run5481_curvature`
1094 `0_index3.root`
- 1095 • Data Map: `maps-20180119/liff/maptree_1024.root`
- 1096 • Spectral Dictionary: `DM_CirrelliSpectrum_dict_gammas.npy`
- 1097 • Analysis wiki: https://private.hawc-observatory.org/wiki/index.php/Glory_Duck_Multi-Experiment_Dark_Matter_Search

1099 **4.2.2 Software Tools and Development**

1100 This analysis was performed using HAL and 3ML [34, 57] in Python version 2. I built software
1101 to implement the *A Poor Particle Physicist Cookbook for Dark Matter Indirect Detection* (PPPC)
1102 [58] DM spectral model and dSphs spatial model from [59] for HAWC analysis. A NumPy version
1103 of this dictionary was made for both Py2 and Py3. The code base for creating this dictionary is
1104 linked on my GitLab sandbox:

- 1105 • Py2: [Dictionary Generator \(Deprecated\)](#)

- 1106 • Py3: [PPPC2Dict](#)

1107 The analysis was performed using the f_{hit} framework as used and described in the HAWC Crab
1108 paper [34]. The Python2 NumPy dictionary file for gamma-ray final states is `dmCirSpecDict.npy`.
1109 The corresponding Python3 file is `DM_CirrelliSpectrum_dict_gammas.npy`. These files can
1110 also be used for decay channels and the PPPC describes how [58]. All other software used for data
1111 analysis, DM profile generation, and job submission to SLURM are also kept in my sandbox for
1112 [the Glory Duck](#) project.

1113 4.2.3 Data Set and Background Description

1114 The HAWC data maps used for this analysis contain 1017 days of data between runs 2104
1115 (2014-11-26) and 7476 (2017-12-20). They were generated from pass 4.0 reconstruction. The
1116 analysis is performed using the f_{hit} energy binning scheme with bins (1-9) similar to what was done
1117 for the Crab and previous HAWC dSph analysis [34, 60]. Bin 0 was excluded as it has substantial
1118 hadronic contamination and poor angular resolution.

1119 This analysis was done on dSphs because of their large DM mass content relative to baryonic
1120 mass. We consider the following to estimate the background to this study.

- 1121 • The dSphs' angular extent are small relative to HAWC's spatial resolution, so the analysis is
1122 not sensitive to large or small scale anisotropies.
- 1123 • The dSphs used in this analysis are off the galactic plane and therefore not contaminated by
1124 diffuse emission from the galaxy.
- 1125 • The dSphs are baryonically faint relative to their expected dark matter content and are not
1126 expected to contain high energy gamma-ray sources.

1127 Therefor we make no additional assumptions on the background from our sources and use
1128 HAWC's standard direct integration method for background estimation [34]. The largest background
1129 under this consideration is from an isotropic flux of cosmic rays. The contamination of this hadronic
1130 flux is worse at lower energies where HAWC's gamma/hadron discrimination worse. It is possible

1131 for gamma rays from DM annihilation to scatter in transit to HAWC via Inverse Compton Scattering
1132 (ICS). This was investigated and its impact on the flux is negligible. Supporting information on
1133 this is in Section 4.7.1

1134 **4.3 Analysis**

1135 The expected differential photon flux from DM-DM annihilation to standard model particles,
1136 $d\Phi_\gamma/dE_\gamma$, over solid angle, Ω , is described by the familiar equation.

$$\frac{d\Phi_\gamma}{dE_\gamma} = \frac{\langle\sigma v\rangle}{8\pi m_\chi^2} \frac{dN_\gamma}{dE_\gamma} \times \int_{\text{source}} d\Omega \int_{l.o.s} dl \rho_\chi^2 J(r, \theta') \quad (4.1)$$

1137 Where $\langle\sigma v\rangle$ is the velocity weighted annihilation cross-section. $\frac{dN}{dE}$ is the expected differential
1138 number of photons produced at each energy per annihilation. m_χ is the rest mass of the supposed
1139 DM particle. ρ_χ is the DM density. J is the astrophysical J-factor and is defined as

$$J = \int d\Omega \int_{l.o.s} dl \rho_\chi^2(r, \theta') \quad (4.2)$$

1140 l is the distance to the source from Earth. r is the radial distance from the center of the source. θ' is
1141 the half angle defining a cone containing the DM source. How each component is synthesized and
1142 considered for HAWC's analysis is presented in the following sections. Section 4.3.1 presents the
1143 particle physics model for DM annihilation. Section 4.3.2 presents the spatial distributions built
1144 for each dSph.

1145 **4.3.1 $\frac{dN_\gamma}{dE_\gamma}$ - Particle Physics Component**

1146 For these spectra, we import the PPPC with Electroweak (EW) corrections [58]. Public versions
1147 of the imported tables are provided by the [authors online](#). The spectrum is implemented as a model
1148 script in astromodels for 3ML. The EW corrections were previously not considered for HAWC and
1149 are significant for DM annihilating to EW coupled SM particles such as all leptons, and the γ ,
1150 Z , and W bosons [60]. Figure 4.2 demonstrates the significance of EW corrections for W boson
1151 annihilation. Across EW SM channels, the gamma-ray spectra become harder than spectra without
1152 EW corrections. Tables from the PPPC were reformatted into Python NumPy dictionaries for
1153 collaboration-wide use. A class in astromodels was developed to include the EW correction from
1154 the PPPC and is aptly named `PPPCSpectra` within `DM_models.py`.

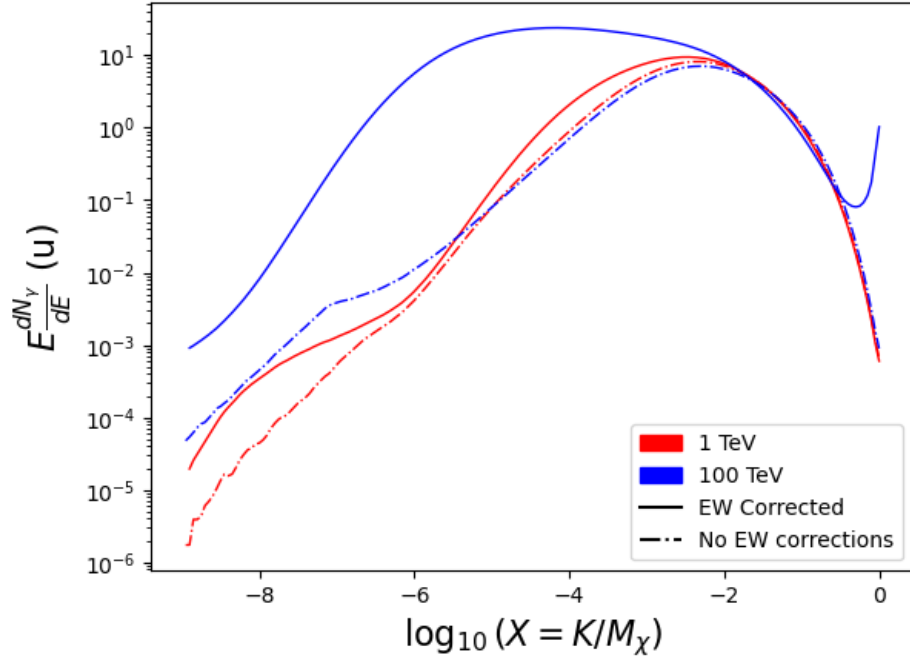


Figure 4.2 Effect of Electroweak (EW) corrections on expected DM annihilation spectrum for $\chi\chi \rightarrow W^-W^+$. Solid lines are spectral models that consider EW corrections. Dash-dot lines are spectral models without EW corrections. Red lines are models for $M_\chi = 1$ TeV. Blue lines represent models for $M_\chi = 100$ TeV. All models are sourced from the PPPC4DMID [58].

1155 4.3.2 J- Astrophysical Component

1156 The J-factor profiles for each source are imported from Geringer-Sameth (referred to with \mathcal{GS})

1157 [59]. \mathcal{GS} fits the Zhao DM profile to the dSphs which has a DM density described as [61]

$$\rho(r) = \frac{\rho_0}{(r/R_s)^\gamma (1 + (r/R_s)^\alpha)^{(\beta-\gamma)}}. \quad (4.3)$$

1158 R_s is the scale radius and free parameter in the model. γ is the logarithmic slope in the region

1159 $r \ll R_s$. β is the logarithmic slope in the region $r \gg R_s$. α is known as the sharpness of transition

1160 where $r \approx R_s$. The classic Navarro-Frenk-White [62] (NFW) can be retrieved from Zhao by fixing

1161 $(\alpha, \beta, \gamma) = (1, 3, 1)$.

1162 \mathcal{GS} best fits were pulled from the publication as $J(\theta)$, where θ is the angular separation from

1163 the center of the source. HAWC requires maps in terms of $\frac{dJ}{d\Omega}$, so the conversion from the maps

1164 was done in the following way...

1165 First, convert the angular distances to solid angles

$$\Omega = 2 \cdot \pi(1 - \cos(\theta)) \quad (4.4)$$

1166 which reduces with a small angle approximation to $\pi\theta^2$. Next, the central difference for both the
1167 ΔJ and $\Delta\Omega$ value were calculated from the discretized $J(\theta)$ with the central difference stencil:

$$\Delta\phi_i = \phi_{i+1} - \phi_{i-1} \quad (4.5)$$

1168 Where ϕ is either Ω or J . These were done separately in case the grid spacing in θ was not uniform.
1169 Finally, these lists are divided so that we are left with an approximation of the $dJ/d\Omega$ profile that
1170 is a function of θ . Admittedly, this is an approximation method for the map which introduces small
1171 errors compared to the true profile estimate. This was checked as a systematic against the author's
1172 profiling of the spatial distribution and is documented in Section 4.8.1.

1173 With $\frac{dJ}{d\Omega}(\theta)$, a map is generated, first by filling in the north-east quadrant of the map. This
1174 quadrant is then reflected twice, vertically then horizontally, to fill the full map. Maps are then
1175 normalized by dividing the discrete 2D integral of the map. The 2D integral was a simple height
1176 of bins, Newton's integral:

$$p^2 \cdot \sum_{i,j=0}^{N,M} \frac{dJ}{d\Omega}(\theta_{i,j}, \phi_{i,j}) \quad (4.6)$$

1177 These maps are HEALpix maps with NSIDE 16384 and saved in the .fits format. The hyper fine
1178 resolution was selected to better preserve the total expected counts after integrating Eq. (4.1) with
1179 the detector response.

1180 Another DM spatial distribution model from Bonnivard (\mathcal{B}) [63] was used for the Glory Duck
1181 study. However, to save computational time, limits from \mathcal{GS} were scaled to \mathcal{B} instead of each
1182 experiment performing a full study a second time. How these models compare is demonstrated
1183 for each dSph in Figure 4.16 and Figure 4.17 Plots of these maps are provided for each source
1184 in chapter A Examples of the two most impactful dSphs derived from \mathcal{GS} , Segue1 and Coma
1185 Berenices are featured in Figure 4.3

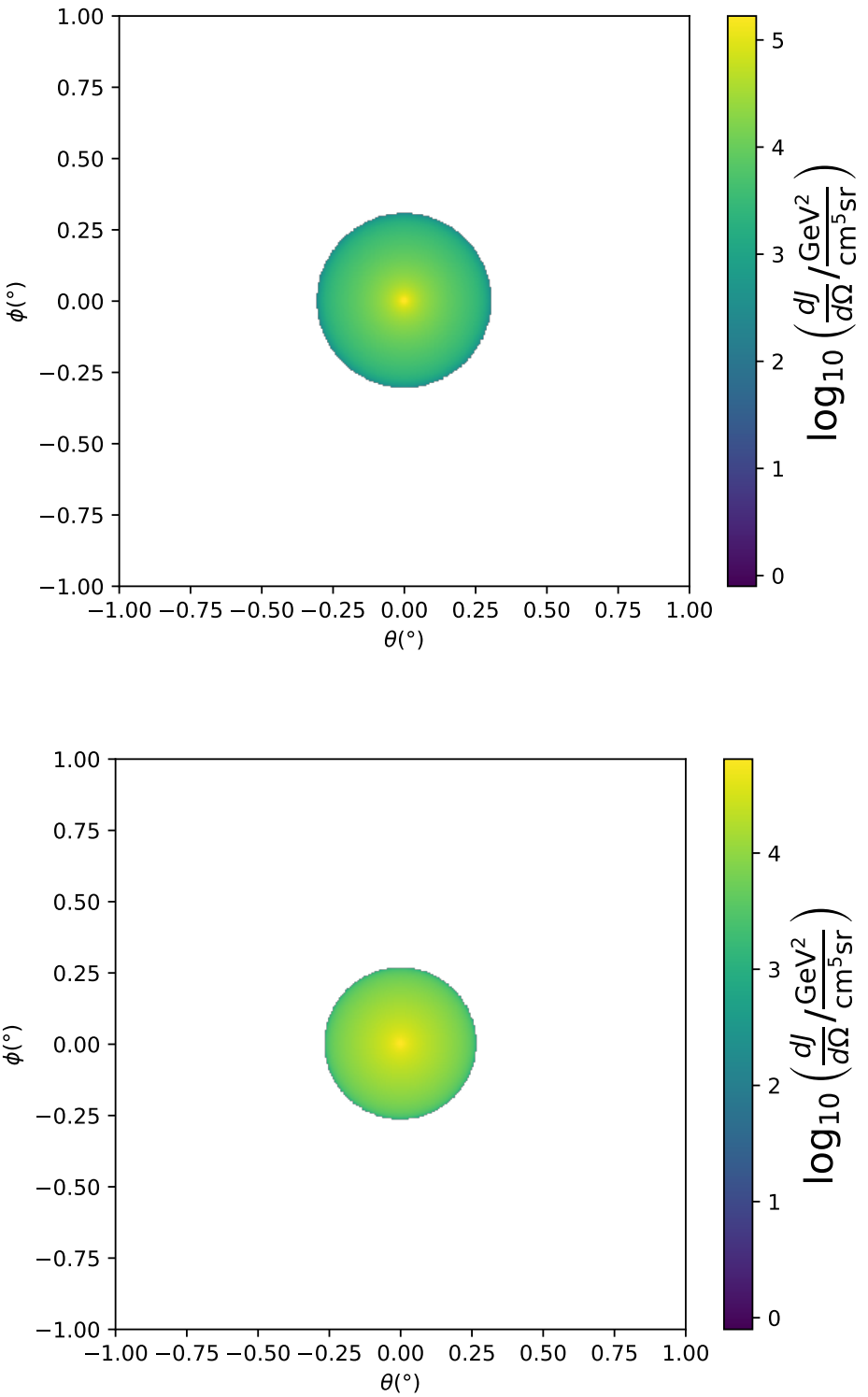


Figure 4.3 $\frac{dJ}{d\Omega}$ maps for Segue1 (top) and Coma Berenices (bottom). Origin is centered on the specific dwarf spheroidal galaxies (dSph). X and Y axes are the angular separation from the center of the dwarf. Profile is truncated at the scale radius. Plots of the remaining 11 dSph HAWC studied are linked in Fig. A.1.

1186 **4.3.3 Source Selection and Annihilation Channels**

1187 We use many of the dSphs presented in HAWC’s previous dSph DM search [60]. HAWC’s
1188 sources for Glory Duck include Boötes I, Coma Berenices, Canes Venatici I + II, Draco, Hercules,
1189 Leo I, II, + IV, Segue 1, Sextans, and Ursa Major I + II. A full description of all sources used
1190 in Glory Duck is found in Table 4.1. Triangulum II was excluded from the Glory Duck analysis
1191 because of large uncertainties in its J factor. Ursa Minor was excluded from HAWC’s contribution
1192 to the combination because the source extension model extended Ursa Minor beyond HAWC’s field
1193 of view. Ursa Minor was not expected to contribute significantly to the combined limit, so work
1194 was not invested in a solution to include Ursa Minor.

1195 This analysis improves on the previous HAWC dSph paper [60] in the following ways. Pre-
1196 viously, the dSphs were treated and implemented as point sources. For this analysis, dSphs are
1197 modeled and treated as extended source. The impact of this change with respect to the upper limit
1198 is source dependent and is explored in Section 4.7.2. Previously, the particle physics model used for
1199 gamma-ray spectra from DM annihilation did not have EW corrections where the PPPC includes
1200 them. Finally, the gamma-ray ray dataset is much larger. The study performed here analyzes over
1201 1000 days of data compared to 507.

1202 The SM annihilation channels probed for the Glory Duck combination include $b\bar{b}$, $e\bar{e}$, $\mu\bar{\mu}$, $\tau\bar{\tau}$,
1203 $t\bar{t}$, W^+W^- , and ZZ . A summary of all sources, with a description of each experiments’ sensitivity
1204 to the source, is provided in Table 4.2.

1205 **4.4 Likelihood Methods**

1206 **4.4.1 HAWC Likelihood**

1207 For every analysis bin in energy, f_{hit} bins (1-9), and location, we can expect N signal events and
1208 B background events. The expected number of excess signal events from dark matter annihilation,
1209 S , is estimated by convolving Equation (4.1) with HAWC’s energy response and pixel point spread
1210 functions. I then compute the test statistic (TS) with the log-likelihood ratio test,

$$TS_{max} = -2 \ln \left(\frac{\mathcal{L}_0}{\mathcal{L}^{max}} \right) \quad (4.7)$$

Table 4.1 Summary of the relevant properties of the dSphs used in the present work. Column 1 lists the dSphs. Columns 2 and 3 present their heliocentric distance and galactic coordinates, respectively. Columns 4 and 5 report the J -factors of each source given from the \mathcal{GS} and \mathcal{B} independent studies and their estimated $\pm 1\sigma$ uncertainties. The values $\log_{10} J$ (\mathcal{GS} set) [59] correspond to the mean J -factor values for a source extension truncated at the outermost observed star. The values $\log_{10} J$ (\mathcal{B} set) [63] are provided for a source extension at the tidal radius of each dSph. **Bolded sources are within HAWC’s field of view and provided to the Glory Duck analysis.**

Name	Distance (kpc)	l, b ($^{\circ}$)	$\log_{10} J$ (\mathcal{GS} set) $\log_{10}(\text{GeV}^2\text{cm}^{-5}\text{sr})$	$\log_{10} J$ (\mathcal{B} set) $\log_{10}(\text{GeV}^2\text{cm}^{-5}\text{sr})$
Boötes I	66	358.08, 69.62	$18.24^{+0.40}_{-0.37}$	$18.85^{+1.10}_{-0.61}$
Canes Venatici I	218	74.31, 79.82	$17.44^{+0.37}_{-0.28}$	$17.63^{+0.50}_{-0.20}$
Canes Venatici II	160	113.58, 82.70	$17.65^{+0.45}_{-0.43}$	$18.67^{+1.54}_{-0.97}$
Carina	105	260.11, -22.22	$17.92^{+0.19}_{-0.11}$	$18.02^{+0.36}_{-0.15}$
Coma Berenices	44	241.89, 83.61	$19.02^{+0.37}_{-0.41}$	$20.13^{+1.56}_{-1.08}$
Draco	76	86.37, 34.72	$19.05^{+0.22}_{-0.21}$	$19.42^{+0.92}_{-0.47}$
Fornax	147	237.10, -65.65	$17.84^{+0.11}_{-0.06}$	$17.85^{+0.11}_{-0.08}$
Hercules	132	28.73, 36.87	$16.86^{+0.74}_{-0.68}$	$17.70^{+1.08}_{-0.73}$
Leo I	254	225.99, 49.11	$17.84^{+0.20}_{-0.16}$	$17.93^{+0.65}_{-0.25}$
Leo II	233	220.17, 67.23	$17.97^{+0.20}_{-0.18}$	$18.11^{+0.71}_{-0.25}$
Leo IV	154	265.44, 56.51	$16.32^{+1.06}_{-1.70}$	$16.36^{+1.44}_{-1.65}$
Leo V	178	261.86, 58.54	$16.37^{+0.94}_{-0.87}$	$16.30^{+1.33}_{-1.16}$
Leo T	417	214.85, 43.66	$17.11^{+0.44}_{-0.39}$	$17.67^{+1.01}_{-0.56}$
Sculptor	86	287.53, -83.16	$18.57^{+0.07}_{-0.05}$	$18.63^{+0.14}_{-0.08}$
Segue I	23	220.48, 50.43	$19.36^{+0.32}_{-0.35}$	$17.52^{+2.54}_{-2.65}$
Segue II	35	149.43, -38.14	$16.21^{+1.06}_{-0.98}$	$19.50^{+1.82}_{-1.48}$
Sextans	86	243.50, 42.27	$17.92^{+0.35}_{-0.29}$	$18.04^{+0.50}_{-0.28}$
Ursa Major I	97	159.43, 54.41	$17.87^{+0.56}_{-0.33}$	$18.84^{+0.97}_{-0.43}$
Ursa Major II	32	152.46, 37.44	$19.42^{+0.44}_{-0.42}$	$20.60^{+1.46}_{-0.95}$
Ursa Minor	76	104.97, 44.80	$18.95^{+0.26}_{-0.18}$	$19.08^{+0.21}_{-0.13}$

Table 4.2 Summary of dSph observations by each experiment used in this work. A ‘-’ indicates the experiment did not observe the dSph for this study. For Fermi-LAT, the exposure at 1 GeV is given. For HAWC, $|\Delta\theta|$ is the absolute difference between the source declination and HAWC latitude. HAWC is more sensitive to sources with smaller $|\Delta\theta|$. For IACTs, we show the zenith angle range, the total exposure, the energy range, the angular radius θ of the signal or ON region, the ratio of exposures between the background-control (OFF) and signal (ON) regions (τ), and the significance of gamma-ray excess in standard deviations, σ .

Source name	Fermi-LAT	HAWC	H.E.S.S, MAGIC, VERITAS						
	Exposure (10^{11} s m 2)	$ \Delta\theta $ ($^\circ$)	IACT	Zenith ($^\circ$)	Exposure (h)	Energy range (GeV)	θ ($^\circ$)	τ	S (σ)
Boötes I	2.6	4.5	VERITAS	15 – 30	14.0	100–41000	0.10	8.6	-1.0
Canes Venatici I	2.9	14.6	–	–	–	–	–	–	–
Canes Venatici II	2.9	15.3	–	–	–	–	–	–	–
Carina	3.1	–	H.E.S.S.	27 – 46	23.7	310 – 70000	0.10	18.0	-0.3
Coma Berenices	2.7	4.9	H.E.S.S.	47 – 49	11.4	550 – 70000	0.10	14.4	-0.4
Draco	3.8	38.1	MAGIC	5 – 37	49.5	60 – 10000	0.17	1.0	–
			MAGIC	29 – 45	52.1	70 – 10000	0.22	1.0	–
			VERITAS	25 – 40	49.8	120 – 70000	0.10	9.0	-1.0
Fornax	2.7	–	H.E.S.S.	11 – 25	6.8	230 – 70000	0.10	45.5	-1.5
Hercules	2.8	6.3	–	–	–	–	–	–	–
Leo I	2.5	6.7	–	–	–	–	–	–	–
Leo II	2.6	3.1	–	–	–	–	–	–	–
Leo IV	2.4	19.5	–	–	–	–	–	–	–
Leo V	2.4	–	–	–	–	–	–	–	–
Leo T	2.6	–	–	–	–	–	–	–	–
Sculptor	2.7	–	H.E.S.S.	10 – 46	11.8	200 – 70000	0.10	19.8	-2.2
Segue I	2.5	2.9	MAGIC	13 – 37	158.0	60 – 10000	0.12	1.0	-0.5
			VERITAS	15 – 35	92.0	80 – 50000	0.10	7.6	0.7
Segue II	2.7	–	–	–	–	–	–	–	–
Sextans	2.4	20.6	–	–	–	–	–	–	–
Ursa Major I	3.4	32.9	–	–	–	–	–	–	–
Ursa Major II	4.0	44.1	MAGIC	35 – 45	94.8	120 – 10000	0.30	1.0	-2.1
Ursa Minor	4.1	–	VERITAS	35 – 45	60.4	160 – 93000	0.10	8.4	-0.1

1211 where \mathcal{L}_0 is the null hypothesis, or no DM emission, likelihood. \mathcal{L}^{\max} is the best fit signal
 1212 hypothesis where $\langle\sigma v\rangle$ maximizes the likelihood. We calculate the likelihood of each source and
 1213 model, assuming events are Poisson distributed, with

$$\mathcal{L} = \prod_i \frac{(B_i + S_i)^{N_i} e^{-(B_i + S_i)}}{N_i!} \quad (4.8)$$

1215 where S_i is the sum of expected number of signal counts. B_i is the number of background counts
 1216 observed. N_i is the total number of counts.

1217 I also calculate an upper limit on $\langle\sigma v\rangle$ by calculating the 95% confidence level (CL). For the
 1218 CL, we define a parameter, TS_{95} , as

$$TS_{95} \equiv \sum_{\text{bins}} \left[2N \ln \left(1 + \frac{\epsilon S_{\text{ref}}}{B} \right) - 2\epsilon S_{\text{ref}} \right] \quad (4.9)$$

1219 where the expected signal counts from a dSph is scaled by ϵ . S_{ref} is the expected number of excess
 1220 counts in a bin from DM emission from a dSph with a corresponding annihilation cross-section,
 1221 $\langle\sigma v\rangle$. We scan ϵ such that

$$2.71 = TS_{\max} - TS_{95} \quad (4.10)$$

1222 HAWC's exclusive results are provided in Section 4.5.

1223 4.4.2 Glory Duck Joint Likelihood

1224 The joint likelihood for the 5-experiment combination was done similarly as Section 4.4.1. We
 1225 calculate upper limits on $\langle\sigma v\rangle$ from the TS, Eq. (4.7), and define the likelihood ratio more generally

$$\lambda(\langle\sigma v\rangle | \mathcal{D}_{\text{dSphs}}) = \frac{\mathcal{L}(\langle\sigma v\rangle; \hat{\nu} | \mathcal{D}_{\text{dSphs}})}{\mathcal{L}(\widehat{\langle\sigma v\rangle}; \hat{\nu} | \mathcal{D}_{\text{dSphs}})} \quad (4.11)$$

1226 $\mathcal{D}_{\text{dSphs}}$ is the totality of observations across experiments and dSphs. ν are the nuisance parameters
 1227 which are the J factors in this study. $\widehat{\langle\sigma v\rangle}$ and $\hat{\nu}$ are the respective estimate that maximize \mathcal{L}
 1228 globally. Finally, $\hat{\nu}$ is the set of nuisance parameters that maximize \mathcal{L} for a fixed value of $\langle\sigma v\rangle$.

1229 The *complete* joint likelihood, \mathcal{L} that encompasses all observations from all instruments and
 1230 dSphs can be factorized into *partial* functions for each dSph l (with $\mathcal{L}_{\text{dSph},l}$) and its J factor (\mathcal{J}_l):

$$\mathcal{L}(\langle\sigma v\rangle; \nu | \mathcal{D}_{\text{dSphs}}) = \prod_{l=1}^{N_{\text{dSphs}}} \mathcal{L}_{\text{dSph},l}(\langle\sigma v\rangle; J_l, \nu_l | \mathcal{D}_l) \times \mathcal{J}_l(J_l | J_{l,\text{obs}}, \sigma_{\log J_l}). \quad (4.12)$$

1231 For this study, $N_{\text{dSphs}} = 20$ is the number of dSphs studied. \mathcal{D}_l are the gamma-ray observations
 1232 of dSph, l . ν_l are the nuisance parameters modifying the gamma-ray observations of dSph, l ,
 1233 but excludes \mathcal{J}_l . \mathcal{J}_l is the J factor for dSph, l , as defined in Equation (4.2), and it is a nuisance
 1234 parameter whose value is unknown. $\log_{10} J_{l,\text{obs}}$ and $\sigma_{\log J_l}$ are obtained by fitting a log-normal
 1235 function of $J_{l,\text{obs}}$ to the posterior distribution of J_l [64]. $\log_{10} J_{l,\text{obs}}$ and $\sigma_{\log J_l}$ values are provided
 1236 in Table 4.1. The term \mathcal{J}_l constraining J_l is written as:

$$\mathcal{J}_l (J_l | J_{l,\text{obs}}, \sigma_{\log J_l}) = \frac{1}{\ln(10) J_{l,\text{obs}} \sqrt{2\pi} \sigma_{\log J_l}} \exp\left(-\frac{(\log_{10} J_l - \log_{10} J_{l,\text{obs}})^2}{2\sigma_{\log J_l}^2}\right). \quad (4.13)$$

1237 Both the \mathcal{GS} and \mathcal{B} , displayed in Table 4.1, sets of J factors are used in this analysis. Equation (4.13)
 1238 is also normalized, so it can also be interpreted as a probability density function (PDF) for $J_{l,\text{obs}}$.
 1239 From Equation (4.1), we can also see that $\langle \sigma v \rangle$ and J_l are degenerate when computing $\mathcal{L}_{\text{dSph},l}$.
 1240 Therefore, as noted in [65], it is sufficient to compute $\mathcal{L}_{\text{dSph},l}$ versus $\langle \sigma v \rangle$ for a fixed value of J_l .
 1241 We used $J_{l,\text{obs}}(\mathcal{GS})$ reported in Tab. 4.1, in order to perform the profile of \mathcal{L} with respect to J_l .
 1242 The degeneracy implies that for any $J'_l \neq J_{l,\text{obs}}$ (in practice in our case we used $J'_l = J_{l,\text{obs}}(\mathcal{B})$ to
 1243 compute results from a different set of J factors):

$$\mathcal{L}_{\text{dSph},l} (\langle \sigma v \rangle; J'_l, \nu_l | \mathcal{D}_l) = \mathcal{L}_{\text{dSph},l} \left(\frac{J'_l}{J_{l,\text{obs}}} \langle \sigma v \rangle; J_{l,\text{obs}}, \nu_l | \mathcal{D}_l \right), \quad (4.14)$$

1244 which is a straightforward rescaling operation that reduces the computational needs of the profiling
 1245 operation since:

$$\mathcal{L} (\langle \sigma v \rangle; \hat{\nu} | \mathcal{D}_{\text{dSphs}}) = \prod_{l=1}^{N_{\text{dSphs}}} \max_{J_l} \left[\mathcal{L}_{\text{dSph},l} (\langle \sigma v \rangle; J_l, \hat{\nu}_l | \mathcal{D}_l) \times \mathcal{J}_l (J_l | J_{l,\text{obs}}, \sigma_{\log J_l}) \right]. \quad (4.15)$$

1246 In addition, Eq. (4.14) enables the combination of data from different gamma-ray instruments and
 1247 observed dSphs via tabulated values of $\mathcal{L}_{\text{dSph},l}$, or equivalently of λ from Eq. (4.11) as was done in
 1248 this work, versus $\langle \sigma v \rangle$. $\mathcal{L}_{\text{dSph},l}$ is computed for a fixed value of J_l and profiled with respect to all
 1249 instrumental nuisance parameters ν_l , these nuisance parameters are discussed in more detail below.
 1250 These values are produced by each detector independently and therefore there is no need to share
 1251 sensitive low-level information used to produce them, such as event lists. Figure 4.4 illustrates the
 1252 multi-instrument combination technique used in this study with a comparison of the upper limit

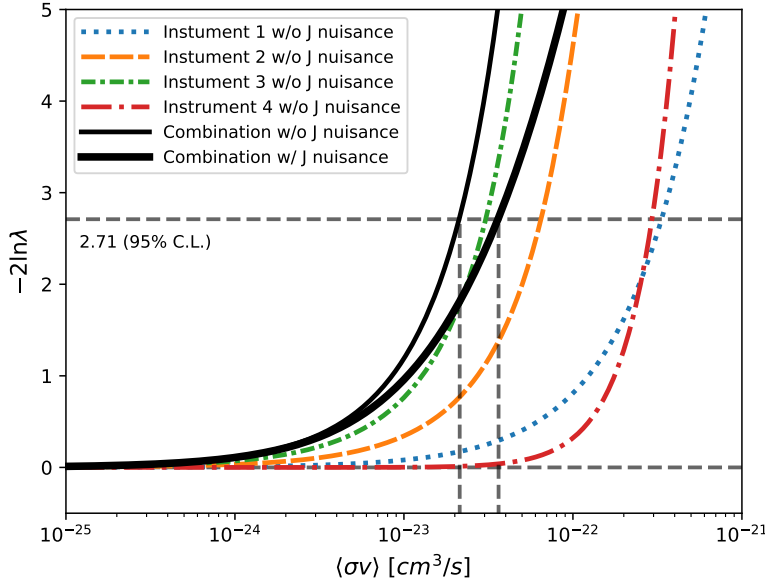


Figure 4.4 Illustration of the combination technique showing a comparison between $-2 \ln \lambda$ provided by four instruments (colored lines) from the observation of the same dSph without any J nuisance and their sum, *i.e.* the resulting combined likelihood (thin black line). According to the test statistics of Equation (4.7), the intersection of the likelihood profiles with the line $-2 \ln \lambda = 2.71$ indicates the 95% C.L. upper limit on $\langle\sigma v\rangle$. The combined likelihood (thin black line) shows a smaller value of upper limit on $\langle\sigma v\rangle$ than those derived by individual instruments. We also show how the uncertainties on the J factor effects the combined likelihood and degrade the upper limit on $\langle\sigma v\rangle$ (thick black line). All likelihood profiles are normalized so that the global minimum $\widehat{\langle\sigma v\rangle}$ is 0. We note that each profile depends on the observational conditions in which a target object was observed. The sensitivity of a given instrument can be degraded and the upper limits less constraining if the observations are performed in non-optimal conditions such as a high zenith angle or a short exposure time.

1253 on $\langle\sigma v\rangle$ obtained from the combination of the observations of four experiments towards one dSph
 1254 versus the upper limit from individual instruments. It also shows graphically the effect of the
 1255 J -factor uncertainty on the combined observations.

1256 The *partial* joint likelihood function for gamma-ray observations of each dSph ($\mathcal{L}_{\text{dSph},l}$) is
 1257 written as the product of the likelihood terms describing the $N_{\text{exp},l}$ observations performed with
 1258 any of our observatories:

$$\mathcal{L}_{\text{dSph},l} (\langle\sigma v\rangle; J_l, \nu_l | \mathcal{D}_l) = \prod_{k=1}^{N_{\text{exp},l}} \mathcal{L}_{lk} (\langle\sigma v\rangle; J_l, \nu_{lk} | \mathcal{D}_{lk}), \quad (4.16)$$

1259 where each \mathcal{L}_{lk} term refers to an observation of the l -th dSph with associated k -th instrument

1260 responses. $N_{\text{exp},l}$ varies from dSph to dSph and can be inferred from Table 4.2.

1261 Each collaboration separately analyzes their data for \mathcal{D}_{lk} corresponding to dSph l and gamma-
 1262 ray detector k , using as many common assumptions as possible in the analysis. HAWC's treatment
 1263 was described earlier in Section 4.4.1 whereas the specifics of the remaining experiments is left to
 1264 the publication. We compute the values for the likelihood functions \mathcal{L}_{lk} (see Eq. (4.16)) for a fixed
 1265 value of J_l and profile over the rest of the nuisance parameters ν_{lk} . Then, values of λ from Eq. (4.11)
 1266 are computed as a function of $\langle\sigma v\rangle$, and shared using a common format. Results are computed for
 1267 seven annihilation channels, W^+W^- , ZZ , $b\bar{b}$, $t\bar{t}$, e^+e^- , $\mu^+\mu^-$, and $\tau^+\tau^-$ over 62 m_χ values between
 1268 5 GeV and 100 TeV provided in [58]. The $\langle\sigma v\rangle$ range is defined between 10^{-28} and $10^{-18}\text{cm}^3 \cdot \text{s}^{-1}$,
 1269 with 1001 logarithmically spaced values. The likelihood combination, i.e. Equation (4.12), and
 1270 profile over the J -factor to compute the profile likelihood ratio λ , Equation (4.11), are carried out
 1271 with two different public analysis software packages, namely `gLike` [66] and `LklCom` [67], that
 1272 provide the same results [68].

1273 As mentioned previously, each experiment computes the \mathcal{L}_{lk} from Equation (4.11) differently.
 1274 The remainder of this section highlights the differences in this calculation across the experiments.
 1275 Four experiments, namely *Fermi*-LAT, H.E.S.S., HAWC and MAGIC, use a binned likelihood to
 1276 compute the \mathcal{L}_{lk} . For these experiments, for each observation \mathcal{D}_{lk} of a given dSph l carried out
 1277 using a given gamma-ray detector k , the binned likelihood function is:

$$\mathcal{L}_{lk} (\langle\sigma v\rangle; J_l, \nu_{lk} | \mathcal{D}_{lk}) = \prod_{i=1}^{N_E} \prod_{j=1}^{N_P} \left[\mathcal{P}(s_{lk,ij}(\langle\sigma v\rangle, J_l, \nu_{lk}) + b_{lk,ij}(\nu_{lk}) | N_{lk,ij}) \right] \times \mathcal{L}_{lk,\nu} (\nu_{lk} | \mathcal{D}_{\nu_{lk}}) \quad (4.17)$$

1278 where N_E and N_P are the number of considered bins in reconstructed energy and arrival direction,
 1279 respectively; \mathcal{P} represents a Poisson PDF for the number of gamma-ray candidate events $N_{lk,ij}$
 1280 observed in the i -th bin in energy and j -th bin in arrival direction, when the expected number is
 1281 the sum of the expected mean number of signal events s_{ij} (produced by DM annihilation) and of
 1282 background events b_{ij} ; $\mathcal{L}_{lk,\nu}$ is the likelihood term for the extra ν_{lk} nuisance parameters that vary
 1283 from one instrument k to another. The expected counts for signal events s_{ij} for a given dSph l and

1284 detector k is given by:

$$s_{ij}(\langle\sigma\nu\rangle, J) = \int_{E'_{\min,i}}^{E'_{\max,i}} dE' \int_{P'_{\min,j}}^{P'_{\max,j}} d\Omega' \int_0^\infty dE \int_{\Delta\Omega_{tot}} d\Omega \int_0^{T_{\text{obs}}} dt \frac{d^2\Phi(\langle\sigma\nu\rangle, J)}{dEd\Omega} \text{IRF}(E', P' | E, P, t) \quad (4.18)$$

1285 where E' and E are the reconstructed and true energies, P' and P the reconstructed and true
1286 arrival directions; $E'_{\min,i}$, $P'_{\min,j}$, $E'_{\max,i}$, and $P'_{\max,j}$ are their lower and upper limits of the i -th
1287 energy bin and the j -th arrival direction bin; T_{obs} is the (dead-time corrected) total observation
1288 time; t is the time along the observations; $d^2\Phi/dEd\Omega$ is the DM flux in the source region (see
1289 Equation (4.1)); and $\text{IRF}(E', P' | E, P, t)$ is the IRF, which can be factorized as the product of the
1290 effective collection area of the detector $A_{\text{eff}}(E, P, t)$, the PDFs for the energy estimator $f_E(E' | E, t)$,
1291 and arrival direction $f_P(P' | E, P, t)$ estimators. Note that for Fermi-LAT, HAWC, MAGIC, and
1292 VERITAS the effect of the finite angular resolution is taken into account through the convolution
1293 of $d\Phi/dEd\Omega$ with f_P in Equation (4.18), whereas in the cases of H.E.S.S. f_P is approximated by a
1294 delta function. This approximation has been made in order to maintain compatibility of the result
1295 with what has been previously published. The difference introduced by this approximation is $< 5\%$
1296 for all considered dSphs. A more comprehensive review of the differences between the analyses of
1297 different instruments can be found in [40].

1298 4.5 HAWC Results

1299 13 of the 20 dSphs considered for the Glory Duck analysis are within HAWC's field of view.
1300 These dSph are analyzed for emission from DM annihilation according to the likelihood method
1301 described in Section 4.4. The 13 likelihood profiles are then stacked to synthesize a combined
1302 limit on the dark matter cross-section, $\langle\sigma\nu\rangle$. This combination is done for the 7 SM annihilation
1303 channels used in the Glory Duck analysis. Figure 4.5 shows the combined limit for all annihilation
1304 channels with HAWC only observations. We also perform 300 studies of Poisson trials on the
1305 background. These trials are used to produce HAWC sensitivities with $\pm 1\sigma$ and $\pm 2\sigma$ uncertainty
1306 bands which were shared with the other collaborators for combination. The results on fitting to
1307 HAWC's Poisson trials of the DM hypothesis is shown in Figure 4.7 for all the DM annihilation
1308 channels studied for Glory Duck.

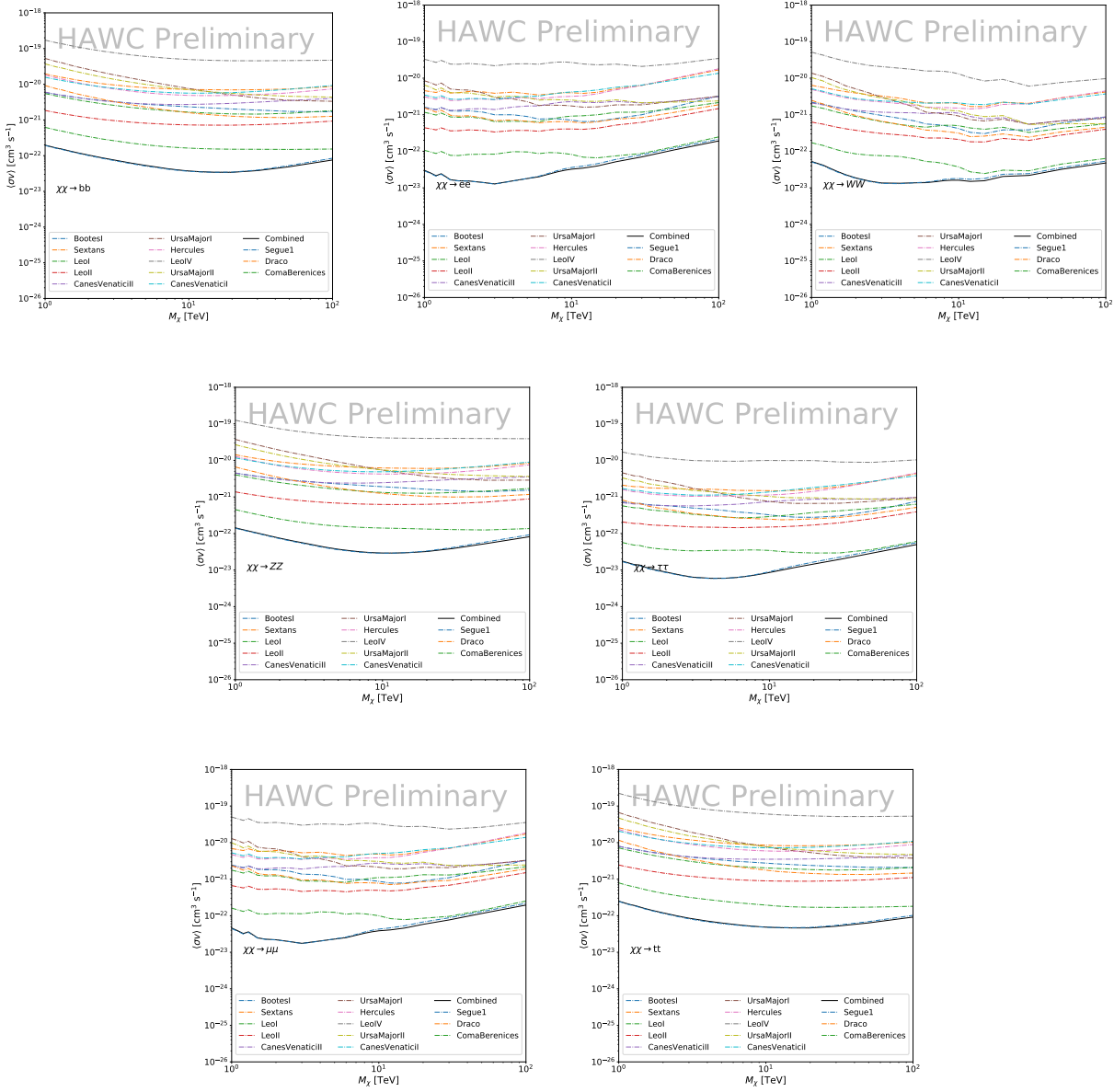


Figure 4.5

1309 No DM was found in HAWC observations. HAWC's limits are dominated by the dSphs Segue1
 1310 and Coma Berenices. The remaining 11 dSphs do not contribute significantly to the limit because
 1311 they are at high zenith and/or have much smaller J factors. Even though some remaining dSphs
 1312 have large J factors, they are towards the edge of HAWC's field of view where HAWC analysis is
 1313 less sensitive.

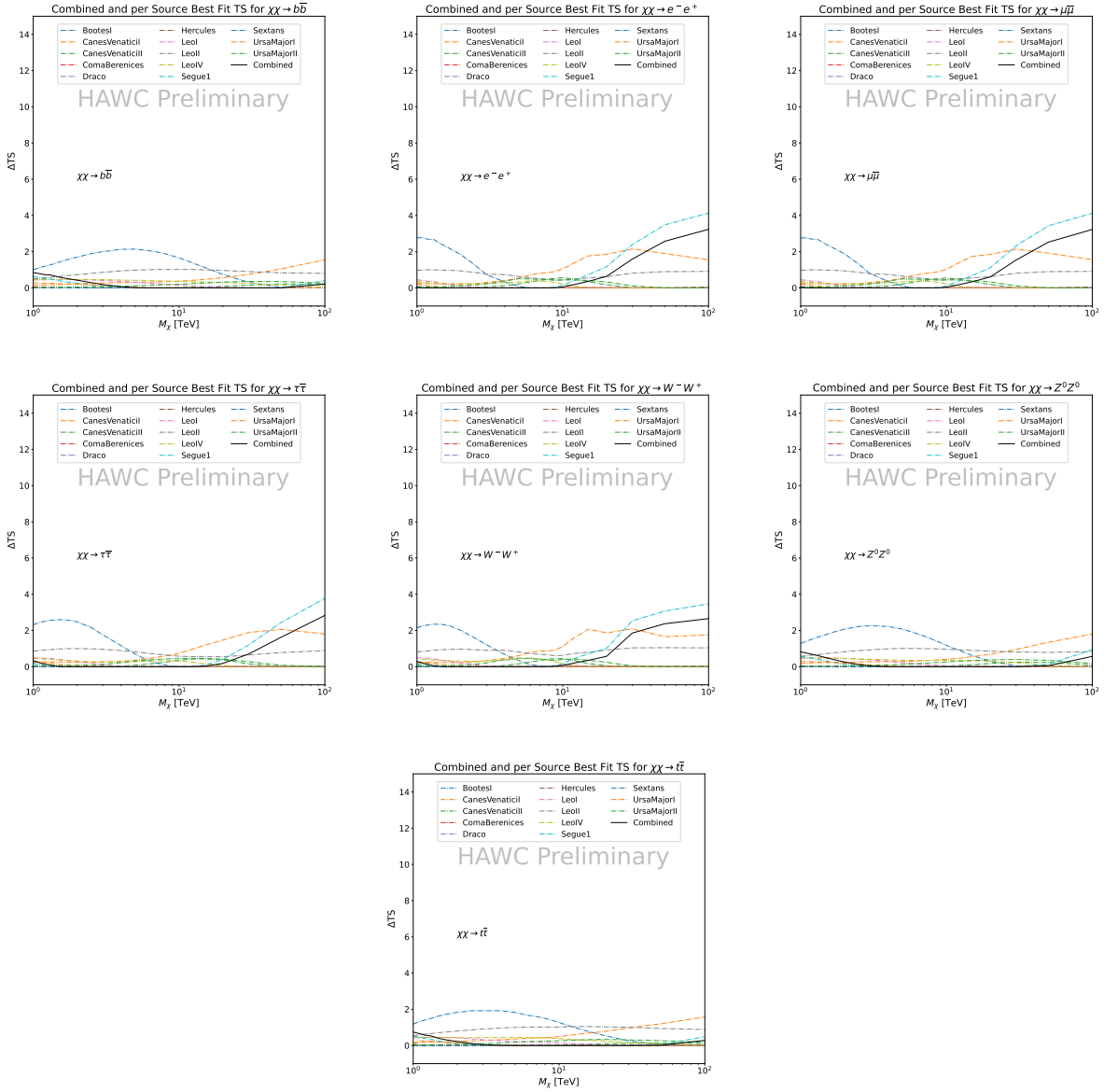


Figure 4.6 HAWC TS values for best fit $\langle\sigma v\rangle$ versus m_χ for seven SM annihilation channels with J factors from \mathcal{GS} . The solid black line shows the combined best fit TS values. The colored, dashed lines are the TS values for each of the 13 sources HAWC studied.

1314 4.6 Glory Duck Combined Results

1315 The crux of this analysis is that HAWC's results are combined with 4 other gamma-ray observa-
 1316 tories: Fermi-LAT, H.E.S.S., MAGIC, and VERITAS. No significant DM emission was observed
 1317 by any of the five instruments. We present the upper limits on $\langle\sigma v\rangle$ assuming seven independent
 1318 DM self annihilation channels, namely W^+W^- , Z^+Z^- , $b\bar{b}$, $t\bar{t}$, e^+e^- , $\mu^+\mu^-$, and $\tau^+\tau^-$. The 68%

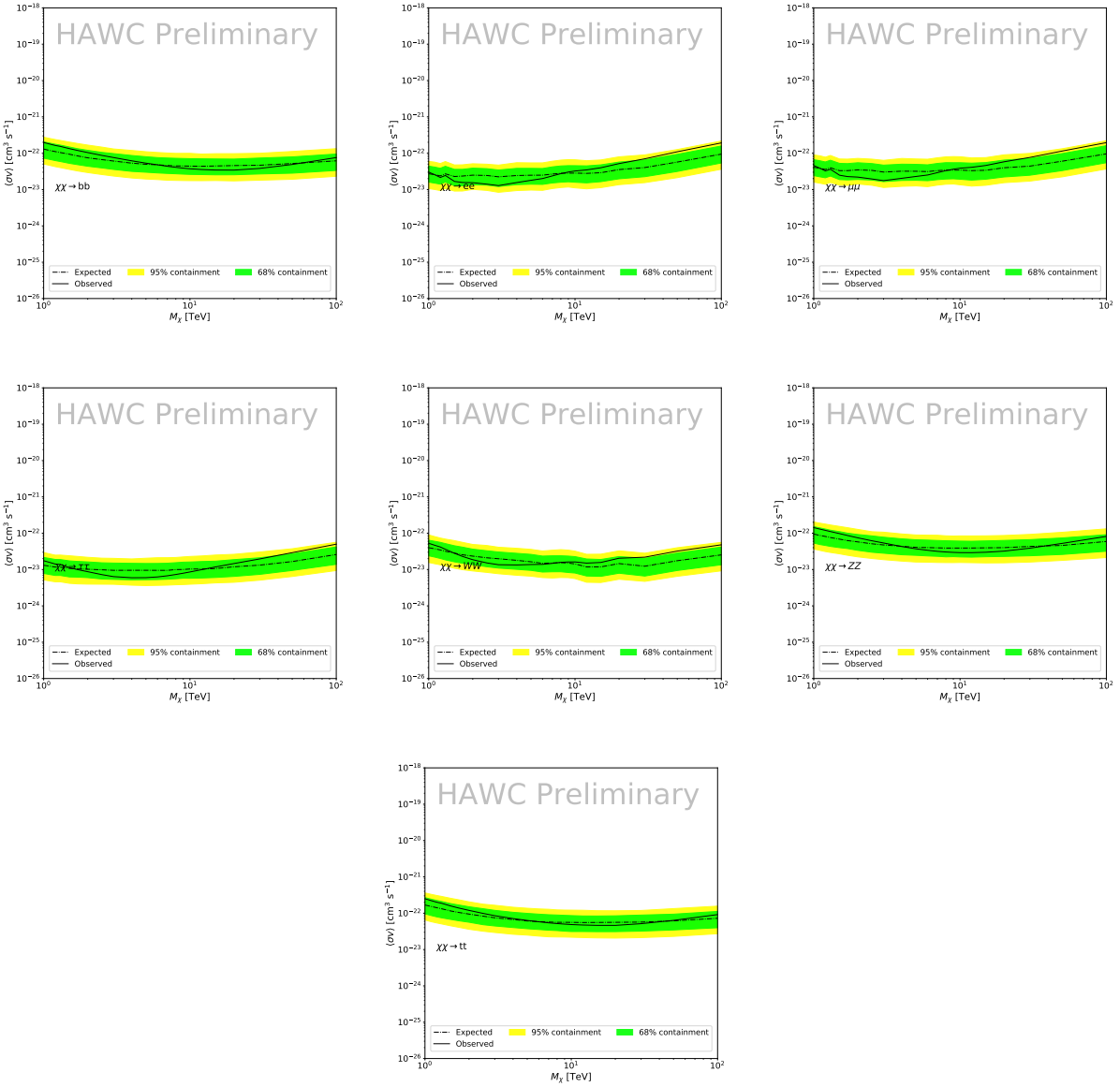


Figure 4.7 HAWC Brazil bands at 95% confidence level on $\langle\sigma v\rangle$ versus DM mass for seven annihilation channels with J -factors from \mathcal{GS} [69]. The solid line represents the combined limit from 13 dSphs. The dashed line is the expected limit. The green band is the 68% containment. The yellow band is the 95% containment.

1319 and 95% containment bands are produced from 300 Poisson realizations of the null hypothesis
 1320 corresponding to each of the combined datasets. These 300 realizations are combined identically
 1321 to dSph observations. The containment bands and the median are extracted from the distribution
 1322 of resulting limits on the null hypothesis. These 300 realizations are obtained either by fast simu-
 1323 lations of the OFF observations, for H.E.S.S., MAGIC, VERITAS, and HAWC, or taken from real

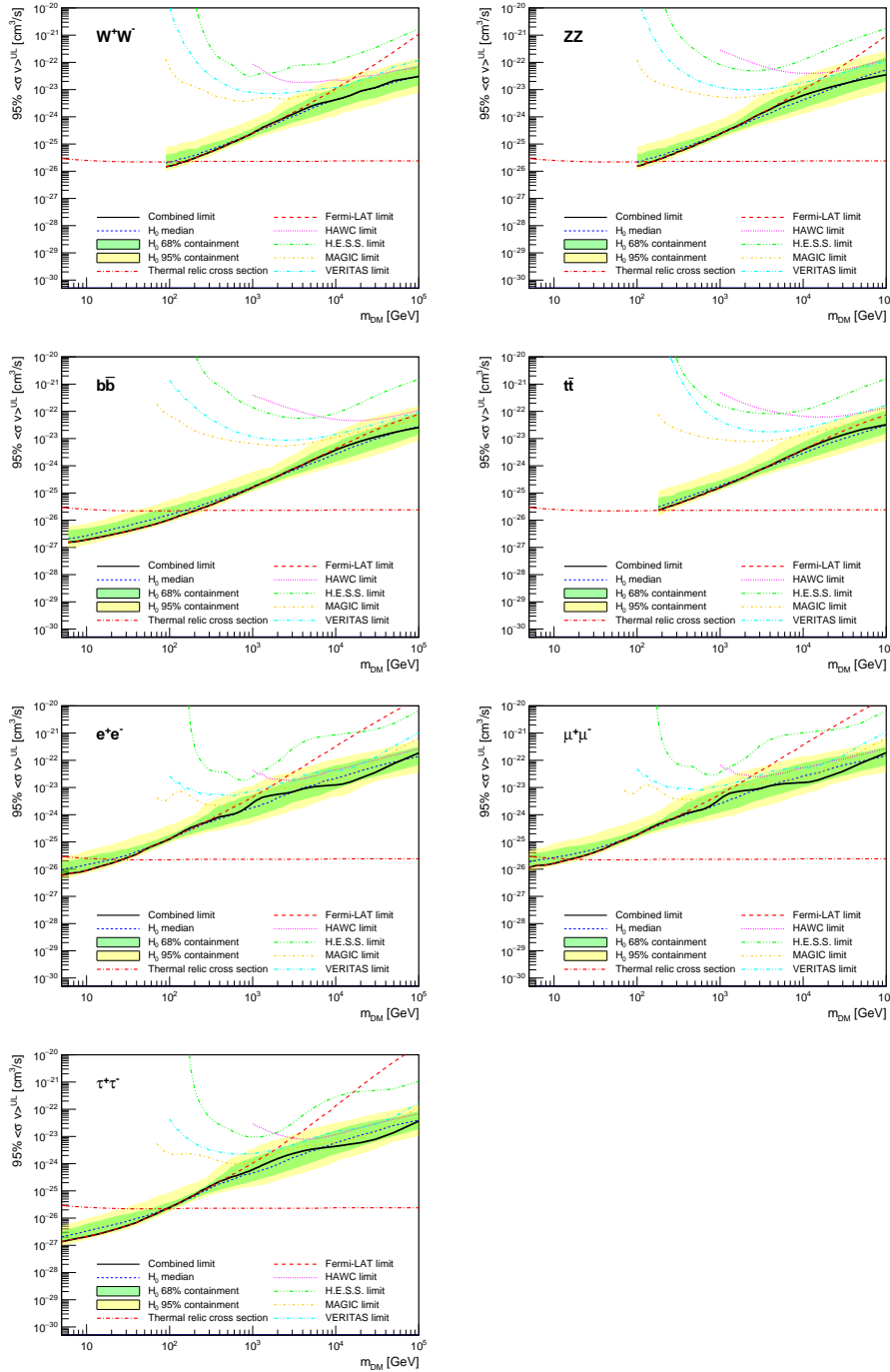


Figure 4.8 Upper limits at 95% confidence level on $\langle\sigma v\rangle$ in function of the DM mass for eight annihilation channels, using the set of J factors from Ref. [69] (\mathcal{GS} set in Table 4.1). The black solid line represents the observed combined limit, the black dashed line is the median of the null hypothesis corresponding to the expected limit, while the green and yellow bands show the 68% and 95% containment bands. Combined upper limits for each individual detector are also indicated as solid, colored lines. The value of the thermal relic cross-section in function of the DM mass is given as the red dotted-dashed line [70].

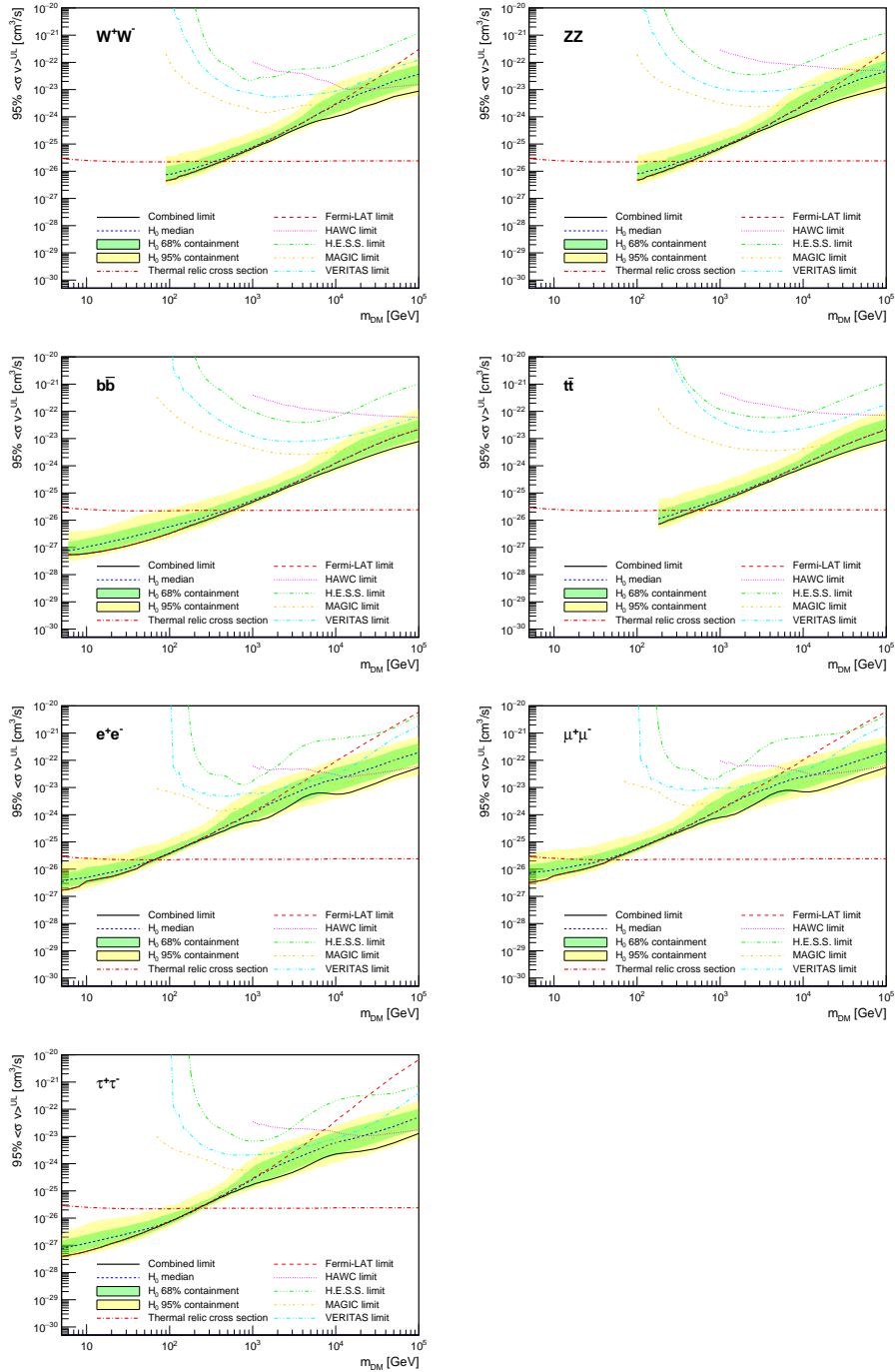


Figure 4.9 Same as Fig. 4.8, using the set of J factors from Ref. [63, 71] (\mathcal{B} set in Table 4.1).

1324 observations of empty fields of view in the case of Fermi-LAT [64, 72, 73].

1325 The obtained limits are shown in Figure 4.8 for the \mathcal{GS} set of J -factors [69] and in Figure 4.9
1326 for the \mathcal{B} set of J -factors [63, 71]. The combined limits are presented with their 68% and 95%
1327 containment bands, and are expected to be close to the median limit when no signal is present.

1328 We observe agreement with the null hypothesis for all channels, within 2σ standard deviations,
1329 between the observed limits and the expectations given by the median limits. Limits obtained from
1330 each detector are also indicated in the figures, where limits for all dSphs observed by the specific
1331 instrument have been combined.

1332 Below ~ 300 GeV, the *Fermi*-LAT dominates the DM limits for all annihilation channels. From
1333 ~ 300 GeV to ~ 2 TeV, *Fermi*-LAT continues to dominate for the hadronic and bosonic DM channels,
1334 yet the IACTs (H.E.S.S., MAGIC, and VERITAS) and *Fermi*-LAT all contribute to the limit for
1335 leptonic DM channels. For DM masses between ~ 2 TeV to ~ 10 TeV, the IACTs dominate leptonic
1336 DM annihilation channels, whereas both the *Fermi*-LAT and the IACTs dominate bosonic and
1337 hadronic DM annihilation channels. From ~ 10 TeV to ~ 100 TeV, both the IACTs and HAWC
1338 contribute significantly to the leptonic DM limit. For hadronic and bosonic DM, the IACTs and
1339 *Fermi*-LAT both contribute strongly.

1340 We notice that the limits computed using the \mathcal{B} set of J -factor are always better compared to the
1341 ones calculated with the \mathcal{GS} set. For the W^+W^- , Z^+Z^- , $b\bar{b}$, and $t\bar{t}$ channels, the ratio between the
1342 limits computed with the two sets of J -factor is varying between a factor of ~ 3 and ~ 5 depending
1343 on the energy, with the largest ratio around 10 TeV. For the channels e^+e^- , $\mu^+\mu^-$, and $\tau^+\tau^-$, the
1344 ratio lies between ~ 2 to ~ 6 , being maximum around 1 TeV. Examining Figure 4.16 and Figure 4.17
1345 in Section 4.8, these differences are explained by the fact that the \mathcal{B} set provides higher J -factors
1346 for the majority of the studied dSphs, with the notable exception of Segue I. The variation on the
1347 ratio of the limits for the two sets is due to different dSph dominating the limits depending on the
1348 energy. One set, \mathcal{B} , pushes the range of which thermal cross-section which can be excluded to
1349 higher mass. This comparison demonstrates the magnitude of systematic uncertainties associated
1350 with the choice of the J -factor calculation. The \mathcal{GS} and \mathcal{B} sets present a difference in the limits for
1351 all channels of about This difference is explained, see Figure 4.16 and Figure 4.17, by the fact that
1352 the \mathcal{B} set provides higher J -factors for all dSph except for Segue I.

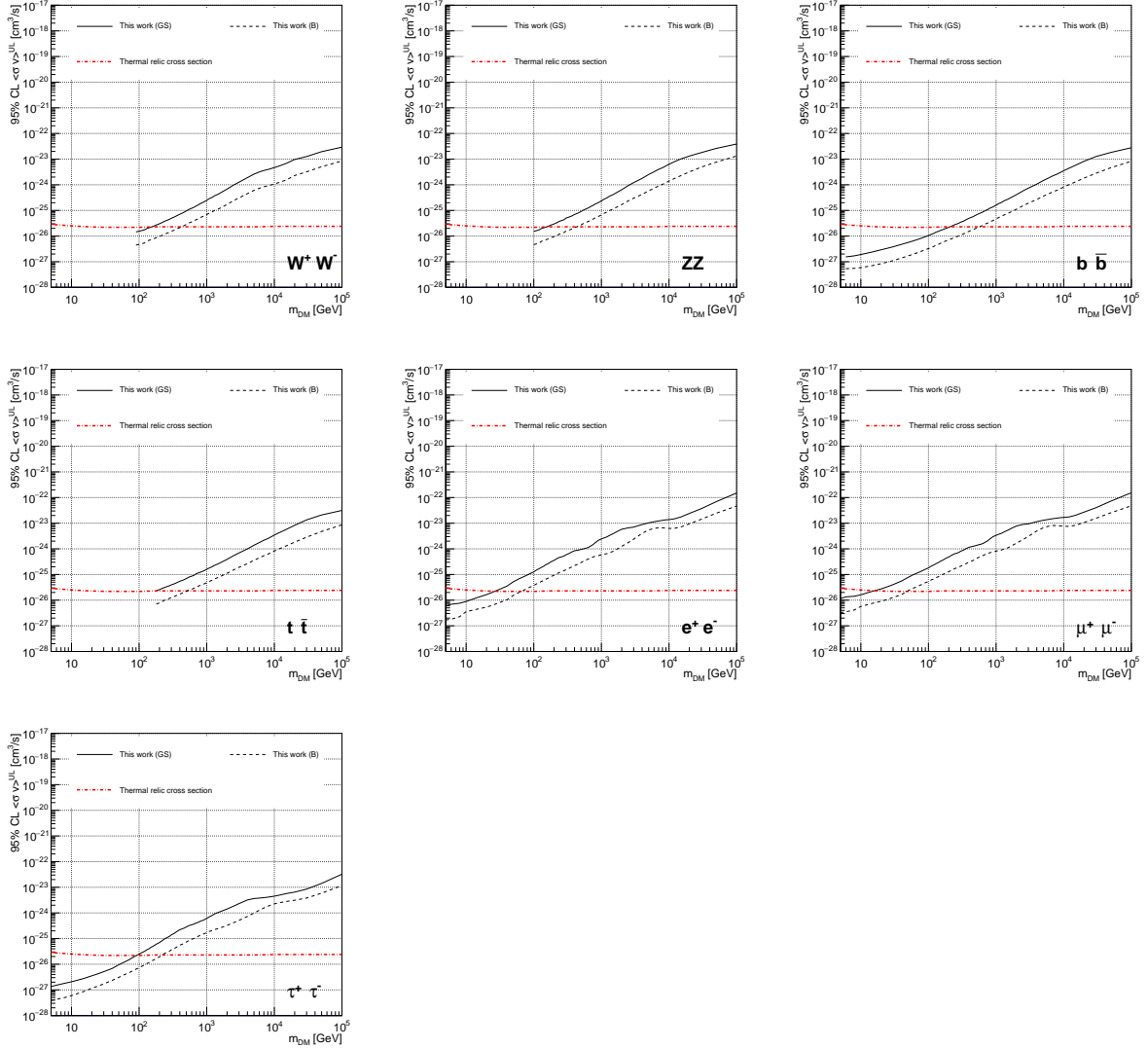


Figure 4.10 Comparisons of the combined limits at 95% confidence level for each of the eight annihilation channels when using the J factors from Ref. [69] (\mathcal{GS} set in Table 4.1), plain lines, and the J factor from Ref. [63, 71] (\mathcal{B} set in Table 4.1), dashed lines. The cross-section given by the thermal relic is also indicated [70].

1353 4.7 HAWC Systematics

1354 4.7.1 Inverse Compton Scattering

1355 The DM-DM annihilation channels produce many high energy electrons regardless of the
 1356 primary annihilation channel. These high energy electrons can produce high energy gamma-rays
 1357 through Inverse Compton Scattering (ICS). If this effect is strong, it would change the morphology
 1358 of the source and increase the total expected gamma-ray counts from any source. The PPPC [58]

1359 provides tools in Mathematica for calculating the impact of ICS for an arbitrary location in the
1360 sky for a specified annihilation channel. We calculated the change in gamma-ray counts for DM
1361 annihilation to primary $e\bar{e}$ for RA and Dec corresponding to Segue1 and Coma Berenices. These
1362 dSphs were chosen because they are the strongest contributors to the limit. $e\bar{e}$ was selected because
1363 it would have the largest number of high energy electrons. The effect was found to be on the order
1364 of 10^{-7} on the gamma-ray spectrum. As a result, this systematic is not considered in our analysis.

1365 **4.7.2 Point Source Versus Extended Source Limits**

1366 The previous DM search toward dSph approximated the dSphs as point sources [60]. In
1367 this analysis, the dSphs are implemented as extended with J-factor distributions following those
1368 produced by [69]. The resolution of the cited map is much finer than HAWC's angular resolution.
1369 The vast majority of the J-factor distribution is represented on the central HAWC pixel of the dSph
1370 spatial map. However, the neighboring 8 pixels are not negligible and contribute to our limit.

1371 Figure 4.11 shows a substantial improvement to the limit for Segue1. Fig. 4.12 however showed
1372 identical limits. These disparities are best explained by the relative difference in their J-Factors.
1373 Both dSphs pass almost overhead the HAWC detector, however Segue1 has the larger J-Factor
1374 between the two. Adjacent pixels to the central pixel will therefore contribute to the limits. This is
1375 the case for other dSph that are closer to the zenith of the HAWC detector.

1376 Comparison plots for all sources and the combined limit can be found in the sandbox for the
1377 Glory Duck project.

1378 **4.7.3 Impact of Pointing Systematic**

1379 During the analysis it was discovered that directional reconstruction of gamma-rays had a
1380 systematic bias at large zenith angles. Slides describing this systematic can be found [here](#). Shown
1381 on the presentation is dependence on the pointing systematic on declination. New spatial profiles
1382 were generated for every dSph and limits were computed for the adjusted declination.

1383 Section 4.7.3 demonstrates the impact of this systematic for all DM annihilation channels
1384 studied by HAWC. The impact is a tiny improvement, yet mostly identical, to the combined limits.

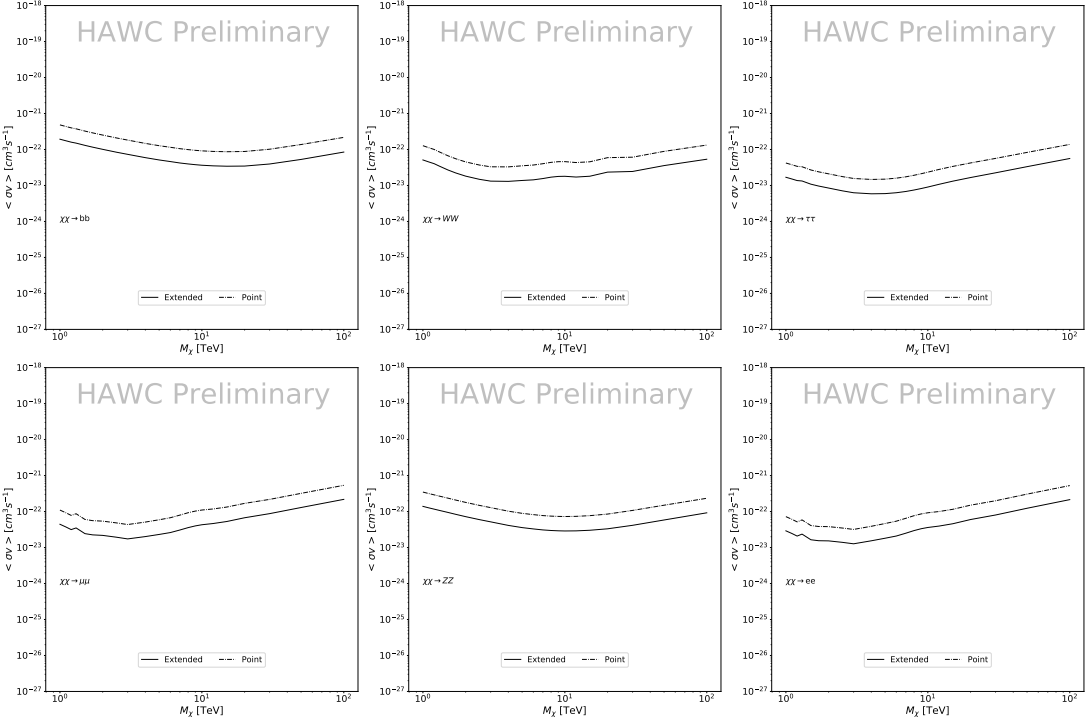


Figure 4.11 Comparisons of the combined limits at 95% confidence level for a point source analysis and extended source using [69] \mathcal{GS} J-factor distributions and PPPC [58] annihilation spectra. Shown are the limits for Segue1 which will have the most significant impact on the combined limit. 6 of the 7 DM annihilation channels are shown. Solid lines are extended source studies. Dashed lines are point source studies. Overall, the extended source analysis improves the limit by a factor of 2.

1385 4.8 J-factor distributions

1386 4.8.1 Numerical integration of \mathcal{GS} maps

1387 It was discovered well after the HAWC analysis was completed that the published tables from
 1388 \mathcal{GS} [59] quoted median J -factors were computed in a non-trivial manner. The assumption myself
 1389 and collaborators had been that the published tables represented the J -factor as a function of θ for
 1390 the best global fit model on a per-source basis. However, this is not the case. Instead, what is
 1391 published are the best fit model for each dwarf that only considers stars up to the angular separation
 1392 θ . Therefore, the model is changing for each value of θ for each dwarf. Yet, the introduced features
 1393 from unique models at each θ are much smaller than the angular resolution of HAWC. It is not
 1394 expected for these effects to impact the limits and TS greatly as a result.

1395 Median J -factor model profiles were provided by the authors. New maps were generated

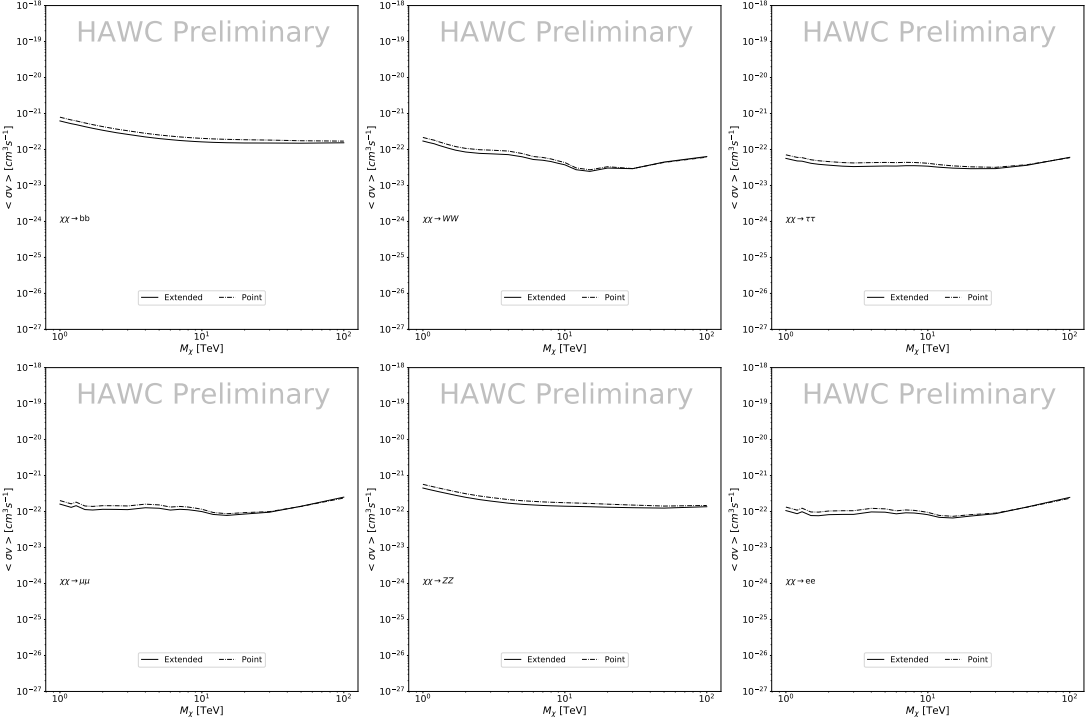


Figure 4.12 Same as Fig. 4.11 on Coma Berenices. This dSph also contributes significantly to the limit. The limits are identical in this case.

1396 and analyzed for Segue1 and Coma Berenices. Figure 4.14 shows the differential between maps
 1397 generated with the method from Section 4.8.1 and from the authors of [59]. These maps were
 1398 reanalyzed for all SM DM annihilation channels. Upper limits for these channels are shown in
 1399 Figure 4.15

1400 From Figure 4.15, we can see that the impact of these model difference was no substantial.
 1401 The observed impact was a fractional effect which is much smaller than the impact from selecting
 1402 another DM spatial distribution model as was shown in Figure 4.10.

1403 **4.8.2 \mathcal{GS} Versus \mathcal{B} spatial models**

1404 We show in this appendix a comparison between the J -factors computed by Geringer-Sameth
 1405 *et al.* [69] (the \mathcal{GS} set) and the ones computed by Bonnivard *et al.* [63, 71] (the \mathcal{B} set). The
 1406 \mathcal{GS} J -factors are computed through a Jeans analysis of the kinematic stellar data of the selected
 1407 dSphs, assuming a dynamic equilibrium and a spherical symmetry for the dSphs. They adopted
 1408 the generalized DM density distribution, known as Zhao-Hernquist, introduced by [61], carrying

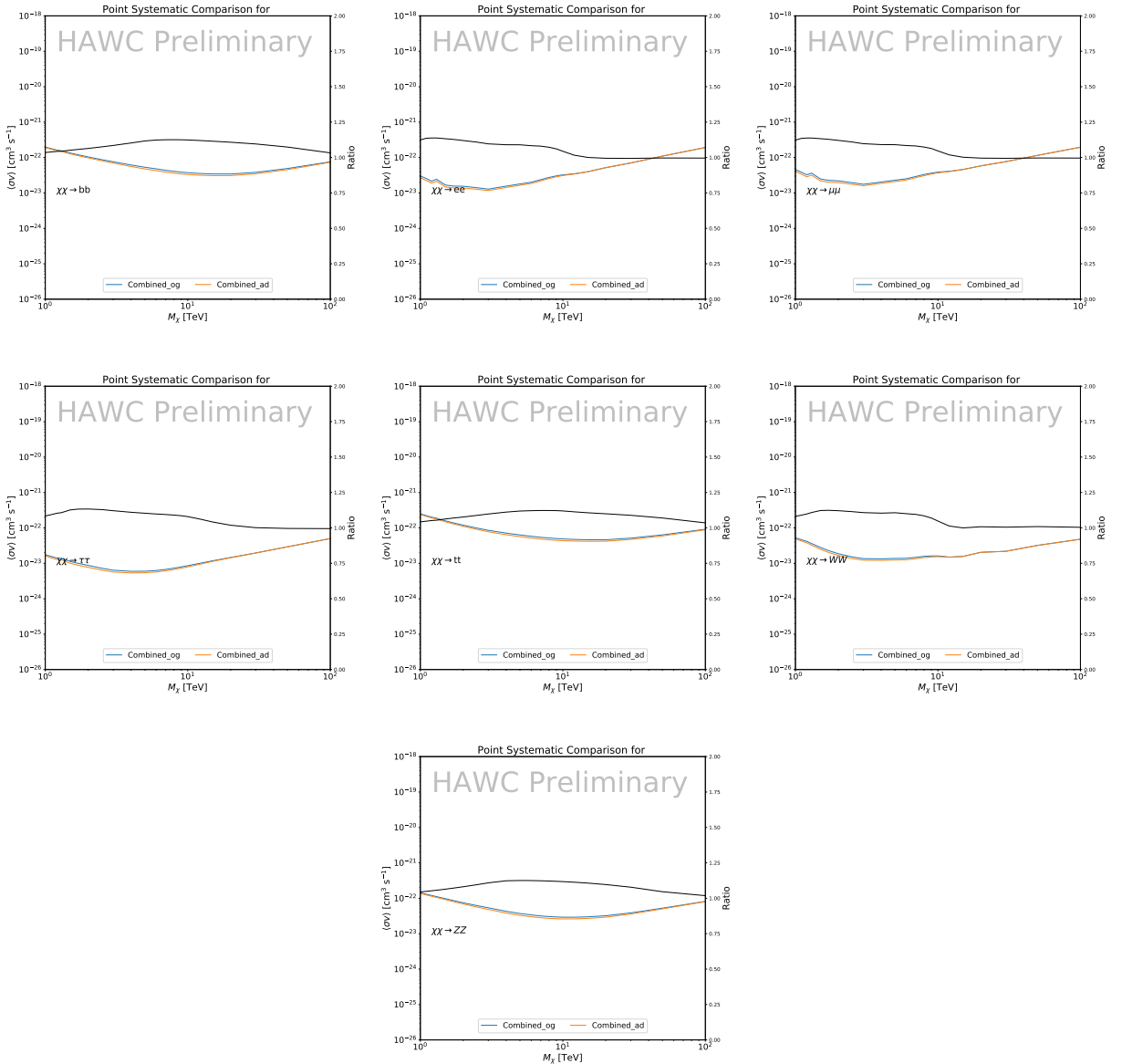


Figure 4.13 Comparison of combined limits when correcting for HAWC's pointing systematic. All DM annihilation channels are shown. The solid black line is the ratio between published limit to the declination corrected limit. The blue solid line or "Combined_og" represented the limits computed for Glory Duck. The solid orange line or "Combined_ad" represented the limits computed after correcting for the pointing systematic.

1409 three additional index parameters to describe the inner and outer slopes, and the break of the
 1410 density profile. Such a profile parametrization allows the reduction of the theoretical bias from
 1411 the choice of a specific radial dependency on the kinematic data. In other words, the increase of
 1412 free parameters with the use of the Zhao-Hernquist profile allows a better description of the mass

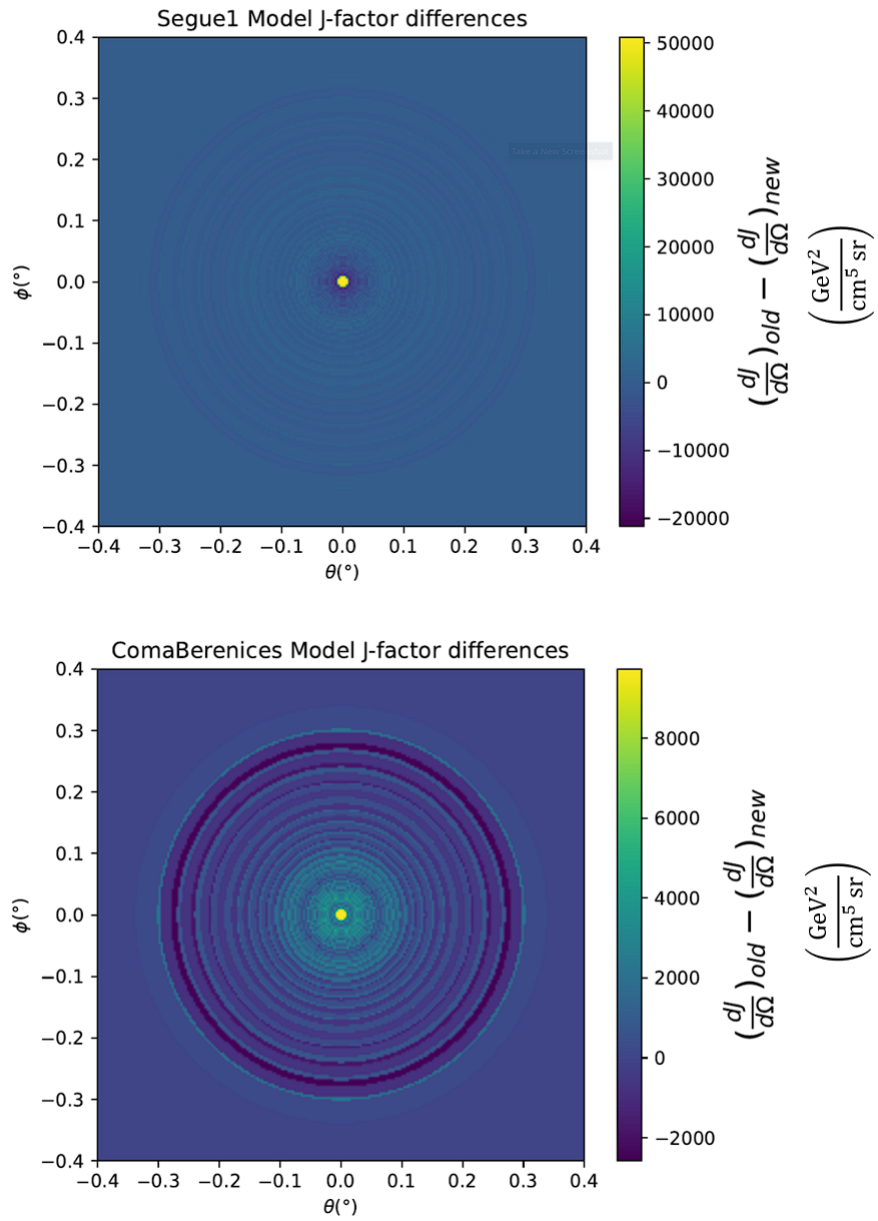


Figure 4.14 Differential map of dJ/Ω from model built in Section 4.8.1 and profiles provided directly from authors. (Top) Differential from Segue1. (bottom) Differential from Coma Berenices. Note that their scales are not the same. Segue1 shows the deepest discrepancies which is congruent with its large uncertainties. Both models show anuli where unique models become apparent.

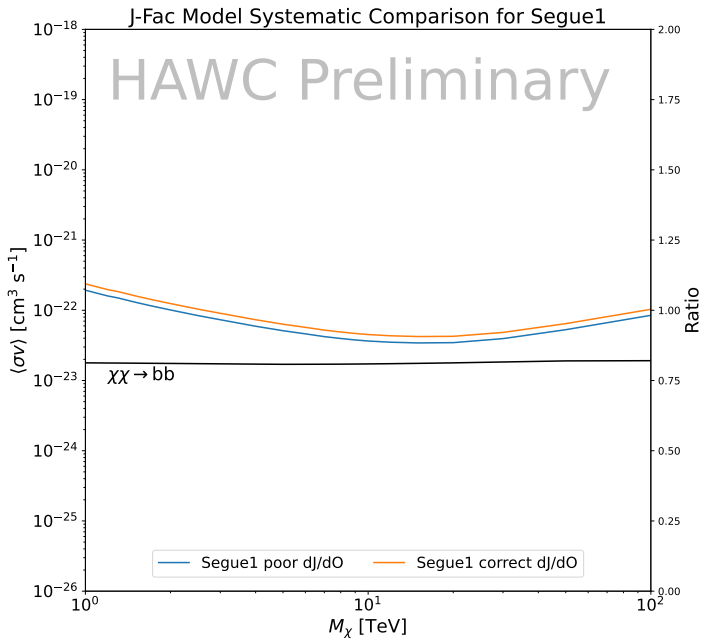
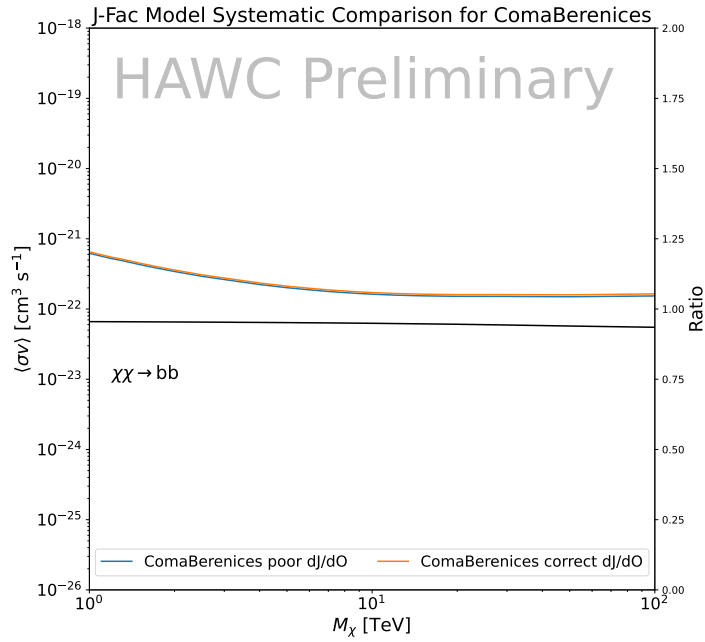


Figure 4.15 HAWC limits for Coma Berenices (top) and Segue1 (bottom) for two different map sets. Blue lines are limits calculated on maps with poor model representation. Orange lines are limits calculated on spatial profiles provided by the authors of [59]. Black line is the ratio of the poor spatial model limits to the corrected spatial models. The left y-axis measures $\langle\sigma v\rangle$ for the blue and orange lines. The right y-axis measures the ratio and is unitless.

1413 density distribution of dark matter.

1414 In addition, a constant velocity anisotropy profile and a Plummer light profile [74] for the stellar
1415 distribution were assumed. The velocity anisotropy profile depends on the radial and tangential
1416 velocity dispersion. However, its determination remains challenging since only the line-of-sight
1417 velocity dispersion can be derived from velocity measurements. Therefore, the parametrization of
1418 the anisotropy profile is obtained from simulated halos (see [75] for more details). They provide the
1419 values of the J -factors of regions extending to various angular radius up to the outermost member
1420 star.

1421 The \mathcal{B} J -factors were computed through a Jeans analysis taking into account the systematic
1422 uncertainties induced by the DM profile parametrization, the radial velocity anisotropy profile, and
1423 the triaxiality of the halo of the dwarf galaxies. They performed a more complete study of the dSph
1424 kinematics and dynamics than \mathcal{GS} for the determination of the J -factor. Conservative values of the
1425 J -factors where obtained using an Einasto DM density profile [76], a realistic anisotropy profile
1426 known as the Baes & Van Hese profile [77] which takes into account that the inner regions can be
1427 significantly non-isotropic, and a Zhao-Hernquist light profile [61].

1428 For both sets, J -factor values are provided for all dSphs as a function of the radius of the
1429 integration region [69, 63, 71]. Table 4.1 shows the heliocentric distance and Galactic coordinates
1430 of the twenty dSphs, together with the two sets of J -factor values integrated up to the outermost
1431 observed star for \mathcal{GS} and the tidal radius for \mathcal{B} . Both J -factor sets were derived through a Jeans
1432 analysis based on the same kinematic data, except for Draco where the measurements of [78] have
1433 been adopted in the computation of the \mathcal{B} value. The computations for producing the \mathcal{GS} and \mathcal{B}
1434 samples differ in the choice of the DM density, velocity anisotropy, and light profiles, for which the
1435 set \mathcal{B} takes into account some sources of systematic uncertainties.

1436 Figure 4.16 and Figure 4.17 show the comparisons for the J -factor versus the angular radius
1437 for each of the 20 dSphs used in this study. The uncertainties provided by the authors are also
1438 indicated in the figures. For the \mathcal{GS} set, the computation stops at the angular radius corresponding
1439 to the outermost observed star, while for the \mathcal{B} set, the computation stops at the angular radius

1440 corresponding to the tidal radius.

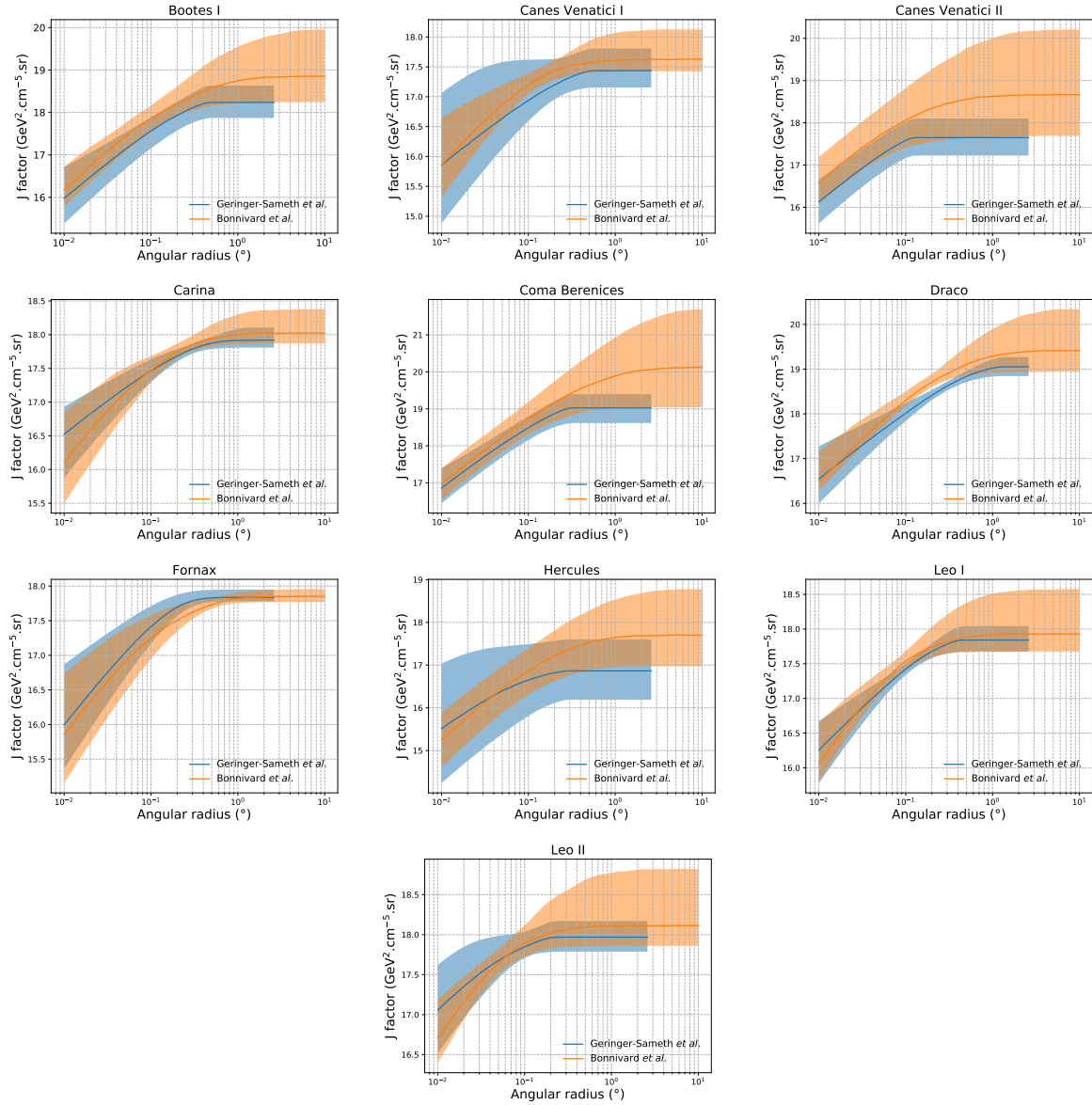


Figure 4.16 Comparisons between the J -factors versus the angular radius for the computation of J factors from Ref. [69] (\mathcal{GS} set in Table 4.1) in blue and for the computation from Ref. [63, 71] (\mathcal{B} set in Tab. 4.1) in orange. The solid lines represent the central value of the J -factors while the shaded regions correspond to the 1σ standard deviation.

1441 4.9 Discussion and Conclusions

1442 In this multi-instrument analysis, we have used observations of 20 dSphs from the gamma-ray
 1443 telescopes Fermi-LAT, H.E.S.S., MAGIC, VERITAS, and HAWC to perform a collective DM
 1444 search annihilation signals. The data were combined across sources and detectors to significantly

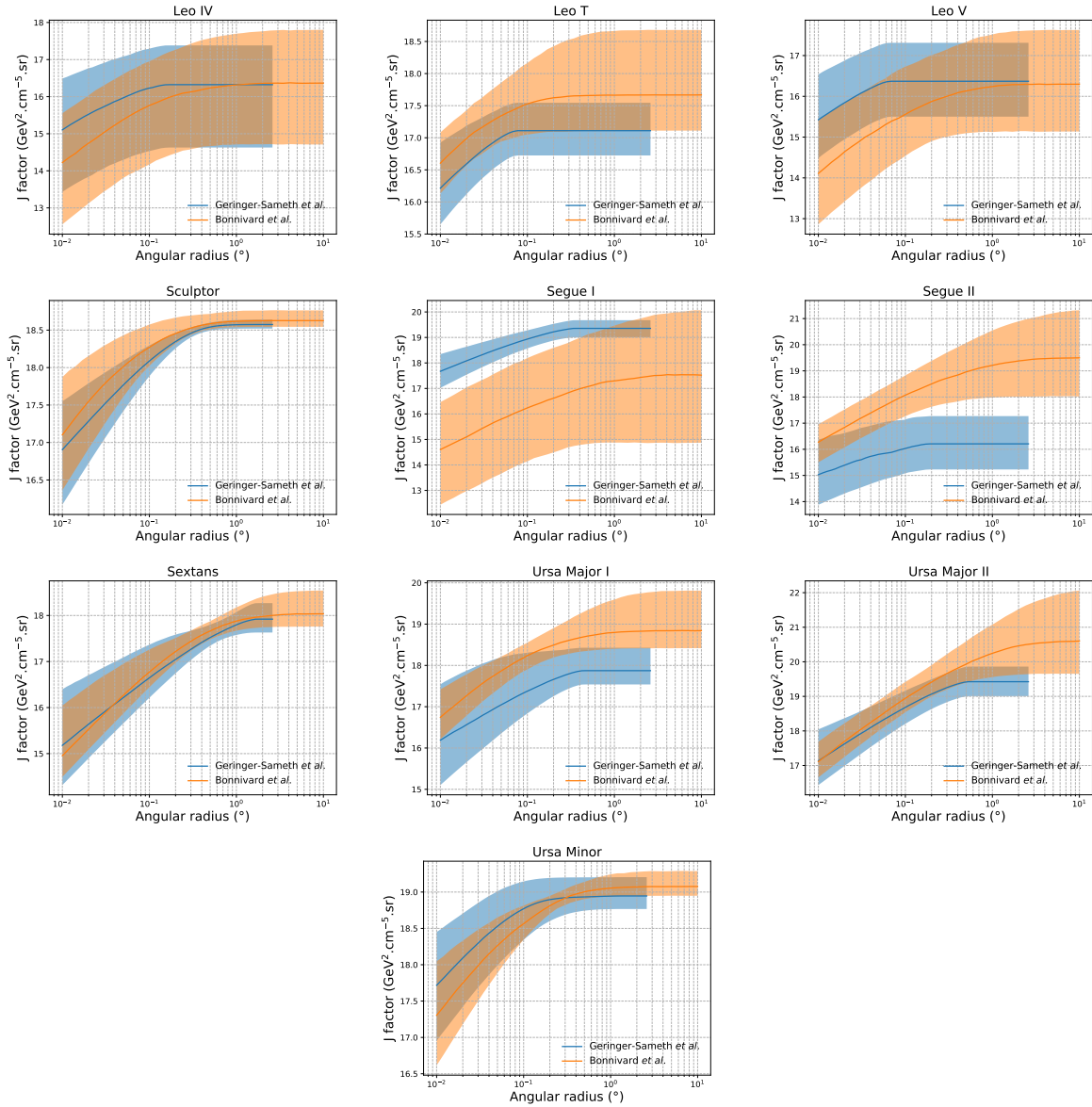


Figure 4.17 Comparisons between the J -factors versus the angular radius for the computation of J factors from Ref. [69] (\mathcal{GS} set in Tab. 4.1) in blue and for the computation from Ref. [63, 71] (\mathcal{B} set in Tab. 4.1) in orange. The solid lines represent the central value of the J -factors while the shaded regions correspond to the 1σ standard deviation.

increase the sensitivity of the search. We have observed no significant deviation from the null, no DM hypothesis, and so present our results in terms of upper limits on the annihilation cross-section for seven potential DM annihilation channels.

Fermi-LAT brings the most stringent constraints for continuum channels below approximately 1 TeV. The remaining detectors dominate at higher energies. Overall, for multi-TeV DM mass,

1450 the combined DM constraints from all five telescopes are 2-3 times stronger than any individual
1451 telescope for multi-TeV DM.

1452 Derived from observations of many dSphs, our results produce robust limits given the DM
1453 content of the dSphs is relatively well constrained. The obtained limits span the largest mass
1454 range of any WIMP DM search. Our combined analysis improves the sensitivity over previously
1455 published results from each detector which produces the most stringent limits on DM annihilation
1456 from dSphs. These results are based on deep exposures of the most promising known dSphs with
1457 the currently most sensitive gamma-ray instruments. Therefore, our results constitute a legacy of
1458 a generation of gamma-ray instruments on WIMP DM searches towards dSphs. Our results will
1459 remain the reference in the field until a new generation of more sensitive gamma-ray instruments
1460 begin operations, or until new dSphs with higher J -factors are discovered.

1461 This analysis serves as a proof of concept for future multi-instrument and multi-messenger
1462 combination analyses. With this collaborative effort, we have managed to sample over four orders
1463 in magnitude in gamma-ray energies with distinct observational techniques. Determining the nature
1464 of DM continues to be an elusive and difficult problem. Larger datasets with diverse measurement
1465 techniques could be essential to tackling the DM problem. A future collaboration using similar
1466 techniques as the ones described in this paper could grow even beyond gamma rays. The models we
1467 used for this study include annihilation channels with neutrinos in the final state. Advanced studies
1468 could aim to merge our results with those from neutrino observatories with large data sets. Efforts
1469 are already underway to add data from the IceCube, ANTARES, and KM3NeT observatories to
1470 these gamma-ray results.

1471 From this work, a selection of the best candidates for observations, according to the latest
1472 knowledge on stellar dynamics and modelling techniques for the derivation of the J -factors on
1473 the potential dSphs targets, is highly desirable at the time that new experiments are starting their
1474 dark matter programs using dSphs. Given the systematic uncertainty inherent to the derivation of
1475 the J -factors, an informed observational strategy would be to select both objects with the highest
1476 J -factors that could lead to DM signal detection, and objects with robust J -factor predictions, i.e.

1477 with kinematic measurements on many bright stars, which would strengthen the DM interpretation
1478 reliability of the observation outcome.

1479 This analysis combines data from multiple telescopes to produce strong constraints on astro-
1480 physical objects. From this perspective, these methods can be applied beyond just DM searches.
1481 Almost every astrophysical study can benefit from multi-telescope, multi-wavelength gamma-ray
1482 studies. We have enabled these telescopes to study the cosmos with greater precision and detail.
1483 Many astrophysical searches can benefit from multi-instrument gamma-ray studies, for which our
1484 analysis lays the foundation.

CHAPTER 5

1485 MULTITHREADING HAWC ANALYSES FOR DARK MATTER SEARCHES

1486 5.1 Introduction

1487 HAWC’s current software suite, plugins to 3ML and HAL [68, 34], do not fully utilize compu-
1488 tational advancements of recent decades. Said advancements include the proliferation of Graphical
1489 Processing Units (GPUs), and multithreading on multicore processors. The analysis described in
1490 chapter 4 took up to 3 months of wall time waiting for the full gambit of data analysis and simulation
1491 of background to compute. Additionally, with the updated 2D energy binning scheme, f_{hit} and
1492 Neural Network (NN), the time needed to compute expected to grow. Although excessive comput-
1493 ing time was, in part, from an intense use of a shared computing cluster, it was evident that there
1494 was room for improvement. In HAWC’s next generation dSph DM search, I decided to develop
1495 codes that would utilize the multicore processors on modern high performance computing clusters.
1496 The results of this work are featured in this chapter and brought a human timing improvement to
1497 computation that scales approximately as $1/N$ where N is the number of threads.

1498 5.2 Dataset and Background

1499 This section enumerates the data and background methods used for HAWC’s multithreaded
1500 study of dSphs. Section 5.2.1 and Section 5.2.2 are most useful for fellow HAWC collaborators
1501 looking to replicate a multithreaded dSph DM search.

1502 5.2.1 Itemized HAWC files

1503 These files are only available withing HAWC’s internal documentation and collaborators. They
1504 are not meant for public access, and are presented here so that HAWC collaborators can reproduce
1505 results accurately.

- 1506 • Detector Resolution: `refit-Pass5-Final-NN-detRes-zenith-dependent.root`
- 1507 • Data Map: `Pass5-Final-NN-maptree-ch103-ch1349-zenith-dependent.root`
- 1508 • Spectral Dictionary: `HDMspectra_dict_gamma.npy`

1509 **5.2.2 Software Tools and Development**

1510 This analysis was performed using HAL and 3ML [34, 57] in Python3. I built software
1511 in collaboration with Michael Martin and Letrell Harris to implement the *Dark Matter Spectra*
1512 *from the Electroweak to the Planck Scale* (HDM) [79] and dSphs spatial model from [80] for
1513 HAWC analysis. A NumPy dictionary of HDM, `HDMspectra_dict_gamma.npy`, was made for
1514 portability within the collaboration. These dictionaries were generated from the [git repository](#) [79].
1515 The analysis was performed using the Neural Network energy estimator for Pass 5.F. A description
1516 of this estimator was provided in chapter 3. [TODO: Define a subsection when it's written](#), and its
1517 key, relevant improvements are an improved energy estimation and improved sensitivities at higher
1518 zenith angles. All other software used for data analysis, DM profile generation, and job submission
1519 to SLURM are also kept in my sandbox in the [Dark Matter HAWC](#) project. The above repository
1520 also incorporates the model inputs used previously in Glory Duck, described in chapter 4, so Glory
1521 Duck remains compatible with modern software.

1522 **5.2.3 Data Set and Background Description**

1523 The HAWC data maps used for this analysis contain 2565 days of data between runs 2104 and
1524 7476. They were generated from pass 5.f reconstruction. The analysis is performed using the NN
1525 energy estimator with bin list:

1526 `B1C0Ea, B1C0Eb, B1C0Ec, B1C0Ed, B1C0Ee, B2C0Ea, B2C0Eb, B2C0Ec, B2C0Ed, B2C0Ee,`
1527 `B3C0Ea, B3C0Eb, B3C0Ec, B3C0Ed, B3C0Ee, B3C0Ef, B4C0Eb, B4C0Ec, B4C0Ed, B4C0Ee,`
1528 `B4C0Ef, B5C0Ec, B5C0Ed, B5C0Ee, B5C0Ef, B5C0Eg, B6C0Ed, B6C0Ee, B6C0Ef, B6C0Eg,`
1529 `B6C0Eh, B7C0Ee, B7C0Ef, B7C0Eg, B7C0Eh, B7C0Ei, B8C0Ee, B8C0Ef, B8C0Eg, B8C0Eh,`
1530 `B8C0Ei, B8C0Ej, B9C0Ef, B9C0Eg, B9C0Eh, B9C0Ei, B9C0Ej, B10C0Eg, B10C0Eh,`
1531 `B10C0Ei, B10C0Ej, B10C0Ek, B10C0El`

1532 Bin 0 was excluded as it has substantial hadronic contamination and poor angular resolution.

1533 Background considerations and source selection was identical to Section 4.2.3, and no additional
1534 arguments are provided here. Many of the HAWC systematics explored in Section 4.7 also apply

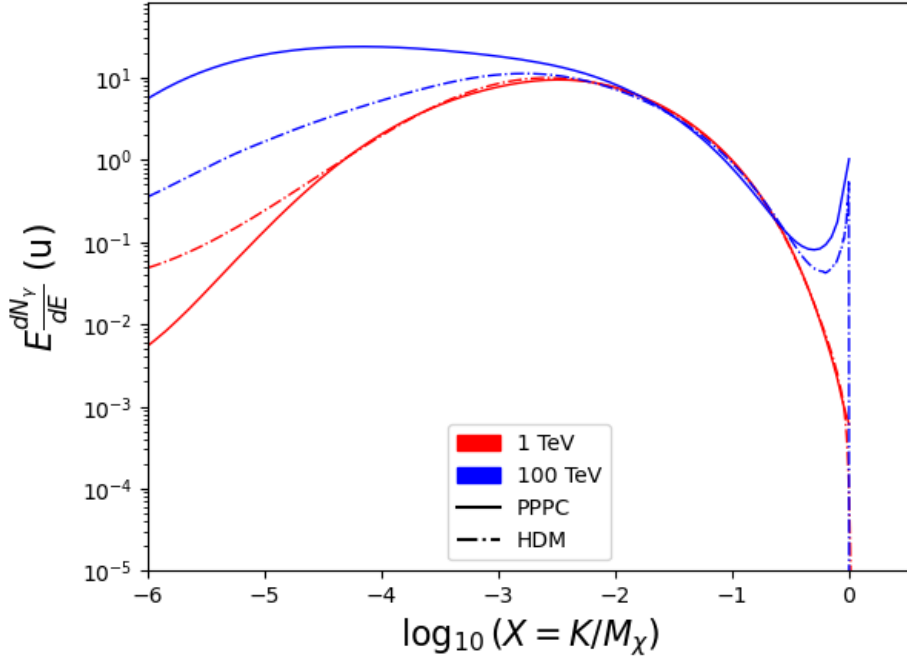


Figure 5.1 Spectral hypotheses from PPPC [58] and HDM [79] for DM annihilation: $\chi\chi \rightarrow W^-W^+$. Solid lines are spectral models with EW corrections from the PPPC. Dash-dot lines are spectral models from HDM. Red lines are models for $M_\chi = 1$ TeV. Blue lines represent models for $M_\chi = 100$ TeV.

1535 for this DM search and are not added upon here.

1536 **5.3 Analysis**

1537 The analysis and its systematics are almost identical to Section 4.3. Importantly, we use the
 1538 same **TODO: fix this ref**Equation (4.1) and Equation (4.2) for estimating the gamma-ray flux at
 1539 HAWC from our sources.

1540 **5.3.1 $\frac{dN_\gamma}{dE_\gamma}$ - Particle Physics Component**

1541 For these spectra, we import HDM with Electroweak (EW) corrections and additional correc-
 1542 tions for neutrinos above the EW scale [79]. The spectra are implemented as a model script in
 1543 astromodels for 3ML. A comprehensive description of EW corrections and neutrino considerations
 1544 are provided later in Sec. 8.

1545 Figure 5.1 demonstrates the impact of changes implemented in HDM on DM annihilation to W
 1546 bosons. A class in astromodels was developed to include HDM and is aptly named **HDMspectra**
 1547 within `DM_models.py`. The SM DM annihilation channels studied here are $\chi\chi \rightarrow:$

1548 e^+e^- , $\mu^+\mu^-$, $\tau^+\tau^-$, $b\bar{b}$, $t\bar{t}$, gg , W^+W^- , ZZ , $c\bar{c}$, $u\bar{u}$, $d\bar{d}$, $s\bar{s}$, $\nu_e\bar{\nu}_e$, $\nu_\mu\bar{\nu}_\mu$, $\nu_\tau\bar{\nu}_\tau$, $\gamma\gamma$, hh .

1549 For $\gamma\gamma$ and ZZ , a substantial fraction of the signal photons are expected to have $E_\gamma = m_\chi$ [79].
 1550 This introduces δ -function that is much narrower than the energy resolution of the HAWC detector.
 1551 To ensure that this feature is not lost in the likelihood fits, the 'line' feature is convolved with a
 1552 Gaussian kernel with a 1σ width of $0.05 \cdot m_\chi$ and total kernel window of $\pm 4\sigma$. This differs from
 1553 HAWC's previous line study where 30% of HAWC's energy resolution was used for the kernel [81].
 1554 The NN energy estimator's strength compared to f_{hit} at low gamma-ray energy enables narrower
 1555 kernels [79]. $\chi\chi \rightarrow \gamma\gamma$ and ZZ spectral hypotheses are shown in Figure 5.2. We did not explore
 1556 how well we reconstruct injected signal events for various kernels widths. This is a systematic
 1557 that should be tested before publication to journal. Spectral models for the remaining annihilation
 1558 channels are plotted for each m_χ in Figure B.1.

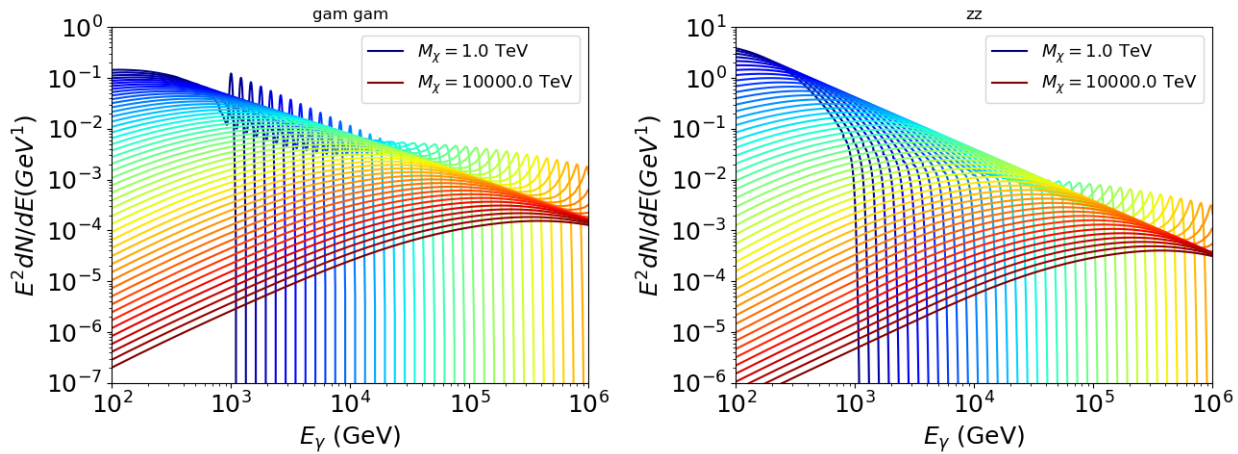


Figure 5.2 Photon spectra for $\chi\chi \rightarrow \gamma\gamma$ (left) and $\chi\chi \rightarrow ZZ$ (right) after Gaussian convolution of line features. Both spectra have δ -features at photon energies equal to the DM mass. Bluer lines are annihilation spectra with lower DM mass. Redder lines are spectra from larger DM mass. All spectral models are sourced from the Heavy Dark Matter models [79]. Axes are drawn roughly according to the energy sensitivity of HAWC.

1559 **5.3.2 J Astrophysical Components**

1560 The J-factor profiles for each source are imported from Louis Strigari et al. (referred to with
 1561 \mathcal{LS}) [80]. The \mathcal{LS} catalog fits a Navarro–Frenk–White (NFW) [62] spatial DM distributions to

1562 the dSphs which has a DM density of

$$\rho(r) = \frac{\rho_0}{\frac{r}{R_s} \left(1 + \frac{r}{R_s}\right)^2}. \quad (5.1)$$

1563 ρ_0 and the scale radius, R_s are free parameters fit for each dSph. r is the distance from the center
1564 of the dSph.

1565 Profiles in $\frac{dJ}{d\Omega}(\theta)$ up to an angular separation $\theta = 0.5^\circ$ were provided directly from the authors.

1566 Map generation from these profiles were almost identical to Section 4.3.2 except that a higher order
1567 trapezoidal integral was used for the normalization of the square, uniformly-spaced map:

$$p^2 \cdot \sum_{i=0}^N \sum_{j=0}^M w_{i,j} \frac{dJ}{d\Omega}(\theta_{i,j}, \phi_{i,j}) \quad (5.2)$$

1568 p is the angular side of one pixel in the map. $w_{i,j}$ is a weight assigned the following ways:

1569 $w_{i,j} = 1$ if $(\theta_{i,j}, \phi_{i,j})$ is fully within the region of integration

1570 $w_{i,j} = 1/2$ if $(\theta_{i,j}, \phi_{i,j})$ is on an edge of the region of integration

1571 $w_{i,j} = 1/4$ if $(\theta_{i,j}, \phi_{i,j})$ is on a corner of the region of integration

1572 Figure 5.3 shows the median and $\pm 1\sigma$ maps used as input for this DM annihilation study.

1573 5.3.3 Source Selection and Annihilation Channels

1574 HAWC's sources for this multithreaded analysis include Coma Berenices, Draco, Segue 1, and
1575 Sextans. \mathcal{LS} observed up to 43 sources in its publication, however only 4 of the best fit profiles
1576 were provided at the time this thesis was written. A full description of each source used in this
1577 analysis is found in Table 5.1.

1578 This analysis improves on chapter 4 in the following ways. Previously, the particle physics
1579 model used for gamma-ray spectra from DM annihilation was from the PPPC [58] which missed
1580 important considerations relevant for the neutrino sector. HDM is used to account for this shortfall
1581 [79]. HDM also models DM to the Planck scale which permits HAWC to probe PeV scale DM. For
1582 this study, we sample DM masses: 1 TeV - 10 PeV with 6 mass bins per decade in DM mass. In

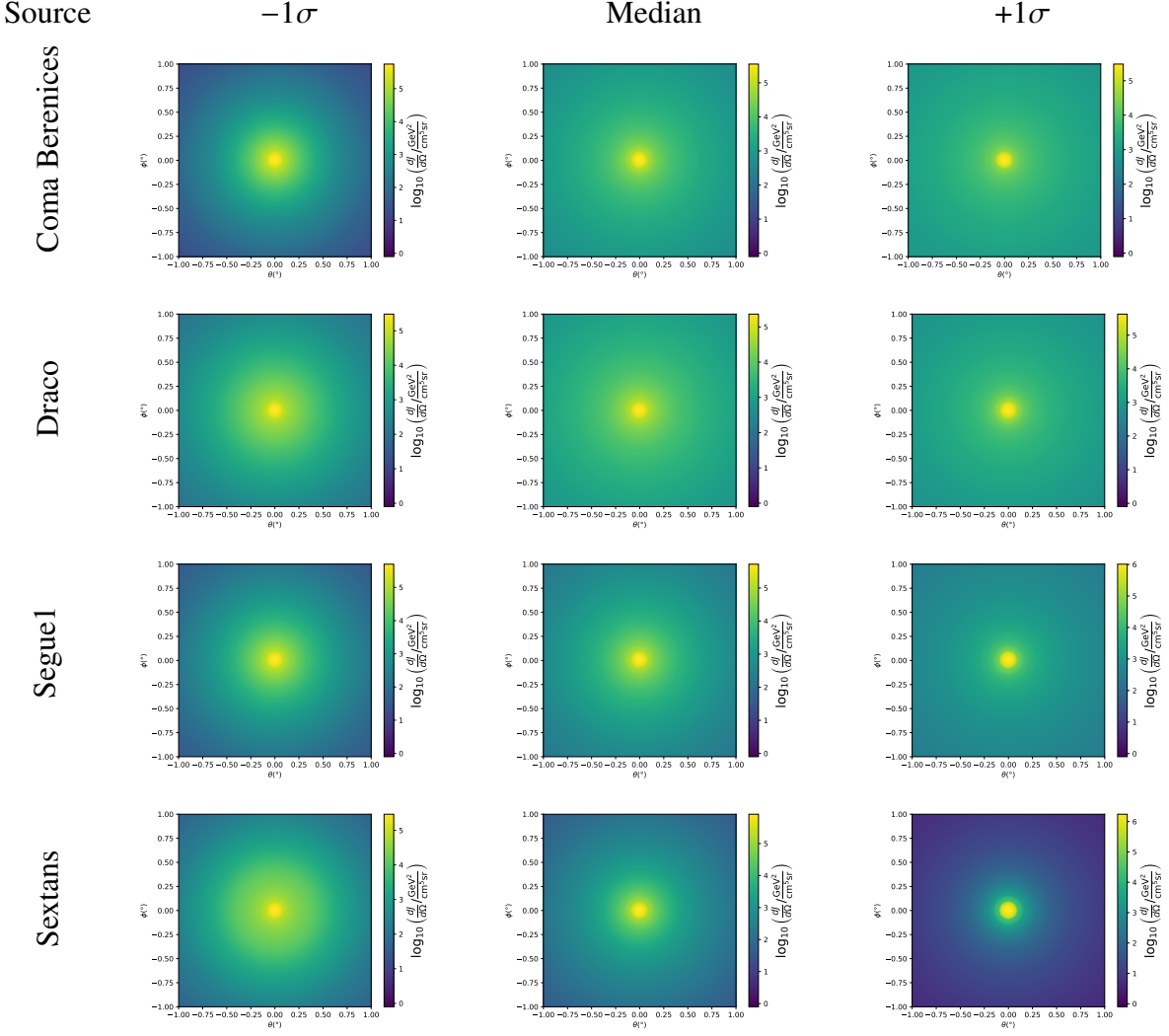


Figure 5.3 $\frac{dJ}{d\Omega}$ maps for Coma Berenices, Draco, Segue1, and Sextans. Columns are divided for the $\pm 1\sigma$ uncertainties in $dJ/d\Omega$ around the mean value from \mathcal{LS} [80]. Origin is centered on the specific dwarf spheroidal galaxies (dSph). θ and ϕ axes are the angular separation from the center of the dwarf. Profiles are truncated at 1° and flattened beyond.

1583 the case of line spectra ($\chi\chi \rightarrow \gamma\gamma$, or ZZ), we double the mass binning to 12 DM mass bins per
 1584 decade in DM mass.

1585 \mathcal{LS} provides 25 sources within HAWC's field of view. Additionally, NFW [62] DM distributions
 1586 have fewer parameters than Zhao [61], so \mathcal{LS} fits ultra-faint dwarves which expands the number of
 1587 sources. However, all sources were not provided by the authors in time for the completion of this
 1588 dissertation. Finally, the gamma-ray ray dataset is much larger. The study performed here analyzes
 1589 2565 days of data compared to 1017 days analyzed in chapter 4.

1590 **5.4 Likelihood Methods**

1591 These are identical to Section 4.4.1 and no additional changes are made to the likelihood. Bins
1592 in this analysis are expanded to include HAWC’s NN energy estimator.

1593 **5.5 Computational Methods: Multithreading**

1594 Previously, as in Section 4.3, the likelihood was minimized for one model at a time. One model
1595 in this case representing a DM annihilation channel (CHAN), DM mass (m_χ), and dSph ((SOURCE)).
1596 In an effort to conserve human and CPU time, jobs submitted for high performance computing
1597 contained a list of m_χ to iterate over for likelihood fitting. Jobs were then trivially parallelized
1598 for each permutation of the two lists: CHANS and SOURCES. The lists for CHANS and SOURCES are
1599 found in Section 5.3.1 and Table 5.1, respectively. Initially, 11 m_χ were serially sampled for one
1600 job defined by a [CHAN, SOURCE] tuple. Computing the likelihoods would take between 1.5 to 2 hrs,
1601 stochastically, for a job. We expect to compute likelihoods for data and 300 Poisson background
1602 trials. The estimated CPU time based on the above for all CHAN (N = 17) and SOURCE (M = 25)
1603 was estimated to 127,925 jobs. In total, 1,407,175 likelihood fits and profiles would be computed
1604 for the 11 mass bins we wished to study. The estimated CPU time ranged between 8k CPU days
1605 to 10k CPU days. Human time is more challenging to estimate as job allocation is stochastic and
1606 highly dependent on what other users are submitting. Yet, it is unlikely that all jobs would run
1607 simultaneously. Therefore, we can expect human time to be about as long as was seen in chapter 4

Name	Distance (kpc)	l, b ($^\circ$)	$\log_{10} J$ (\mathcal{LS} set) $\log_{10}(\text{GeV}^2 \text{cm}^{-5} \text{sr})$
Coma Berenices	44	241.89, 83.61	$19.00^{+0.36}_{-0.35}$
Draco	76	86.37, 34.72	$18.83^{+0.12}_{-0.12}$
Segue I	23	220.48, 50.43	$19.12^{+0.49}_{-0.58}$
Sextans	86	243.50, 42.27	$17.73^{+0.13}_{-0.12}$

Table 5.1 Summary of the relevant properties of the dSphs used in the present work. Column 1 lists the dSphs. Columns 2 and 3 present their heliocentric distance and galactic coordinates, respectively. Column 4 reports the J -factors of each source given from the \mathcal{LS} studies and estimated $\pm 1\sigma$ uncertainties. The values $\log_{10} J$ (\mathcal{LS} set) [80] correspond to the mean J -factor values for a source extension truncated at 0.5° .

1608 which was on the order of months to fully compute on a smaller analysis. A visual aid to describe
1609 how jobs were organized is provided in Figure 5.4.

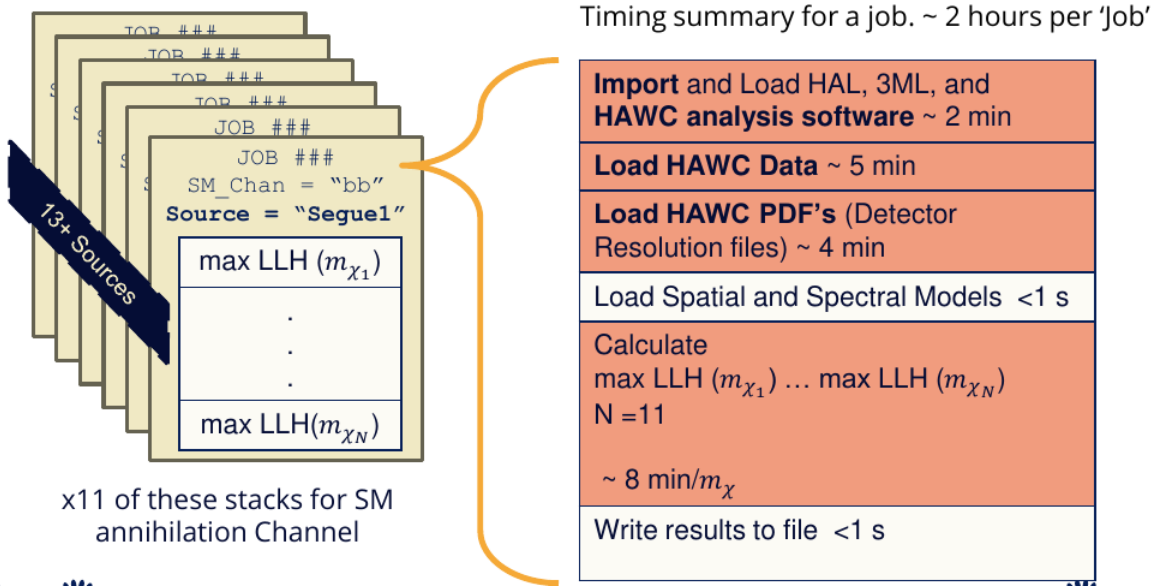


Figure 5.4 Infographic on how jobs and DM computation was organized in Section 4.3. Jobs were built for each permutation of CHANS and SOURCES shown by the left block in the figure. Each job, which took on the order 2 hrs to compute, had the following work flow: 1. Import HAWC analysis software, 2 min to run. 2. Load HAWC count maps, 5 min to run. 3. Load HAWC energy and spatial resolutions, 4 min. 5. Load DM spatial source templates and spectral models, less than 1 s. 6. Perform likelihood fit on data and model, about 8 min per DM mass. 7. Write results to file, less than 1s.

1610 The computational needs for this next generation DM analysis are extreme and is unlike other
1611 analyses performed on HAWC. It became clear that there was a lot to gain from optimizing how
1612 the likelihoods are computed. This section discusses how multi-threading was applied to solve and
1613 reduce HAWC's computing of likelihoods for large parameter spaces like in DM searches.

1614 5.5.1 Relevant Foundational Information

1615 The profiling of the likelihood for HAWC is done via gradient descent where the normalization
1616 of Equation (4.1) (linearly correlated with $\langle \sigma v \rangle$) is rescaled in the descent. Additionally, we sample
1617 the likelihood space for a defined list of $\langle \sigma v \rangle$'s described in Section 4.4.2. The time to compute
1618 these values is not predictable or consistent because many variables can change across the full
1619 model-space. Comprehensively, these variables are:

1620 • m_χ : DM rest mass
 1621 • CHAN : DM annihilation channel in SM.
 1622 • SOURCE : dSph. Involves a spatial template AND coordinate in HAWC data.
 1623 • $\langle\sigma v\rangle$: Effectively the flux normalization and free parameter in the likelihood fit.
 1624 Therefore, we develop an asynchronous, functional-parallel coding pattern. Asynchronous meaning
 1625 the instructions within a function are independent and permitted to be out of sync with sibling
 1626 computations. Functional-parallel meaning that instructions are the subject of parallelization
 1627 rather than threading the likelihood computation. This is close to trivial parallelization seen in
 1628 Figure 5.4 except that we seek to consolidate the loading stages (software, data, and detector
 1629 resolution loading). Multiple asynchronous threads are expected to reduce total serial processing
 1630 time and total overhead across the entire project in addition to saving human time.

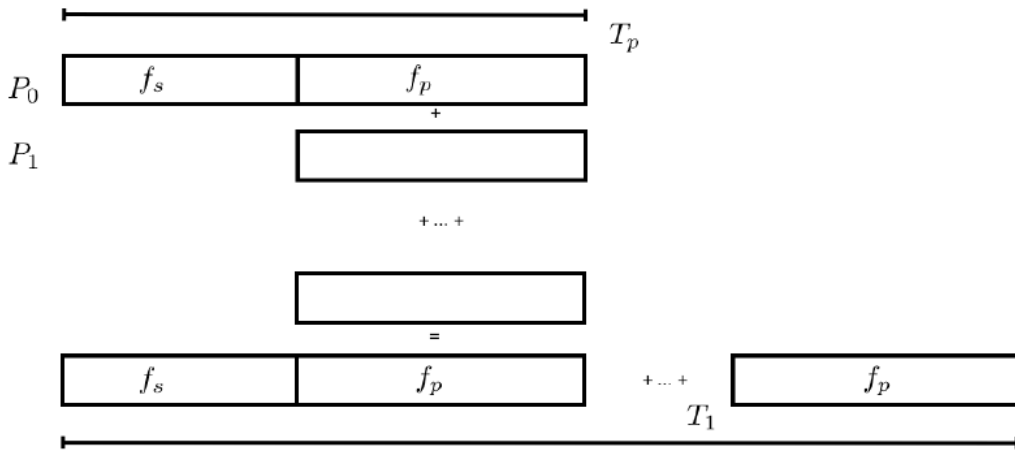


Figure 5.5 Graphic of Gustafson parallel coding pattern. f_s is the fraction of a program, in time, spent on serial computation. f_p is the fraction of computing time that is parallelizable. T_p is the total time for a parallel program to run. T_1 is the total time for a parallel program to run if only 1 processor is allocated. P_N is the N -th processor where its row is the computation the processor performs. The Gustafson pattern is most similar to what is implemented for this analysis. Figure is pulled from [82].

1631 We need a way to measure and compare the expected speedup and efficiency gain for this
 1632 asynchronous coding pattern. I pull inspiration for timing measurement from [82] and use *Amdahl's*

1633 law with hybrid programming. Hybrid programming meaning that the computation is a mix of
1634 distributed and shared memory programming. If we assume the code is fully parallelizable over p
1635 processors and c threads, the ideal speedup is simply pc , and ideal run-time is $T_1/(pc)$. T_1 is the
1636 total time for a parallel program to run if only 1 processor is allocated. However, the coding pattern
1637 contains some amount of unavoidable serial computation, as shown in Figure 5.5. In our case, the
1638 run time, $T_{p,c}$, is estimated to be

$$T_{p,c} = \frac{T_1}{pc} (1 + F_s(c - 1)). \quad (5.3)$$

1639 F_s is the fraction of CPU time dedicated to serial computation. The expected speedup, $S_{p,c}$, is

$$S_{p,c} \equiv \frac{T_1}{T_{p,c}} = \frac{pc}{1 + F_s(c - 1)}. \quad (5.4)$$

1640 From Equation (5.4), we can see that the speed-up scales with p/F_s . We are free to minimize F_s
1641 asymptotically by enlarging the total models that are submitted to the thread pool, thereby shrinking
1642 the CPU fraction dedicated to serial operation. We are also free to define exactly how many threads
1643 and processors we utilize, yet eventually hit a hard cap at the hardware available on our computing
1644 cluster. HAWC uses Intel Xeon™processors with 48 cores and 96 threads. We see that a successful
1645 code will scale well as the expected speedup is inversely correlated with F_s . As the total number
1646 of models sampled grows, the speedup will also.

1647 5.5.2 Implementation

1648 The multithreaded code was written in Python3 and is documented in the `dark_matter_hawc`
1649 [repository](#) within the script named `mpu_analysis.py`. A version of the script as of April 25
1650 **TODO: make sure to update on this date** is also provided in Section B.2. It has many dependencies
1651 including the HAWC analysis software. Figure 5.6 displays the workflow of a job with 3 threads.
1652 Within a job, SOURCE is kept fixed and CHANS remains 17 elements long. More m_χ are sampled
1653 from 11 bins up to 49 (for $\gamma\gamma$ and ZZ) and 25 (for remaining CHANS) which amounts to 12 or 6
1654 mass bins per decade. m_χ and CHANS are permuted into a 473 element list which is split evenly
1655 across N threads where N is [2, 8, 16]. For each m_χ -CHAN tuple, 1001 $\langle\sigma v\rangle$ values are sampled in

Timing summary for a multi-threaded job.

Import and Load HAL, 3ML, and HAWC analysis software ~ 2 min		
Load HAWC Data ~ 5 min		
Load HAWC PDF's (Detector Resolution files) ~ 4 min		
Load Spatial Model < 1s		
Load Spectra Models <1 s	Load Spectra Models <1 s	Load Spectra Models <1 s
Calculate max LLH (Chan_0, m_{χ_1}) ... max LLH (Chan_?, m_{χ_N}) N = TOTAL/N_THREADS ~ 8 min/Spec_model	Calculate max LLH (Chan_?, m_{χ_1}) ... max LLH (Chan_?, m_{χ_N}) N = TOTAL/N_THREADS ~ 8 min/Spec_model	Calculate max LLH (Chan_?, m_{χ_1}) ... max LLH (Chan_?, m_{χ_N}) N = TOTAL/N_THREADS ~ 8 min/Spec_model
Write results to file <1 s	Write results to file <1 s	Write results to file <1 s
Join Threads and terminate < 1s		

Figure 5.6 Task chart for one multithreaded job developed for this project. Green blocks indicate a shared resource across the threads AND computation performed serially. Red blocks indicate functional parallel processing within each thread. 3 threads are represented here, yet many more can be employed during the full analysis. Jobs are defined by the SOURCE as these require unique maps to be loaded into the likelihood estimator. The m_{χ} , CHAN, and $\langle \sigma v \rangle$ variables are entered into the thread pool and allocated as evenly as possible across the threads.

1656 the likelihood, and the value of $\langle \sigma v \rangle$ that maximizes the likelihood is found. Although rare, fits
 1657 that failed are handled on a case by case basis.

1658 5.5.3 Performance

M Tasks	$T_{p,c}$ (hr:min:s)			
	$T_{1,1}$	$T_{1,2}$	$T_{1,8}$	$T_{1,16}$
50	1:40:37.5	0:52:43.7	0:19:13.8	0:13:44.0
74	2:22:30.0	1:15:00.6	0:25:21.3	0:15:49.8
100	(3:07:51.9)	1:40:10.5	0:30:44.4	0:20:01.4
200	(6:02:20.6)	-	1:00:32.0	0:30:35.0
473	(13:58:40.3)	-	2:01:41.4	1:07:53.2

Table 5.2 Timing summaries for analyses for serial and multithreaded processes. M tasks is the number of functional-parallel tasks ran for the computation. $T_{p,c}$ is a single run time in hours:minutes:seconds for runs utilizing p nodes and c threads. Runs are run interactively on the same computer to maximize consistency. Empty entries are indicated with '-'. (·) entries are estimated entries extrapolated from data earlier in the column.

1659 We see a significant reduction to wall time needed for our dSph analyses to run. Table 5.2

1660 shows the timing summaries for analyses of different sizes and thread counts. Additionally, the
 1661 efficiency gained when consolidating the serial loading of data is also apparent in our ability to
 1662 study many more tasks in about the same amount of wall time as a smaller serial computation. Trials
 1663 represented in the table were run on an AMD Opteron® processor 6344 with 48 cores, 2 threads per
 1664 core; 2.6 GHz clock. This is not the same architecture used for analysis on the HAWC computing
 1665 cluster however they are similar enough that results shown here are reasonably representative of
 1666 computing on the HAWC computing cluster. I use Tab. 5.2 for the inferences and conclusions in
 1667 the following paragraphs.

1668 First, we want to find T_s , the time of serial computation. From Fig. 5.5, the timing for our
 1669 coding pattern can be written as

$$T_s + Mt_p = T_{1,1}^M. \quad (5.5)$$

1670 M is the number of functional-parallel tasks (represented as column 1 of Tab. 5.2), and t_p is the
 1671 average time to complete a single parallel task. $T_{1,1}^M$ is the total time for a parallel program to run if
 1672 only 1 processor is allocated for M parallel task. With two runs of different M (M_1 and M_2), we
 1673 can use a system of equations to compute

$$T_s = 803.1\text{s} \text{ and } t_p = 104.6\text{s} \quad (5.6)$$

1674 Now, we have specific estimation for the fraction of serial computing time, F_s :

$$F_s = \frac{803.1}{803.1 + 104.6 \cdot M}. \quad (5.7)$$

1675 The maximum M for this study is 473 which evaluates to: $F_s = 0.016$ or 1.6% of computing time.
 1676 Table 5.3 shows the resulting speedups.

1677 We see a speedup that generally exceeds expectations from Eq. (5.4) for real trail runs. We also
 1678 see that there are diminishing returns as the number of threads increases. For small jobs with large c ,
 1679 both the expected and observed speedup are significantly smaller than c . One thing not considered
 1680 in Eq. (5.4) is the time incurred via communication latency. Communication latency increases
 1681 with the number of threads and contributes to diminishing returns. Additionally, these values are

M Tasks	F_s	$S_{1,2}$	$S_{1,8}$	$S_{1,16}$
50	1.33 E-1	1.90 [1.76]	5.23 [4.14]	6.35 [5.34]
74	9.40 E-2	1.90 [1.83]	5.62 [4.82]	9.00 [6.64]
100	7.13 E-2	1.88 [1.87]	6.11 [5.34]	9.38 [7.73]
200	3.70 E-2	- [1.93]	5.98 [6.36]	11.85 [10.29]
473	1.60 E-2	- [1.97]	6.89 [7.20]	12.35 [12.91]

Table 5.3 Speed up summaries for analyses for serial and multithreaded processes. M tasks is the number of functional-parallel tasks ran for the computation. $S_{p,c}$ is a single speedup comparison for runs utilizing p nodes and c threads. [·] are the estimated speedups calculated from Tab. 5.2, Eq. (5.7), and Eq. (5.4). Empty entries are indicated with '-'.

for single runs and do not consider the stochastic variation expected in a shared high performance computing resource. Therefor, these results are not strictly conclusive, yet demonstrate the merits of multi-threading. We see very clearly that there is a lot to gain, and this new coding pattern will expand HAWC's analysis capabilities.

5.6 Analysis Results

3 of the 43 $\mathcal{L}\mathcal{S}$ dSphs considered for the multithreaded analysis. These dSph are analyzed for emission from DM annihilation according to the likelihood method described in Section 4.4. The three likelihood profiles are then stacked to synthesize a combined limit on the dark matter annihilation cross-section, $\langle\sigma v\rangle$. This combination is done each of the 17 SM annihilation channels. Figure 5.7 and Fig. 5.8 show the combined limits for all annihilation channels with HAWC's observations. Test statistics of the best fit $\langle\sigma v\rangle$ values for each m_χ and CHAN are shown in Fig. 5.9 and Fig. 5.10. We also compare these limits to HAWC's Glory Duck limits shown in Section 4.5. The comparison to Glory Duck are featured in Fig. 5.11 for all the DM annihilation channels studied for Glory Duck. A full comparison is provided in the appendix in Fig. B.2, Fig. B.3, and Fig. B.4. Here, we show updated limits for $\chi\chi \rightarrow b\bar{b}, e\bar{e}, \mu\bar{\mu}, \tau\bar{\tau}, t\bar{t}, W^+W^-$, $\gamma\gamma$ and ZZ . For the first time ever, we show limits for $\chi\chi \rightarrow c\bar{c}, s\bar{s}, u\bar{u}, d\bar{d}, \nu_e\bar{\nu}_e, \nu_\mu\bar{\nu}_\mu, \nu_\tau\bar{\nu}_\tau, gg$, and hh .

No DM was found in HAWC observations. The largest excess found in HAWC data was for DM annihilating to W -bosons or $\nu_e\bar{\nu}_e$ for $m_\chi = 10$ TeV at significance 2.11σ and 2.14σ respectively. HAWC's limits and excesses are dominated by Segue1. Coma Berenices shows excesses at higher DM mass, yet no similar excesses were observed in Segue1 or Sextans. Sextans did not contribute

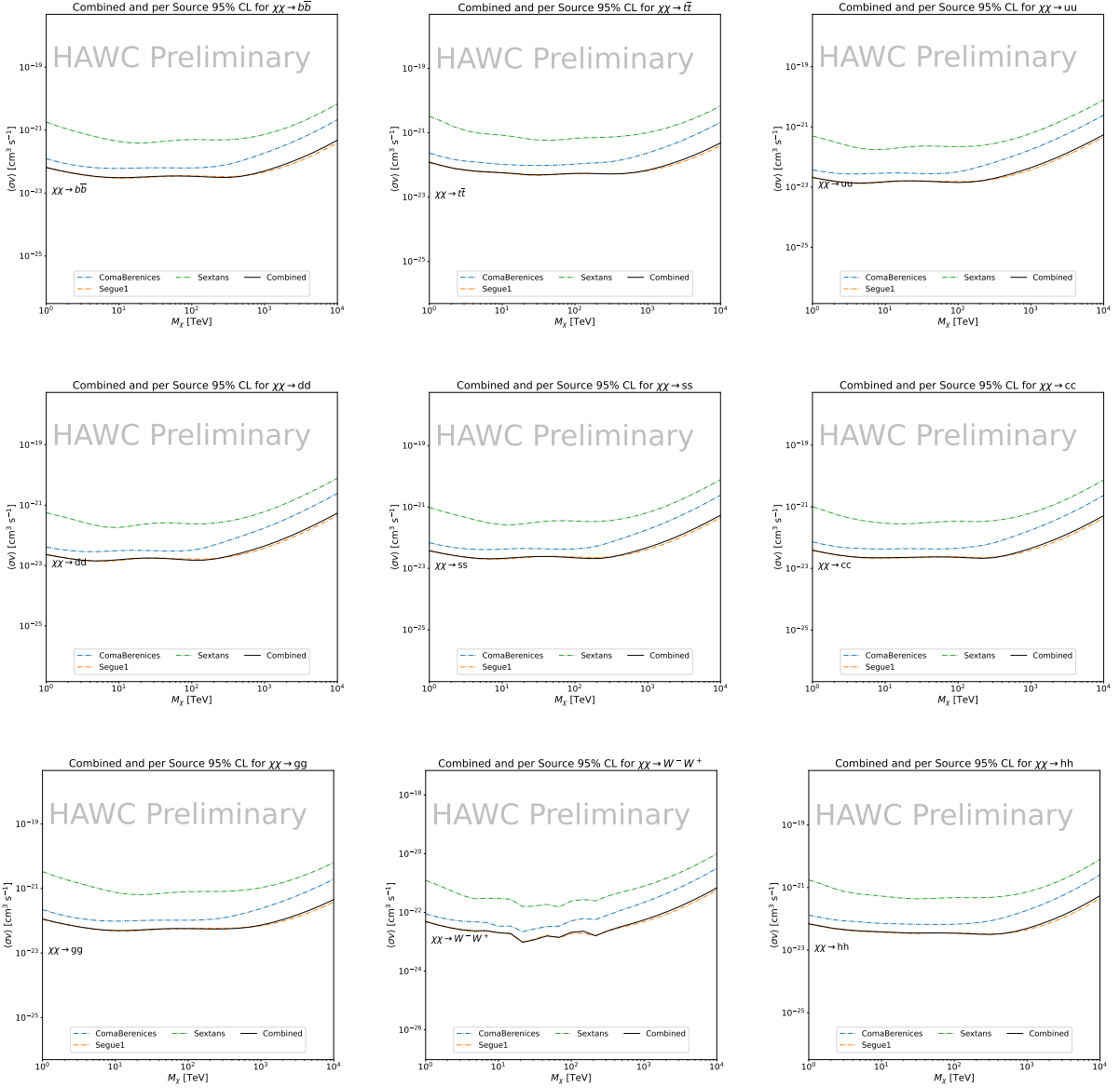


Figure 5.7 HAWC upper limits at 95% confidence level on $\langle\sigma v\rangle$ versus m_χ for $\chi\chi \rightarrow b\bar{b}$, $t\bar{t}$, $u\bar{u}$, $d\bar{d}$, $s\bar{s}$, $c\bar{c}$, gg , W^+W^- , and hh . Limits are with $\mathcal{L}\mathcal{S}$ J -factors [80]. The solid line represents the observed combined limit. Dashed lines represent limits from individual dSphs.

1702 significantly to signal excesses or the combined limit as it is at high zenith. Draco was not included
 1703 as the PDF of some of our analysis bins were wider than what is reasonable for a point source
 1704 analysis. Draco is at a high zenith for HAWC, so the effort required to include it was not justified
 1705 by the benefits.

1706 We did not generate background trials in time of writing this thesis. These are not shown and

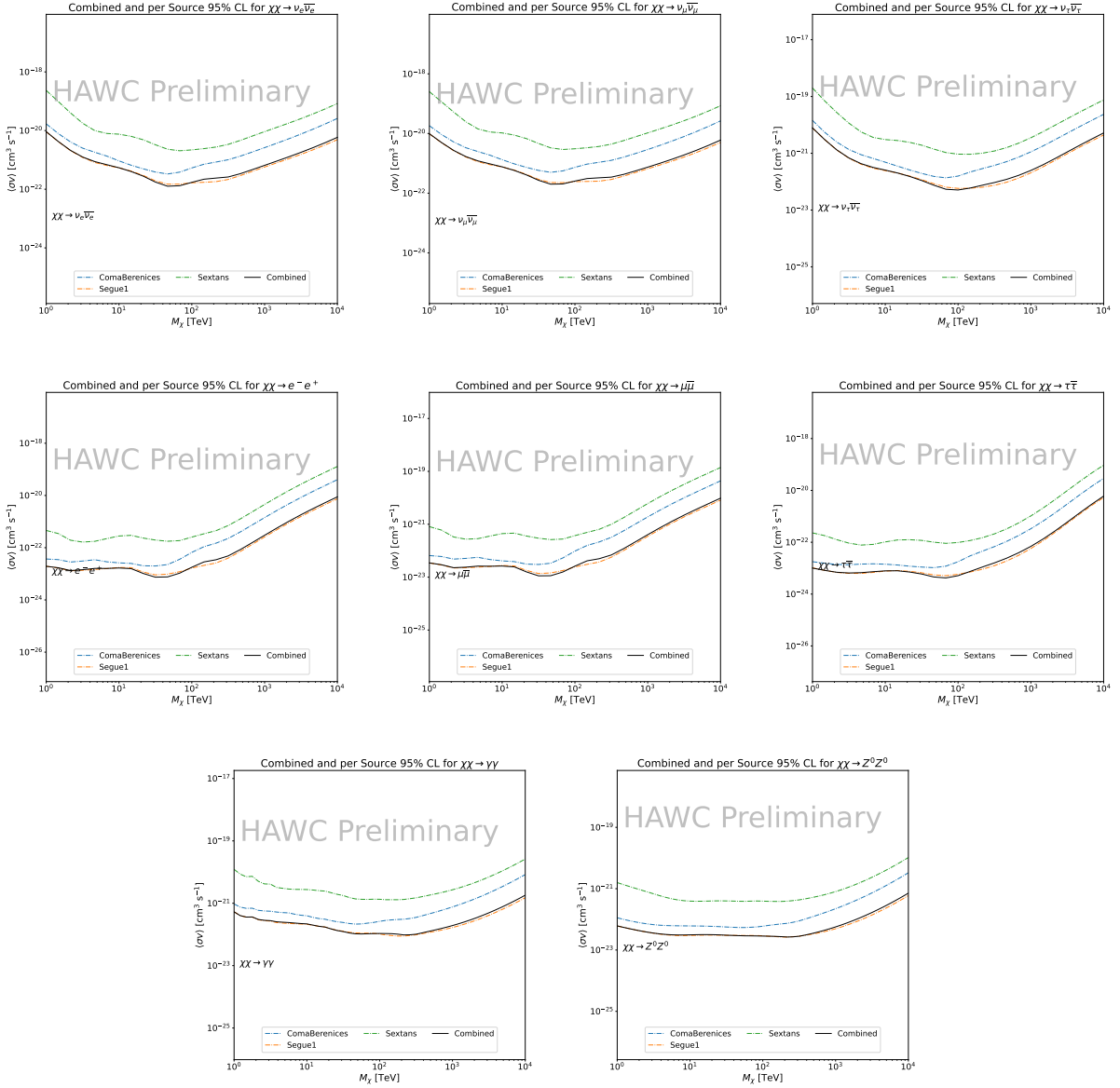


Figure 5.8 HAWC upper limits at 95% confidence level on $\langle\sigma v\rangle$ versus m_χ for $\chi\chi \rightarrow \nu_e \bar{\nu}_e$, $\nu_\mu \bar{\nu}_\mu$, $\nu_\tau \bar{\nu}_\tau$, $e \bar{e}$, $\mu \bar{\mu}$, $\tau \bar{\tau}$, $\gamma\gamma$ and ZZ . Limits use $\mathcal{L}S$ J -factors [80]. The solid line represents the observed combined limit. Dashed lines represent limits from individual dSphs.

1707 are an immediate next step for this analysis before publication.

1708 When comparing these results to Section 4.5, we see an overall decrease to the confidence limit
 1709 therefore improvement to HAWC's expected sensitivity. This improvement is generally stronger
 1710 than a doubling of data, or a factor $\sqrt{2}$ decrease. The comparison is somewhat complex and
 1711 dependent on the dSph and SM annihilation channel. Figure 5.11 shows the comparisons of limits

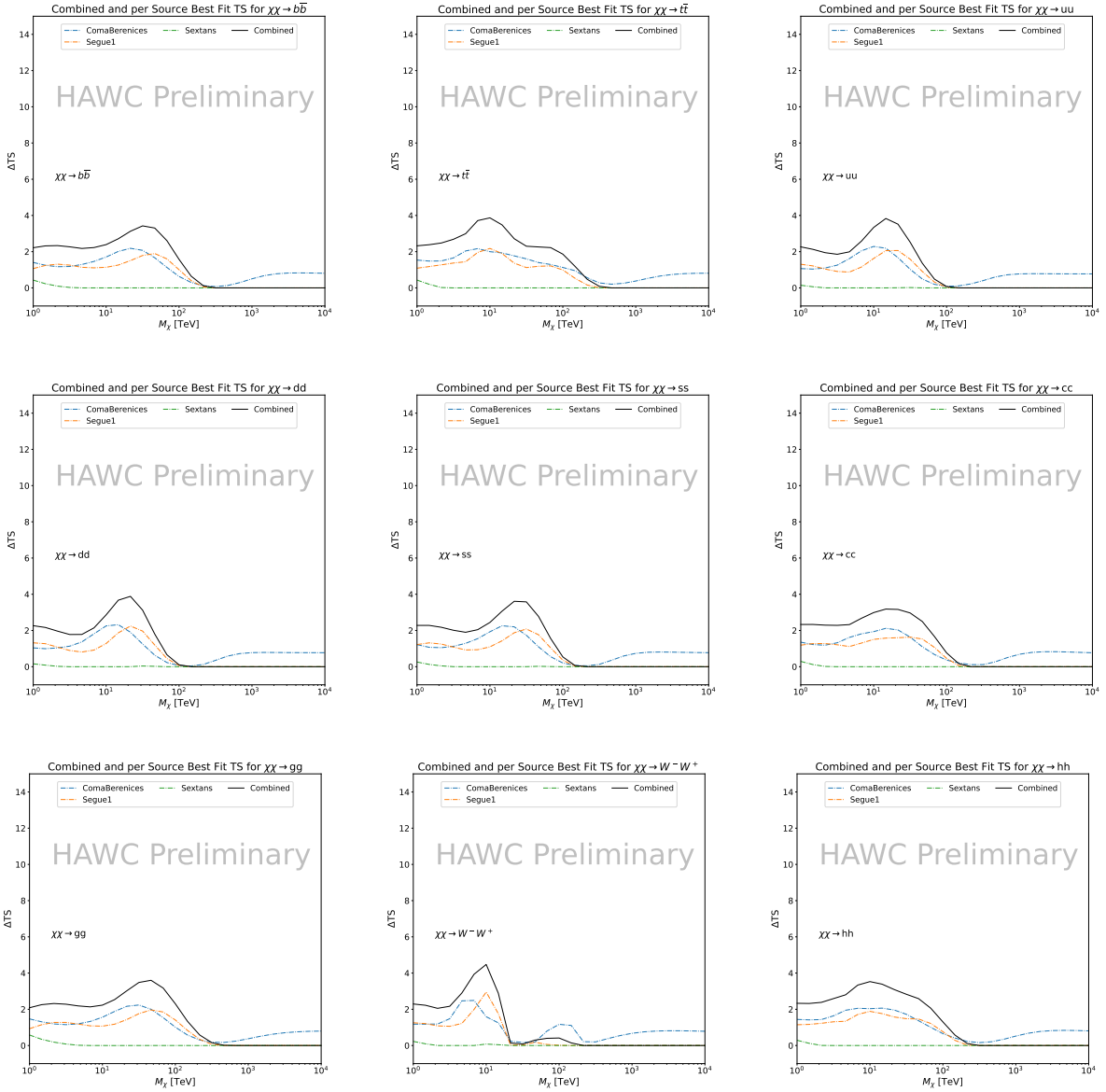


Figure 5.9 HAWC TS values for best fit $\langle\sigma v\rangle$ versus m_χ for SM annihilation channels: $\chi\chi \rightarrow b\bar{b}$, $t\bar{t}$, $u\bar{u}$, $d\bar{d}$, $s\bar{s}$, $c\bar{c}$, gg , W^-W^+ , and hh . Limits use \mathcal{LS} J -factors. The solid black line shows the combined best fit TS values. The colored, dashed lines are the TS values from each dSph.

1712 calculated for this analysis and Glory Duck (Section 4.5). Segue 1 and Coma Berenices are low
 1713 zenith where improvements to HAWC's analysis come only from energy estimation. Differences
 1714 between these two are dominantly from their differences in J -factor, half-light radii of the dSphs,
 1715 and the particle physics inputs. Substantial gains in HAWC's analysis methods (pass 5.F) were
 1716 made at high zenith which is important for sources like Sextans. The HDM particle physics model

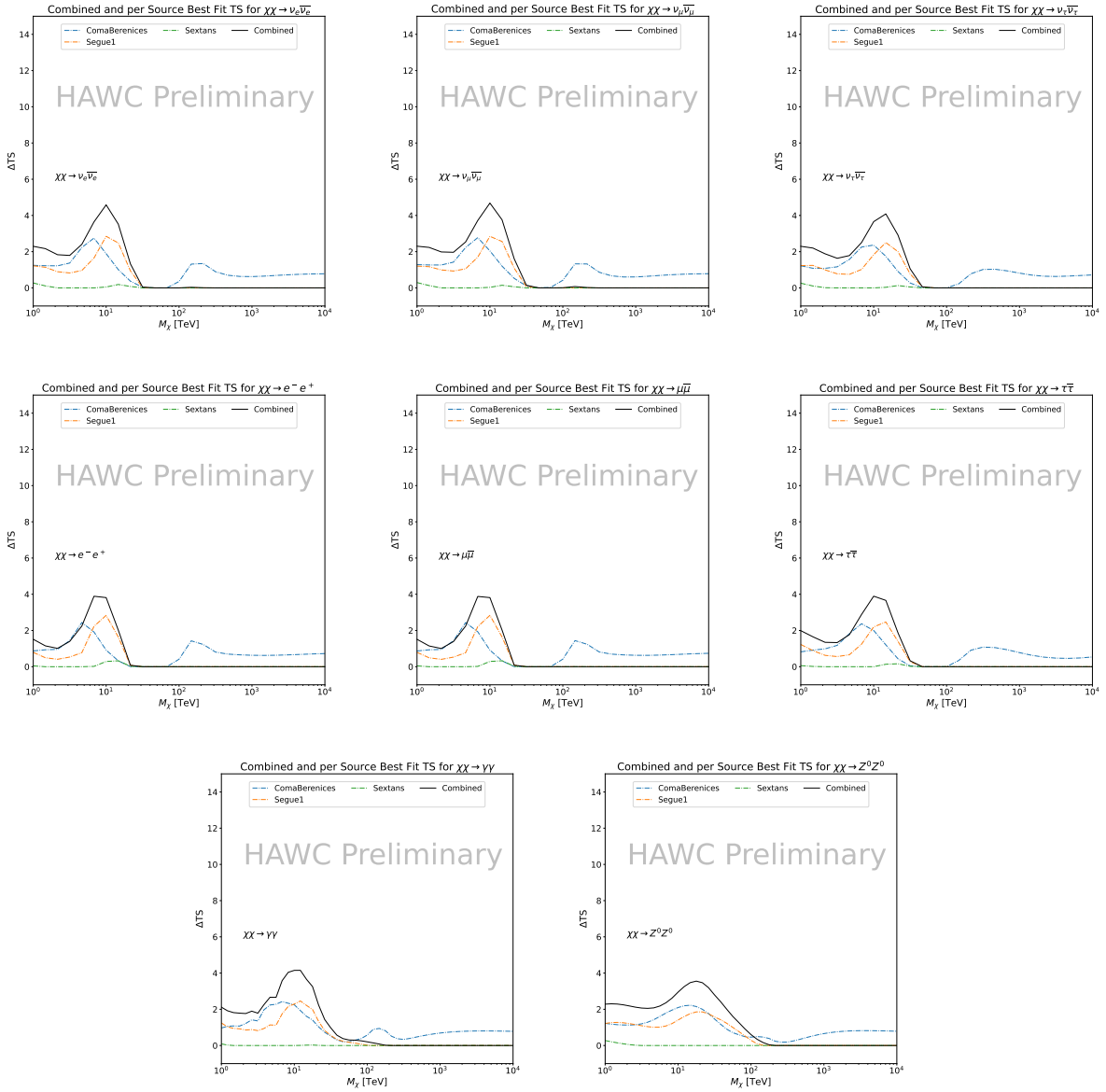


Figure 5.10 HAWC TS values for best fit $\langle\sigma v\rangle$ versus m_χ for SM annihilation channels: $\chi\chi \rightarrow \nu_e \bar{\nu}_e$, $\nu_\mu \bar{\nu}_\mu$, $\nu_\tau \bar{\nu}_\tau$, $e^- e^+$, $\mu \bar{\mu}$, $\tau \bar{\tau}$, $\gamma\gamma$ and ZZ . Limits use \mathcal{LS} J -factors. The solid black line shows the combined best fit TS values. The colored, dashed lines are the TS values from each dSph.

1717 produces almost identical spectra to the PPPC for $\chi\chi \rightarrow e^- e^+$. This channel can be used to
 1718 compare limits between dSph spatial models. Overhead sources see minimal improvement to the
 1719 limits, while high zenith sources see an order of magnitude improvement for all DM masses. Softer
 1720 SM annihilation channels see broad improvements to the limit compared to harder channels.

1721 **5.7 Systematics**

1722 Systematics to this analysis are identical to what was performed earlier in Glory Duck, Sec-
1723 tion 4.7. We are also sensitive to the choice in spatial template, and this was explored in Section 4.7.2
1724 and Section 4.8.2.

1725 **5.8 Conclusion and Discussion**

1726 In this multithreaded analysis, we have used observations of 3 dSphs from HAWC to perform
1727 a collective DM annihilation search towards dSphs. The data were combined across sources
1728 to significantly increase the sensitivity of the search. Advanced computational techniques were
1729 deployed to accelerate wall-time spent analyzing by an order of magnitude. We have observed
1730 no significant deviation from the null, no DM hypothesis, and so present our results in terms of
1731 upper limits on the velocity-weighted cross-section, $\langle\sigma v\rangle$, for seventeen potential DM annihilation
1732 channels across four decades of DM mass.

1733 This analysis serves as a proof of concept for multithreaded HAWC analyses with large parameter
1734 spaces. Larger datasets with fast techniques will be essential to tackling the DM problem. The
1735 models we used for this study include annihilation channels with neutrinos in the final state.
1736 Advanced studies could aim to merge our results with those from neutrino observatories with large
1737 data sets.

1738 A full HAWC analysis will include systematic studies of the J -factor distributions. Additionally,
1739 because of the timing reduction, the study can be doubled in size to include DM decay. We have not
1740 yet received the remaining spatial profiles to the \mathcal{LS} catalog, and limits can be quickly computed
1741 once these are received. Finally, statistical studies with Poisson variation of HAWC's background
1742 are essential to a comprehensive understanding of our observed excesses.

Segue1

Coma Berenices

Sextans

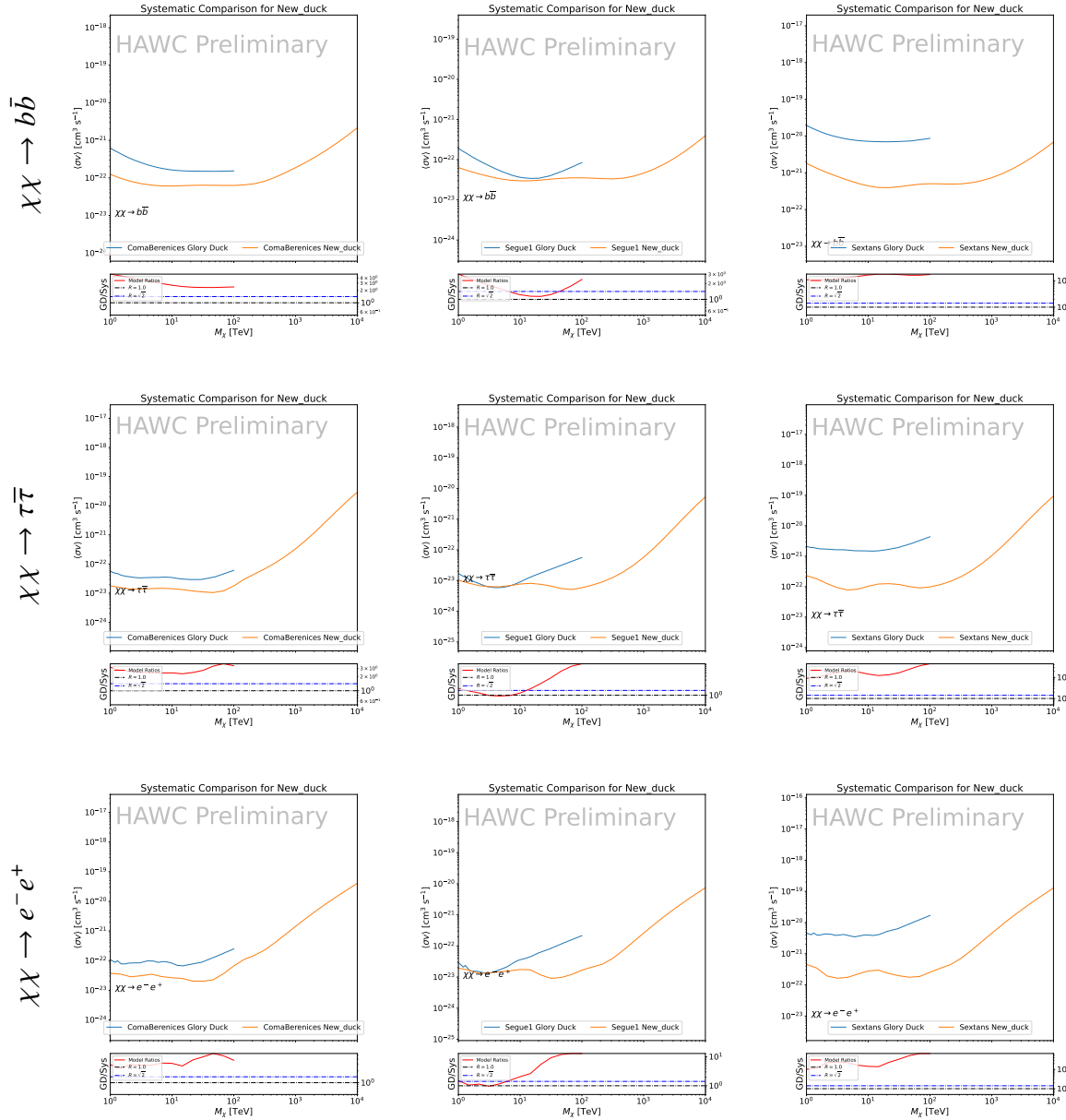


Figure 5.11 Comparison of HAWC limits from this analysis to Glory Duck (Fig. 4.5) for 3 dSphs and 3 DM annihilation channels: $b\bar{b}$, $\tau\bar{\tau}$, and $e\bar{e}$. Each sector shows the 95% confidence limit from Glory Duck (blue line) and this analysis (orange line) in the top plot. The lower plot features the ratio in log scale of Glory Duck to this analysis in a red solid line. Horizontal dashed lines are for ratios of 1.0 (black) and $\sqrt{2}$ (blue). Ratios larger than 1.0 are for limits smaller, or stricter, than Glory Duck. Ratios larger than $\sqrt{2}$ indicates limits are stricter than a simple doubling of the Glory Duck data.

CHAPTER 6

ICECUBE NEUTRINO OBSERVATORY



Figure 6.1 TODO: IceCube[NEEDS A SOURCE][FACT CHECK THIS]

1744 Located at the South Pole, the IceCube Neutrino Observatory is a pivotal instrument for
1745 neutrino astronomy. IceCube's primary function is the detection and analysis of elusive, high-
1746 energy neutrinos. These neutrinos carry information from the most energetic and distant cosmic
1747 phenomena. The observatory uses thousands of digital optical modules embedded in a cubic
1748 kilometer of Antarctic ice to detect Cherenkov radiation. This radiation occurs when neutrinos
1749 interact with the ice, revealing their origin and energy.

1750 IceCube is a critical component in the multi-messenger astrophysics toolkit, especially in the
1751 search for dark matter and beyond standard model (BSM) astrophysical processes. The observa-
1752 tory's analysis of neutrino signals enhances our understanding of the universe by correlating these
1753 signals with other cosmic messengers, including electromagnetic, gravitational waves, and cosmic

1754 rays.

1755 The following sections will discuss the observatory's design, data acquisition, event recon-
1756 struction methodologies, and its significance in observing the Northern Sky. These details will
1757 underscore IceCube's role in advancing our understanding of the cosmos through data-driven
1758 insights.

1759 **6.1 The Detector**

1760 The IceCube Neutrino Observatory is embedded within a cubic kilometer of Antarctic ice at
1761 the South Pole. IceCube's modules are designed to detect neutrinos through Cherenkov radiation
1762 emitted during neutrino interactions with the ice. It comprises 5160 Digital Optical Modules
1763 (DOMs), arranged across 86 strings that span depths of 1450 m to 2450 m beneath the surface. This
1764 arrangement allows IceCube to capture high-energy neutrinos across a broad neutrino spectrum.

1765 **6.1.1 Hardware and Construction**



Figure 6.2 TODO: DOM photo[NEEDS A SOURCE][FACT CHECK THIS]

1766 Digital Optical Modules (DOMs) are at the core of IceCube's detection technology, each encased
1767 in a glass sphere to withstand deep-ice pressures. A DOM features a 10-inch photomultiplier tube
1768 (PMT) for Cherenkov light detection, a high-voltage power supply for the PMT, and a Main
1769 Board for signal digitization and timestamping. An LED Flasher Board is included for calibration
1770 purposes, assisting in verifying DOM responses and measuring ice optical properties. The DOMs
1771 are deployed along cables on strings in a hexagonal grid pattern, which spans a cubic kilometer.
1772 Strings are placed with 125 meters of horizontal spacing, and DOMs are vertically separated
1773 by 17 meters on each string, chosen to optimize detection capability for neutrinos within the
1774 teraelectronvolt (TeV) to petaelectronvolt (PeV) energy range.

1775 DeepCore and IceTop, additional components of IceCube, extend its research capabilities.
1776 DeepCore, with its denser array of DOMs, targets lower energy neutrinos for studies such as
1777 neutrino oscillations and dark matter. IceTop, situated at the ice surface, measures cosmic rays,
1778 contributing data that complement the neutrino observations from below the ice.



Figure 6.3 TODO: ICL[NEEDS A SOURCE][FACT CHECK THIS]

1779 The central hub for IceCube's operations is the IceCube Laboratory (ICL), situated at the
1780 surface at the center of the array. This facility houses the servers and computers responsible for
1781 data acquisition and online filtering, connected to the DOMs via cables routed up from beneath the
1782 ice [83]. The ICL plays a crucial role in managing the data flow from the ice, ensuring continuous
1783 operation and data integrity. It is designed to maintain optimal conditions for its electronic
1784 equipment, including temperature control and protection against electromagnetic interference,
1785 which is vital for the accurate processing and analysis of the collected data [83].

1786 **6.1.2 Data Acquisition**

1787 **6.2 Track Event Reconstruction**

1788 **6.2.1 Angle**

1789 **6.2.2 Energy**

1790 **6.3 Background**

1791 **6.4 North Sky Tracks**

CHAPTER 7

HEAVY DARK MATTER ANNIHILATION SEARCH WITH ICECUBE'S NORTH SKY TRACK DATA

7.1 Introduction

Neutrinos are another astrophysical messenger than can travel long distances without significant attenuation or deflection. Additionally, Neutrinos come in three flavors which triples the multiplicity of the particles we are searching for. Uniquely, they interact less readily than photons especially above PeV energies. Neutrinos therefore provide another window through which we can perform dark matter searches.

The previous IceCube DM annihilation analysis towards dwarf galaxies was performed in 2013 [84] which, in technical terms, is more than a minute ago. This is in spite of IceCube's crucial sensitivity afforded from neutrino spectral lines [85]. A lot has changed in IceCube since its previous DM annihilation search such as, additional strings, more sophisticated analysis methods, and more accurate theory modeling. It has come time for IceCube to make a DM dSph contribution.

IceCube is sensitive to annihilating DM for DM masses above 1 TeV. Additionally, IceCube's sensitivity is comparable gamma-ray observatories in spectral models that produce hard neutrino features. The goal of this analysis is to perform a DM annihilation search using the Northern Sky Tracks datasets. The search will only be towards dwarf spheroidal galaxies (dSph) for the strengths mentioned in Section 4.3.3. These sources are treated as point sources for IceCube with little loss to sensitivity or model dependence on how the DM is distributed. DM masses from 500 GeV to 100 PeV are considered for this analysis. Several DM annihilation channels available from the HDMspectra [79] are studied in this analysis. This chapter presents the analysis work for IceCube to update our DM searches toward dSphs.

7.2 Dataset and Background

This section enumerates the data and background methods used for IceCube's study of dSphs. Section 7.2.1 and Section 7.2.2 are most useful for fellow IceCube collaborators looking to replicate this analysis.

1818 **7.2.1 Itemized IceCube files**

1819 These files are only available within IceCube’s internal documentation and wikis. They are not
1820 meant for public access, and are presented here so that IceCube collaborators can reproduce results
1821 accurately.

1822 • Software Environment: CVMFS Py3-v4.1.1

1823 • Data Sample: Northern Tracks NY86v5p1

1824 • Analysis Software: csky ([nu_dark_matter](#))

1825 • Analysis wiki: https://wiki.icecube.wisc.edu/index.php/Dark_Matter_Annihilation_Search_towards_dwarf_spheroidals_with_NST_and_DNN_Cascades

1827 • Project repository

1828 **7.2.2 Software Tools and Development**

1829 This analysis was performed inside IceCube’s CVMFS (3.4.1.1) software environment using
1830 csky for likelihood calculations. Csky at first did not come with dark matter spectral models nor
1831 could accommodate custom flux models. We developed these capacities for single source and
1832 stacked source studies for this analysis. The analysis code is held in a separate repository from
1833 csky. The [nu_dark_matter branch of csky](#) manages the input of custom dark matter spectra and
1834 accompanied DM astrophysical source. Csky also enables the use of multithreading which was
1835 shown to be crucial for DM searches (see Sec. 5). Csky then calculates likelihoods with a selected
1836 data sample. The [IceCube Dark Matter dSph repository](#) manages the generation of spectral models
1837 for neutrinos, physics parameter extraction from n_{sig} , J -factor per source inputs, and bookkeeping
1838 for the large parameter space. The project repository required a secondary software environment
1839 for neutrino oscillations. How to launch and run those calculations are documented in the project
1840 repository and the Docker image is additionally saved in Section C.1.

1841 **7.2.3 Data Set and Background Description**

1842 For this analysis, I use the Northern Sky Tracks (NST) Sample (Version V005-P01). The sample
1843 contains up-going track-like events, usually from ν_μ and ν_τ , with a superior angular resolution
1844 compared to the cascade dataset. This sample covers 10.4 years of data (IC86_2011-2021). The
1845 accepted neutrino energy range used for the analysis is unique from most other IceCube searches
1846 because DM spectra are hard with large contributions close to $E_\nu = m_\chi$. Therefore, the sampled
1847 energy range is $1 < \log(E_\nu/\text{GeV}) < 9.51$ with step size 0.125.

1848 The strengths of a dwarf analysis is that there are no additional background considerations
1849 beyond nominal, baseline background estimations (see Section 4.2.3). For NST, the nominal
1850 contributions come from atmospheric neutrinos and isotropic astrophysical neutrinos. We estimate
1851 the background by scrambling NST data along Right Ascension.

1852 **7.3 Analysis**

1853 The expected differential neutrino flux from DM-DM annihilation to standard model particles,
1854 $d\Phi_\nu/dE_\nu$, over solid angle, Ω is described by the familiar equation.

$$\frac{d\Phi_\nu}{dE_\nu} = \frac{\langle\sigma\nu\rangle}{8\pi m_\chi^2} \frac{dN_\nu}{dE_\nu} \times \int_{\text{source}} d\Omega \int_{l.o.s} \rho_\chi^2 dl(r, \theta') \quad (7.1)$$

1855 This is identical to Eq. (4.1) except that there are 3 neutrino flavors, so there are a corresponding
1856 3 flux equations. Section 4.3 has a complete description of each term in Eq. (7.1). Additionally,
1857 neutrinos oscillate between flavors which needs to be considered for the expected neutrino flux
1858 at Earth. Section 7.3.1 presents the particle physics model and processing for DM annihilation.
1859 Section 7.3.2 presents the spatial distributions built for each dSph.

1860 **7.3.1 $\frac{dN_\nu}{dE_\nu}$ - Particle Physics Component**

1861 Neutrino spectra from heavy DM annihilation were generated using HDMspectra [79] and
1862 χ arov [86]. HDMspectra has tables for the decay and annihilation of heavy DM for different
1863 dark DM and SM primary annihilation channels. The simulation includes electroweak or gluon
1864 radiative corrections and higher order loop corrections from the W and Z bosons (WWZ and $WW\gamma$).
1865 These corrections are especially important for accurately estimating the prompt neutrino flux. This

1866 publication also pushes the simulated DM mass to the Plank scale (1 EeV), however this study will
1867 not explore that high.

1868 An important feature in the spectra is that neutrino line channels will be accompanied by a low
1869 energy tail [79], see Fig. 7.1. Thus, the Earth will not fully attenuate a heavy neutrino line-like
1870 signal from high declination sources where the neutrino flux must first traverse through the Earth.
1871 The DM annihilation channels that feature lines include all leptonic channels: $\nu_{e,\mu,\tau}$, e , μ , and τ . We
1872 use the `xarov` software to propagate and oscillate the neutrinos from the source to Earth. Because
1873 these sources are quite large in absolute terms, and also far (order 10 kpc or more), the resulting
1874 flavor spectra are the averages of the transition probabilities [86]:

$$P(\nu_\alpha \rightarrow \nu_\beta) \approx \begin{bmatrix} 0.55 & 0.18 & 0.27 \\ 0.18 & 0.44 & 0.38 \\ 0.27 & 0.38 & 0.35 \end{bmatrix} \quad (7.2)$$

1875 Examples of the spectra before and after propagation are shown in Fig. 7.1.

1876 When calculating the expected contribution to n_s , only ν_μ and ν_τ are considered as NST's
1877 effective area to ν_e is negligible [87]. Therefore, the expected composite neutrino spectrum is the
1878 sum of the two flavors: $\frac{dN\nu_\mu}{dE\nu_\mu} + \frac{dN\nu_\tau}{dE\nu_\tau}$. The spectral tables are then converted to splines to condense
1879 information, enable random sampling of the spectra, and reduce computing times. The spectral
1880 splines are finally implemented as a DM class in csky.

1881 7.3.1.1 Treatment of Neutrino Line Features

1882 All DM annihilation channels into leptons $\chi\chi \rightarrow [\nu_{e,\mu,\tau}, e, \mu, \tau]$ develop a prominent and
1883 narrow spectral line feature. For all neutrino flavors, this line is visible and prominent in all m_χ
1884 studied in this analysis. For charged leptons, the feature typically manifests at $m_{ch} > 10$ TeV, yet
1885 its prominence varies slightly between the flavors. Examples for lines in the annihilation spectra
1886 with neutrinos or charged leptons are provided in Fig. 7.1.

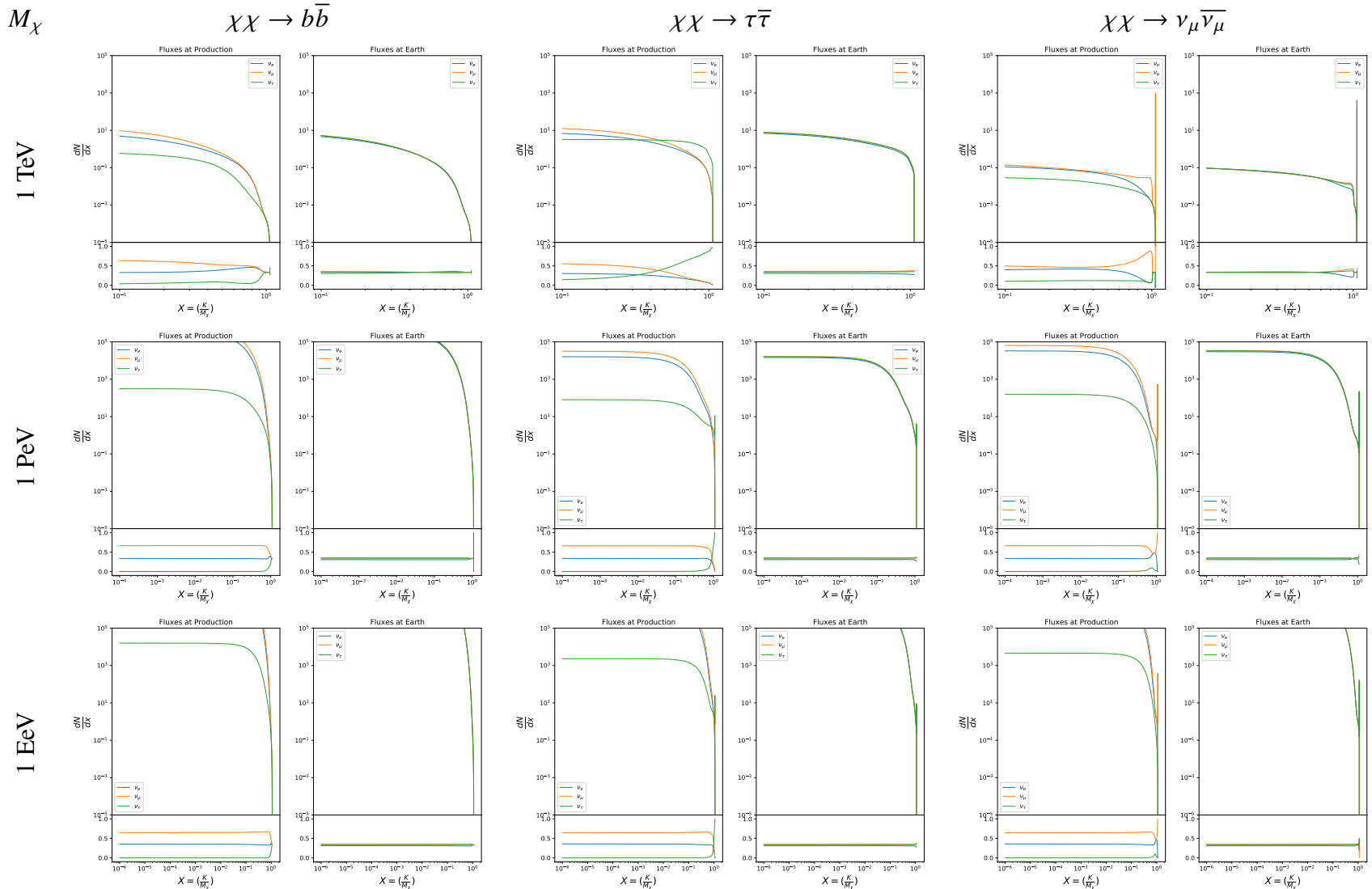


Figure 7.1 Neutrino spectra at production (left panels) and after oscillation at Earth (right panels). Blue, orange, and green lines are the ν_e , ν_μ , and ν_τ spectra respectively. Top panels show the spectra in $\frac{dN}{dE}$. Lower panels plot the flavor ratio to $\nu_e + \nu_\mu + \nu_\tau$. SM annihilation channels $b\bar{b}$, $\tau\bar{\tau}$, and $\nu_\mu\bar{\nu}_\mu$ are shown for $M_\chi = 1 \text{ PeV}$, TeV , and EeV .

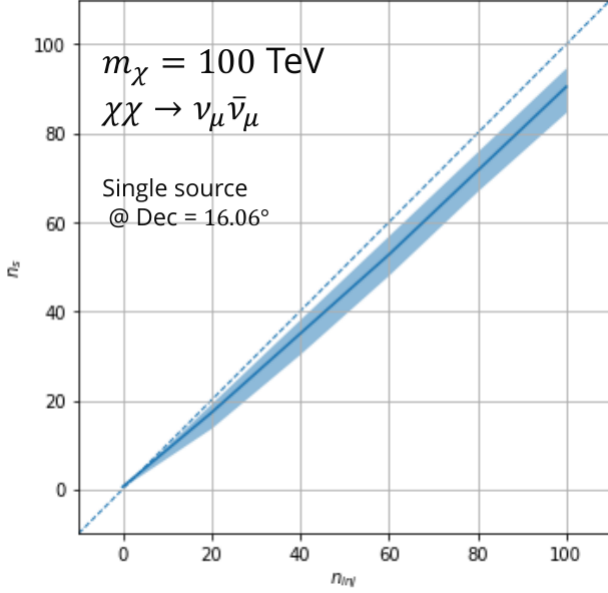


Figure 7.2 Signal recovery for 100 TeV DM annihilation into $\nu_\mu \bar{\nu}_\mu$ for a source at Dec = 16.06°. n_{inj} is the number of injected signal events in simulation. n_s is the number of reconstructed signal events from the simulation data. Although the uncertainties are small and tight, the reconstructed n_s are systematically underestimated.

1887 The neutrino line feature is so narrow relative the sampled energy range that the random
 1888 sampling of the spectra and likelihood fitting rarely capture the line in computation. As a result,
 1889 often the best fit to simulation of background will always floor to TS = 0 and the signal recovery
 1890 systematically underestimates the signal (see Fig. 7.2).

1891 To remedy this, we take a similar approach to the IceCube’s decay analysis [88] and the previous
 1892 gamma-ray study in Section 5.3.1. Two smoothing kernels were tested (Gaussian and uniform)
 1893 to widen the line feature. The widths were tuned such that the signal recovery approached unity
 1894 for DM mass 100 TeV to 1 PeV for a source at Segue 1’s declination, 16.06°. Near horizon
 1895 was chosen in order to isolate loss in signal recovery away from Earth’s attenuation of very high
 1896 energy neutrinos and atmospheric backgrounds. The kernel convolution needed closely preserve
 1897 the integrated counts of neutrinos. The optimized kernel parameters for all lines are summarized
 1898 as:

- 1899 • Gaussian kernel with 1σ width = $1.75E-3 \cdot m_\chi$
 1900 • Minimum energy included in convolution = $\text{MIN}[0.995 \cdot m_\chi, E(\nu_{\text{line}}) - 4\sigma]$

- 1901 • Maximum energy included in convolution = $\text{MAX}[1.005 \cdot m_\chi, E(\nu_{\text{line}}) + 4\sigma]$

1902 where $E(\nu_{\text{line}})$ is the neutrino energy where the neutrino line is at the maximum.

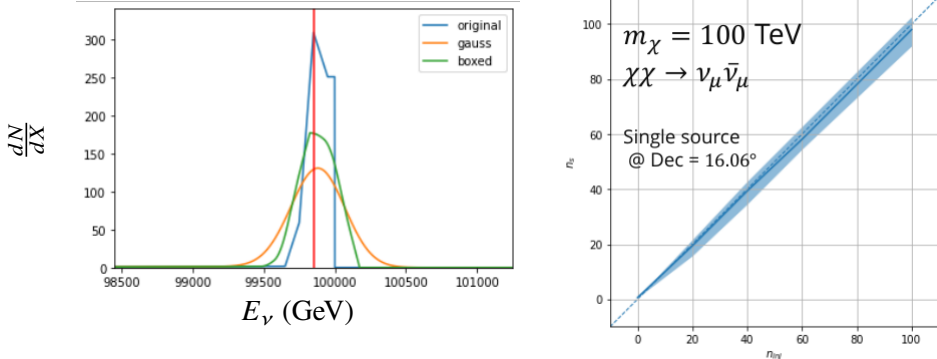


Figure 7.3 Left panel shows the two kernels overlaying the original spectrum from $\chi\text{aron}\nu$ after propagation to Earth [86]. The vertical red line indicates where the original neutrino line is maximized. Blue line is the output from $\chi\text{aron}\nu$. Green line is the spectrum after convolution with a flat kernel. Orange line is the spectrum after Gaussian convolution. Right panel shows the signal recovery of the spectral model using the Gaussian kernel with parameters enumerated above.

1903 These parameters broadly improved the signal recovery of the line spectra. An example is in
1904 Fig. 7.3. Analysis level signal recovery studies are expanded upon in Section 7.6.

1905 7.3.1.2 Spline Fitting

1906 In an effort to reduce computational work, memory burden, and align with point source methods
1907 used for NGC1068 [89], spectral splines were created and adopted for estimating the neutrino flux
1908 for the different spectral models. Software was written to generate, book keep, and calculate values
1909 on the splines.

1910 When using splines, one has to be careful of the goodness to fit. The spline software used
1911 here, Photospline [90], uses the penalized spline technique [91]. Through the penalized technique,
1912 poor fits are penalized according to the accuracy of the nominal value, and the smoothness of the
1913 first and second derivatives. However, this construction does not penalize on the integral of the
1914 fit distribution which is critical in low signal studies, such as DM searches. There are additional
1915 caveats when testing the goodness to fit to the MC generated above for all DM annihilation channels.

- 1916 • The splines must be Log10(*) in Energy and dN/dX to account for the exponential nature of
 1917 the flux.
- 1918 • The fidelity of the fit matters more at $E_\nu \approx m_\chi$ where the model uncertainties are minimal
 1919 and physical considerations (like the cut-off) are most important.
- 1920 • The fidelity of the fit matters less at low E_ν as the model uncertainties are large AND
 1921 IceCube's sensitivity diminishes significantly below 500 GeV.
- 1922 • Total integrated counts should be well-preserved.

1923 The resulting cost function was built to evaluate the goodness of spline fits to account for the above
 1924 considerations.

$$e_i = x_i \cdot \left(\frac{dN_i}{dX_i} - 10^{\hat{e}_i} \right) \quad (7.3)$$

1925 Where \hat{e}_i is the spline estimator's value for x_i . $x_i = E_{\nu_i}/m_\chi$. $\frac{dN_i}{dX_i}$ is the flux value from MC. I then
 1926 take the RMS of the error distribution and the resulting value, err, is used to evaluate the fidelity of
 1927 the spectral spline.

$$\text{err} = \sqrt{\frac{1}{x_{\max} - x_{\min}} \int_{x_{\min}}^{x_{\max}} e^2 dx} \quad (7.4)$$

1928 x_{\min} and x_{\max} are the scope of the error evaluation and are provided in Tab. 7.1.

1929 Each SM channel had unique tolerances for 'err'. Channels with very hard cut-offs had looser
 1930 tolerance for err because a significant error would be generated from single counts over/underes-
 1931 timated at the cut-off. Soft channels do not share this issue, so the tolerance is much stricter. All
 1932 annihilation channels from HDM are modeled well below IceCube's NST sensitivity which falls
 1933 off substantially below 100 GeV [87]. We do not think it is necessary to evaluate the spline fits
 1934 below 100 GeV and use this value as the default lower cut-off. Yet, HDM's model uncertainties
 1935 at $E_\nu < 10^{-6} \cdot m_\chi$ span an order of magnitude [79]. We also choose not to evaluate the splines
 1936 below this critical value if it is within IceCube's sensitivity. Finally, the smoothing of the spectral
 1937 lines in leptonic annihilation channels are ignored for evaluating the fit. We used the lower limit of

$\chi\chi \rightarrow$	GOOD	OK	FAIL	Limits of err calc [X_{min}, X_{max}]
$Z^0 Z^0, W^+ W^-$	1.0E-3	1.0E-3, 1.0E-2	1.0E-2	MAX[100GeV/ m_χ , 10^{-6}], 1.0
$t\bar{t}, hh$	1.0E-5	1.0E-5, 1.0E-4	1.0E-4	MAX[100GeV/ m_χ , 10^{-6}], 1.0
$b\bar{b}, d\bar{d}, u\bar{u}$	9.0E-7	9.0E-7, 9.0E-6	9.0E-6	MAX[100GeV/ m_χ , 10^{-6}], 1.0
$\nu\bar{\nu}_{e,\mu,\tau}$	1.0E-3	1.0E-3, 1.0E-2	1.0E-2	MAX[100GeV/ m_χ , 10^{-6}], MIN[0.995, ($E_n(\nu_{line}) - 4\sigma$)/ M_χ]
$e\bar{e}, \mu\bar{\mu}, \tau\bar{\tau}$	1.0E-3	1.0E-3, 1.0E-2	1.0E-2	MAX[100GeV/ m_χ , 10^{-6}], MIN[0.995, ($E_n(\nu_{line}) - 4\sigma$)/ M_χ]

Table 7.1 Spline err tolerances used for input in particle physics component to Eq. (4.1). Column 1 is the DM annihilation channel being fit. Columns 2, 3, and 4 are the tolerances for "GOOD" (pass), "OK" requires inspection, and "FAIL" (tune and refit) respectively. Column 5 has the X ranges over which the error is evaluated. MAX/MIN [·, ·] takes the maximum or minimum of the two enclosed values.

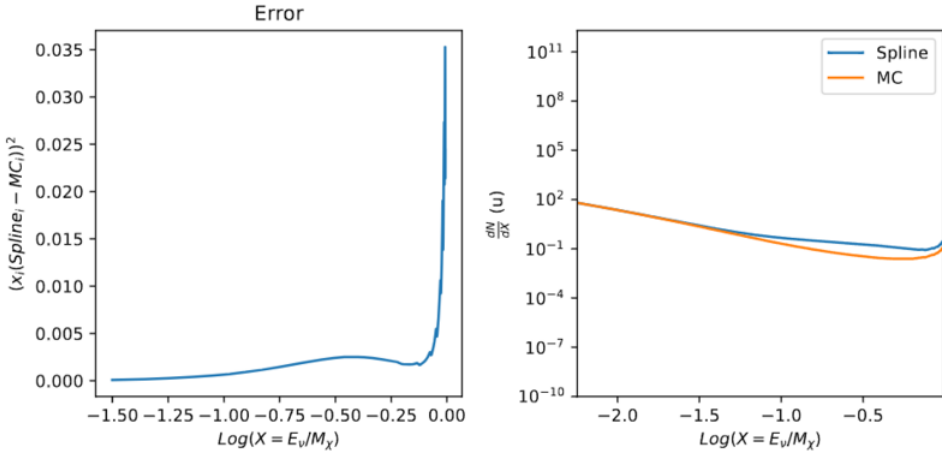


Figure 7.4 Example spline that failed the fit. Failed splined are corrected on a case by case basis unless the SM channel has a systematic problem fitting the splines. In this case, I made a bookkeeping error and loaded the incorrect spectral model

1938 the kernel mask as the upper limit of evaluation. Table 7.1 summarizes the tolerances for the DM
1939 annihilation channels used for this analysis.

1940 The errors are then assesed in two ways. First, FAIL and OK are directly plotted with e_i as a
1941 function of x with the full spline and MC. An example of a single failure is provided in Fig. 7.4.
1942 Second, a summary plot of all the splines is plotted and colors coded. Figure C.1 are the spline
1943 summaries as of writing this thesis. The goal broadly is to eliminate all red and inspect yellow
1944 statuses.

1945 The ν_e spectra at Earth are not considered in this analysis, so no work was done to refine the

1946 spline fits for this flavor. Finally, I perform a visual inspection of the splines to verify that the spline
 1947 fitting did not introduce spurious features that would corrupt the likelihood fitting.

1948 7.3.1.3 Composite Neutrino Spectra

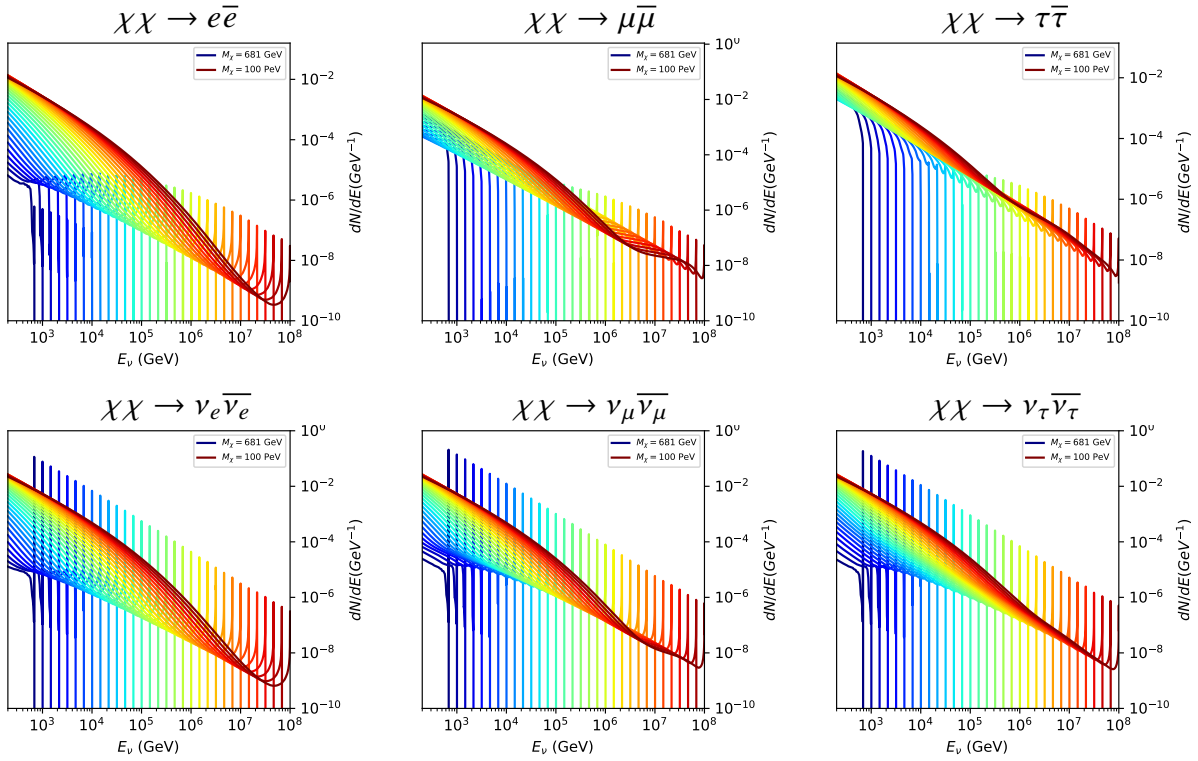


Figure 7.5 Summary of input spectral models that were smoothed with Gaussian kernels. Spectral models are for $\chi\chi \rightarrow e\bar{e}$, $\mu\bar{\mu}, \tau\bar{\tau}$, $\nu_e\bar{\nu}_e$, $\nu_\mu\bar{\nu}_\mu$, and $\nu_\tau\bar{\nu}_\tau$. These spectra are the composite ($\nu_\mu + \nu_\tau$) of neutrino flavors. Every spectral model used for this analysis is featured as a colored solid line. Bluer lines are for low m_χ models. m_χ ranges from 681 GeV to 100 PeV. HDM [79], χ arov [86], and Photospline [90] are used to generate these spectra. Energy (x-axis) was chosen to roughly represent the energy sensitivity of NST.

1949 With all the previously mentioned pieces, we are ready to fully assemble a comprehensive
 1950 description of the particle physics term dN/dE in Eq. (7.1).

$$\frac{dN_\nu}{dE_{\nu \oplus}} = \left(\frac{dN_{\nu_e}}{dE_{\nu_e}} + \frac{dN_{\nu_\mu}}{dE_{\nu_\mu}} + \frac{dN_{\nu_\tau}}{dE_{\nu_\tau}} \right)_{\text{src}} \cdot \mathbf{P}(\nu_\alpha \rightarrow \nu_\beta) \quad (7.5)$$

1951 Figure 7.5 shows the spectral models that required Gaussian smoothing, the leptonic annihilation
 1952 channels. The remaining models where the only processing were spline fitting and neutrino
 1953 oscillation are documented in Section C.3. Notice that the different neutrino flavors are unique,

1954 especially in their low energy tails. Therefore, this analysis will be sensitive to DM annihilating to
1955 the distinct neutrino flavors.

1956 **7.3.2 J- Astrophysical Component**

1957 For this analysis, we re-adopt the \mathcal{GS} model [59] used in Sec. 4 for dSphs. These models
1958 are based on a modified Navarro-Frenk-White (NFW) profile where the indices of the NFW
1959 (traditionally 1,3,1) are allowed to float. The angular width of these sources is much smaller than
1960 the angular resolution of IceCube NST [89]. We therefore treat these sources as point sources
1961 in this analysis, and forgo generating maps. These sources and the \mathcal{GS} model have already been
1962 discussed at length in Section 4.3.2 and is not repeated here. IceCube uses identical sources to
1963 Tab. 4.1 except we analyze source with declinations above 0.0° .

1964 **7.3.3 Source Selection and Annihilation Channels**

1965 We use all the dSphs presented in IceCube’s previous dSph DM search [84] and expand beyond
1966 it. IceCube’s sources for this analysis studies include Boötes I, Canes Venatici I, Canes Venatici II,
1967 Coma Berenices, Draco, Hercules, Leo I, Leo II, Leo V, Leo T, Segue 1, Segue 2, Ursa Major I,
1968 Ursa Major II, and Ursa Minor. A full description of all sources used is in Table 4.1. Sources with
1969 declinations less than 0.0 are excluded from this analysis.

1970 This analysis improves on the previous IceCube dSph paper [84] in the following ways. Previ-
1971 ously, the IceCube detector was not yet completed to the 86 string configuration. Many more dSphs
1972 will be observed, from 4 to 15. Previously, the particle physics model used for neutrino spectra
1973 from DM annihilation did not have EW corrections where they are now included [79]. The spectral
1974 models also predict substantial differences between the neutrino flavors, so this analysis will be the
1975 first DM dwarf analysis to discriminate between primary neutrino flavors. The study performed
1976 here studies 10.4 years of data.

1977 The SM annihilation channels probed for this study include $\chi\chi \rightarrow$

1978 $b\bar{b}, t\bar{t}, u\bar{u}, d\bar{d}, e\bar{e}, \mu\bar{\mu}, \tau\bar{\tau}, ZZ, W^+W^-, \nu_e\bar{\nu}_e, \nu_\mu\bar{\nu}_\mu$, and $\nu_\tau\bar{\nu}_\tau$

1979 **7.4 Likelihood Methods**

1980 I use the Point-Source search likelihood which is widely used in IceCube analyses. The
1981 likelihood function is defined as the following:

$$L(n_s) = \prod_{i=1}^N \left[\frac{n_s}{N} S_i + \left(1 - \frac{n_s}{N}\right) B_i \right] \quad (7.6)$$

1982 where i is an event index, S and B are the signal PDF and background PDF respectively. For a joint
1983 analysis where the sources are stacked the likelihood is expanded in the simplified way:

$$L(n_s) = \prod_{i=1}^{N_{\text{sources}}} L_i(n_s) \quad (7.7)$$

1984 Where L_i is the likelihood from the i -th source in the stacked analysis. The Test Statistic (TS)
1985 definition remains the same as Eq. (4.7)

1986 **7.5 Background Simulation**

1987 Before we look at data, we must first analyze background and signal injection to validate our
1988 analysis. We set out to characterize the TS distributions for each source, annihilation channel, and
1989 m_χ . Previous IceCube DM searches [88, 92] showed TS distributions that did not behave according
1990 to a χ^2 distribution with 1 degree of freedom. TS distributions can also vary significantly between
1991 DM mass and annihilation models. Therefore, Wilk's theorem may not be applicable to the analysis.
1992 Instead, a critical value is defined from many background trials. We study the TS distributions
1993 first for each source, then for the stacked analysis. The following sections show the results of the
1994 likelihood fitting for a suite of background trials.

1995 I assume that TS values are physical: $TS \geq 0$. $\epsilon[x]$ indicate the fraction of events where $TS < x$.
1996 For TS plots shown here, the decimal values of x are 1.0e-2 and 1.0e-3. Each subplot represents
1997 a simulation of 100,000 data-scrambled background trials. Section 7.5.1 show the background TS
1998 distributions obtained from Segue 1, a source with little Earth attenuation and large J -factor, and
1999 Ursa Major II, which has similarly large J -factor but significantly more Earth attenuation, assuming
2000 DM annihilation into $b\bar{b}$, $\tau\bar{\tau}$, and $\nu_\mu\bar{\nu}_\mu$. I show the TS distributions of a stacked study of 15 sources
2001 for all DM annihilation channels.

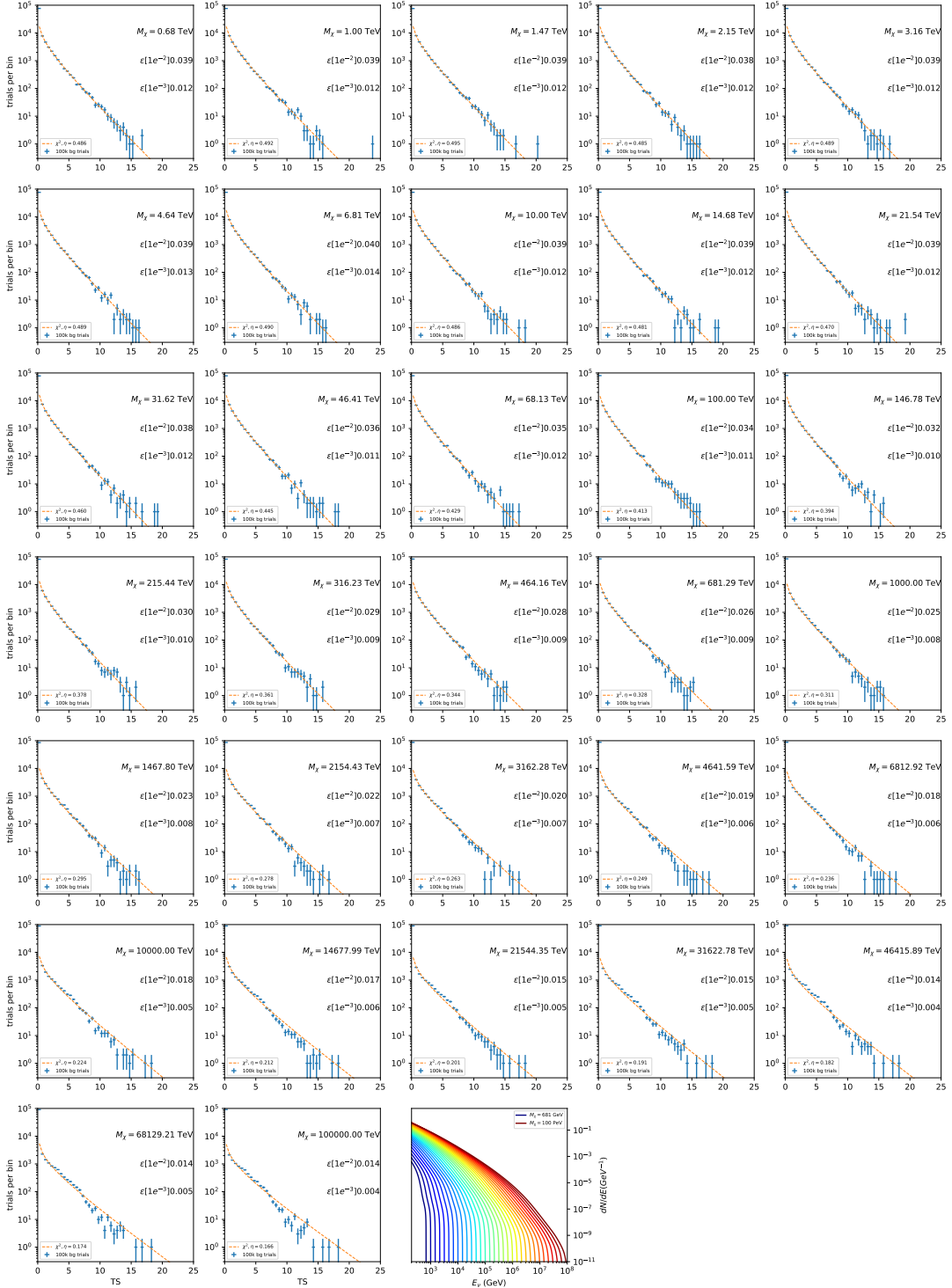


Figure 7.6 Test statistic (TS) distributions for Segue 1 and $\chi\chi \rightarrow b\bar{b}$. Each subplot, except the final, is the TS distribution for a specific DM mass listed in the subplot. Orange dashed lines are the traces for a χ^2 distribution with 1 degree of freedom. $\epsilon[\cdot]$ is the fraction of trials smaller than the bracketed value. The final subplot features the all DM spectral models, similar to Fig. 7.5, used as input for the TS distributions.

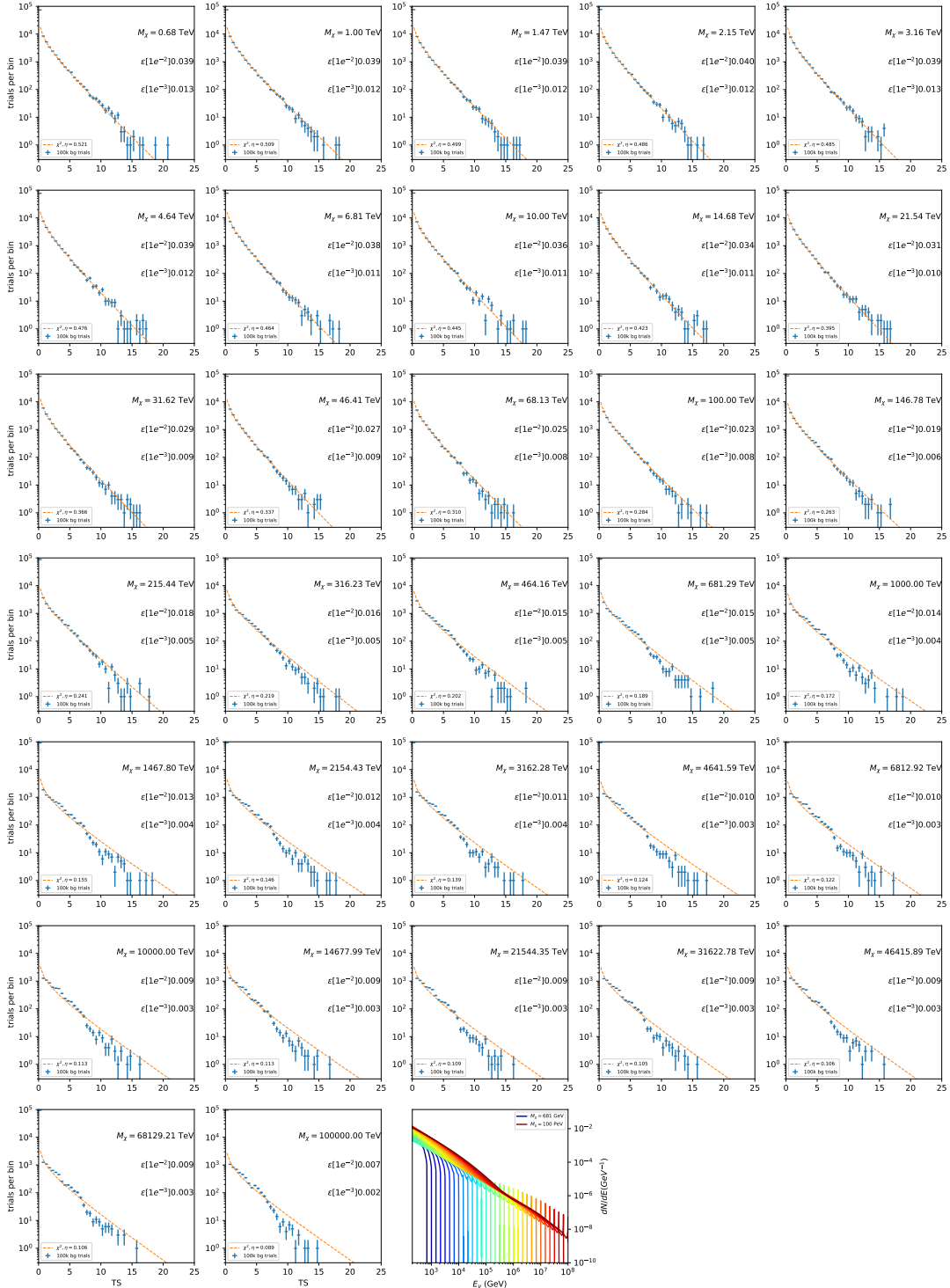


Figure 7.7 Same as Fig. 7.6 for Segue 1 $\chi\chi \rightarrow \tau\bar{\tau}$.

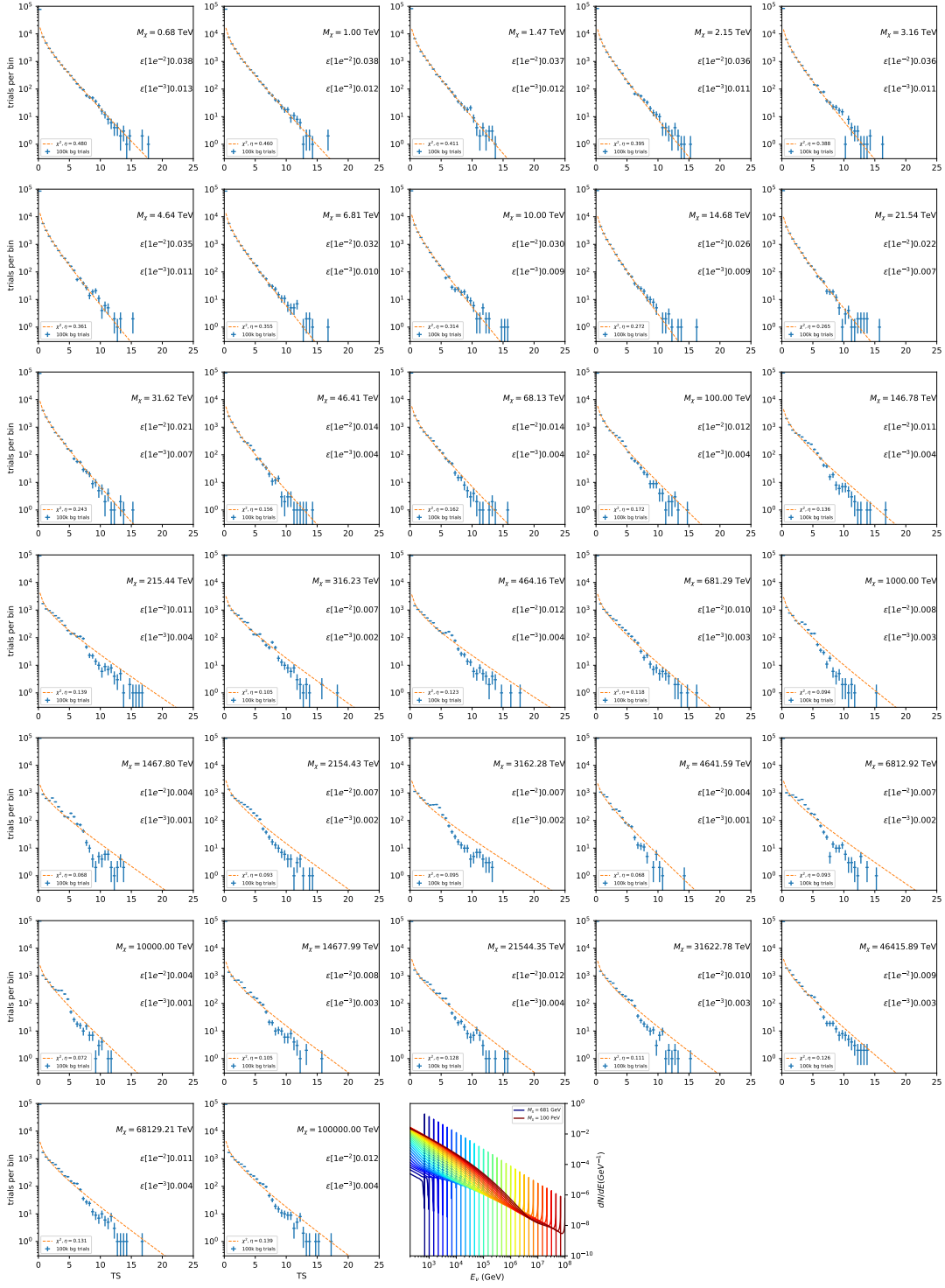


Figure 7.8 Same as Fig. 7.6 for Segue 1 $\chi\chi \rightarrow \nu_\mu\bar{\nu}_\mu$.

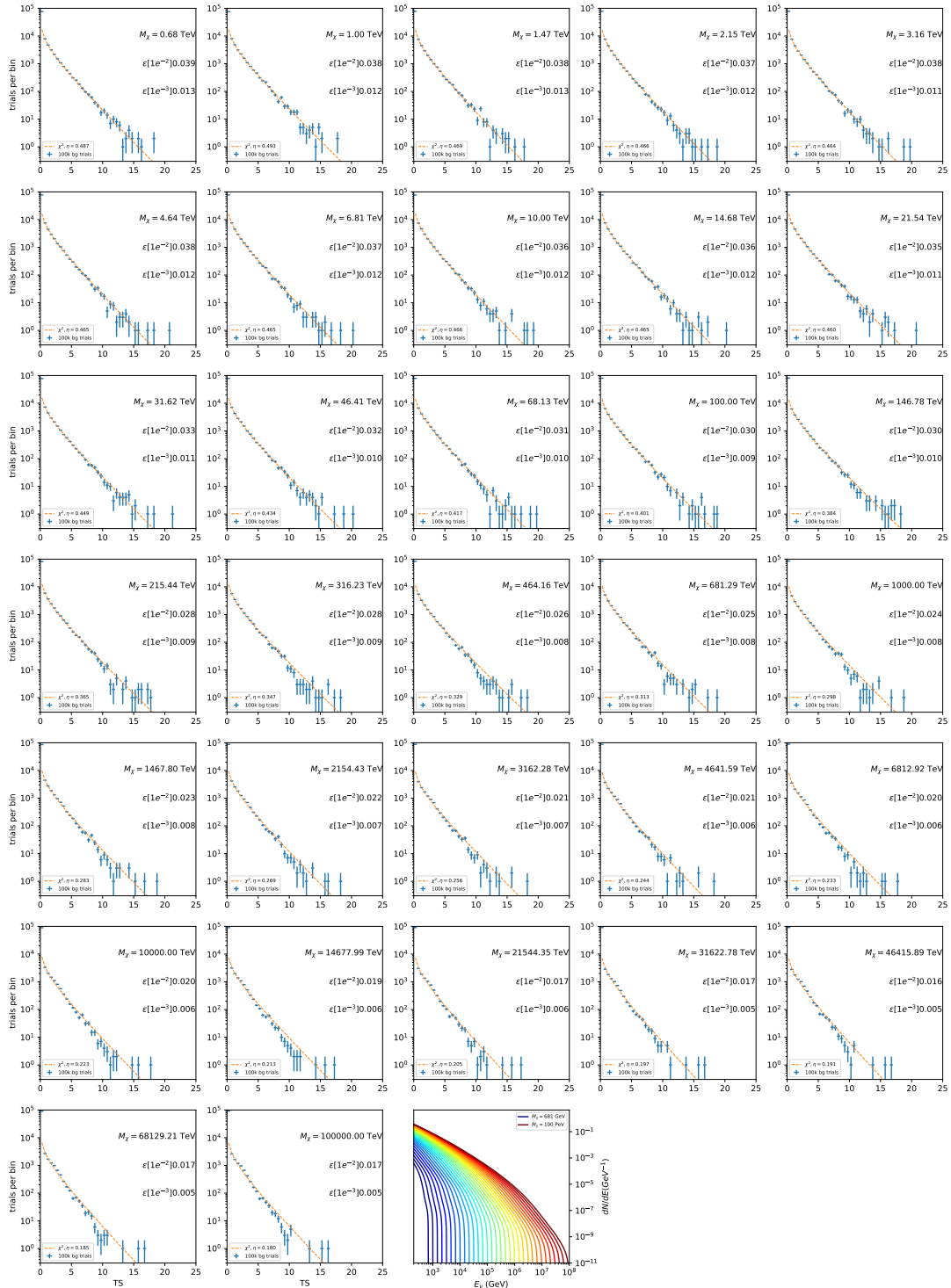


Figure 7.9 Same as Fig. 7.6 for Ursa Major II 1 $\chi\chi \rightarrow b\bar{b}$.

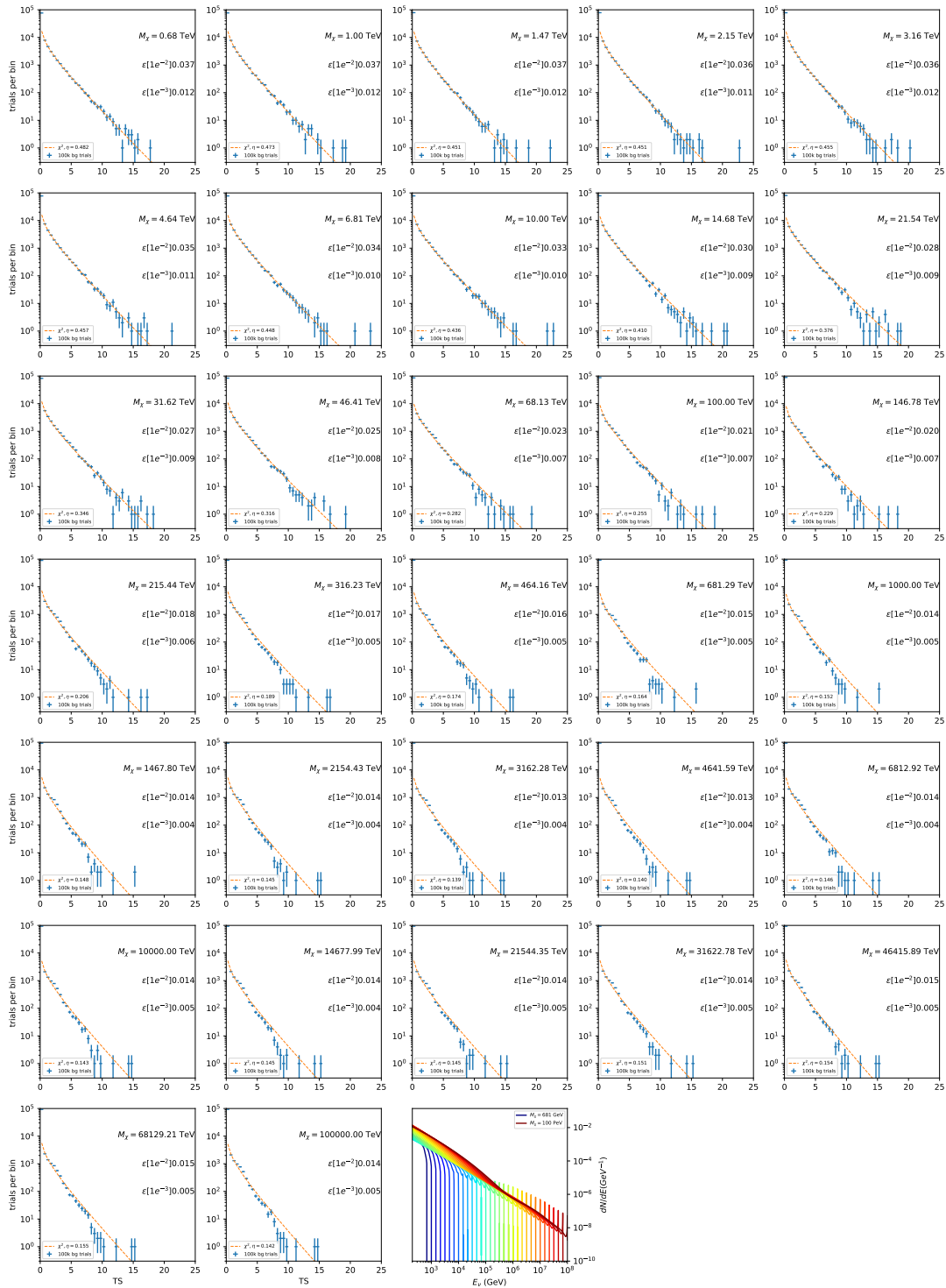


Figure 7.10 Same as Fig. 7.6 for Ursa Major II 1 $\chi\chi \rightarrow \tau\bar{\tau}$.

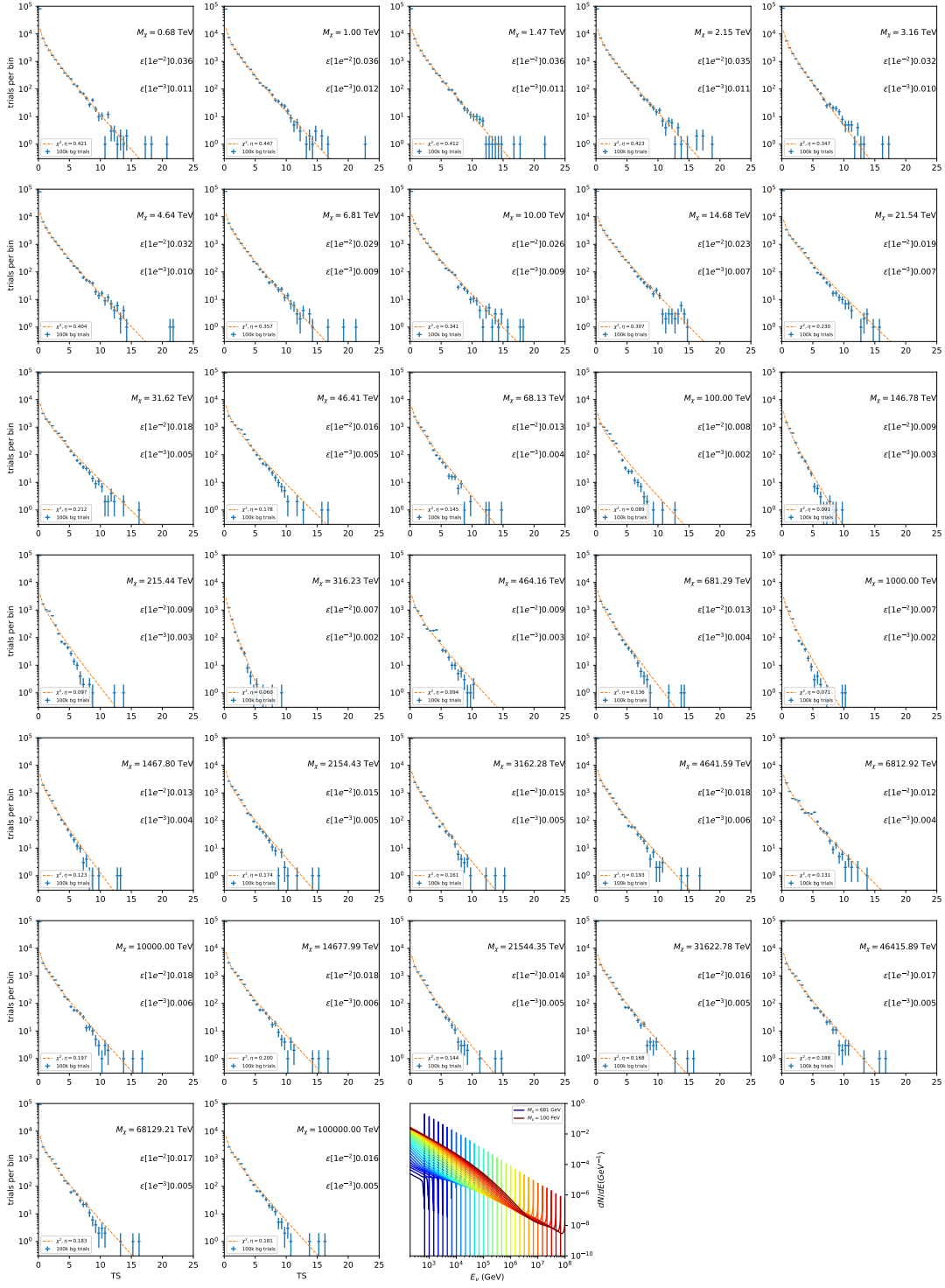


Figure 7.11 Same as Fig. 7.6 for Ursa Major II 1 $\chi\chi \rightarrow \nu_\mu\bar{\nu}_\mu$.

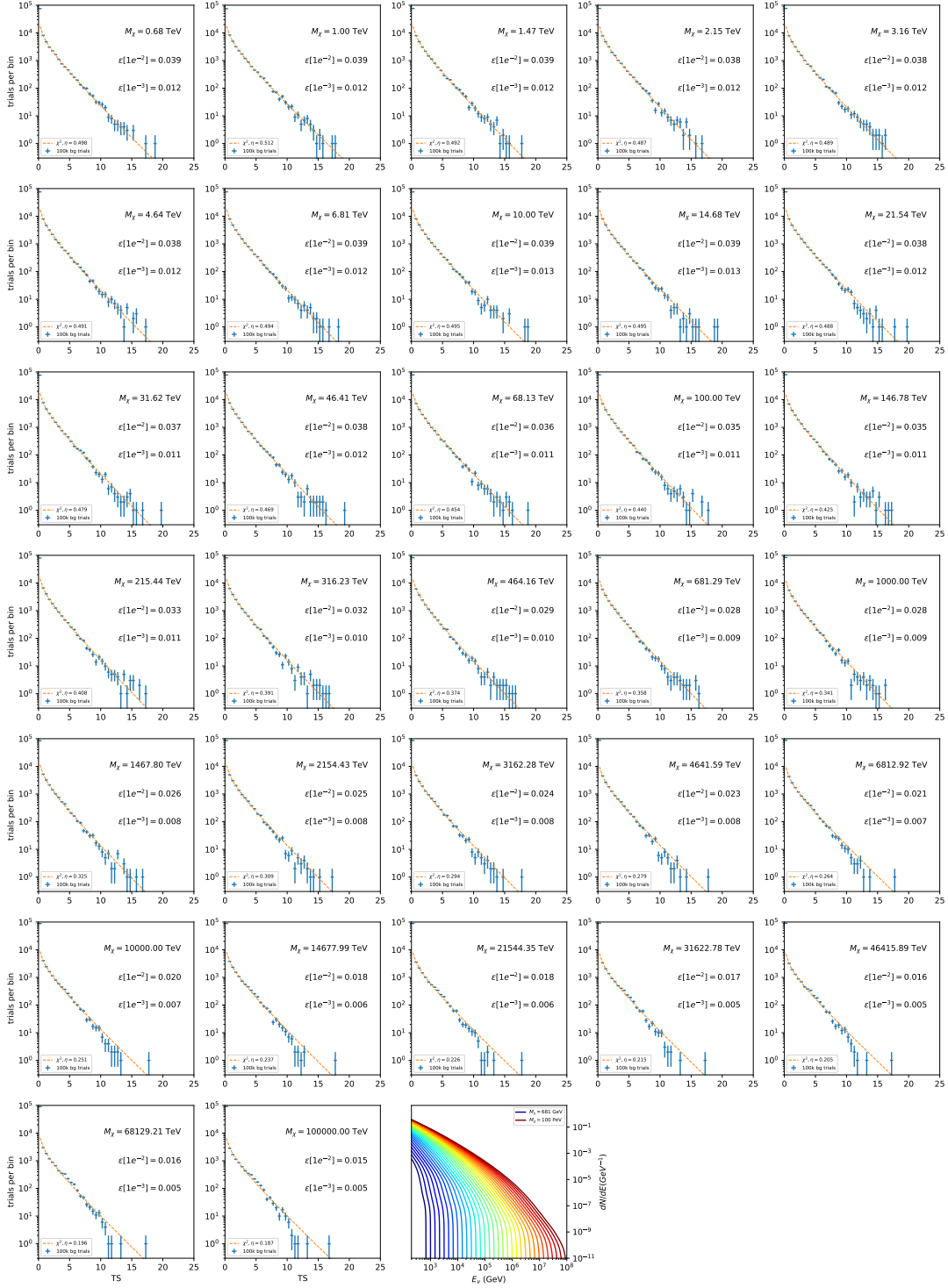


Figure 7.12 Same as Fig. 7.6 for 15, \mathcal{GS} J -factor, stacked sources and $\chi\chi \rightarrow b\bar{b}$.

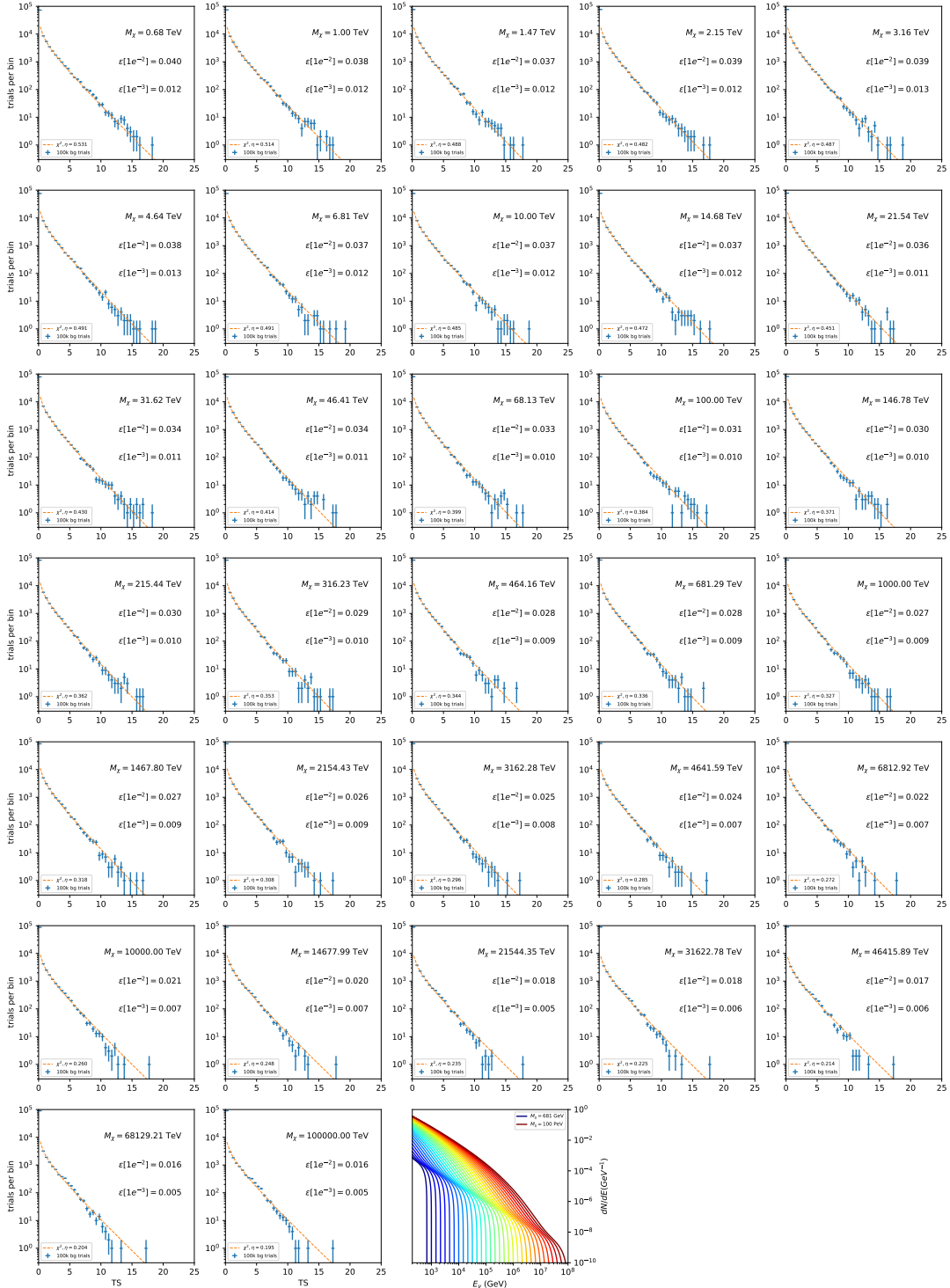


Figure 7.13 Same as Fig. 7.6 for 15, \mathcal{GS} J -factor, stacked sources and $\chi\chi \rightarrow t\bar{t}$.

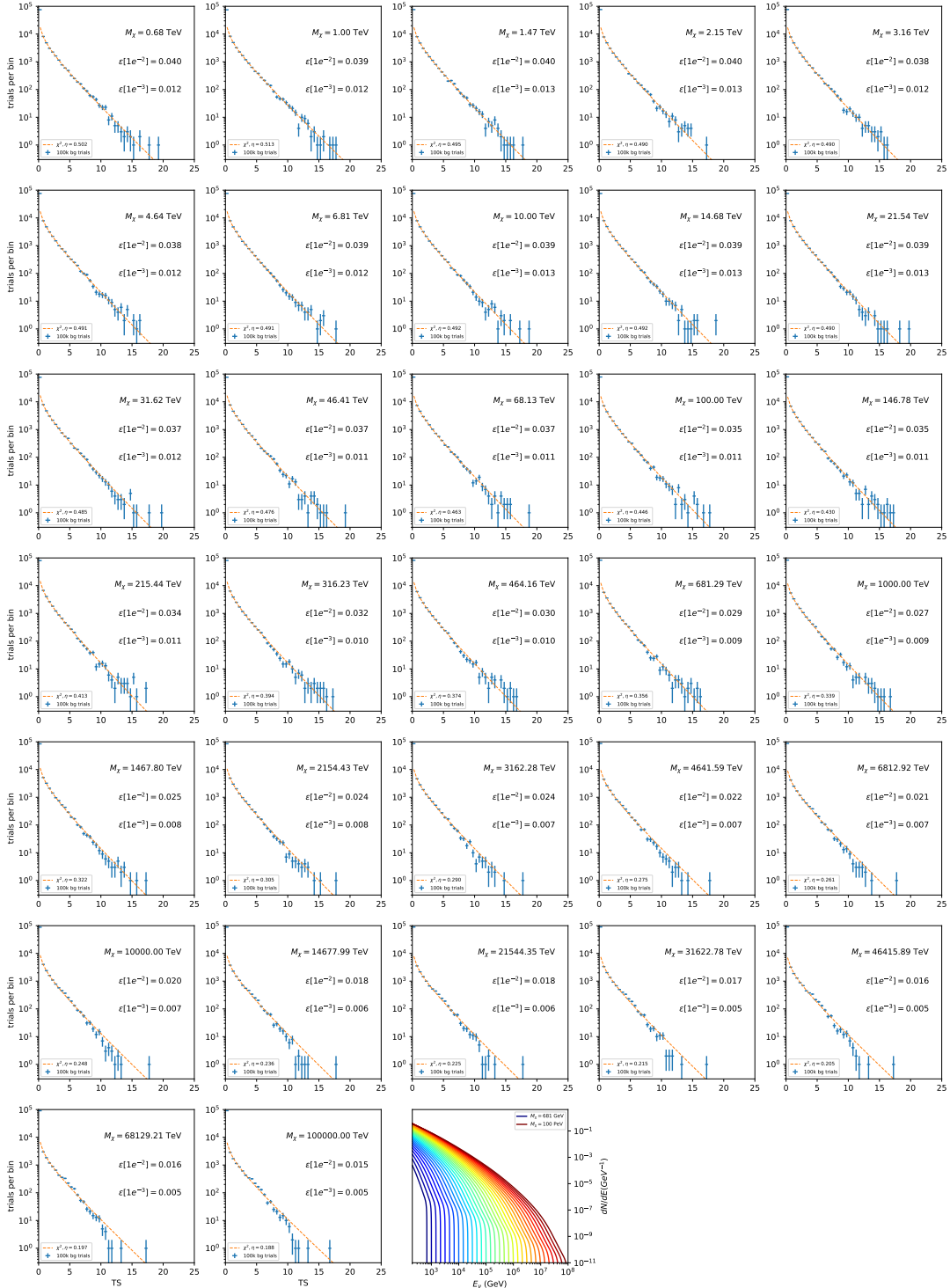


Figure 7.14 Same as Fig. 7.6 for 15, \mathcal{GS} J-factor, stacked sources and $\chi\chi \rightarrow u\bar{u}$.

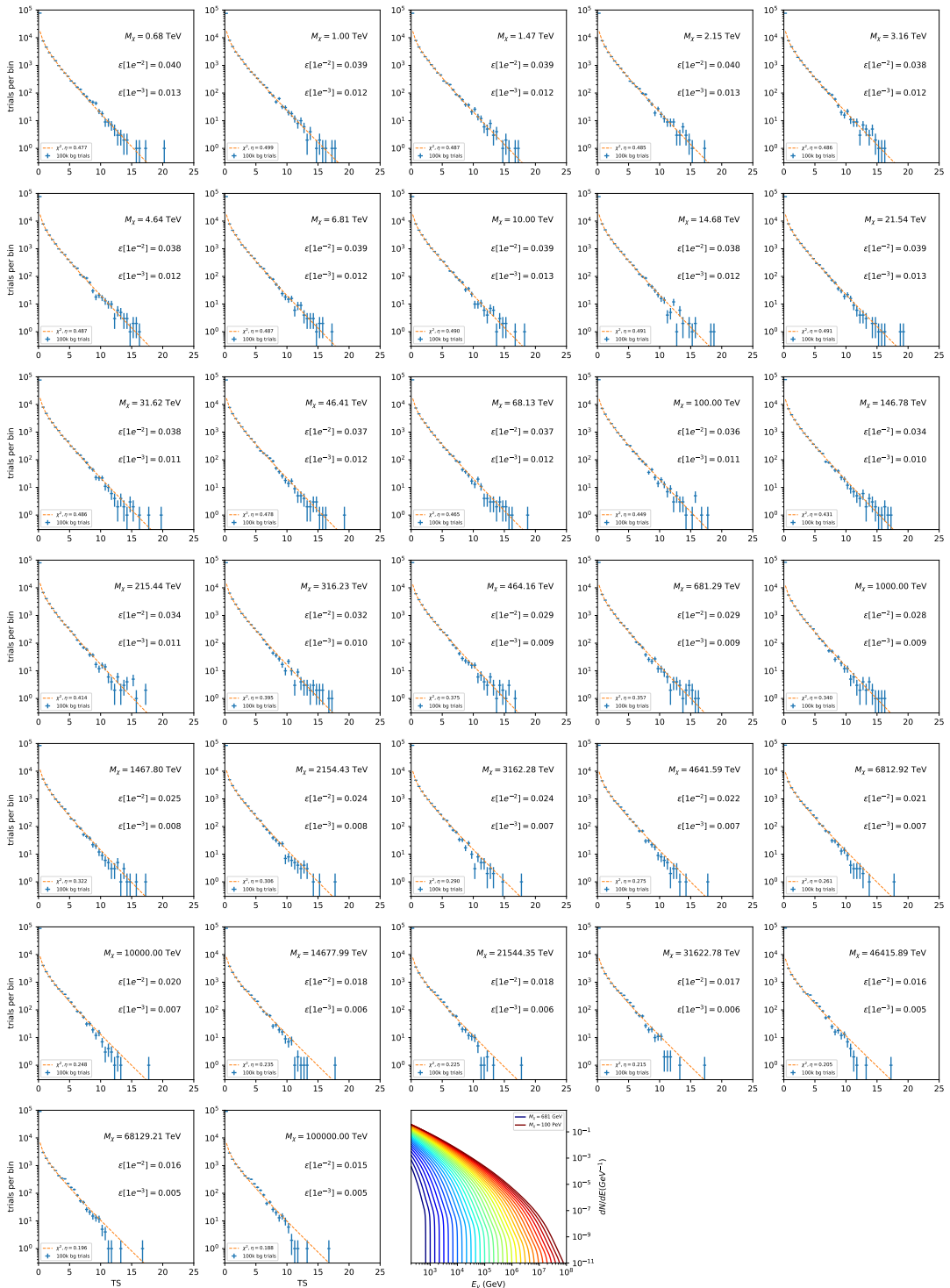


Figure 7.15 Same as Fig. 7.6 for 15, \mathcal{GS} J-factor, stacked sources and $\chi\chi \rightarrow d\bar{d}$.

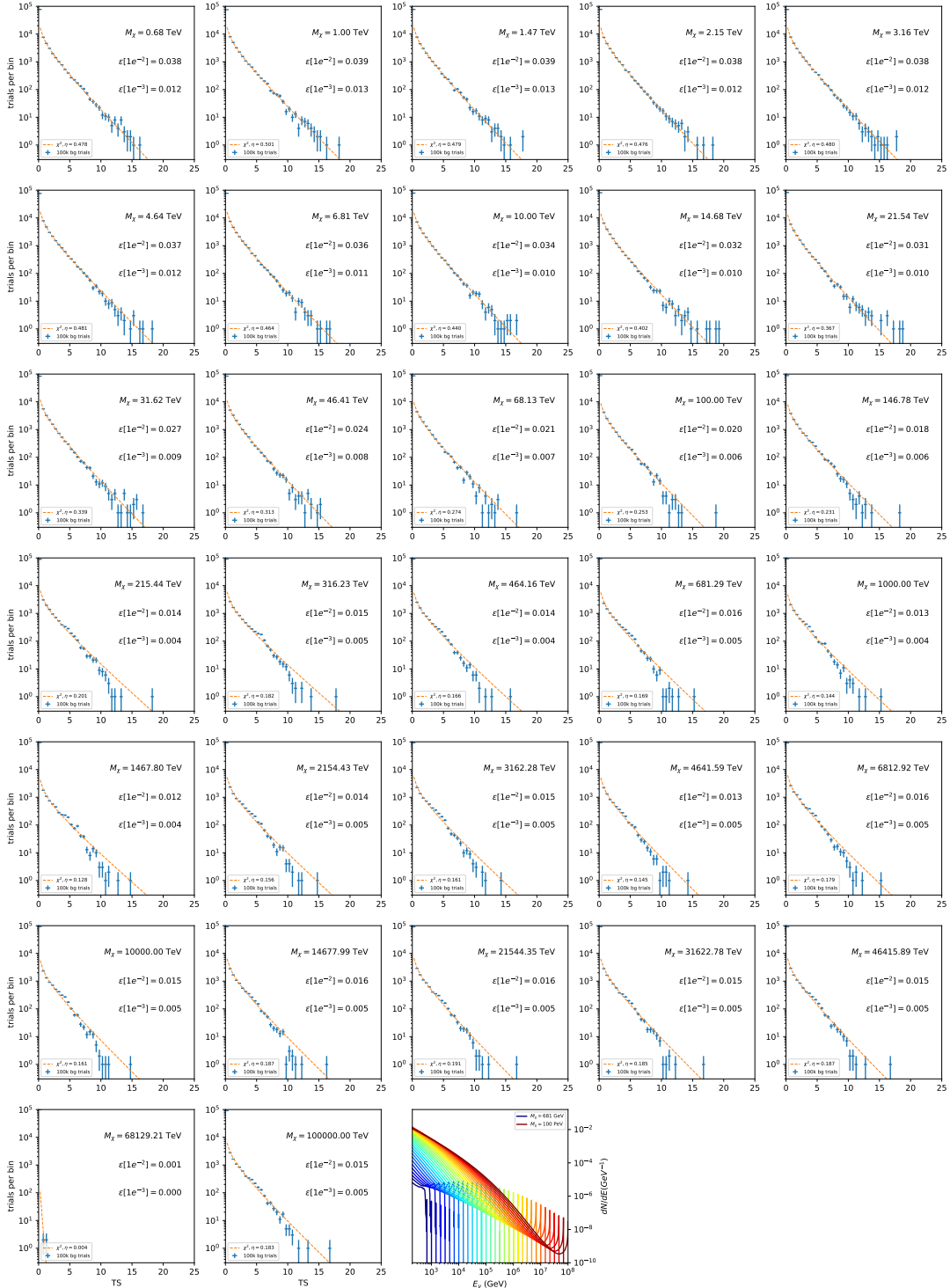


Figure 7.16 Same as Fig. 7.6 for 15, \mathcal{GS} J-factor, stacked sources and $\chi\chi \rightarrow e\bar{e}$.

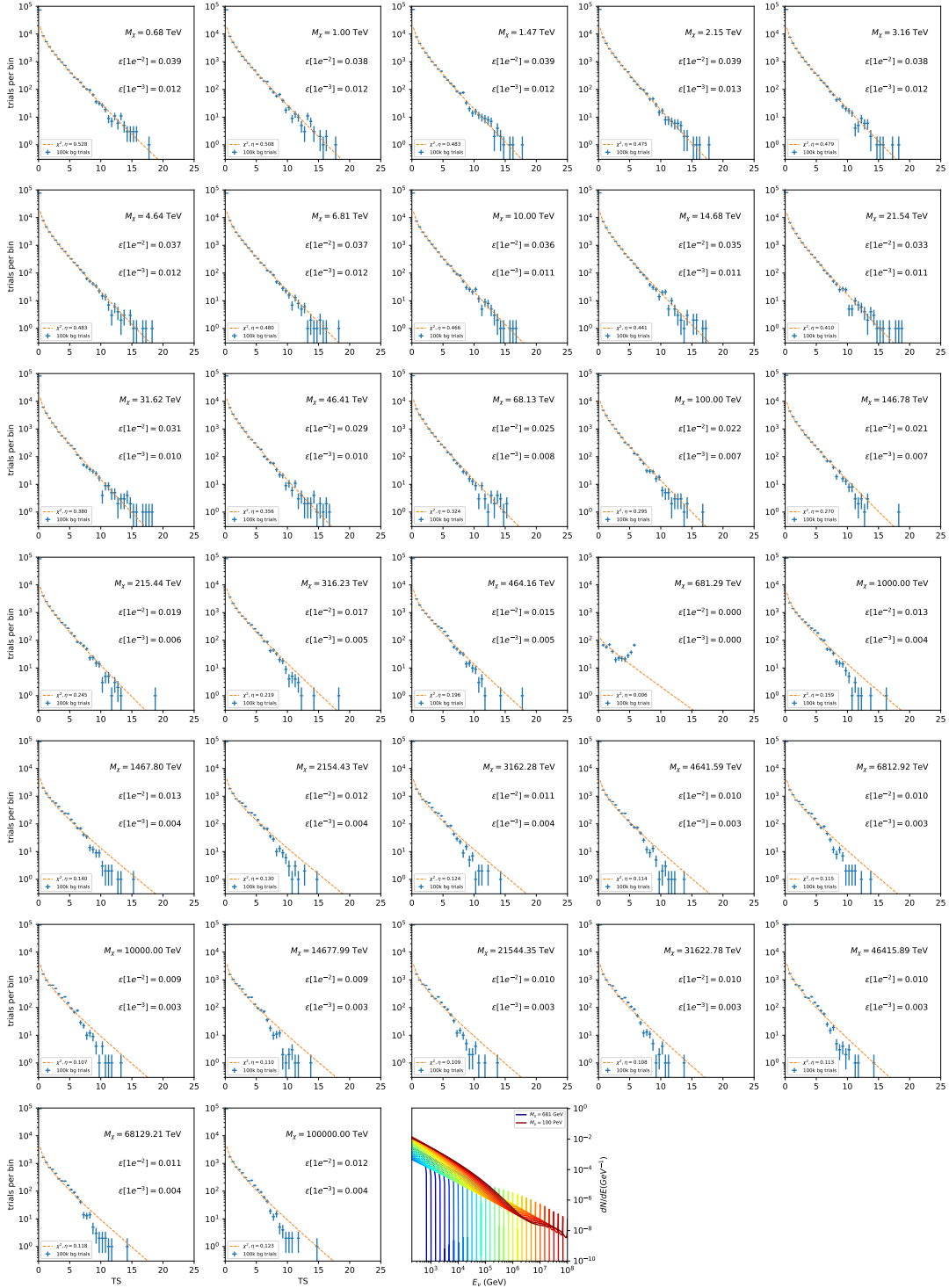


Figure 7.17 Same as Fig. 7.6 for 15, \mathcal{GS} J -factor, stacked sources and $\chi\chi \rightarrow \mu\bar{\mu}$.

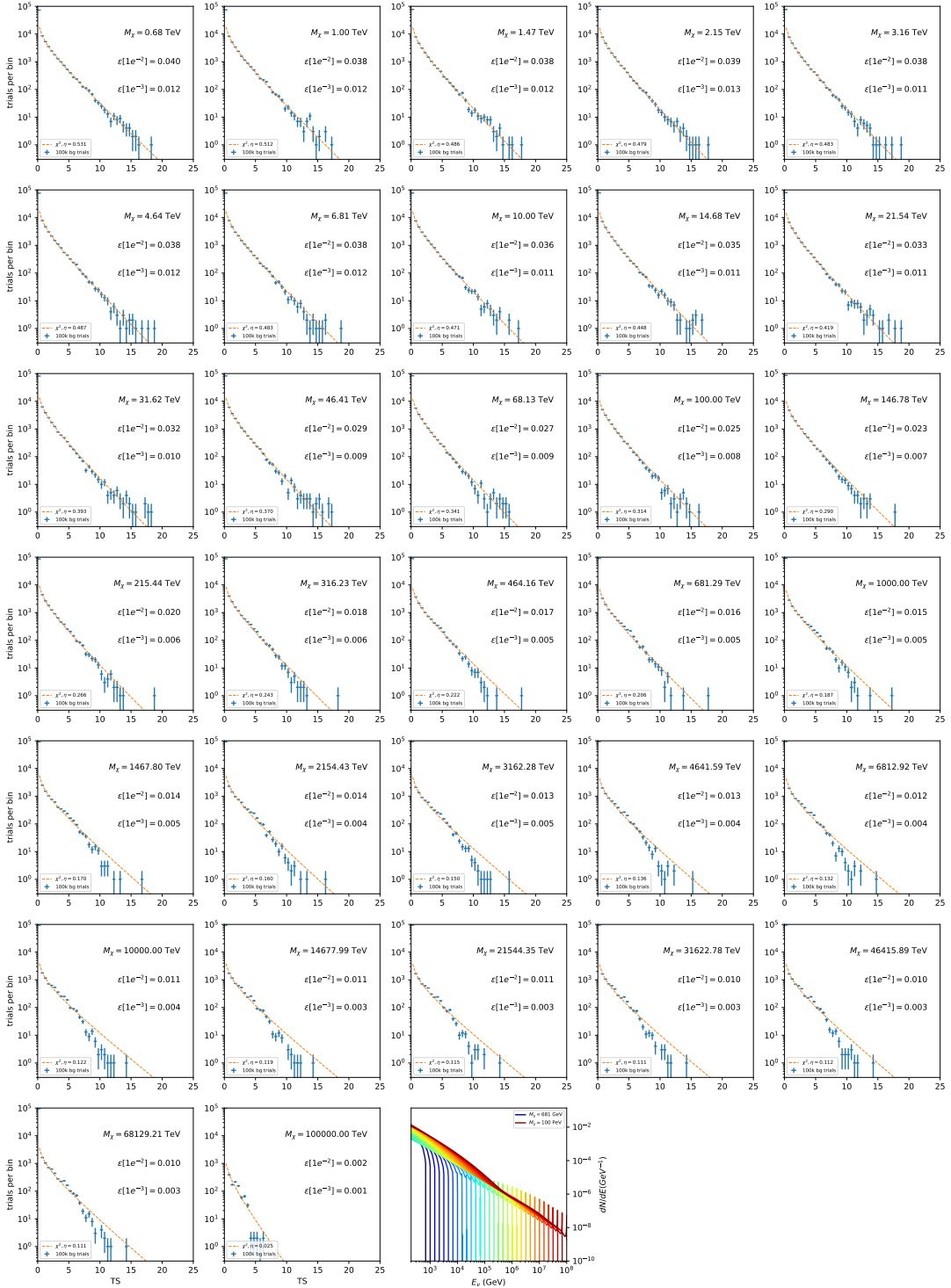


Figure 7.18 Same as Fig. 7.6 for 15, \mathcal{GS} J -factor, stacked sources and $\chi\chi \rightarrow \tau\bar{\tau}$.

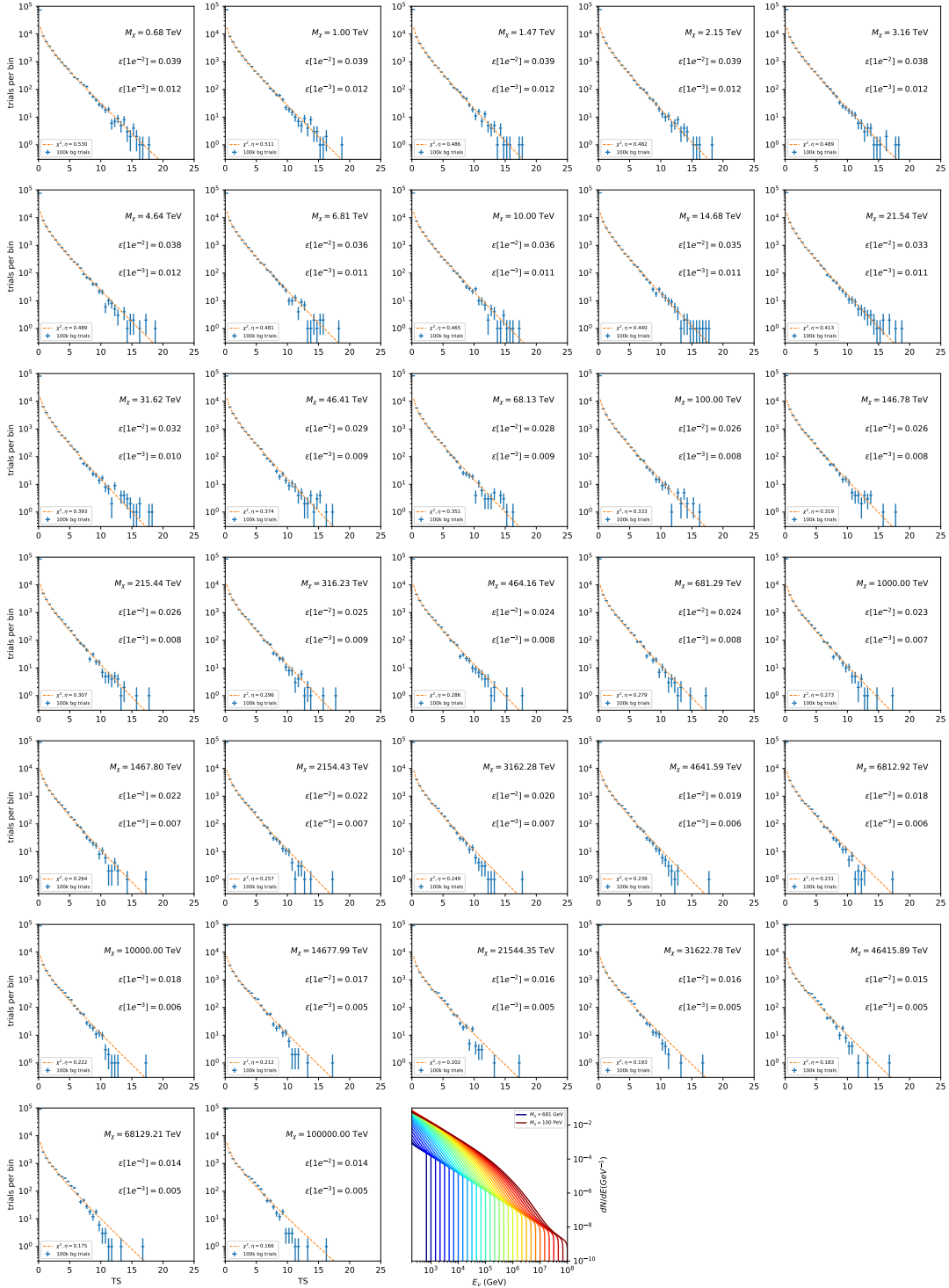


Figure 7.19 Same as Fig. 7.6 for 15, \mathcal{GS} J-factor, stacked sources and $\chi\chi \rightarrow W^+W^-$.

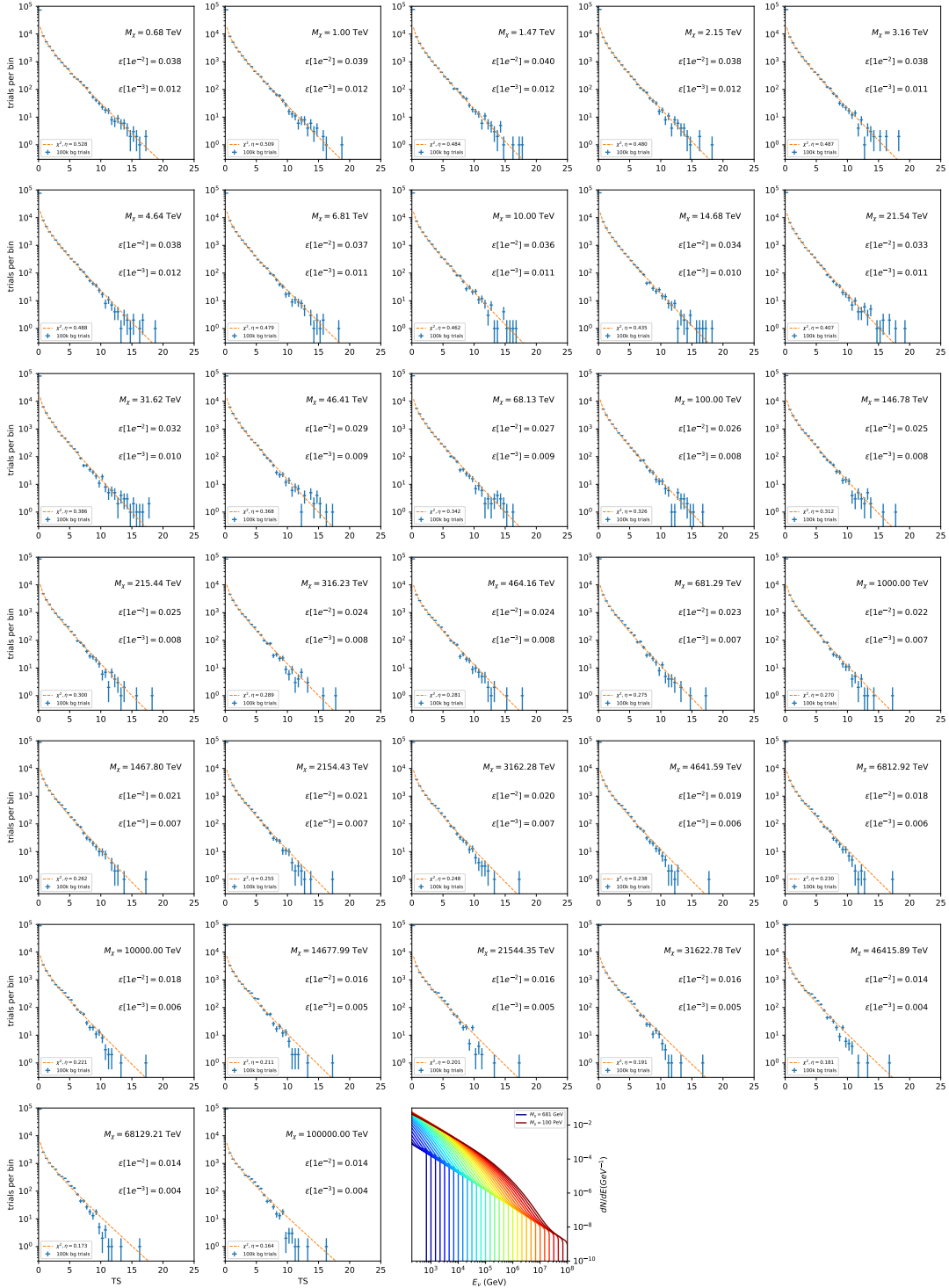


Figure 7.20 Same as Fig. 7.6 for 15, \mathcal{GS} J-factor, stacked sources and $\chi\chi \rightarrow ZZ$.

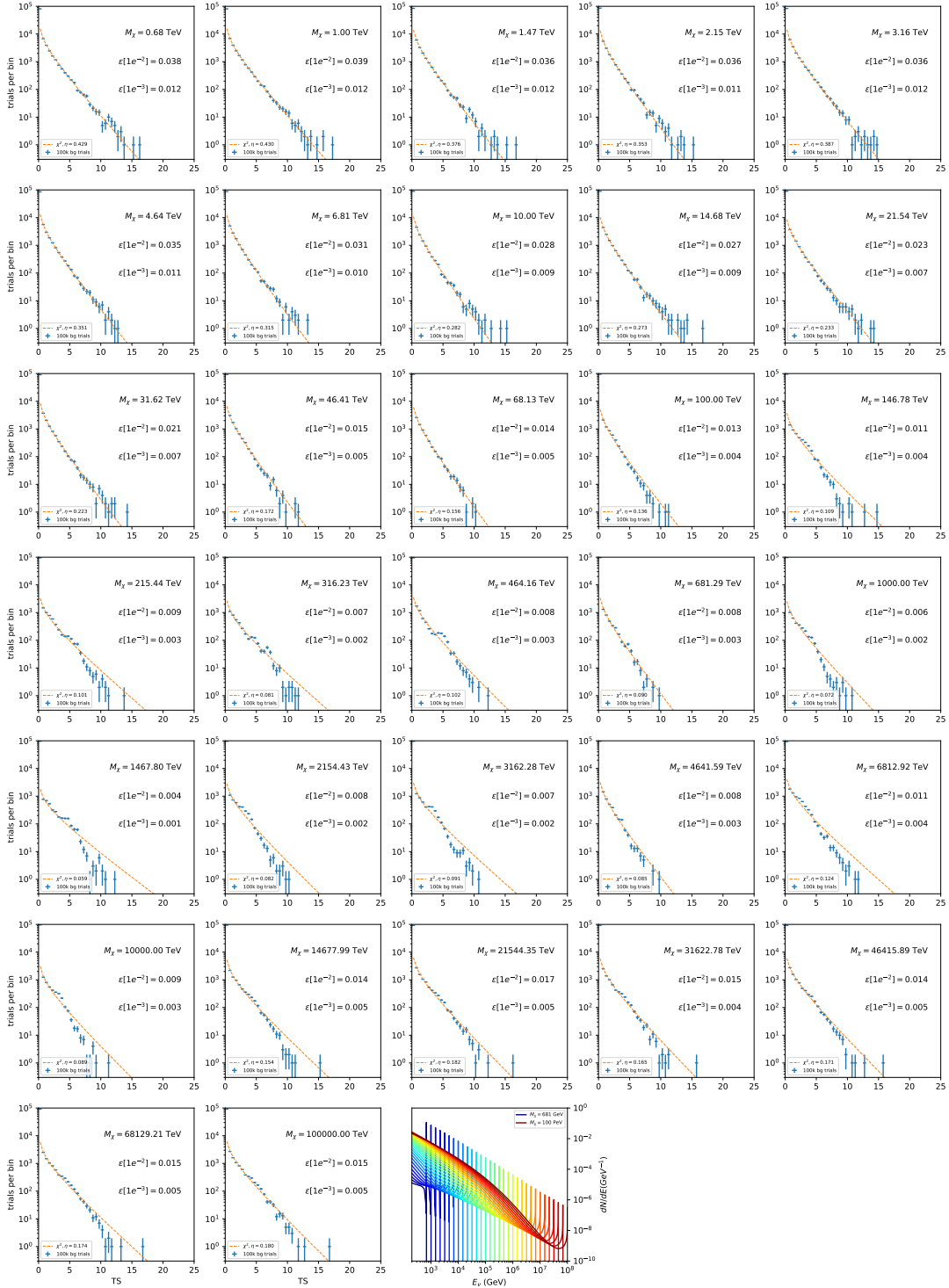


Figure 7.21 Same as Fig. 7.6 for 15, \mathcal{GS} J-factor, stacked sources and $\chi\chi \rightarrow \nu_e \overline{\nu}_e$.

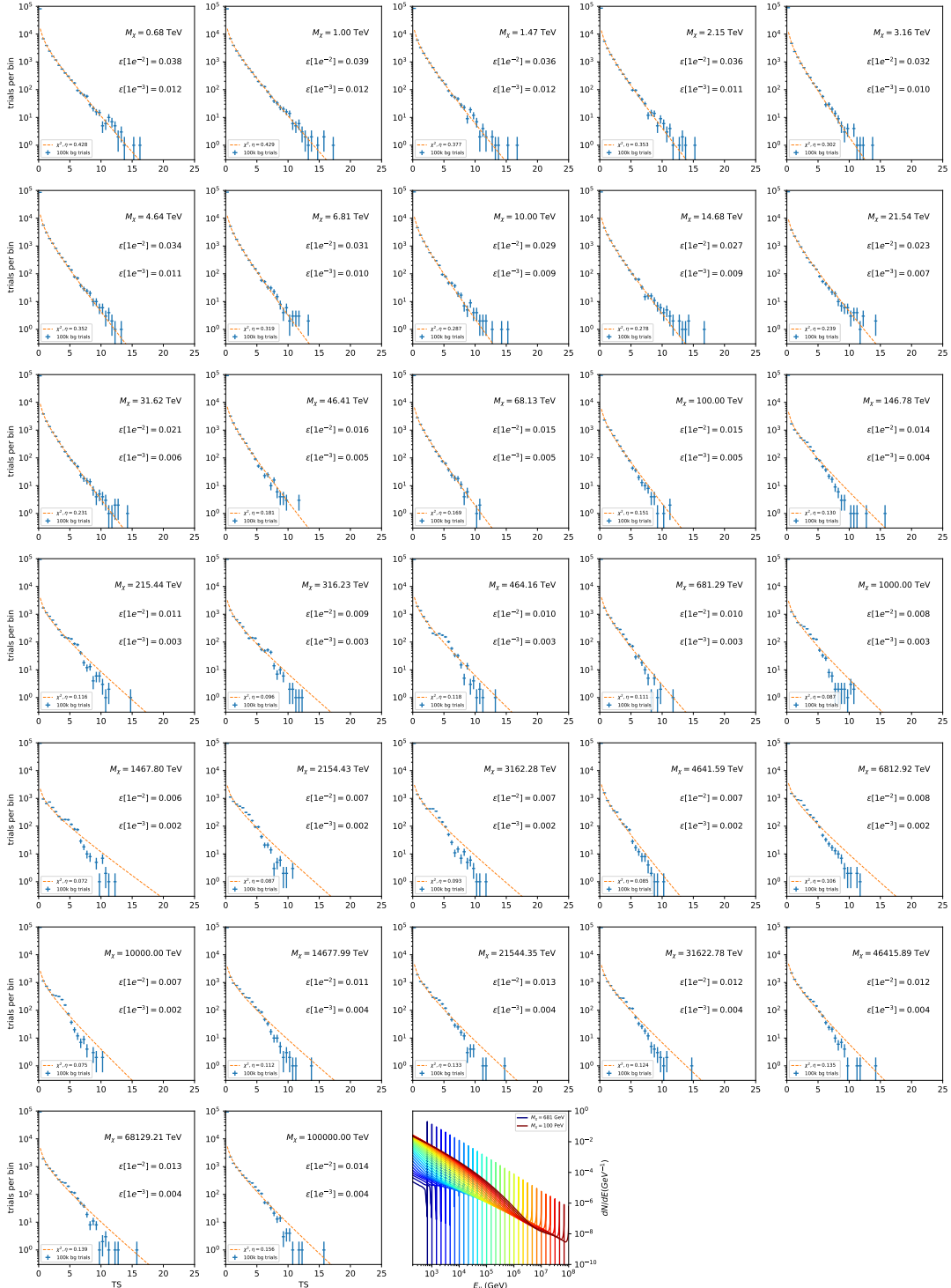


Figure 7.22 Same as Fig. 7.6 for 15, GS J-factor, stacked sources and $\chi\chi \rightarrow \nu_\mu \bar{\nu}_\mu$.

2002 **7.5.1 TS per Source**

2003 Figure 7.6 to Figure 7.11 present the TS distributions for Segue 1 and Ursa Major II for 100,000
2004 trials. More studies for all annihilation channels and remaining 13 sources were also performed
2005 and are documented in IceCube’s internal wiki.

2006 Almost every distribution produced follows a χ^2 distribution with 1 degree of freedom. This is
2007 more true for low m_χ than high m_χ models. These observations are important for future assumptions
2008 made in Sec. 8 and may justify statistical calculations assuming our test statistics follow a χ^2 with
2009 1 degree of freedom.

2010 **7.5.2 Stacked TS**

2011 Figure 7.12 to Figure 7.22 present the TS distributions for a stacked study of 15 sources with
2012 \mathcal{GS} J -factors on 100,000 trials. The presentation of these plots are identical to the single source
2013 distributions in Section 7.5.1. We see similar behaviour in the stacked TS distributions compared
2014 to the single source studies.

2015 **7.6 Signal Recovery**

2016 We also wish to understand how well the analysis is able to reconstruct signal neutrinos. In
2017 order to test this, we inject neutrinos from our spectral models randomly then attempt to discern
2018 the number of signal neutrinos in the simulated data. Figure 7.23 and Figure 7.24 show this study
2019 for $\chi\chi \rightarrow b\bar{b}$, $t\bar{t}$, and $\nu_\mu\bar{\nu}_\mu$ for a stacked analysis of 15 sources. Figure C.3 to Figure C.8 show
2020 identical studies for Segue 1 and Ursa Major II. We see that the analysis is conservative at smaller
2021 m_χ , yet improves at larger m_χ . We also see that the uncertainty is small for the neutrino annihilation
2022 spectra, and the uncertainty is larger for softer channels like $b\bar{b}$.

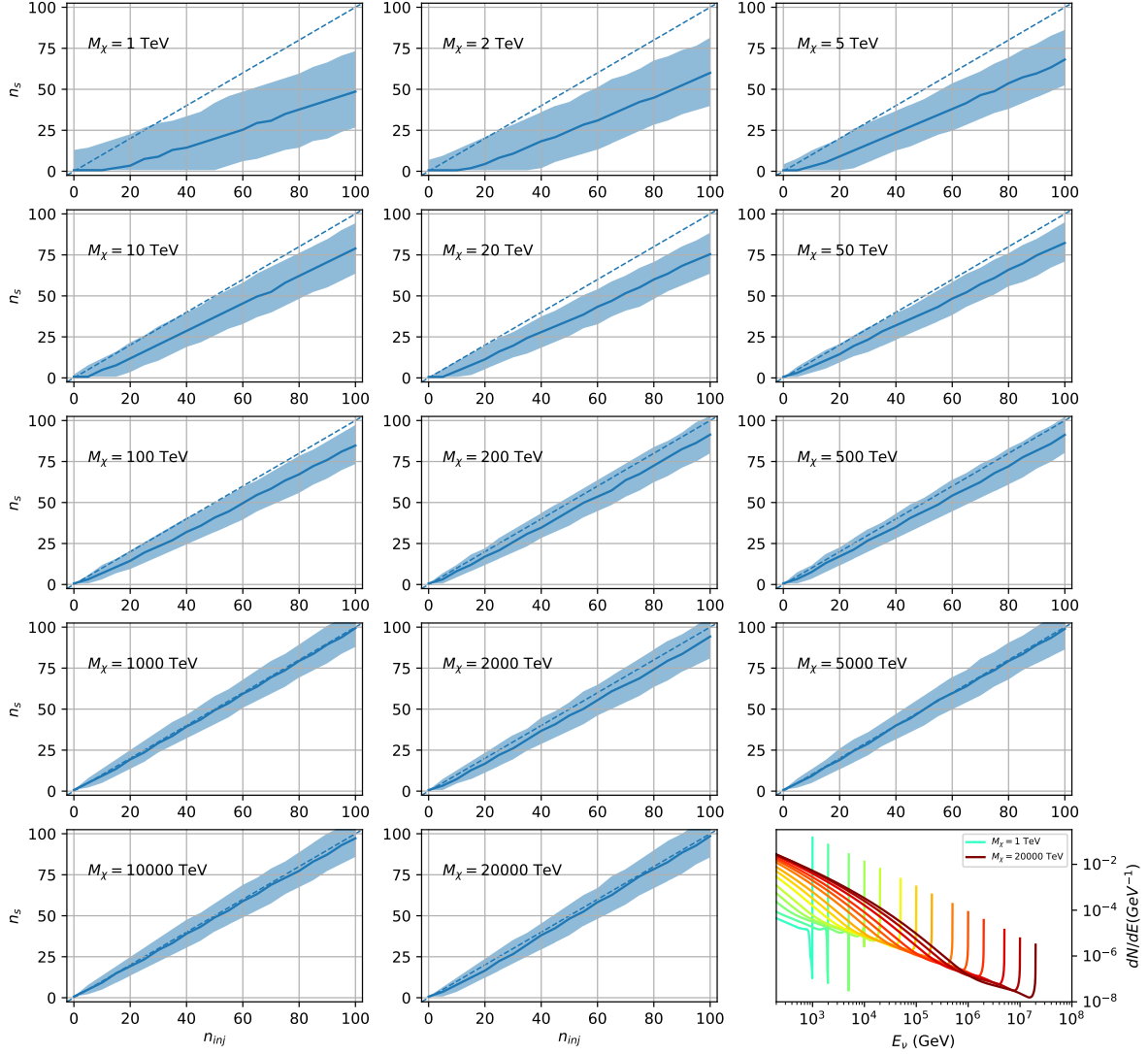


Figure 7.23 Signal Recovery study for an analysis with 15 stacked sources using the \mathcal{GS} J -factors [59]. Above shows 14 studies for DM mass ranging between 1 TeV and 20 PeV for $\chi\chi \rightarrow \mu_\mu\bar{\mu}_\mu$. The bottom right subplot features every spectral model used as input for the remaining subplots. The remaining subplots show n_{inj} as the number of signal events injected into background simulation. Whereas, n_s is the number of signal events recovered from analyzing the injected simulation. Blue line represents the median values of 100 simulations. Light blue bands show the 1σ statistical uncertainty around the median.

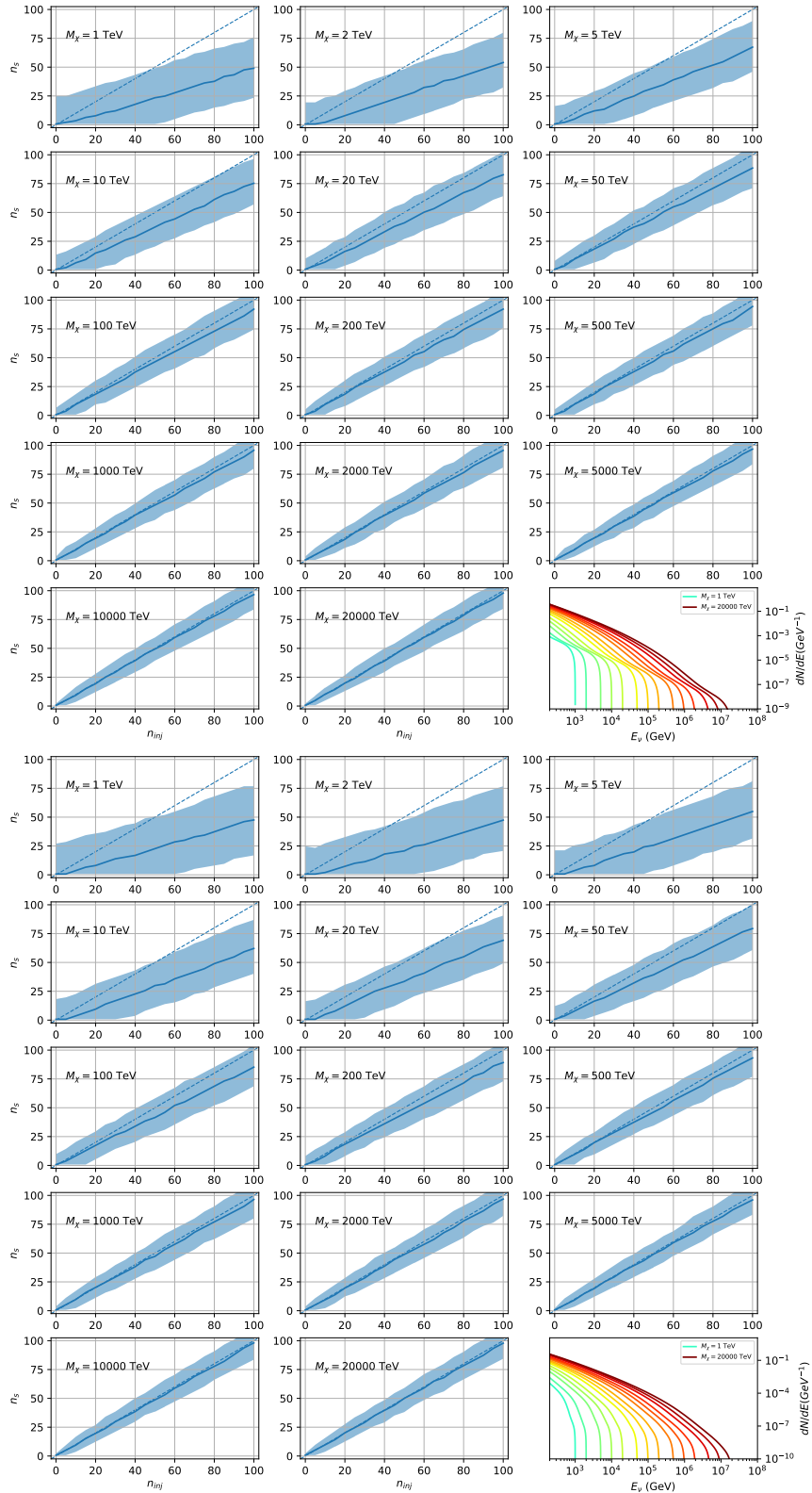


Figure 7.24 Same as Fig. 7.23 but for $\chi\chi \rightarrow t\bar{t}$ (top) and $b\bar{b}$ (bottom).

2023 **7.6.1 Sensitivities**

2024 In IceCube, we usually define the 90% confidence level (CL), as the minimum number of signal
2025 events (n_s) required to have a Type I error rate smaller than 0.5 and Type II error rate of 0.1. We
2026 compute n_s from the following equation

$$n_s = T_{\text{live}} \int_0^{\Delta\Omega} d\Omega \int_{E_{\min}}^{E_{\max}} dE_\nu A_{\text{eff}}(\hat{n}, E_\nu) \frac{d\Phi_\nu}{d\Omega dE_\nu}(\hat{n}, E_\nu), \quad (7.8)$$

2027 to extract the sensitivity on the dark matter velocity-weighted annihilation cross-section, $\langle\sigma v\rangle$. T_{live}
2028 is the detector live time, A_{eff} is the effective area of the detector, and E_{\min} , E_{\max} are the minimum,
2029 maximum energies of the expected neutrinos, respectively.

2030 Sensitivities are calculated for each source individually as if they were the only source and as a
2031 stack over 1000 trials. From Eq. (7.8) and Eq. (7.1) we can compute the $\langle\sigma v\rangle$ at a 90% confidence
2032 level. Figure 7.26 and Fig. 7.25 show the sensitivities for some DM annihilation channels. Not
2033 all channels computed successfully in time for the writing of this dissertation. Among channels
2034 missing include the charged leptons: e and τ .

2035 **7.7 Systematics**

2036 The current analysis plan is to compare these sensitivities to another J -factor catalog such as
2037 \mathcal{LS} [80] although this was not completed in time for this dissertation. Additionally, we set out to
2038 perform a standard suite of IceCube systematic studies which include: DOM efficiency, Hole ice,
2039 ice absorption, and photon scattering. We do study Earth attenuation, and Section 7.7.1 enumerates
2040 the impact of the Earth on our hardest neutrino spectra.

2041 **7.7.1 Earth Effects**

2042 We look to quantify the impact of the Earth on our sensitivity to $\chi\chi \rightarrow \nu_\mu \bar{\nu}_\mu$. This channel is
2043 expected to be among the significantly impacted annihilation channels because it has a significant
2044 contribution at PeV energies for $m_\chi \geq 1\text{PeV}$. The Earth is expected to attenuate these higher energy
2045 neutrinos. However, these neutrino spectra have significant low energy contributions, so we do not
2046 expect to entirely lose our sensitivity. This motivated a study examining our $\langle\sigma v\rangle$ sensitivity over
2047 all DM masses sampled for a selection of declinations.

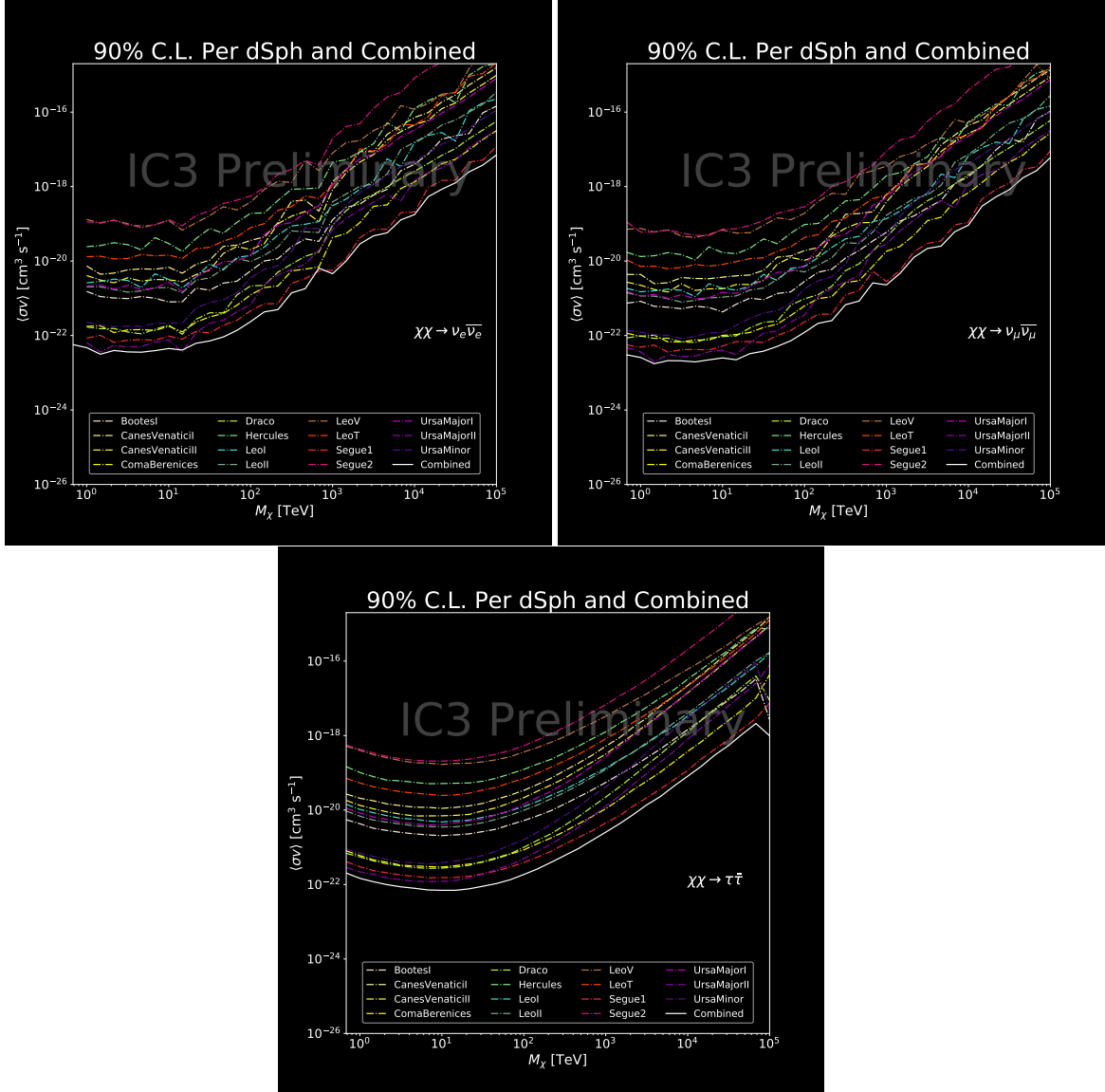


Figure 7.25 IceCube North Sky Track Sensitivities. Each panel shows sensitivity curves for various DM annihilation channels. Sensitivities are for the velocity-weighted cross-section $\langle\sigma v\rangle$ versus m_χ . Dotted, colored lines are sensitivities for individual sources. Solid white lines are for the combined sensitivity of all 15 \mathcal{GS} sources used in this study.

For this systematic study, I sample 6 DM masses per decade from 681 GeV to 100 PeV. I select declinations that are shared with sources in the \mathcal{GS} catalog: Boötes I, Canes Venatici II, Leo V, Ursa Major I, and Ursa Minor. I study a fake source who's J -factor is shared with Ursa Major II, but who's coordinates belong to the aforementioned list. The sensitivity studies performed for each source (Fig. 7.25 and Section C.5) provided n_s for 1000 trials which we extracted from Eq. (7.8). We derive $\langle\sigma v\rangle$ using $\log_{10} J = 19.42 \log_{10}(\text{GeV}^2 \text{cm}^{-5})$. Figure 7.28 shows the results.

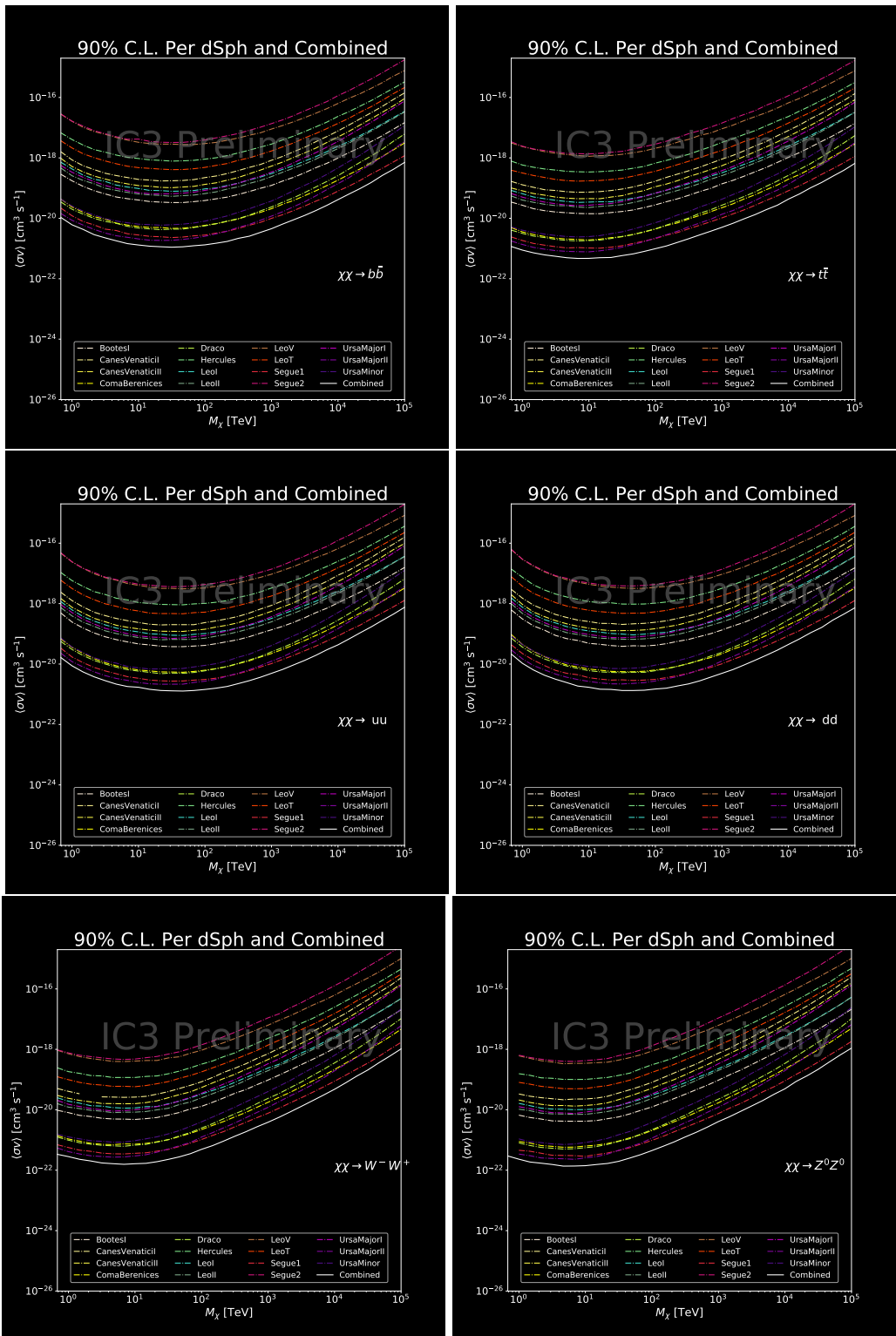


Figure 7.26 Same as Fig. 7.25 for three additional DM annihilation channels.

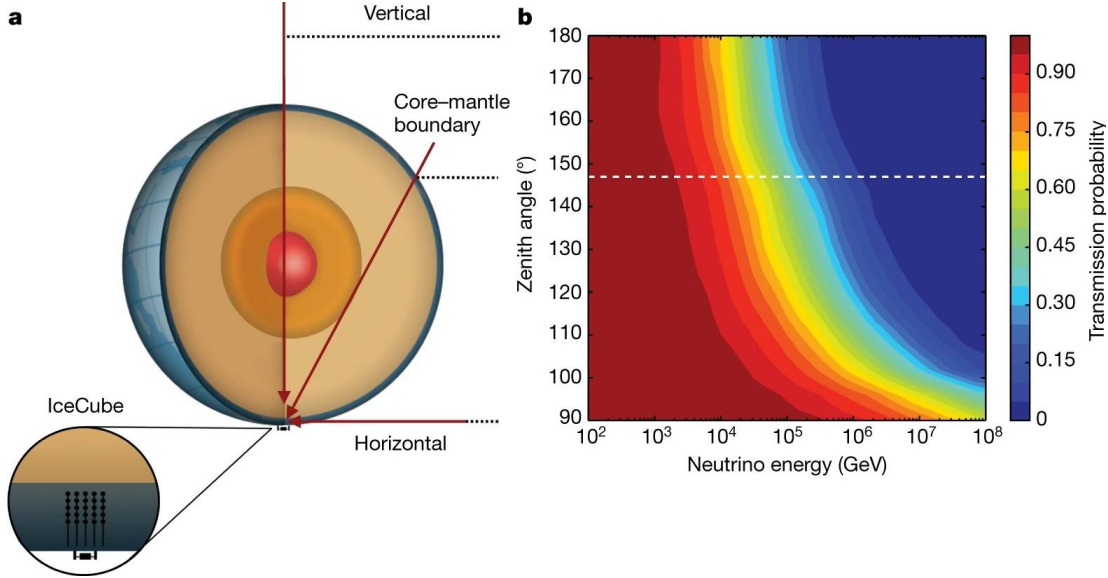


Figure 7.27 Panel A: Neutrino's from the Northern sky and incident on the IceCube detector will travel through the Earth. How much of the Earth these neutrinos travels is a function of zenith from the vertical axis. Panel B: SM prediction of neutrino transmission probabilities for neutrinos arriving at $90^\circ - 180^\circ$ zenith and with 100 GeV to 100 PeV energies. High-energy neutrinos traversing the whole Earth are completely absorbed, whereas low-energy neutrinos pass through unimpeded. Neutrinos coming from above the horizon will arrive unimpeded for all neutrino energies. Figure pulled from [93].

2054 Figure 7.28 shows that we have significant but diminishing sensitivity to sources at high
 2055 declination. We see in the worse case, the sensitivity at high declination is up to an order of
 2056 magnitude worse than at low declination. However, for $m_\chi < 1$ PeV, the sensitivities are very
 2057 similar. The comparable sensitivities imply that a stacking analysis with IceCube is most powerful
 2058 in the 500 GeV to 1 PeV region. Above 1 PeV, our limits and sensitivities are dominated by sources
 2059 near the horizon. When we additionally consider the J -factors, we expect Segue 1 to dominate
 2060 contributions to sensitivity and limits where $m_\chi > 1$ PeV.

2061 **7.8 Conclusions**

2062 We utilized advanced computing techniques like parallel programming and spline fitting of
 2063 particle physics Monte Carlo to greatly expand and refine IceCube's sensitivity to DM annihilation
 2064 from dSphs. Furthermore, we imported updated astrophysical and particle physics models that
 2065 better represent what we believe neutrino signals from DM annihilation should look like. We, for
 2066 the first time, build an analysis that is sensitive to PeV DM annihilation.

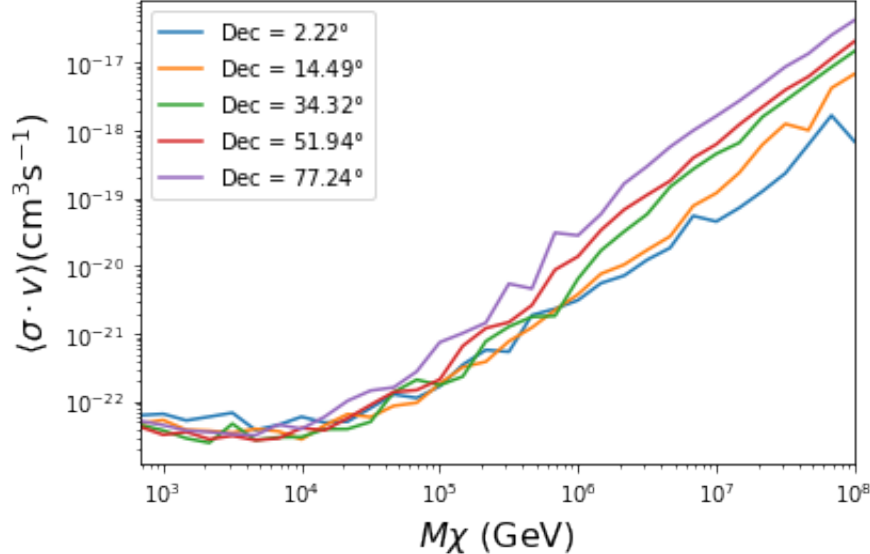


Figure 7.28 $\langle \sigma v \rangle$ sensitivities for 5 imaginary sources with $\log_{10} J = 19.42$ $\log_{10}(\text{GeV}^2 \text{cm}^{-5})$. Each imaginary source shares a declination with a source in Tab. 4.1

When we compare to previous IceCube publications of dSphs [84], we see an order of magnitude improvement to our sensitivity. This analysis has been working group approved within IceCube and is currently under collaboration review before unblinding. These processes did not complete in time for this dissertation. Therefore we do not show data for this thesis and is the clear next step.

The test statistic distributions in this analysis also demonstrate more characteristic behavior compared to previous DM analyses [88, 92]. With a 10-year dataset, we finally have enough statistics to almost trivially combine with other photon observatories, such as HAWC. The first groundwork for a multi-messenger DM search is provided with concluding remarks in chapter 8.

CHAPTER 8

2075 NU DUCK: CONCLUSIONS AND FUTURE DIRECTIONS

2076 8.1 Conclusions

2077 **TODo: Chat GPT the shit of everything below**In this work, three analyses were performed
2078 with data from the HAWC and IceCube observatories in order to explore some of the fundamental
2079 questions in particle astrophysics. Thegoal was to contribute to the understanding of the sources of
2080 cosmic rays, their acceleration mechanisms, and the nature of dark matter. The detection techniques
2081 and reconstruction methods for both observatories were described, along with the properties that
2082 make them ideal instruments to perform such searches.

2083 This dissertation used data from the HAWC detector to probe cutting-edge physics beyond
2084 the Standard Model. The techniques by which HAWC is able to detect cosmic gamma rays were
2085 demonstrated and the many advantages of HAWC in probing ultra-high energy gamma-ray physics
2086 were detailed. It was shown how HAWC data can be used to explore unanswered questions such as
2087 the nature of dark matter and the limits of Lorentz invariance. In particular, a search for evidence of
2088 WIMP dark matter in the Milky Way Galactic Halo was performed. To accomplish this, simulations
2089 of the dark matter density profile were combined with estimates of the HAWC sensitivity to dark
2090 matter-like energy spectra. This allowed strong constraints on dark matter annihilation and decay
2091 from the Galactic Halo to be derived that are insensitive to the large uncertainties arising from
2092 systematics in the dark matter spatial distribution. Multi-hundred TeV photon spectra were also
2093 significantly detected from HAWC sources within the Galactic Plane. These results lead to the
2094 strongest constraints on Lorentz invariance violation to be published at the time of writing.

2095 The work of this dissertation was made possible by the ongoing development of new algorithms
2096 and reconstruction techniques within the HAWC collaboration. Probing the Galactic Halo required
2097 the creation of a novel background estimation technique that relied on HAWC's wide field of view
2098 and strong ability to discriminate between gamma rays and cosmic rays. Meanwhile, the constraints
2099 on Lorentz invariance violation were enabled by the improved energy resolution from a machine
2100 learning technique. HAWC has recently completed a reprocessing of all archival data using an

updated set of algorithms that can lead to compelling follow-up work on these results. Combining the new background technique with the re-optimized energy estimators will allow for Galactic dark matter to be probed at even higher masses, as well as for analyses that require precise energy resolution such as gamma-ray line searches.

8.2 Future Directions: Multi-Messenger Dark Matter Search

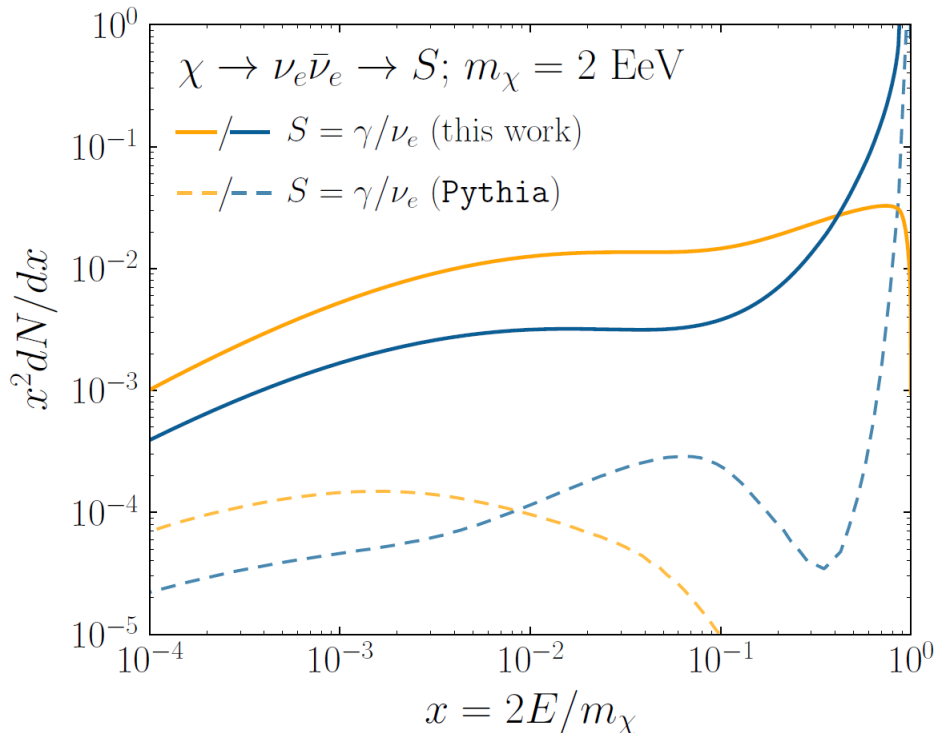


Figure 8.1 The prompt electron neutrino and photon spectrum resulting from the decay of a 2EeV DM particle to $\nu_e \bar{\nu}_e$, as currently being searched for at IceCube [5]. Solid curves represent the results of this work, and predict orders of magnitude more flux at certain energies than the dashed results of Pythia 8.2, one of the only existing methods to generate spectra at these masses. In both cases energy conservation is satisfied: there is a considerable contribution to a δ -function at $x = 1$, associated with events where an initial W or Z was never emitted and thus no subsequent shower developed. Large disagreements are generically observed at these masses for electroweak dominated channels, while the agreement is better for colored initial SM states.

As I have shown previously in Sec. 4 and Sec. 5, we can build a fast and robust analysis that shares tools with the field. The hope being that IceCube can eventually combine data with gamma-ray observatories.



Figure 8.2 TODO: neutrino and bb plot with nu Sensitivities[NEEDS A SOURCE][FACT CHECK THIS]

MULTI-EXPERIMENT SUPPLEMENTARY FIGURES

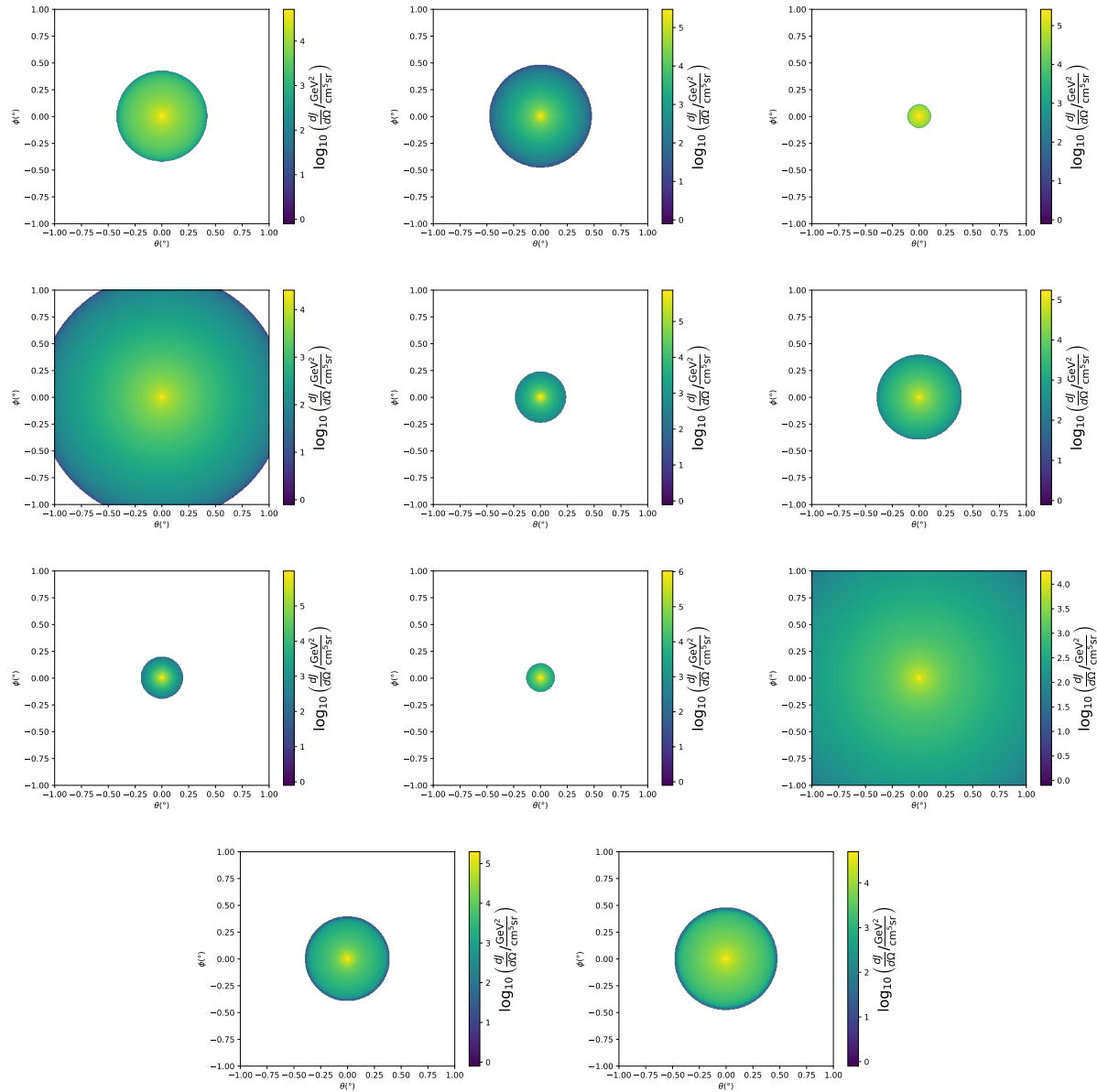


Figure A.1 Sister figure to Figure 4.3. Sources in the first row from left to right: Bootes I, Canes Venatici I, II. In second row: Draco, Hercules, Leo I. In the first row: Leo II, Leo IV, Sextans. In the final row: Ursa Major I, Ursa Major II.

APPENDIX B

MULTITHREADING DARK MATTER ANALYSES SUPPLEMENTARY MATERIAL

2111 B.1 Remaining Spectral Models

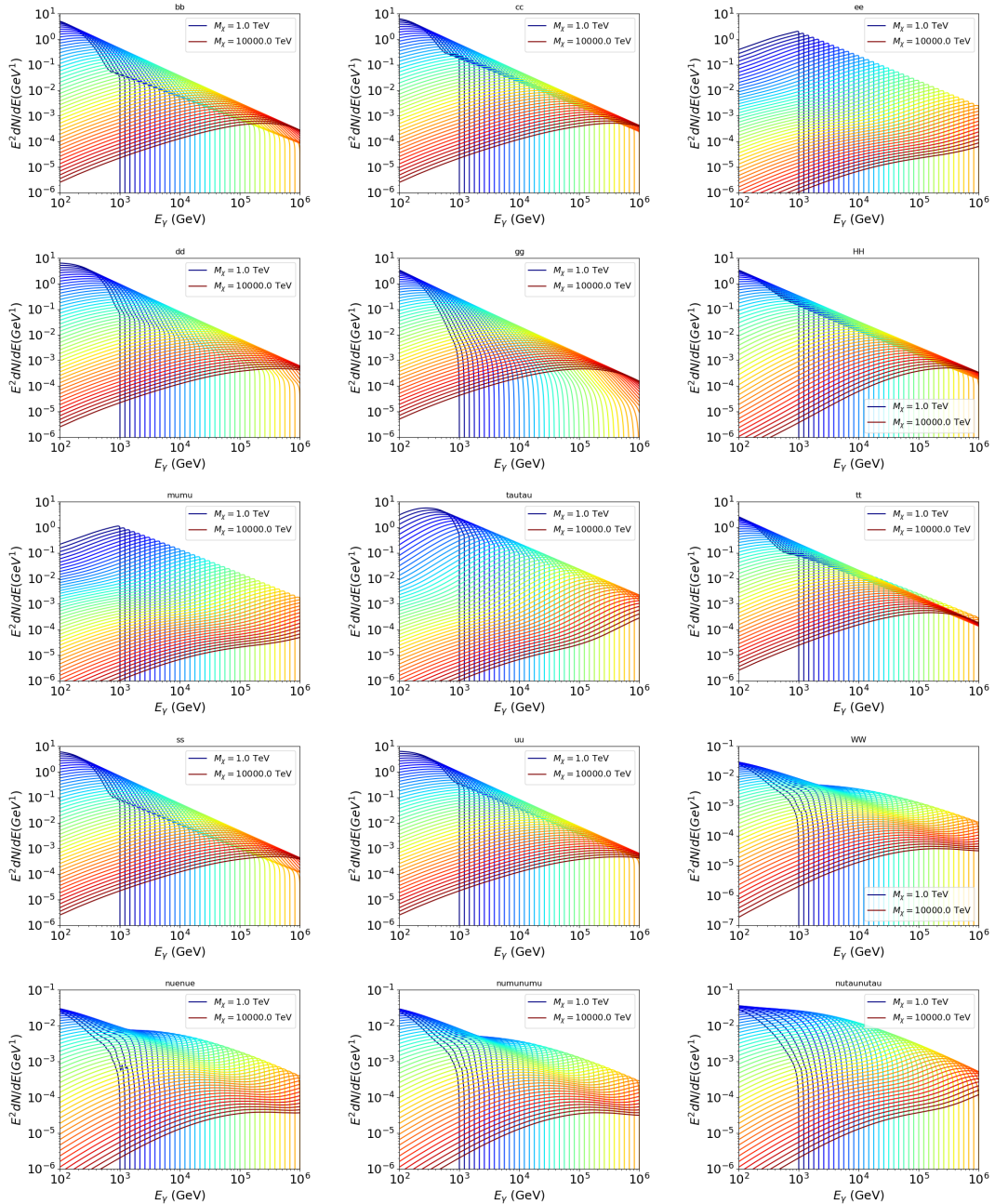


Figure B.1 Sister figure to Figure 5.2 for remaining SM primary annihilation channels studied for this thesis. These did not require any post generation smoothing and so are directly pulled from [79] with a binning scheme most helpful for a HAWC analysis.

2112 B.2 mpu_analysis.py

```
21131 import warnings
21142 with warnings.catch_warnings():
21153     warnings.simplefilter("ignore")
21164 # Python base libraries
21175 import os
21186 import sys
21197 import time
21208 # Import general libraries with namespace
21219 import matplotlib
21220 # Necessary for computing on cluster
21231 matplotlib.use("agg")
21242 import numpy as np
21253 import multiprocessing as mp
21264 # Import HAWC software
21275 sys.path.insert(1, os.path.join(os.environ['HOME'], 'hawc_software', 'threeML-
2128     analysis-scripts', 'fitModel'))
21296 from analysis_modules import *
21307 from threeML import *
21318 from hawc_hal import HAL, HealpixConeROI
21329 from threeML.minimizer.minimization import FitFailed
21330 # Import Dark Matter HAWC Libraries
21341 import analysis_utils as au
21352 import spectra as spec
21363 import sources as srcs
21374
21385 #* READ ONLY PATHS This block will change eventually
21396 MASS_LIST = './plotting/studies/nd/masses.txt'
21407 CHAN_LIST = './plotting/studies/nd/chans.txt'
21418
21429 #* WRITE PATHS, default location is to scratch
21430 OUT_PATH = os.path.join(os.environ["SCRATCH"], os.environ["USER"], 'New_duck')
```

```

21441 print('Our out path is going to be {}'.format(OUT_PATH))
21452
21463 # Define parallel Function. Can also be run serially
21474 def some_mass_fit(sigVs, datalist, shape, dSph, jfactor, mass_chan,
21485                         progress=None, log_file='', queue=None, i_job=0):
21496
21507     if progress is None:
21518         progress = [0]
21529     else: # Create log files for each thread
21530         log_file = log_file.replace('.log', '_ThreadNo_')
21541         log_file = log_file + str(i_job) + ".log"
21552         sys.stdout = open(log_file, "w")
21563
21574     fits = []
21585
21596     try:
21607         for m_c in mass_chan:
21618             print(f'Mass chan tuple: {m_c}')
21629             mass = int(m_c[0])
21630             ch = m_c[1]
21641             # Build path to output files
21652             outPath = os.path.join(OUT_PATH, ch, dSph)
21663             au.ut.ensure_dir(outPath)
21674
21685             if progress[i_job] < 0:
21696                 # If the master gets a Keyboard interrupt, commit suicide.
21707                     break
21718
21729                     ### Start Model Building for DM mass and SM channel #####
21730                     spectrum = spec.DM_models.HDMSpectra()
21741                     spectrum.set_channel(ch)
21752
21763                     myDwarf = ExtendedSource(dSph, spatial_shape=shape,

```

```

21774                     spectral_shape=spectrum)
21785
21796             spectrum.J = jfactor * u.GeV**2 / u.cm**5
21807             spectrum.sigmav = 1e-24 * u.cm**3 / u.s
21818             spectrum.set_dm_mass(mass * u.GeV)
21829
21830             spectrum.sigmav.bounds = (1e-30, 1e-12)
21841             model = Model(myDwarf)
21852             ##### End model Building #####
21863
21874             jl = JointLikelihood(model, datalist, verbose=False)
21885
21896             try:
21907                 result, lhdf = jl.fit(compute_covariance=False)
21918                 ts = -2.* (jl.minus_log_like_profile(1e-30) - jl.
2192 _current_minimum)
21939                 # Also profile the LLH vs sv
21940                 ll = jl.get_contours(spectrum.sigmav, sigVs[0],
21951                                     sigVs[-1], len(sigVs),
21962                                     progress=False, log=['False'])
21973
21984                 sigv_ll = au.ut.calc_95_from_profile(ll[0], ll[2])
21995                 # Write results to file
22006                 outFileLL = outPath+f"/LL_{dSph}_{ch}_mass{int(mass)}_GD.txt"
22017                 np.savetxt(outFileLL, (sigVs, ll[2]),
22028                               delimiter='\t', header='sigV\tLL\n')
22039
22040                 with open(outPath+f"/results_{dSph}_{ch}_mass{int(mass)}_GD.
2205 txt", "w") as results_file:
22061                     results_file.write("mDM [GeV]\tsigV_95\tsigV_B.F.\n")
22072
22083                     results_file.write("%i\t%.5E\t%.5E\t%.5E"%(mass, sigv_ll,
22094                                         ts, result.value[0]))

```

```

22105         # End write to file
22106     except FitFailed: # Don't kill all threads if a fit fails
22107         print("Fit failed. Go back and calculate this spectral model
22108             later")
22109
22110         fits.append((ch, mass, -1, -1))
22111
22112         with open(log_file+'.fail', 'w') as f_file:
22113             f_file.write(f'{ch}, {mass}\n')
22114
22115
22116         progress[i_job] += 1
22117
22118         matplotlib.pyplot.close() # Prevent leaky memory
22119
22120
22121         fits.append((ch, mass, result.value[0], ts))
22122
22123         progress[i_job] += 1
22124
22125         matplotlib.pyplot.close()
22126
22127     except KeyboardInterrupt:
22128
22129         progress[i_job] = -1
22130
22131
22132         fits = np.array(fits)
22133
22134         if queue is None:
22135
22136             return fits
22137
22138         else:
22139
22140             queue.put((i_job, fits))
22141
22142
22143 def main(args):
22144
22145     masses = np.loadtxt(MASS_LIST, dtype=int)
22146
22147     chans = np.loadtxt(CHAN_LIST, delimiter=',', dtype=str)
22148
22149     mass_chan = au.ut.permute_lists(chans, masses)
22150
22151
22152     print(f"DM masses for this study are: {masses}")
22153
22154     print(f"SM Channels for this study are XX -> {chans}")
22155
22156     print(mass_chan)
22157
22158
22159     # extract information from input argument

```

```

22437 dSph = args.dSph
22448 data_mngr = au.ut.Data_Selector('P5_NN_2D')
22459 dm_profile = srcts.Spatial_DM(args.catalog, dSph, args.sigma, args.decay)
22460
22471     ### Extract Source Information ####
22482 if dm_profile.get_dec() < -22.0 or dm_profile.get_dec() > 62.0:
22493     raise ValueError("HAWC can't see this source D: Exitting now...")
22504
22515 print(f'{dSph} information')
22526 print(f'jfac: {dm_profile.get_factor()}\tRA: {dm_profile.get_ra()}\tDec: {dm_profile.get_dec()}\n')
2253
22547
22558 shape = SpatialTemplate_2D(fits_file=dm_profile.get_src_fits())
22569     ### Finish Extract Source Information ####
22570
22581     ### LOAD HAWC DATA ####
22592 roi = HealpixConeROI(data_radius=2.0, model_radius=8.0,
22603                         ra=dm_profile.get_ra(), dec=dm_profile.get_dec())
22614 bins = choose_bins.analysis_bins(args, dec=dm_profile.get_dec())
22625
22636 hawc = HAL(dSph, data_mngr.get_datmap(), data_mngr.get_detres(), roi)
22647 hawc.set_active_measurements(bin_list=bins)
22658 datalist = DataList(hawc)
22669     ### FINISH LOAD HAWC DATA ####
22670
22681 # set up SigV sampling. This sample is somewhat standardized
22692 sigVs = np.logspace(-28,-18, 1001, endpoint=True) # NOTE This will change
2270 with HDM
22713
22724 if args.n_threads == 1:
22735     # No need to start || programming just iterate over the masses
22746     kw_arg = dict(sigVs=sigVs, datalist=datalist, shape=shape, dSph=dSph,
22757                     jfactor=dm_profile.get_factor(), mass_chan=mass_chan,

```

```

22768             log_file=args.log)
22769             some_mass_fit(**kw_arg)
22780         else:
22791             # I Really want to suppress TQMD output
22802             from tqdm import tqdm
22813             from functools import partialmethod
22824             tqdm.__init__ = partialmethod(tqdm.__init__, disable=True)
22835
22846             x = np.array_split(mass_chan, args.n_threads)
22857             n_jobs = len(x)
22868
22879             print("Thread jobs summary by mass and SM channel")
22880             for xi in x:
22891                 print(f'{xi}')
22902
22913             queue = mp.Queue()
22924             progress = mp.Array('i', np.zeros(n_jobs, dtype=int))
22935
22946             # Define task pool that will be split amongsts threads
22957             kw_args = [dict(sigVs=sigVs, datalist=datalist, shape=shape,
22968                             dSph=dSph, jfactor=dm_profile.get_factor(),
22979                             mass_chan=mass_chan, progress=progress,
22980                             queue=queue, i_job=i, log_file=args.log)
22991                 for i, mass_chan in enumerate(x)]
23002
23013             # Define each process
23024             procs = [mp.Process(target=some_mass_fit, kwargs=kw_args[i]) \
23035                 for i in range(n_jobs)]
23046
23057             ### Start MASTER Thread only code block ###
23068             # Begin running all child threads
23079             for proc in procs: proc.start()
23080

```

```

23091     try:
23102         # In this case, the master does nothing except monitor progress of
2311         the threads
23123         # In an ideal world, the master thread also does some computation.
23134         n_complete = np.sum(progress)
23145         while_count = 0
23156
23167             while n_complete < len(mass_chan):
23178
23189                 if np.any(np.asarray(progress) < 0):
23190                     # This was no threads are stranded when killing the script
23201                     raise KeyboardInterrupt()
23212                     if while_count%1000 == 0:
23223                         print(f"{np.sum(progress)} of {len(mass_chan)} finished")
23234
23245                         n_complete = np.sum(progress)
23256                         time.sleep(.25)
23267                         while_count += 1
23278
23289                     except KeyboardInterrupt:
23290                         # signal to jobs that it's time to stop
23301                             for i in range(n_jobs):
23312                                 progress[i] = -2
23323                                 print('\nKeyboardInterrupt: terminating early.')
23334                         ### End MASTER Thread only code block ###
23345
23356                         fitss = [queue.get() for proc in procs]
23367                         print(fitss)
23378                         print(f'Thread statuses: {progress[:]}')
23389
23390                         # putting results in a file
23401
23412                         print("QUACK! All Done!")

```

```

23423
23434
23445 if __name__ == '__main__':
23456     import argparse
23467
23478     p = argparse.ArgumentParser(description="Run a DM annihilation analysis on
2348         a dwarf spheroidal for a specific SM channel for DM masses [1 TeV to 10
2349         PeV]")
23509
23510     # Dwarf spatial modeling arguements
23521     p.add_argument("-ds", "--dSph", type=str,
23532             help="dwarf spheroidal galaxy to be studied", required=
2354        True)
23553     p.add_argument("-cat", "--catalog", type=str, choices=['GS15', 'LS20'],
23564             default='LS20', help="source catalog used")
23575     p.add_argument("-sig", "--sigma", type=int, choices=[-1, 0, 1], default=0,
23586             help="Spatial model uncertainty. 0 corresponds to the
2359 median. +/-1 correspond to the +/-1sigma uncertainty respectively.")
23607
23618     # Arguements for the energy estimators
23629     p.add_argument("-e", "--estimator", type=str,
23630             choices=['P5_NHIT', 'P5_NN_2D'],
23641             default="P5_NN_2D", required=False,
23652             help="The energy estimator choice. Options are: P5_NHIT,
2366 P5_NN_2D. GP not supported (yet).")
23673     p.add_argument("--use-bins", default=None, nargs="*",
23684             help="Bins to use for the analysis", dest="use_bins")
23695     p.add_argument('--select_bins_by_energy', default=None, nargs="*",
23706             help="Does nothing. May fill in later once better
2371 understood")
23727     p.add_argument('--select_bins_by_fhit', default=None, nargs="*",
23738             help="Also does nothing see above")
23749     p.add_argument( '-ex', "--exclude", default=None, nargs="*",

```

```

23750         help="Exclude Bins", dest="exclude")

23761

23772 # Computing and logging arguements.

23783 p.add_argument('-nt', '--n_threads', type=int, default=1,
23794                         help='Maximum number of threads spawned by script. Default
2380      is 4')

23815 p.add_argument('-log', '--log', type=str, required=True,
23826                         help='Name for log files. Especially needed for threads')

23837

23848 p.add_argument('--decay', action="store_true",
23859                         help='Set spectral DM hypothesis to decay')

23860

23871 args = p.parse_args()

23882 print(args.decay)

23893 if args.exclude is None: # default exclude bins 0 and 1
23904     args.exclude = ['B0C0Ea', 'B0C0Eb', 'B0C0Ec', 'B0C0Ed', 'B0C0Ee']

23915

23926 if args.decay: OUT_PATH += '_dec'
23937 else: OUT_PATH += '_ann'

23948

23959 OUT_PATH = OUT_PATH + '_' + args.catalog
23960 if args.sigma != 0: OUT_PATH += f'_{args.sigma}sig'

23971

23982 main(args)

```

2399 **B.3 Comparison with Glory Duck**

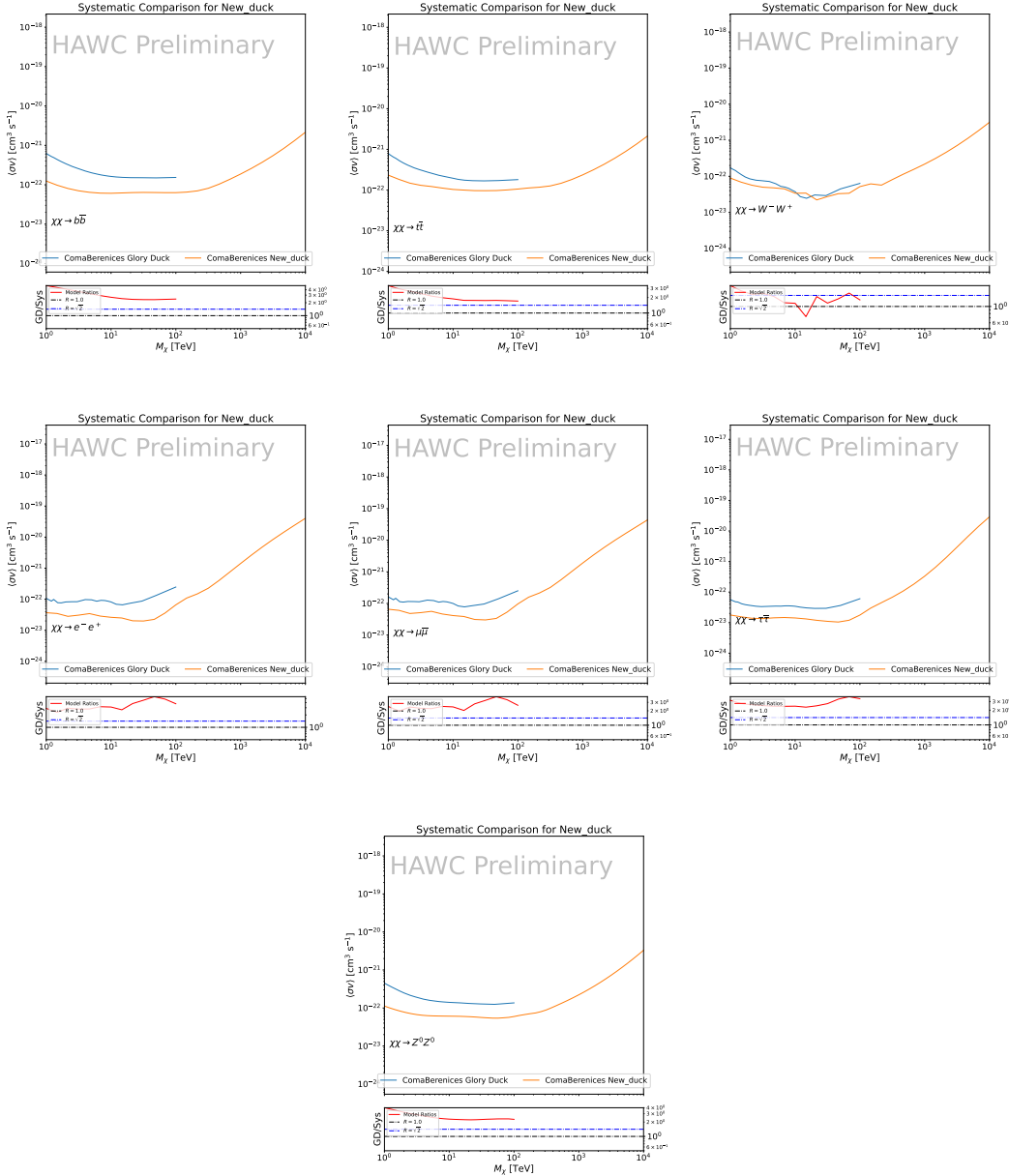


Figure B.2 Comparison of HAWC limits from this analysis to Glory Duck (Fig. 4.5) for Coma Berenices and 7 DM annihilation channels.

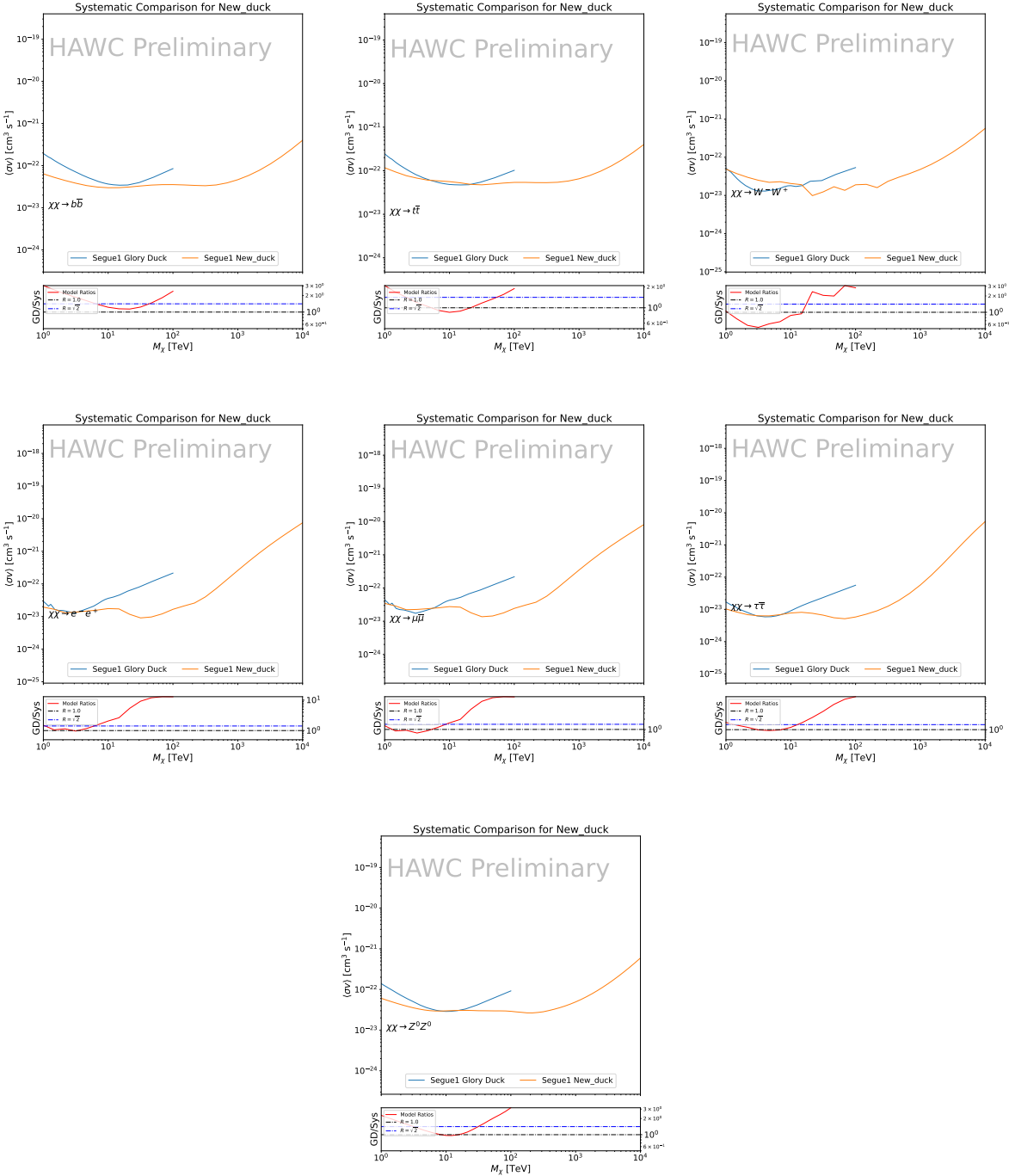


Figure B.3 Same as Fig. B.2 but for Segue 1.

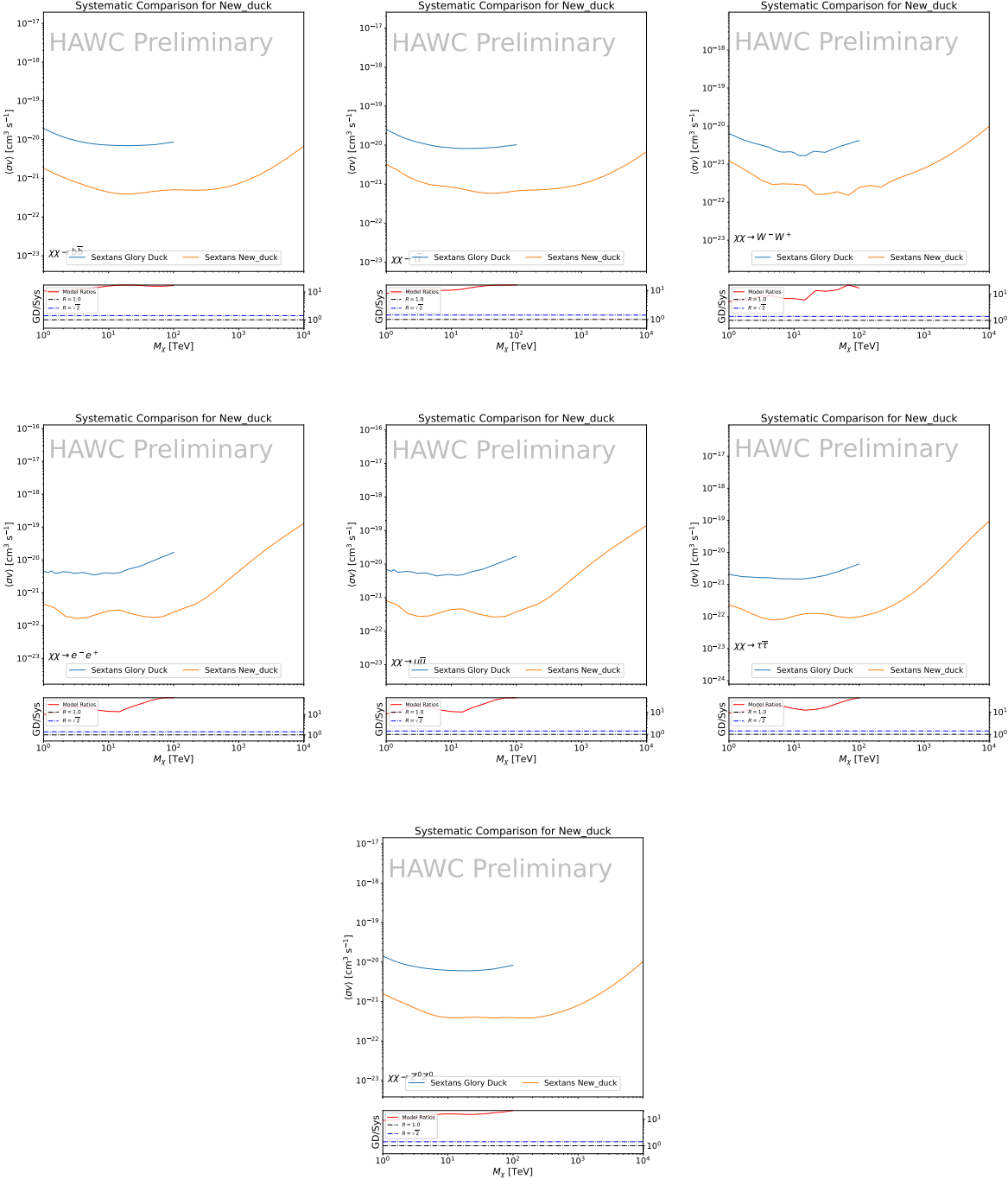


Figure B.4 Same as Fig. B.2 but for Sextans.

APPENDIX C

2400 ICECUBE HEAVY DARK MATTER ANALYSIS SUPPLEMENTARY MATERIAL

2401 C.1 Docker Image for Oscillating Neutrino Spectra

```
24021 FROM ubuntu:18.04
24032
24043 # Execute commands to install software packages
24054 RUN apt -y update
24065
24076 # Install utility programs
24087 RUN apt -y install vim wget git cmake
24098
24109 ARG DEBIAN_FRONTEND=noninteractive
24110
24121 # Install python
24132 RUN apt -y install python python-dev python-pip libjpeg-dev zlib1g-dev
24143
24154 # We need Python2 for installing Charon.
24165 RUN apt -y install python-numpy python-sympy python-matplotlib \
24176           python-sympy python-h5py python-astropy python-ipython
24187
24198 # Install dependencies of Charon : SQuIDS, NuSQuIDS
24209 RUN apt -y install libgsl-dev libgslcblas0 libgsl23 gsl-bin pkg-config
24210 # Install SQuIDS
24221 RUN mkdir /home/SQuIDS /home/SQuIDS_install
24232 WORKDIR /home/SQuIDS
24243 RUN git clone https://github.com/jsalvado/SQuIDS.git
24254 WORKDIR /home/SQuIDS/SQuIDS
24265 RUN git checkout 7ad9ba7c6ad06d1f0fa8418f937ebf1a403fef90
24276 # Before executing "make install" an environmental variable has to be set.
24287 ENV PKG_CONFIG_PATH=/home/SQuIDS/SQuIDS/lib
24298 RUN ./configure --prefix=../SQuIDS_install \
```

```

24309    && make
24310 RUN make install
24321
24322 # Set up an environmental variable that is required to install nuSQuIDS..
24323 ENV SQuIDS=/home/SQuIDS/SQuIDS
24324 ENV LD_LIBRARY_PATH=$SQuIDS/lib:$LD_LIBRARY_PATH
24325
24326 # Install NuSQuIDS
24327 RUN mkdir /home/nuSQuIDS
24328 WORKDIR /home/nuSQuIDS
24329 RUN git clone https://github.com/qrliu/nuSQuIDS.git
24330 WORKDIR /home/nuSQuIDS/nuSQuIDS
24331 RUN git checkout 072d8ef740e2fc7330f1fabaea94f0f4540c46f9
24332 RUN apt -y install libhdf5-dev hdf5-tools
24333 RUN apt -y install libboost1.65-all-dev
24334 RUN ./configure --with-squids=$SQuIDS --with-python-bindings --prefix=../
24335     nuSQuIDS_install \
24336     && make \
24337     && make install
24338
24339 # Set up an environmental variable for nuSQuIDS.
24340 ENV nuSQuIDS=/home/nuSQuIDS/nuSQuIDS
24341 ENV LD_LIBRARY_PATH=$nuSQuIDS/lib:$LD_LIBRARY_PATH
24342
24343 # Build the python bindings
24344 WORKDIR /home/nuSQuIDS/nuSQuIDS/resources/python/src
24345 RUN make
24346
24347
24348 # Set up an environmental variable for the python bindings.
24349 ENV PYTHONPATH=$nuSQuIDS/resources/python/bindings/:$PYTHONPATH
24350
24351 # Install Charon in the /home/Charon/charon directory.
24352 RUN mkdir /home/Charon

```

```
24631 WORKDIR /home/Charon
24642 RUN git clone https://github.com/icecube/charon.git \
24653   && apt -y install unzip python-scipy
24664 WORKDIR charon
24675 RUN git checkout c531efe4e01dc364a60d1c83f950f04526ccd771
24686 RUN unzip ./charon/xsec/xsec.zip -d charon/xsec/ \
24697
24708 # Download neutrino spectra tables in the /home/Charon/charon/data directory
2471 .
24729 && mkdir ./charon/data
24730 WORKDIR ./charon/data
24741 RUN wget --no-check-certificate https://icecube.wisc.edu/~qliu/charon/
2475   SpectraEW.hdf5 \
24762 && wget --no-check-certificate https://icecube.wisc.edu/~qliu/charon/
2477   Spectra_PYTHIA.hdf5 \
24783 && wget --no-check-certificate https://icecube.wisc.edu/~qliu/charon/
2479   Spectra_noEW.hdf5
24804
24815 WORKDIR ../..
24826 RUN python setup.py install
24837 WORKDIR /home
```

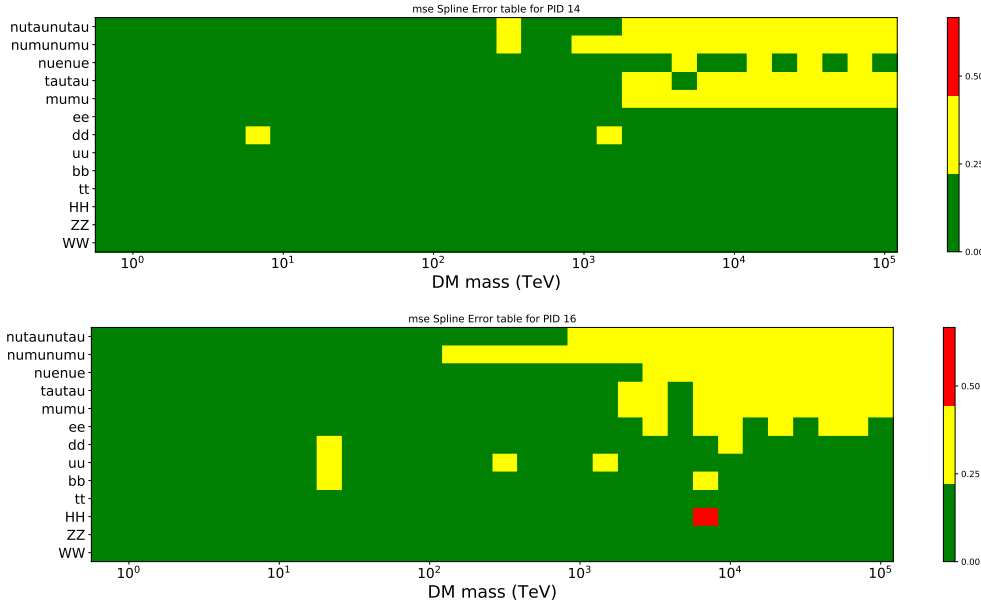


Figure C.1 Current status of spline tables according to constraints defined by Tab. 7.1. Green splines are splines that passed under the GOOD tolerance. Yellow are splines that are OK. Red are splines that FAIL. All yellow splines were inspected individually before running the analysis. Splines were made for the μ (PID 14; top panel) flavor and τ (PID 16; bottom panel) neutrino flavors.

2485 C.3 Neutrino Composite Spectra

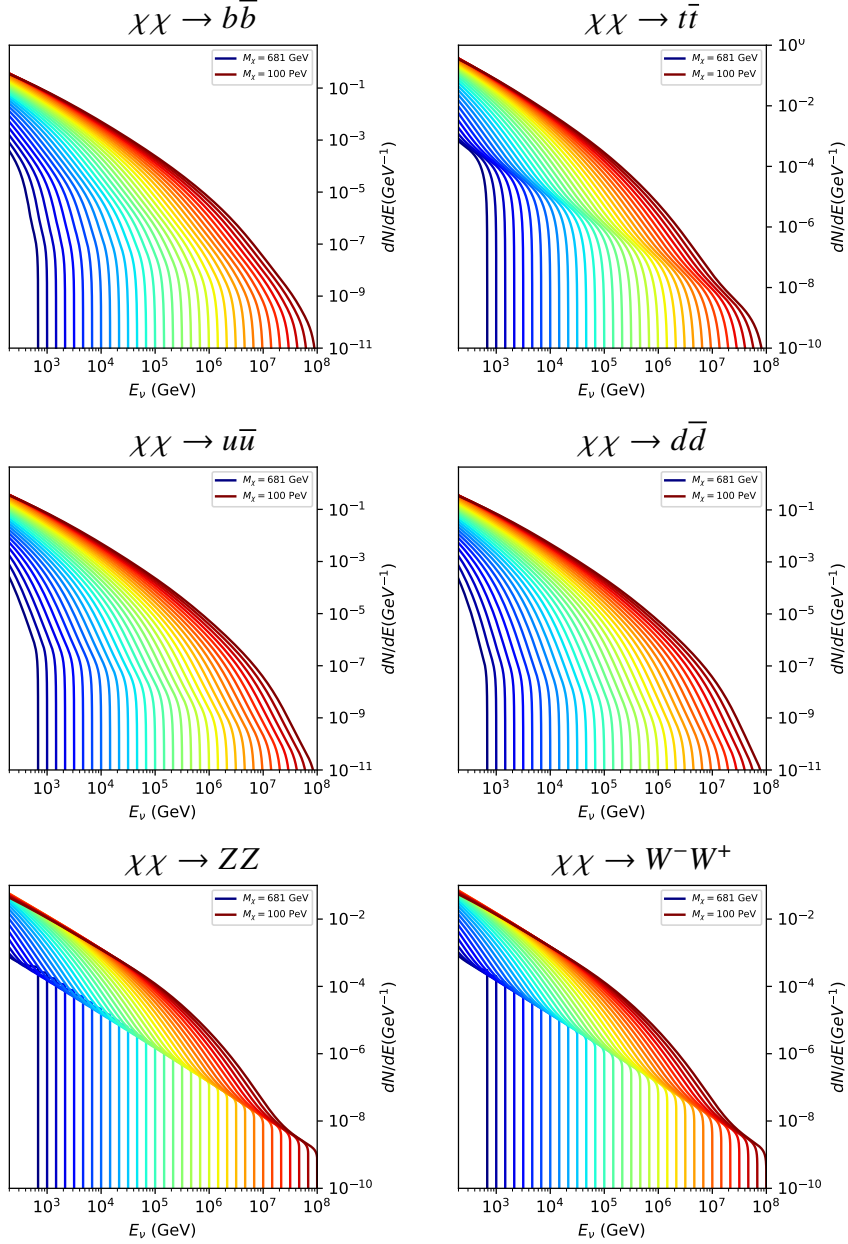


Figure C.2 Sister figure to Fig. 7.5 for annihilation channels that did not require kernel smoothing. These spectra are the composite ($\nu_\mu + \nu_\tau$) of neutrino flavors. Every spectral model used for this analysis is featured as a colored solid line. Bluer lines are for lower DM mass spectral models. DM masses range from 681 GeV to 100 PeV.

2486 C.4 Segue 1 And Ursa Major II Signal Recovery

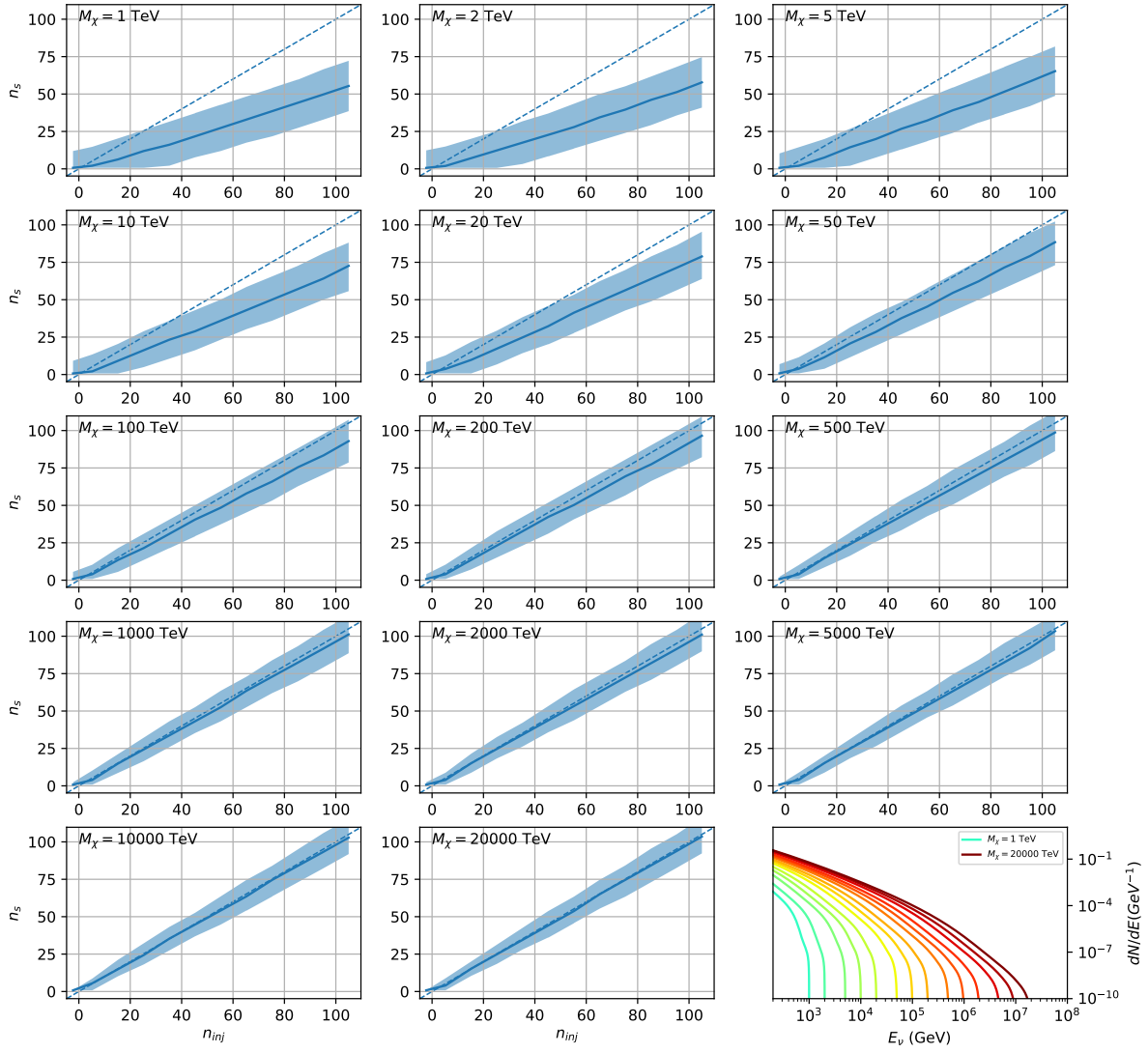


Figure C.3 Same as Fig. 7.23 but for Segue 1 and $\chi\chi \rightarrow b\bar{b}$.

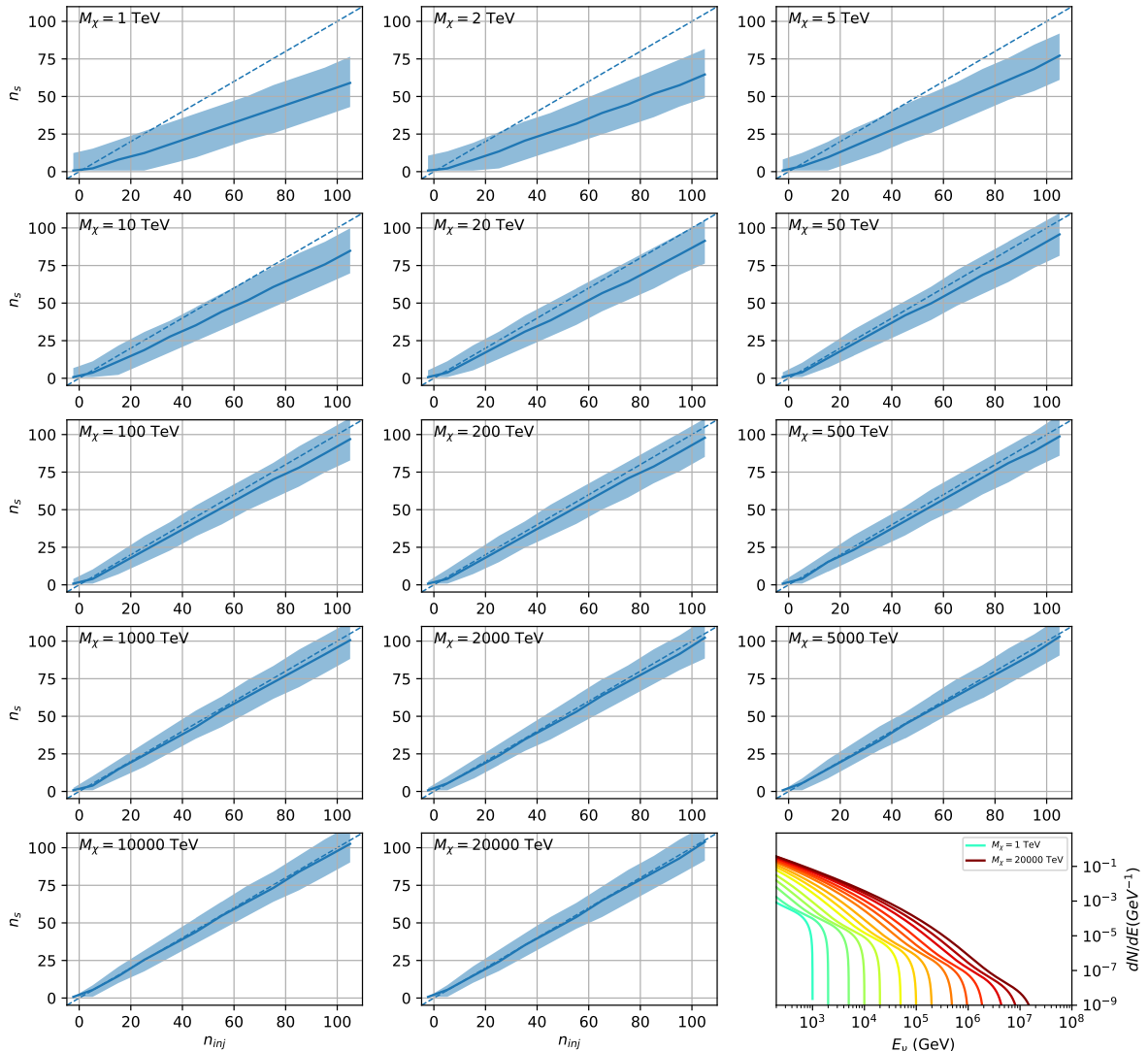


Figure C.4 Same as Fig. 7.23 but for Segue 1 and $\chi\chi \rightarrow t\bar{t}$.

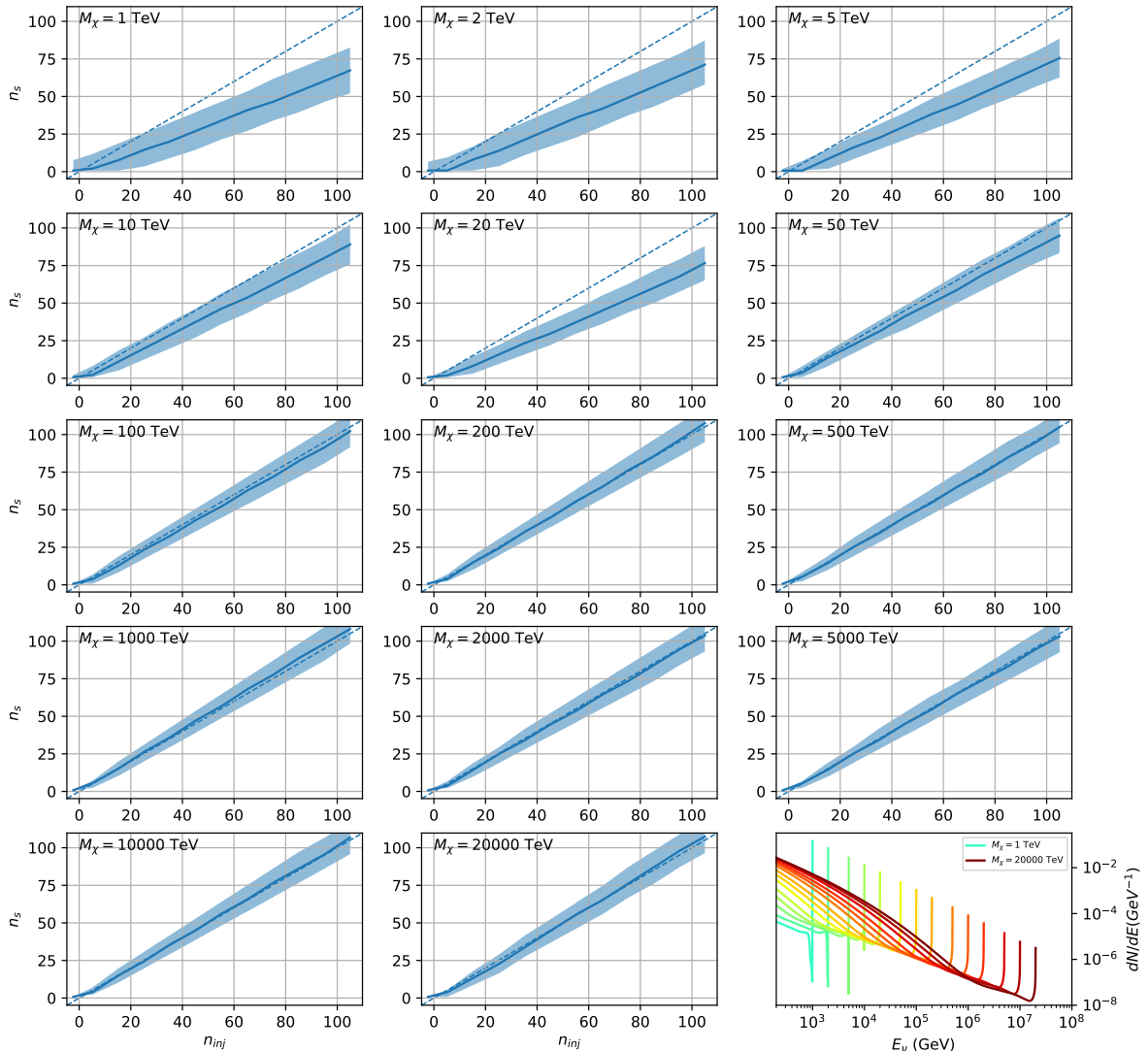


Figure C.5 Same as Fig. 7.23 but for Segue 1 and $\chi\chi \rightarrow \nu_\mu \bar{\nu}_\mu$.

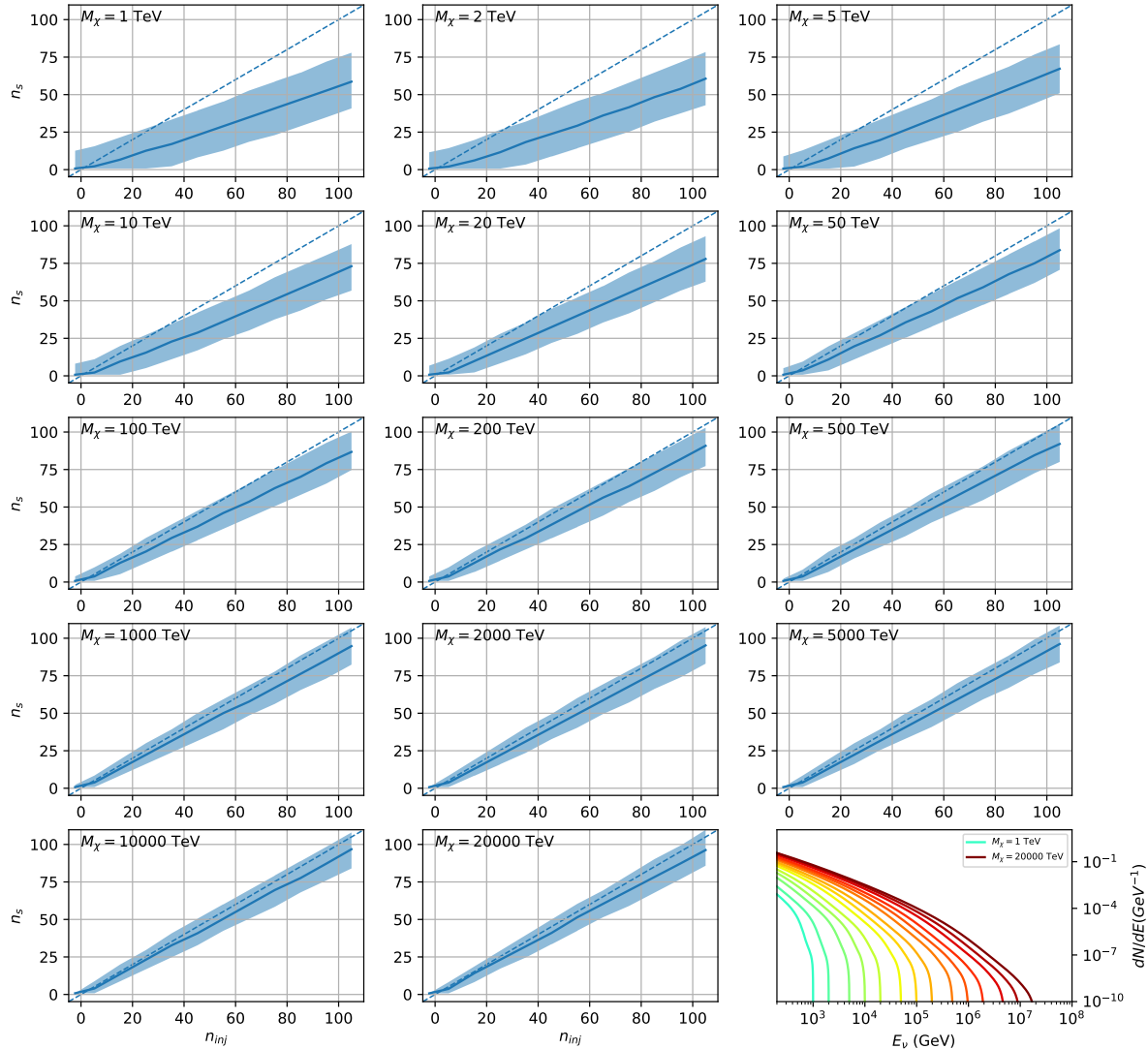


Figure C.6 Same as Fig. 7.23 but for Ursa Major II and $\chi\chi \rightarrow b\bar{b}$.

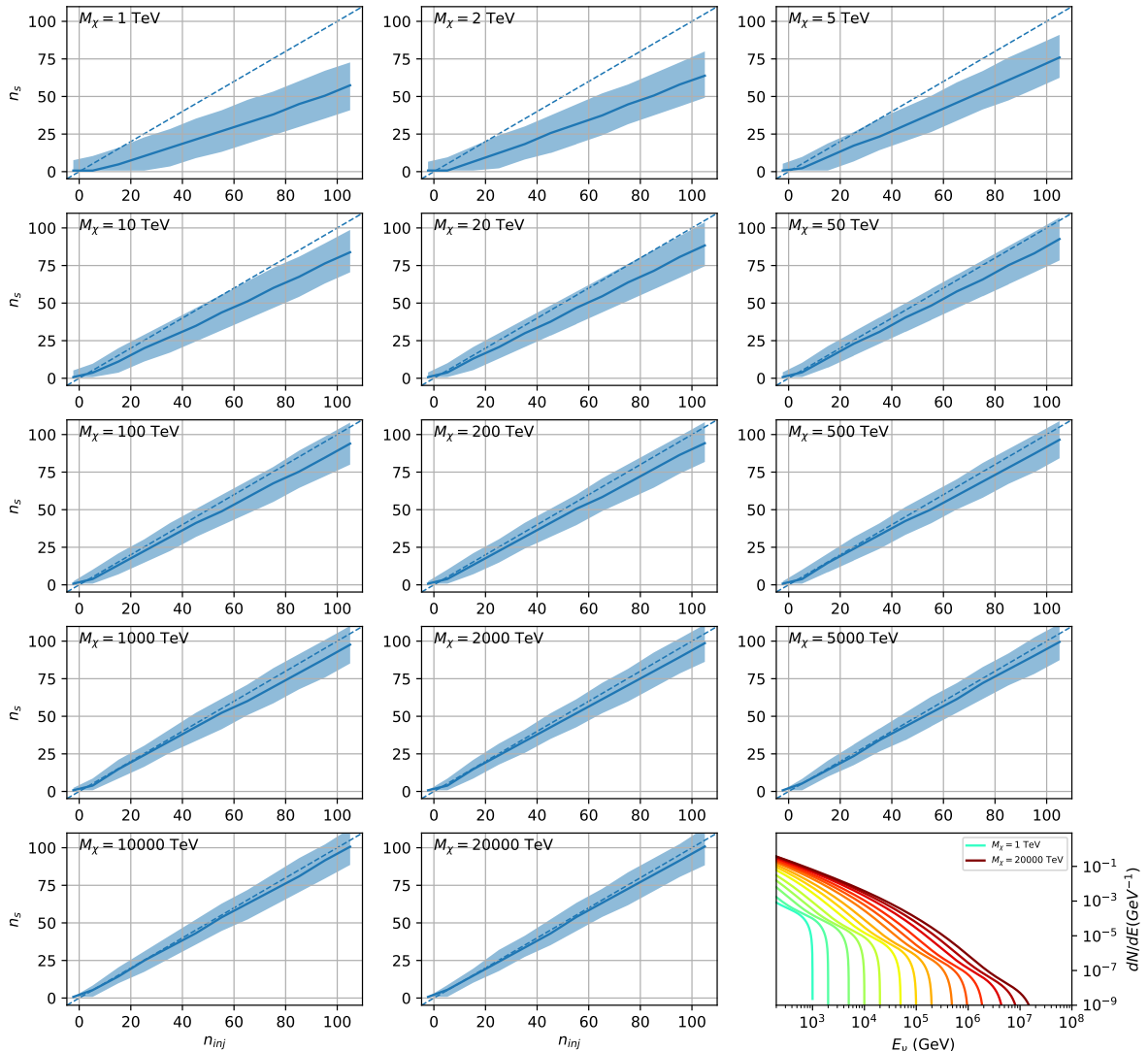


Figure C.7 Same as Fig. 7.23 but for Ursa Major II and $\chi\chi \rightarrow t\bar{t}$.

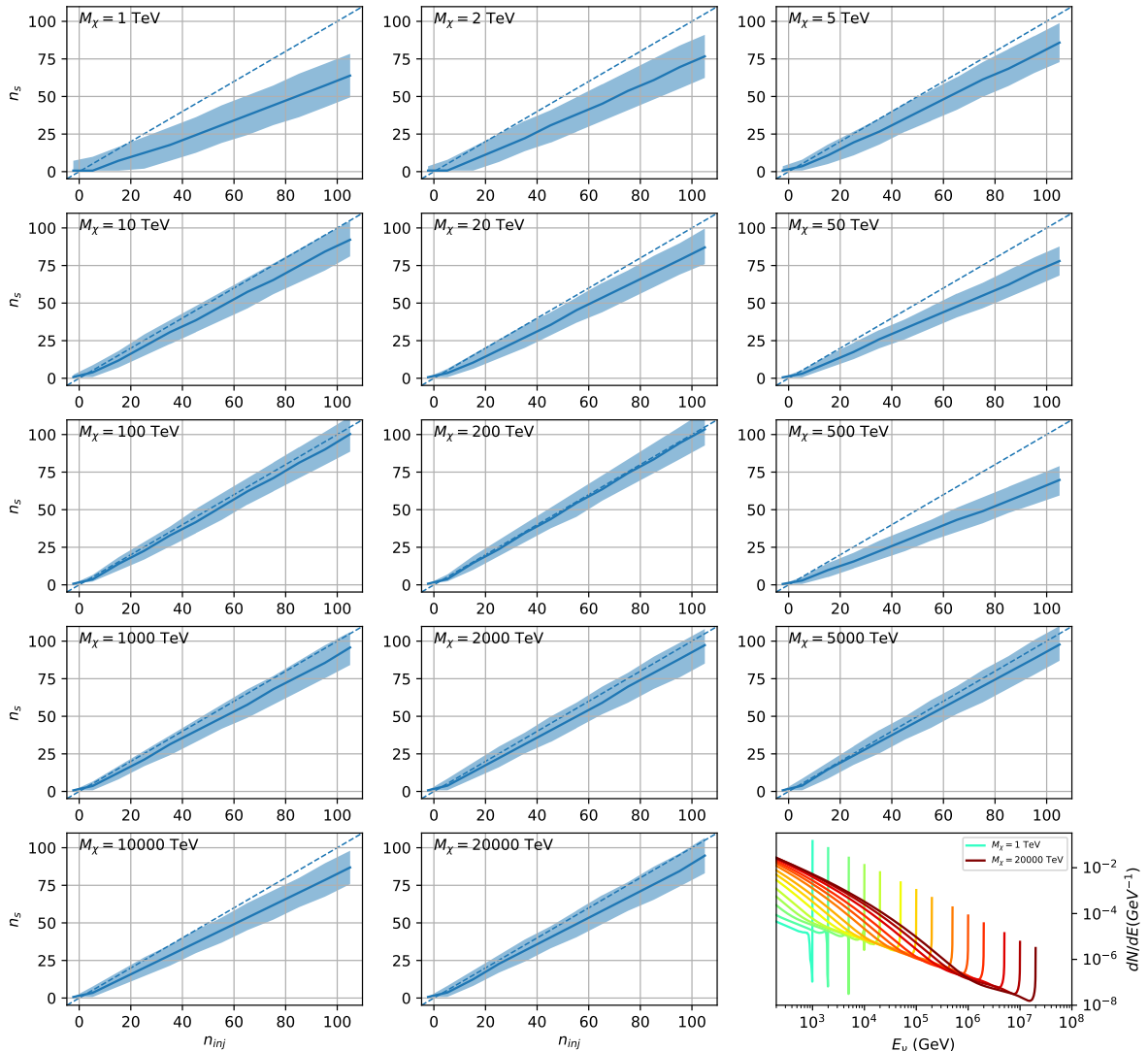


Figure C.8 Same as Fig. 7.23 but for Ursa Major II and $\chi\chi \rightarrow \nu_\mu \bar{\nu}_\mu$.

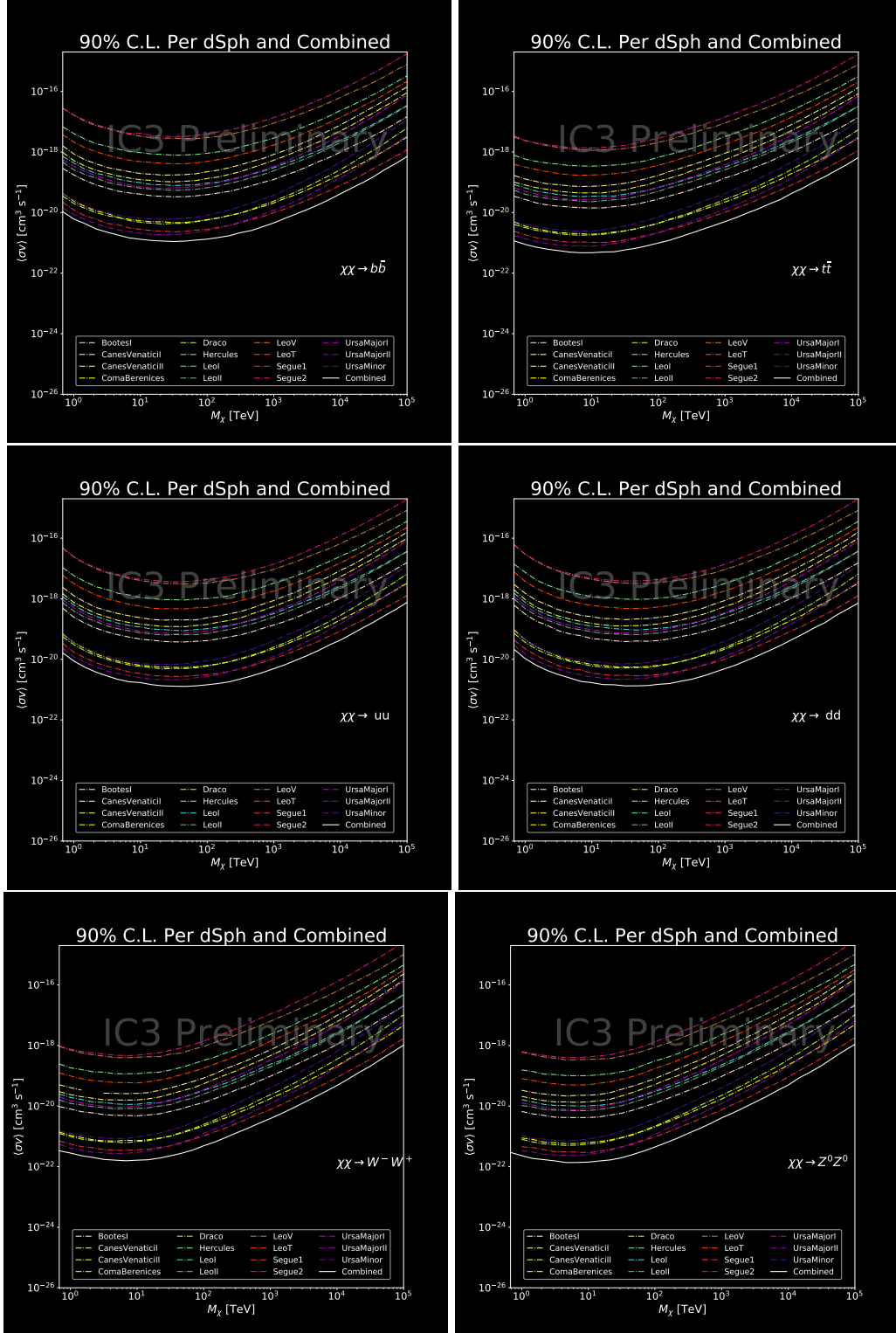


Figure C.9 IceCube North Sky Track Sensitivities for $n_s/\langle N \rangle$. n_s values are the counts fed into Eq. (7.8) to produce Fig. 7.26 and Fig. 7.25.

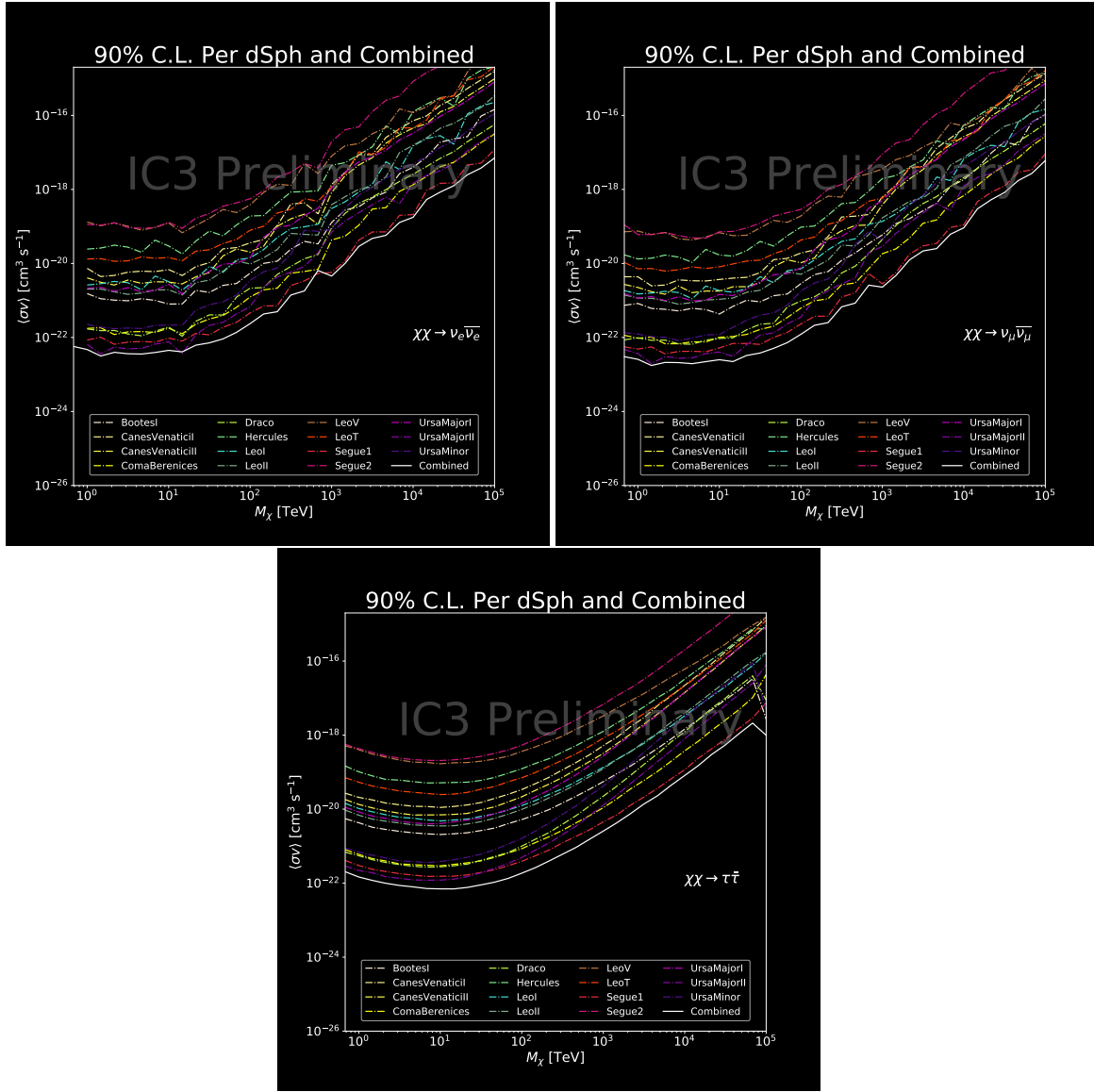


Figure C.10 Same as Fig. C.9 for three additional DM annihilation channels.

BIBLIOGRAPHY

- 2489 [1] Anne M. Green. “Dark matter in astrophysics/cosmology”. In: *SciPost Phys. Lect.*
 2490 *Notes* (2022), p. 37. doi: [10.21468/SciPostPhysLectNotes.37](https://doi.org/10.21468/SciPostPhysLectNotes.37). URL: <https://scipost.org/10.21468/SciPostPhysLectNotes.37>.
- 2492 [2] Bing-Lin Young. “A survey of dark matter and related topics in cosmology”. In: *Frontiers*
 2493 *of Physics* 12 (Oct. 2016). doi: <https://doi.org/10.1007/s11467-016-0583-4>.
 2494 URL: <https://doi.org/10.1007/s11467-016-0583-4>.
- 2495 [3] Gianfranco Bertone, Dan Hooper, and Joseph Silk. “Particle dark matter: evidence,
 2496 candidates and constraints”. In: *Physics Reports* 405.5 (2005), pp. 279–390. ISSN:
 2497 0370-1573. doi: <https://doi.org/10.1016/j.physrep.2004.08.031>. URL:
 2498 <https://www.sciencedirect.com/science/article/pii/S0370157304003515>.
- 2499 [4] Gianfranco Bertone and Dan Hooper. “History of dark matter”. In: *Rev. Mod. Phys.*
 2500 90 (4 Aug. 2018), p. 045002. doi: [10.1103/RevModPhys.90.045002](https://doi.org/10.1103/RevModPhys.90.045002). URL: <https://link.aps.org/doi/10.1103/RevModPhys.90.045002>.
- 2502 [5] Fritz Zwicky. “The Redshift of Extragalactic Nebulae”. In: *Helvetica Physica Acta* 6.
 2503 (1933), pp. 110–127. doi: [10.5169/seals-110267](https://doi.org/10.5169/seals-110267).
- 2504 [6] Vera C. Rubin and Jr. Ford W. Kent. “Rotation of the Andromeda Nebula from a
 2505 Spectroscopic Survey of Emission Regions”. In: *ApJ* 159 (Feb. 1970), p. 379. doi:
 2506 [10.1086/150317](https://doi.org/10.1086/150317).
- 2507 [7] K. G. Begeman, A. H. Broeils, and R. H. Sanders. “Extended rotation curves of spiral galax-
 2508 ies: dark haloes and modified dynamics”. In: *Monthly Notices of the Royal Astronomical So-*
 2509 *ciety* 249.3 (Apr. 1991), pp. 523–537. ISSN: 0035-8711. doi: [10.1093/mnras/249.3.523](https://doi.org/10.1093/mnras/249.3.523).
 2510 eprint: <https://academic.oup.com/mnras/article-pdf/249/3/523/18160929/mnras249-0523.pdf>. URL: <https://doi.org/10.1093/mnras/249.3.523>.
- 2512 [8] *Different types of gravitational lenses*. website. Feb. 2004. URL: <https://esahubble.org/images/heic0404b/>.
- 2514 [9] Douglas Clowe et al. “A Direct Empirical Proof of the Existence of Dark Matter”. In: *apjl*
 2515 648.2 (Sept. 2006), pp. L109–L113. doi: [10.1086/508162](https://doi.org/10.1086/508162). arXiv: [astro-ph/0608407](https://arxiv.org/abs/astro-ph/0608407)
 2516 [[astro-ph](#)].
- 2517 [10] Planck Collaboration and N. et. al. Aghanim. “Planck 2018 results I. Overview and the
 2518 cosmological legacy of Planck”. In: *A&A* 641 (2020). doi: [10.1051/0004-6361/201833880](https://doi.org/10.1051/0004-6361/201833880). URL: <https://doi.org/10.1051/0004-6361/201833880>.
- 2520 [11] Wayne Hu. *Matter Density Animation*. web. 2024. URL: <http://background.uchicago.edu/~whu/animbut/anim2.html>.

- 2522 [12] Wenlong Yuan et al. “A First Look at Cepheids in a Type Ia Supernova Host with JWST”. in:
2523 *The Astrophysical Journal Letters* 940.1 (Nov. 2022). doi: [10.3847/2041-8213/ac9b27](https://doi.org/10.3847/2041-8213/ac9b27).
2524 URL: <https://dx.doi.org/10.3847/2041-8213/ac9b27>.
- 2525 [13] Wendy L. Freedman. “Measurements of the Hubble Constant: Tensions in Perspective”. In:
2526 *The Astrophysical Journal* 919.1 (Sept. 2021), p. 16. doi: [10.3847/1538-4357/ac0e95](https://doi.org/10.3847/1538-4357/ac0e95).
2527 URL: <https://dx.doi.org/10.3847/1538-4357/ac0e95>.
- 2528 [14] Jodi Cooley. “Dark Matter direct detection of classical WIMPs”. In: *SciPost Phys. Lect.*
2529 *Notes* (2022), p. 55. doi: [10.21468/SciPostPhysLectNotes.55](https://doi.org/10.21468/SciPostPhysLectNotes.55). URL: <https://scipost.org/10.21468/SciPostPhysLectNotes.55>.
- 2531 [15] “Search for new phenomena in events with an energetic jet and missing transverse momentum
2532 in pp collisions at $\sqrt{s} = 13$ TeV with the ATLAS detector”. In: *Phys. Rev. D* 103
2533 (11 July 2021), p. 112006. doi: [10.1103/PhysRevD.103.112006](https://doi.org/10.1103/PhysRevD.103.112006). URL: <https://link.aps.org/doi/10.1103/PhysRevD.103.112006>.
- 2535 [16] *Jetting into the dark side: a precision search for dark matter*. website. July 2020. URL:
2536 <https://atlas.cern/updates/briefing/precision-search-dark-matter>.
- 2537 [17] Celine Armand et. al. “Combined dark matter searches towards dwarf spheroidal galaxies
2538 with Fermi-LAT, HAWC, H.E.S.S., MAGIC, and VERITAS”. in: *Proceedings of Science*.
2539 Vol. 395. Mar. 2022. doi: <https://doi.org/10.22323/1.395.0528>.
- 2540 [18] Tracy R. Slatyer. “Les Houches Lectures on Indirect Detection of Dark Matter”. In: *SciPost*
2541 *Phys. Lect. Notes* (2022), p. 53. doi: [10.21468/SciPostPhysLectNotes.53](https://doi.org/10.21468/SciPostPhysLectNotes.53). URL:
2542 <https://scipost.org/10.21468/SciPostPhysLectNotes.53>.
- 2543 [19] Christian W Bauer, Nicholas L. Rodd, and Bryan R. Webber. “Dark matter spectra from
2544 the electroweak to the Planck scale”. In: *Journal of High Energy Physics* 2021.1029-8479
2545 (June 2021). doi: [https://doi.org/10.1007/JHEP06\(2021\)121](https://doi.org/10.1007/JHEP06(2021)121).
- 2546 [20] Riccardo Catena and Piero Ullio. “A novel determination of the local dark matter density”.
2547 In: *Journal of Cosmology and Astroparticle Physics* 2010.08 (Aug. 2010), p. 004. doi:
2548 [10.1088/1475-7516/2010/08/004](https://doi.org/10.1088/1475-7516/2010/08/004). URL: <https://dx.doi.org/10.1088/1475-7516/2010/08/004>.
- 2550 [21] B. P. Abbott et al. “Observation of Gravitational Waves from a Binary Black Hole Merger”.
2551 In: *Phys. Rev. Lett.* 116 (6 Feb. 2016), p. 061102. doi: [10.1103/PhysRevLett.116.061102](https://doi.org/10.1103/PhysRevLett.116.061102). URL: <https://link.aps.org/doi/10.1103/PhysRevLett.116.061102>.
- 2553 [22] R. Abbasi et. al. “Observation of high-energy neutrinos from the Galactic plane”. In: *Science*
2554 380.6652 (June 2023), pp. 1338–1343.
- 2555 [23] NASA Goddard Space Flight Center. *Fermi’s 12-year view of the gamma-ray sky*. website.

- 2556 2022. URL: <https://svs.gsfc.nasa.gov/14090>.
- 2557 [24] Marco Cirelli et al. “PPPC 4 DM ID: a poor particle physicist cookbook for dark matter
2558 indirect detection”. In: *Journal of Cosmology and Astroparticle Physics* 2011.03 (Mar.
2559 2011), p. 051. doi: [10.1088/1475-7516/2011/03/051](https://doi.org/10.1088/1475-7516/2011/03/051). URL: <https://dx.doi.org/10.1088/1475-7516/2011/03/051>.
- 2560
- 2561 [25] The HAWC Collaboration. “The High-Altitude Water Cherenkov (HAWC) observatory in
2562 México: The primary detector”. In: *Nuclear Instruments and Methods in Physics Research
2563 Section A: Accelerators, Spectrometers, Detectors and Associated Equipment* 1052 (2023),
2564 p. 168253. ISSN: 0168-9002. doi: <https://doi.org/10.1016/j.nima.2023.168253>.
2565 URL: <https://www.sciencedirect.com/science/article/pii/S0168900223002437>.
- 2566
- 2567 [26] Alicia Lopez Oramas. “Multi-year Campaign of the Gamma-Ray Binary LS I +61° 303
2568 and Search for VHE Emission from Gamma-Ray Binary Candidates with the MAGIC
2569 Telescopes”. PhD thesis. Instituto de Astrofísica de Canarias, 2014. doi: <http://dx.doi.org/10.13140/RG.2.1.4140.4969>.
- 2570
- 2571 [27] A.U. Abeysekara et. al. “The High-Altitude Water Cherenkov (HAWC) observatory in Méx-
2572 ico: The primary detector”. In: *Nuclear Instruments and Methods in Physics Research
2573 Section A: Accelerators, Spectrometers, Detectors and Associated Equipment* 1052 (2023),
2574 p. 168253. ISSN: 0168-9002. doi: <https://doi.org/10.1016/j.nima.2023.168253>.
2575 URL: <https://www.sciencedirect.com/science/article/pii/S0168900223002437>.
- 2576
- 2577 [28] Hamamatsu Photonics KK. *Large Photocathode Area Photomultiplier Tubes*. 2019. URL:
2578 https://www.hamamatsu.com/content/dam/hamamatsu-photonics/sites/documents/99_SALES_LIBRARY/etd/LARGE_AREA_PMT TPMH1376E.pdf.
- 2579
- 2580 [29] The HAWC Collaboration. “Data acquisition architecture and online processing system
2581 for the HAWC gamma-ray observatory”. In: *Nuclear Instruments and Methods in Physics
2582 Research Section A: Accelerators, Spectrometers, Detectors and Associated Equipment* 888
2583 (2018), pp. 138–146. ISSN: 0168-9002. doi: <https://doi.org/10.1016/j.nima.2018.01.051>. URL: <https://www.sciencedirect.com/science/article/pii/S0168900218300688>.
- 2584
- 2585
- 2586 [30] The Milagro Collaboratio. “Milagrito, a TeV air-shower array”. In: *Nuclear Instruments
2587 and Methods in Physics Research Section A: Accelerators, Spectrometers, Detectors and
2588 Associated Equipment* 449.3 (2000), pp. 478–499. ISSN: 0168-9002. doi: [https://doi.org/10.1016/S0168-9002\(00\)00146-7](https://doi.org/10.1016/S0168-9002(00)00146-7). URL: <https://www.sciencedirect.com/science/article/pii/S0168900200001467>.
- 2589
- 2590
- 2591 [31] Ian Gabriel Wisher. “Real-time Transient Monitoring With the HAWC Detector: Design
2592 and Performance”. PhD thesis. The University of Wisconsin - Madison, 2016.

- 2593 [32] The ZeroMQ authors. “ZeroMQ An open-source universal messaging library”. In: (2021).
2594 URL: <https://zeromq.org>.
- 2595 [33] Zigfried Hampel-Archisman. “Cosmic Ray Observations at the TeV Scale with the HAWC
2596 Observatory”. PhD thesis. University of Wisconsin-Madison, 2017.
- 2597 [34] A. U. Abeysekara et al. “Observation of the Crab Nebula with the HAWC Gamma-Ray
2598 Observatory”. In: *The Astrophysical Journal* 843.1 (June 2017), p. 39. doi: [10.3847/1538-4357/aa7555](https://doi.org/10.3847/1538-4357/aa7555). URL: <https://doi.org/10.3847/1538-4357/aa7555>.
- 2600 [35] Kenneth Greisen. “Cosmic Ray Showers”. In: *ANNUAL REVIEW OF NUCLEAR AND
2601 PARTICLE SCIENCE* 10 (1960), pp. 63–108.
- 2602 [36] The HAWC Collabortion. “Sensitivity of the high altitude water Cherenkov detector to
2603 sources of multi-TeV gamma rays”. In: *Astroparticle Physics* 50-52 (2013), pp. 26–32. ISSN:
2604 0927-6505. doi: <https://doi.org/10.1016/j.astropartphys.2013.08.002>. URL:
2605 <https://www.sciencedirect.com/science/article/pii/S0927650513001230>.
- 2606 [37] The HAWC Collaboration. “Measurement of the Crab Nebula Spectrum Past 100 TeV with
2607 HAWC”. in: *The Astrophysical Journal* 881.2 (Aug. 2019), p. 134. doi: [10.3847/1538-4357/ab2f7d](https://doi.org/10.3847/1538-4357/ab2f7d). URL: <https://dx.doi.org/10.3847/1538-4357/ab2f7d>.
- 2609 [38] Samuel Miranelli. “CONSTRAINTS ON LORENTZ-INVARIANCE VIOLATION WITH
2610 THE HAWC OBSERVATORY”. PhD thesis. Michigan State University, 2019.
- 2611 [39] A. A. Abdo et al. “OBSERVATION AND SPECTRAL MEASUREMENTS OF THE
2612 CRAB NEBULA WITH MILAGRO”. in: *The Astrophysical Journal* 750.1 (Apr. 2012),
2613 p. 63. doi: [10.1088/0004-637X/750/1/63](https://doi.org/10.1088/0004-637X/750/1/63). URL: <https://dx.doi.org/10.1088/0004-637X/750/1/63>.
- 2615 [40] Javier Rico. “Gamma-Ray Dark Matter Searches in Milky Way Satellites—A Comparative
2616 Review of Data Analysis Methods and Current Results”. In: *Galaxies* 8.1 (Mar. 2020), p. 25.
2617 doi: [10.3390/galaxies8010025](https://doi.org/10.3390/galaxies8010025). arXiv: [2003.13482 \[astro-ph.HE\]](https://arxiv.org/abs/2003.13482).
- 2618 [41] W. B. Atwood et al. “The Large Area Telescope on the Fermi Gamma-Ray Space Telescope
2619 Mission”. In: *apj* 697.2 (June 2009), pp. 1071–1102. doi: [10.1088/0004-637X/697/2/1071](https://doi.org/10.1088/0004-637X/697/2/1071). arXiv: [0902.1089 \[astro-ph.IM\]](https://arxiv.org/abs/0902.1089).
- 2621 [42] M. Ackermann et al. “Searching for Dark Matter Annihilation from Milky Way Dwarf
2622 Spheroidal Galaxies with Six Years of Fermi Large Area Telescope Data”. In: *prl* 115.23,
2623 231301 (Dec. 2015), p. 231301. doi: [10.1103/PhysRevLett.115.231301](https://doi.org/10.1103/PhysRevLett.115.231301). arXiv:
2624 [1503.02641 \[astro-ph.HE\]](https://arxiv.org/abs/1503.02641).
- 2625 [43] Mattia Di Mauro, Martin Stref, and Francesca Calore. “Investigating the effect of Milky
2626 Way dwarf spheroidal galaxies extension on dark matter searches with Fermi-LAT data”.

- 2627 In: *Phys. Rev. D* 106 (12 Dec. 2022), p. 123032. doi: [10.1103/PhysRevD.106.123032](https://doi.org/10.1103/PhysRevD.106.123032).
2628 URL: <https://link.aps.org/doi/10.1103/PhysRevD.106.123032>.
- 2629 [44] F. et al. Aharonian. “Observations of the Crab Nebula with H.E.S.S.”. In: *Astron. Astrophys.*
2630 457 (2006), pp. 899–915. doi: [10.1051/0004-6361:20065351](https://doi.org/10.1051/0004-6361:20065351). arXiv: [astro-ph/0607333](https://arxiv.org/abs/astro-ph/0607333).
- 2632 [45] J. Albert et al. “VHE γ -Ray Observation of the Crab Nebula and its Pulsar with the MAGIC
2633 Telescope”. In: *The Astrophysical Journal* 674.2 (Feb. 2008), p. 1037. doi: [10.1086/525270](https://doi.org/10.1086/525270). URL: <https://dx.doi.org/10.1086/525270>.
- 2635 [46] N. Park. “Performance of the VERITAS experiment”. In: *Proceedings, 34th International
2636 Cosmic Ray Conference (ICRC2015): The Hague, The Netherlands, July, 30th July - 6th
2637 August*. Vol. 34. 2015, p. 771. arXiv: [1508.07070](https://arxiv.org/abs/1508.07070) [astro-ph.IM].
- 2638 [47] A. Abramowski et al. “H.E.S.S. constraints on Dark Matter annihilations towards the Sculptor
2639 and Carina Dwarf Galaxies”. In: *Astropart. Phys.* 34 (2011), pp. 608–616. doi: [10.1016/j.astropartphys.2010.12.006](https://doi.org/10.1016/j.astropartphys.2010.12.006). arXiv: [1012.5602](https://arxiv.org/abs/1012.5602) [astro-ph.HE].
- 2641 [48] A. Abramowski et al. “Search for dark matter annihilation signatures in H.E.S.S. observations
2642 of Dwarf Spheroidal Galaxies”. In: *Phys. Rev. D* 90 (2014), p. 112012. doi: [10.1103/PhysRevD.90.112012](https://doi.org/10.1103/PhysRevD.90.112012). arXiv: [1410.2589](https://arxiv.org/abs/1410.2589) [astro-ph.HE].
- 2644 [49] H. Abdalla et al. “Searches for gamma-ray lines and ‘pure WIMP’ spectra from Dark
2645 Matter annihilations in dwarf galaxies with H.E.S.S”. in: *JCAP* 11 (2018), p. 037. doi:
2646 [10.1088/1475-7516/2018/11/037](https://doi.org/10.1088/1475-7516/2018/11/037). arXiv: [1810.00995](https://arxiv.org/abs/1810.00995) [astro-ph.HE].
- 2647 [50] J. Aleksić et al. “Optimized dark matter searches in deep observations of Segue 1 with
2648 MAGIC”. in: *JCAP* 1402 (2014), p. 008. doi: [10.1088/1475-7516/2014/02/008](https://doi.org/10.1088/1475-7516/2014/02/008).
2649 arXiv: [1312.1535](https://arxiv.org/abs/1312.1535) [hep-ph].
- 2650 [51] V.A. Acciari et al. “Combined searches for dark matter in dwarf spheroidal galaxies observed
2651 with the MAGIC telescopes, including new data from Coma Berenices and Draco”. In: *Physics of the Dark Universe* (2021), p. 100912. ISSN: 2212-6864. doi: <https://doi.org/10.1016/j.dark.2021.100912>. URL: <https://www.sciencedirect.com/science/article/pii/S2212686421001370>.
- 2655 [52] M. L. Ahnen et al. “Indirect dark matter searches in the dwarf satellite galaxy Ursa Major II
2656 with the MAGIC Telescopes”. In: *JCAP* 1803.03 (2018), p. 009. doi: [10.1088/1475-7516/2018/03/009](https://doi.org/10.1088/1475-7516/2018/03/009). arXiv: [1712.03095](https://arxiv.org/abs/1712.03095) [astro-ph.HE].
- 2658 [53] S. et al. Archambault. “Dark matter constraints from a joint analysis of dwarf Spheroidal
2659 galaxy observations with VERITAS”. in: *prd* 95.8 (Apr. 2017). doi: [10.1103/PhysRevD.95.082001](https://doi.org/10.1103/PhysRevD.95.082001). arXiv: [1703.04937](https://arxiv.org/abs/1703.04937) [astro-ph.HE].

- 2661 [54] Louise Oakes et al. “Combined Dark Matter searches towards dwarf spheroidal galaxies with
2662 Fermi-LAT, HAWC, HESS, MAGIC and VERITAS”. in: *Proceedings of Science*. 2019.
- 2663 [55] Celine Armand et al. on behalf of the Fermi-LAT, HAWC, HESS, MAGIC, VERITAS.
2664 “Combined Dark Matter searches towards dwarf spheroidal galaxies with Fermi-LAT,
2665 HAWC, HESS, MAGIC and VERITAS”. in: *Proceedings of Science*. 2021.
- 2666 [56] Daniel Kerszberg et al. on behalf of the Fermi-LAT, HAWC, HESS, MAGIC, and VER-
2667 TIAS collaborations. “Search for dark matter annihilation with a combined analysis of
2668 dwarf spheroidal galaxies from Fermi-LAT, HAWC, H.E.S.S., MAGIC and VERITAS”. in:
2669 *Proceedings of Science*. 2023.
- 2670 [57] Giacomo Vianello et al. *The Multi-Mission Maximum Likelihood framework (3ML)*. 2015.
2671 arXiv: [1507.08343 \[astro-ph.HE\]](https://arxiv.org/abs/1507.08343).
- 2672 [58] Marco Cirelli et al. “PPPC 4 DM ID: a poor particle physicist cookbook for dark matter
2673 indirect detection”. In: *Journal of Cosmology and Astroparticle Physics* 2011.03 (Mar.
2674 2011). ISSN: 1475-7516. doi: [10.1088/1475-7516/2011/03/051](https://doi.org/10.1088/1475-7516/2011/03/051). URL: <http://dx.doi.org/10.1088/1475-7516/2011/03/051>.
- 2676 [59] Alex Geringer-Sameth, Savvas M. Koushiappas, and Matthew Walker. “DWARF GALAXY
2677 ANNIHILATION AND DECAY EMISSION PROFILES FOR DARK MATTER EXPERI-
2678 MENTS”. in: *The Astrophysical Journal* 801.2 (Mar. 2015), p. 74. ISSN: 1538-4357. doi:
2679 [10.1088/0004-637x/801/2/74](https://doi.org/10.1088/0004-637x/801/2/74). URL: <http://dx.doi.org/10.1088/0004-637X/801/2/74>.
- 2681 [60] A. Albert et al. “Dark Matter Limits from Dwarf Spheroidal Galaxies with the HAWC
2682 Gamma-Ray Observatory”. In: *The Astrophysical Journal* 853.2 (Feb. 2018), p. 154. ISSN:
2683 1538-4357. doi: [10.3847/1538-4357/aaa6d8](https://doi.org/10.3847/1538-4357/aaa6d8). URL: <http://dx.doi.org/10.3847/1538-4357/aaa6d8>.
- 2685 [61] HongSheng Zhao. “Analytical models for galactic nuclei”. In: *Mon. Not. Roy. Astron. Soc.*
2686 278 (1996), pp. 488–496. doi: [10.1093/mnras/278.2.488](https://doi.org/10.1093/mnras/278.2.488). arXiv: [astro-ph/9509122](https://arxiv.org/abs/astro-ph/9509122)
2687 [[astro-ph](https://arxiv.org/abs/astro-ph/9509122)].
- 2688 [62] Julio F. Navarro, Carlos S. Frenk, and Simon D. M. White. “The Structure of Cold Dark
2689 Matter Halos”. In: *ApJ* 462 (May 1996), p. 563. doi: [10.1086/177173](https://doi.org/10.1086/177173). eprint:
2690 [astro-ph/9508025](https://arxiv.org/abs/astro-ph/9508025) ([astro-ph](#)).
- 2691 [63] V. Bonnivard et al. “Spherical Jeans analysis for dark matter indirect detection in dwarf
2692 spheroidal galaxies - Impact of physical parameters and triaxiality”. In: *Mon. Not. Roy.
2693 Astron. Soc.* 446 (2015), pp. 3002–3021. doi: [10.1093/mnras/stu2296](https://doi.org/10.1093/mnras/stu2296). arXiv:
2694 [1407.7822 \[astro-ph.HE\]](https://arxiv.org/abs/1407.7822).
- 2695 [64] M. Ackermann et al. “Searching for Dark Matter Annihilation from Milky Way Dwarf

- 2696 Spheroidal Galaxies with Six Years of Fermi Large Area Telescope Data”. In: *prl* 115.23,
2697 231301 (Dec. 2015), p. 231301. doi: [10.1103/PhysRevLett.115.231301](https://doi.org/10.1103/PhysRevLett.115.231301). arXiv:
2698 [1503.02641 \[astro-ph.HE\]](https://arxiv.org/abs/1503.02641).
- 2699 [65] M. L. Ahnen et al. “Limits to Dark Matter Annihilation Cross-Section from a Combined
2700 Analysis of MAGIC and Fermi-LAT Observations of Dwarf Satellite Galaxies”. In: *JCAP*
2701 1602.02 (2016), p. 039. doi: [10.1088/1475-7516/2016/02/039](https://doi.org/10.1088/1475-7516/2016/02/039). arXiv: [1601.06590](https://arxiv.org/abs/1601.06590)
2702 [astro-ph.HE].
- 2703 [66] Javier Rico et al. *gLike: numerical maximization of heterogeneous joint
2704 likelihood functions of a common free parameter plus nuisance parameters.*
2705 <https://doi.org/10.5281/zenodo.4601451>. Version v0.09.03. Mar. 2021. doi: [10.5281/zenodo.4601451](https://doi.org/10.5281/zenodo.4601451). URL: <https://doi.org/10.5281/zenodo.4601451>.
- 2707 [67] Tjark Miener and Daniel Nieto. *LklCom: Combining likelihoods from different experiments.*
2708 <https://doi.org/10.5281/zenodo.4597500>. Version v0.5.3. Mar. 2021. doi: [10.5281/zenodo.4597500](https://doi.org/10.5281/zenodo.4597500). URL: <https://doi.org/10.5281/zenodo.4597500>.
- 2710 [68] T. Miener et al. “Open-source Analysis Tools for Multi-instrument Dark Matter Searches”.
2711 In: *arXiv e-prints*, arXiv:2112.01818 (Dec. 2021), arXiv:2112.01818. arXiv: [2112.01818](https://arxiv.org/abs/2112.01818)
2712 [astro-ph.IM].
- 2713 [69] Alex Geringer-Sameth and Matthew Koushiappas Savvas M. and Walker. “Dwarf galaxy
2714 annihilation and decay emission profiles for dark matter experiments”. In: *Astrophys.
2715 J.* 801.2 (2015), p. 74. doi: [10.1088/0004-637X/801/2/74](https://doi.org/10.1088/0004-637X/801/2/74). arXiv: [1408.0002](https://arxiv.org/abs/1408.0002)
2716 [astro-ph.CO].
- 2717 [70] Gianfranco Bertone, Dan Hooper, and Joseph Silk. “Particle dark matter: evidence, can-
2718 didates and constraints”. In: *Physics Reports* 405.5-6 (Jan. 2005), pp. 279–390. ISSN:
2719 0370-1573. doi: [10.1016/j.physrep.2004.08.031](https://doi.org/10.1016/j.physrep.2004.08.031). URL: <http://dx.doi.org/10.1016/j.physrep.2004.08.031>.
- 2721 [71] V. Bonnivard et al. “Dark matter annihilation and decay in dwarf spheroidal galaxies: The
2722 classical and ultrafaint dSphs”. In: *Mon. Not. Roy. Astron. Soc.* 453.1 (2015), pp. 849–867.
2723 doi: [10.1093/mnras/stv1601](https://doi.org/10.1093/mnras/stv1601). arXiv: [1504.02048 \[astro-ph.HE\]](https://arxiv.org/abs/1504.02048).
- 2724 [72] A. et al. Albert. “Searching for Dark Matter Annihilation in Recently Discovered Milky Way
2725 Satellites with Fermi-LAT”. in: *Astrophys. J.* 834.2 (2017), p. 110. doi: [10.3847/1538-4357/834/2/110](https://doi.org/10.3847/1538-4357/834/2/110). arXiv: [1611.03184 \[astro-ph.HE\]](https://arxiv.org/abs/1611.03184).
- 2727 [73] Mattia Di Mauro and Martin Wolfgang Winkler. “Multimessenger constraints on the dark
2728 matter interpretation of the Fermi-LAT Galactic Center excess”. In: *prd* 103.12, 123005
2729 (June 2021), p. 123005. doi: [10.1103/PhysRevD.103.123005](https://doi.org/10.1103/PhysRevD.103.123005). arXiv: [2101.11027](https://arxiv.org/abs/2101.11027)
2730 [astro-ph.HE].

- 2731 [74] H. C. Plummer. “On the Problem of Distribution in Globular Star Clusters: (Plate 8.)”
2732 In: *Monthly Notices of the Royal Astronomical Society* 71.5 (Mar. 1911), pp. 460–470.
2733 ISSN: 0035-8711. doi: [10.1093/mnras/71.5.460](https://doi.org/10.1093/mnras/71.5.460). eprint: <https://academic.oup.com/mnras/article-pdf/71/5/460/2937497/mnras71-0460.pdf>. URL:
2734 <https://doi.org/10.1093/mnras/71.5.460>.
- 2736 [75] Daniel R. Hunter. “Derivation of the anisotropy profile, constraints on the local velocity
2737 dispersion, and implications for direct detection”. In: *JCAP* 02 (2014), p. 023. doi:
2738 [10.1088/1475-7516/2014/02/023](https://doi.org/10.1088/1475-7516/2014/02/023). arXiv: [1311.0256 \[astro-ph.CO\]](https://arxiv.org/abs/1311.0256).
- 2739 [76] Barun Kumar Dhar and Liliya L. R. Williams. “Surface mass density of the Einasto family
2740 of dark matter haloes: are they Sersic-like?” In: *Mon. Not. Roy. Astron. Soc.* (2010). doi:
2741 [10.1111/j.1365-2966.2010.16446.x](https://doi.org/10.1111/j.1365-2966.2010.16446.x).
- 2742 [77] M. Baes and E. Van Hese. “Dynamical models with a general anisotropy profile”. In: *Astron. Astrophys.* 471 (2007), p. 419. doi: [10.1051/0004-6361:20077672](https://doi.org/10.1051/0004-6361:20077672). arXiv:
2743 [0705.4109 \[astro-ph\]](https://arxiv.org/abs/0705.4109).
- 2744 [78] Matthew G. Walker, Edward W. Olszewski, and Mario Mateo. “Bayesian analysis of re-
2745 solved stellar spectra: application to MMT/Hectochelle observations of the Draco dwarf
2746 spheroidal”. In: *mnras* 448.3 (Apr. 2015), pp. 2717–2732. doi: [10.1093/mnras/stv099](https://doi.org/10.1093/mnras/stv099).
2747 arXiv: [1503.02589 \[astro-ph.GA\]](https://arxiv.org/abs/1503.02589).
- 2749 [79] Nicholas L. Rodd et al. “Dark matter spectra from the electroweak to the Planck scale”. In:
2750 *J. High Energy Physics* 121.10.1007 (June 2021).
- 2751 [80] Pace, Andrew B and Strigari, Louis E. “Scaling relations for dark matter annihilation and
2752 decay profiles in dwarf spheroidal galaxies”. In: *Monthly Notices of the Royal Astronomical
2753 Society* 482.3 (Oct. 2018), pp. 3480–3496. ISSN: 0035-8711. doi: [10.1093/mnras/sty2839](https://doi.org/10.1093/mnras/sty2839).
- 2755 [81] Albert, A. et al. “Search for gamma-ray spectral lines from dark matter annihilation in
2756 dwarf galaxies with the High-Altitude Water Cherenkov observatory”. In: *Phys. Rev. D* 101 (10 May 2020), p. 103001. doi: [10.1103/PhysRevD.101.103001](https://doi.org/10.1103/PhysRevD.101.103001). URL:
2757 <https://link.aps.org/doi/10.1103/PhysRevD.101.103001>.
- 2759 [82] Victor Eijkhout and Edmund Show and Robert van de Geijn. *The Science of Computing. The Art of High Performance Computing*. Vol. 3. Open Copy published under CC-BY 4.0
2760 license, 2023, pp. 63–66.
- 2762 [83] The IceCube Collaboration. “The IceCube Neutrino Observatory: instrumentation and
2763 online systems”. In: *Journal of Instrumentation* 12.03 (Mar. 2017), P03012. doi: [10.1088/1748-0221/12/03/P03012](https://doi.org/10.1088/1748-0221/12/03/P03012). URL: <https://dx.doi.org/10.1088/1748-0221/12/03/P03012>.

- 2766 [84] Aartsen, M. et al. “IceCube search for dark matter annihilation in nearby galaxies and galaxy
2767 clusters”. In: *Phys. Rev. D* 88 (12 Dec. 2013), p. 122001. doi: [10.1103/PhysRevD.88.122001](https://doi.org/10.1103/PhysRevD.88.122001). URL: <https://link.aps.org/doi/10.1103/PhysRevD.88.122001>.
- 2769 [85] Pearl Sandick et al. “Sensitivity of the IceCube neutrino detector to dark matter annihilating
2770 in dwarf galaxies”. In: *Phys. Rev. D* 81 (8 Apr. 2010), p. 083506. doi: [10.1103/PhysRevD.81.083506](https://doi.org/10.1103/PhysRevD.81.083506). URL: <https://link.aps.org/doi/10.1103/PhysRevD.81.083506>.
- 2772 [86] Qinrui Liu and Jeffrey Lazar and Carlos A. Argüelles and Ali Kheirandish. “χaro: a tool
2773 for neutrino flux generation from WIMPs”. In: *Journal of Cosmology and Astroparticle
2774 Physics* 2020.10 (Oct. 2020), p. 043. doi: [10.1088/1475-7516/2020/10/043](https://doi.org/10.1088/1475-7516/2020/10/043). URL:
2775 <https://dx.doi.org/10.1088/1475-7516/2020/10/043>.
- 2776 [87] Tessa Cerver. “Time Integrated searches for Astrophysical Neutrino Sources using the
2777 IceCube Detector and Gender in Physics studies for the Genera Project”. PhD thesis.
2778 UNIVERSITE DE GEN ´ EVE, 2019, pp. 57–64.
- 2779 [88] Minjin Jeong on behalf of the IceCube Collaboration. “Search for Dark Matter Decay in
2780 Nearby Galaxy Clusters and Galaxies with IceCube”. In: *Proceedings of Science* 444.38
2781 (2023).
- 2782 [89] IceCube Collaboration. “Evidence for neutrino emission from the nearby active galaxy NGC
2783 1068”. In: *Science* 378.6619 (2022).
- 2784 [90] Nathan Whitehorn and Jakob van Santen. *Photospline*. IceCube: GitHub.
- 2785 [91] Paul H. C. Eilers and Brian D. Marx. “Flexible smoothing with B-splines and penalties”.
2786 In: *Statistical Science* 11.2 (1996), pp. 89–121. doi: [10.1214/ss/1038425655](https://doi.org/10.1214/ss/1038425655). URL:
2787 <https://doi.org/10.1214/ss/1038425655>.
- 2788 [92] The IceCube Collaboration. *Search for neutrino lines from dark matter annihilation and
2789 decay with IceCube*. 2023. arXiv: [2303.13663 \[astro-ph.HE\]](https://arxiv.org/abs/2303.13663).
- 2790 [93] The IceCube Collaboration. “Measurement of the multi-TeV neutrino interaction cross-
2791 section with IceCube using Earth absorption”. In: *Nature* 551 (2017).